



UNIVERSITÀ
DEGLI STUDI
DI PADOVA

Università degli Studi di Padova
Dipartimento di Fisica e Astronomia "Galileo Galilei"

SCUOLA DI DOTTORATO DI RICERCA IN FISICA
CICLO XXVI

**Study of Lepton Number
Conserving and Non-Conserving
Processes
Using GERDA Phase I Data**

Doctoral Dissertation of
Sabine Elisabeth Hemmer

Director of the Doctoral School:
Prof. Andrea Vitturi

Supervisor:
Prof. Riccardo Brugnera

Für meinen Opa Hans

Abstract

The GERMANIUM DETECTOR ARRAY (GERDA) experiment, located underground at the INFN Laboratori Nazionali del Gran Sasso (LNGS) in Italy, uses high-purity germanium detectors to search for neutrinoless double beta decay ($0\nu\beta\beta$) of ^{76}Ge . The first phase of the experiment lasted from November 2011 to May 2013 and collected data with a total exposure of $21.6 \text{ kg} \cdot \text{yr}$. In this thesis, a thorough analysis of these data was performed.

A background model was developed to decompose the observed energy spectrum in its individual contributions. The region around the Q-value of $0\nu\beta\beta$, $Q_{\beta\beta}$, at 2039 keV was studied in great detail. As main contributions to the background in this region, alpha and beta decays of the ^{238}U chain, beta decays of the ^{232}Th chain, and beta decays of ^{42}K were identified. It was shown that the background around $Q_{\beta\beta}$ can be approximated with a flat distribution.

Neutrino accompanied double beta decay ($2\nu\beta\beta$) is a lepton number conserving process allowed by the Standard Model. Due to the low background in the experiment, in the region dominated by $2\nu\beta\beta$ a signal-to-background ratio of 3 : 1 could be reached. This allowed to measure the half-life of the decay with a precision unprecedented by previous experiments, $T_{1/2}^{2\nu} = (1.96 \pm 0.13) \cdot 10^{21} \text{ yr}$.

Several beyond-Standard Model theories predict neutrinoless double beta decay with majoron emission ($0\nu\beta\beta\chi(\chi)$). Depending on the theory, this process can be lepton number violating or lepton number conserving. A search in the GERDA Phase I data gave no indication of contributions to the observed energy spectra for any of the majoron models. The lower limit on the half-life for the ordinary majoron model (spectral index $n = 1$) was determined to be $T_{1/2}^{0\nu\chi} > 4.15 \cdot 10^{23} \text{ yr}$ (90% quantile). This limit and the limits derived for the other majoron modes constitute the most stringent limits on $0\nu\beta\beta\chi(\chi)$ of ^{76}Ge measured to date.

The primary scope of the GERDA experiment was the search for $0\nu\beta\beta$ of ^{76}Ge . This lepton number violating decay is expected by extensions of the Standard Model. The observation of $0\nu\beta\beta$ would be the proof that the neutrino has a non-vanishing Majorana mass component. The analysis of the GERDA Phase I data did not reveal any hint for the presence of a signal from $0\nu\beta\beta$. A lower limit on the half-life was derived, $T_{1/2}^{0\nu} > 1.83 \cdot 10^{25} \text{ yr}$ (90% quantile).

Sommario

L'esperimento GERMANIUM DETECTOR ARRAY (GERDA), situato nei Laboratori Nazionali del Gran Sasso (LNGS) dell'INFN, utilizza rivelatori al germanio ultra-puro per la ricerca del doppio decadimento beta senza neutrini ($0\nu\beta\beta$). Tali rivelatori sono arricchiti nell'isotopo ^{76}Ge . La prima fase dell'esperimento è durata da novembre 2011 a maggio 2013 ed ha raccolto dati con un'esposizione totale di $21.6 \text{ kg} \cdot \text{yr}$.

In questa tesi è stato sviluppato dapprima un modello dei fondi per scomporre lo spettro energetico osservato nei suoi singoli componenti. La regione intorno al Q-valore della reazione $0\nu\beta\beta$, $Q_{\beta\beta}$, a 2039 keV è stata studiata in modo dettagliato. I contributi principali al fondo in questa regione sono: i decadimenti alfa e beta della catena del ^{238}U , i decadimenti beta della catena del ^{232}Th ed i decadimenti beta del ^{42}K . È stato dimostrato inoltre che il fondo intorno a $Q_{\beta\beta}$ può essere descritto con una costante.

Il doppio decadimento beta con emissione di due neutrini ($2\nu\beta\beta$) è un processo che conserva il numero leptonic ed è previsto dal Modello Standard. Nella regione dominata dagli eventi $2\nu\beta\beta$ è stato raggiunto un rapporto fra segnale e fondo di $3 : 1$. Questo risultato ha permesso di misurare il tempo di dimezzamento del decadimento con una precisione ineguagliata dagli esperimenti precedenti, $T_{1/2}^{2\nu} = (1.96 \pm 0.13) \cdot 10^{21} \text{ yr}$.

Alcuni modelli di fisica oltre il Modello Standard prevedono il doppio decadimento beta senza neutrini con emissione di uno o due majoroni ($0\nu\beta\beta\chi(\chi)$). In base alla teoria, questo processo può violare o conservare il numero leptonic. Un'analisi dei dati della prima fase di GERDA non ha fornito alcun riscontro di contributi di uno di questi modelli agli spettri energetici osservati. Il limite inferiore sul tempo di dimezzamento per il modello ordinario del majorone (indice spettrale $n = 1$) è stato stimato pari a $T_{1/2}^{0\nu\chi} > 4.15 \cdot 10^{23} \text{ yr}$ (quantile del 90%). Questo valore e quelli ricavati per altri modelli del majorone costituiscono i limiti più stringenti su $0\nu\beta\beta\chi(\chi)$ nel ^{76}Ge misurati fino ad ora.

Lo scopo primario dell'esperimento GERDA è la ricerca del $0\nu\beta\beta$ nel ^{76}Ge . Questo processo, che viola il numero leptonic, è previsto dalle estensioni del Modello Standard e la sua osservazione dimostrerebbe che la massa del neutrino ha una componente di tipo Majorana. L'analisi dei dati della prima fase di GERDA non ha rivelato nessun cenno della presenza di un segnale di $0\nu\beta\beta$. È stato così determinato un limite inferiore sul tempo di dimezzamento, $T_{1/2}^{0\nu} > 1.83 \cdot 10^{25} \text{ yr}$ (quantile del 90%).

Contents

1	Introduction	1
2	Neutrinos	3
2.1	Neutrinos in the Standard Model	3
2.2	Neutrino Oscillations	4
2.3	Neutrino Masses	6
2.4	Measurement of the Neutrino Mass	8
3	Double Beta Decay	9
3.1	Neutrino Accompanied Double Beta Decay	9
3.2	Neutrinoless Double Beta Decay	9
3.3	Neutrinoless Double Beta Decay with Majoron Emission	13
4	Double Beta Decay Experiments	17
4.1	Direct Searches	17
4.1.1	Experimental Requirements	17
4.1.2	Experiments	19
4.2	Indirect Searches	21
5	Germanium Detectors	23
5.1	Interaction of Photons, Electrons, Positrons, and α -particles with Matter	23
5.1.1	Photons	23
5.1.2	Electrons, Positrons, and α -particles	25
5.2	Semiconductor Detectors	25
5.3	Germanium Detector Properties	26
5.3.1	Detector Geometries	26
5.3.2	Operating Voltage	26
5.3.3	Operating Temperature	27
5.3.4	Energy Resolution	28
5.4	Signal Formation	28
5.4.1	Charge Carrier Drift	28
5.4.2	Pulse Shapes	29
5.5	Background Rejection	29

6	The GERDA Experiment	33
6.1	Experimental Setup	33
6.2	Detectors	35
6.2.1	Phase I Detectors	35
6.2.2	Phase II Detectors	36
7	GERDA Phase I Data	39
7.1	Data Processing	39
7.2	Energy Calibration	40
7.3	Data taking summary	43
7.4	Background Contributions and Background Index	47
7.5	Photon Line Intensities	52
8	Monte Carlo Simulation of the GERDA Experiment	55
8.1	Monte Carlo Description of the GERDA Experiment	55
8.2	Monte Carlo Event Processing	56
8.3	Simulated Background Sources	60
8.3.1	Results from Screening Measurements	61
8.3.2	Details of the Simulated Spectra	61
9	Background Model for the GERDA Phase I Data	83
9.1	Statistical Analysis Method	83
9.2	Background Model for the Golden Data Set	86
9.2.1	High Energy Region	86
9.2.2	Full Background Model	88
9.3	Background Model for the BEGe Sum Data Set	103
9.3.1	High Energy Region	103
9.3.2	Full Background Model	105
9.4	Summary	119
10	Neutrino Accompanied Double Beta Decay and Neutrinoless Double Beta Decay with Majoron Emission in GERDA Phase I	121
10.1	Statistical Analysis Method	121
10.2	Fit Results	123
10.2.1	Measurement of $T_{1/2}^{2\nu}$	123
10.2.2	Limits for $T_{1/2}^{0\nu\chi(\chi)}$	124
10.3	Systematic Uncertainties	128
10.3.1	Fit Model	129
10.3.2	MC Simulation	132
10.3.3	Data Acquisition and Selection	133
10.3.4	Total Systematic Uncertainty	133
10.4	Final Results and Discussion	135
10.4.1	Results for $2\nu\beta\beta$	135
10.4.2	Results for $0\nu\beta\beta\chi(\chi)$	137

11 Neutrinoless Double Beta Decay in GERDA Phase I	139
11.1 Statistical Analysis Method	139
11.1.1 Counting Method	139
11.1.2 Spectral Fit	142
11.1.3 Common Definitions	144
11.2 Pulse Shape Analysis	145
11.2.1 PSA for the BEGe detectors	145
11.2.2 PSA for the coaxial detectors	147
11.3 Input Parameters	149
11.4 Sensitivity	152
11.5 Data Analysis	156
11.6 Systematic Uncertainties	159
11.7 Final Results and Discussion	161
12 Conclusions and Outlook	163
A List of Monte Carlo Simulations	167
A.1 Alpha Model	167
A.2 Golden Data Set	168
A.3 BEGe Sum Data Set	170
B First Measurement of the Half-life of Neutrino Accompanied Double Beta Decay with GERDA Phase I	173
B.1 The Data Set	173
B.2 The Monte Carlo Simulation	173
B.3 Statistical Analysis Method and Fit Model	174
B.4 Crosschecks and Systematic Uncertainties	176
B.5 Results and Conclusion	180
C Fit Models and Posterior Probability Distributions for $0\nu\beta\beta\chi(\chi)$ with $n = 2, 3$ and 7	181
C.1 $0\nu\beta\beta\chi$ with $n = 2$	182
C.2 $0\nu\beta\beta\chi(\chi)$ with $n = 3$	184
C.3 $0\nu\beta\beta\chi\chi$ with $n = 7$	186
D Average Detection Efficiency $\langle\varepsilon\rangle$ of $0\nu\beta\beta$	189
Bibliography	191
Acknowledgments	205

Chapter 1

Introduction

More than 50 years have passed since the discovery of the neutrino. Oscillation measurements have established that the neutrinos are massive particles and the two squared mass differences have been measured, one in absolute value, one also in sign. However, many of the neutrino's characteristics are still a mystery today: Is the neutrino a Majorana particle, that is its own antiparticle? Is the neutrino mass hierarchy normal or inverted? What is the absolute neutrino mass scale? Is CP violated in the lepton sector?

The only practical way to experimentally test the nature of the neutrino is the search for neutrinoless double beta decay ($0\nu\beta\beta$). The observation of this process would be the proof that the neutrino has at least a Majorana component with a non-zero mass [1]. Neutrino accompanied double beta decay ($2\nu\beta\beta$) has been observed for several nuclei that cannot decay via single beta decay [2]. In this Standard-Model allowed decay, the nucleus undergoes double beta decay under emission of two electrons and two anti-neutrinos. If neutrinos are Majorana particles, the anti-neutrino emitted in one beta decay can be absorbed in the other, leading to $0\nu\beta\beta$. This process is not allowed by the Standard Model and the lepton number is violated by two units. Assuming the exchange of a light neutrino to be the dominant mechanism of the process allows to extract also information on the absolute mass scale. Several theories exist that predict neutrinoless double beta decay with majoron emission ($0\nu\beta\beta\chi(\chi)$). In this case, the decay is accompanied by the emission of one or two massless or very light bosons, the majorons. Depending on the theory, the process can conserve or violate lepton number. Details about the theory of neutrinos and double beta decay can be found in Chapters 2 and 3.

The first search for double beta decay dates back to 1948 [3]. Since then, a multitude of experiments using different isotopes and techniques has been conducted. An overview about the most recent results is given in Chapter 4. The most stringent lower limits on the half-life of $0\nu\beta\beta$ derive from searches with ^{76}Ge and ^{136}Xe [4–8]. They are of the order of 10^{25} yr. In all cases, the main limitation of the sensitivity is the background from natural radioactivity. A claim of observation of $0\nu\beta\beta$ [9] of ^{76}Ge has not been confirmed.

Germanium detectors are an attractive option for the search of $0\nu\beta\beta$. Since ^{76}Ge

is an isotope that undergoes double beta decay, the detector is also the source. Germanium can be produced very radio-pure, guaranteeing a small intrinsic background and the typical energy resolution is of the order of $(0.1 - 0.2)\%$. The main characteristics of germanium detectors are summarized in Chapter 5.

The GERMANIUM DETECTOR ARRAY (GERDA) [10, 11] is an experiment designed for the search of $0\nu\beta\beta$ of ^{76}Ge . It is located underground at the INFN Laboratori Nazionali del Gran Sasso (LNGS) in Italy. The environmental background component is reduced by passive shielding and minimization of material close to the detectors. To this scope, the bare detectors are directly submersed into a cryostat filled with liquid argon. The experiment is operated in two phases. The first phase lasted from November 2011 to May 2013 and collected a total of $21.6 \text{ kg} \cdot \text{yr}$ of data with detectors enriched in ^{76}Ge . The second phase is planned to start in 2014. Additional 20 kg of enriched detectors of a novel design featuring enhanced pulse shape analysis techniques and the read-out of scintillation light in the liquid argon will allow an improvement of the sensitivity by a factor ten. Details about the GERDA experiment and the Phase I data taking can be found in Chapters 6 and 7.

In a Monte Carlo campaign, all possible background sources contributing to the energy spectra of GERDA Phase I were simulated. This is described in Chapter 8.

Using the simulations, a background model describing the observed energy spectra was developed and the background composition around 2039 keV, the Q-value of double beta decay, was studied in detail. This analysis is presented in Chapter 9.

With the help of the background model, the half-life of $2\nu\beta\beta$ of ^{76}Ge was measured. A search for contributions from $0\nu\beta\beta\chi(\chi)$ in the GERDA Phase I data was performed for a variety of models predicting the emission of majorons in double beta decay. Chapter 10 gives all details of these analyses.

Finally, Chapter 11 describes the search for $0\nu\beta\beta$ in the GERDA Phase I data.

Chapter 2

Neutrinos

2.1 Neutrinos in the Standard Model

The neutrino was postulated by Wolfgang Pauli in 1930 to conserve energy and momentum in nuclear beta decay [12]. It was assumed to be a chargeless Dirac particle with a very small or even vanishing mass. The neutrino, ν , and anti-neutrino, $\bar{\nu}$, were considered distinct particles. Following theories, such as Enrico Fermi's theory describing beta decay [13, 14], were based on this assumption. Already in 1937, however, Ettore Majorana suggested a Majorana nature of the neutrino, implying that the neutrino was its own anti-particle, $\nu = \bar{\nu}$ [15]. Due to its only weakly interacting, it was only in 1956 that the (anti-)neutrino was observed directly by Reines and Cowan [16, 17] via the reaction

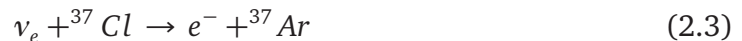


in a reactor experiment.

In order to study the difference between the neutrinos accompanying e^+ and e^- , respectively, Raymond Davis searched for the reaction



with a negative result [18], while reactions analogous to



could be observed. The conclusion from these observations was that ν and $\bar{\nu}$ are distinct particles and *lepton number* L was introduced: $L_{\nu_e} = L_{e^-} = +1$, $L_{\bar{\nu}_e} = L_{e^+} = -1$. By requiring lepton number conservation, reaction (2.2) is forbidden. All these observations pointed at a Dirac nature of the neutrino.

After theoretical suggestions by Tsung Dao Lee and Chen Ning Yang [19], in 1957 parity violation in weak decays was observed [20, 21]. Assuming a massless neutrino when solving the Dirac equation, this can be explained if either only the left-handed neutrinos and right-handed anti-neutrinos, $(\nu_L, \bar{\nu}_R)$, or only the right-handed neutrinos

and left-handed anti-neutrinos, $(\nu_R, \bar{\nu}_L)$, participate in the weak interaction [22–24]. The mystery was solved by the Goldhaber experiment in 1958 [25], which established the V–A structure of weak interaction by showing that only $(\nu_L, \bar{\nu}_R)$ is realized in nature. This result led to a new possible interpretation on why reaction (2.2) was not observed. This could either be due to the fact that the neutrino and the anti-neutrino are intrinsically different particles or it could simply be explained by the different helicities of the neutrino and the anti-neutrino. The experiment conducted by Raymond Davis could therefore not be used to distinguish between Dirac and Majorana neutrinos.

In the *Standard Model of Particle Physics (SM)*, the neutrino and the anti-neutrino are assumed to be different particles, with lepton number +1 and -1, respectively. Three lepton families exist: electron (e), muon (μ), and tau (τ). The analysis of the decay-width of the Z^0 boson confirmed the existence of only three types of light, active neutrinos [26]. Each lepton family contains a left-handed leptonic doublet formed by a charged lepton and a neutral, massless Dirac-neutrino, $(l, \nu_l)_L$, with $l = e, \mu, \tau$. The doublet is accompanied by a right-handed singlet l_R of the charged lepton. Right-handed neutrinos are not present in the SM. The lepton number is found to be conserved, i.e. the number of leptons is the same in the initial and final state of an interaction.

2.2 Neutrino Oscillations

An experiment carried out by Raymond Davis and his team in the Homestake Gold Mine at Lead, South Dakota, in the late 1960s, aiming at detecting solar neutrinos predicted by the *Standard Solar Model (SSM)*, observed a clear deficit in the ν_e flux [27] compared to the predictions [28]. Already in 1957, Bruno Pontecorvo and in 1962 Ziro Maki, Masami Nakagawa, and Shoichi Sakata had suggested a mechanism of *neutrino oscillations* [29–31] that could have explained this mystery known as the *solar neutrino problem*. In the following years, many experiments like Kamiokande [32], SAGE [33], and Gallex [34] confirmed this deficit in the measured ν_e flux from the sun. Also for the atmospheric neutrinos an anomaly was observed: the measured ν_μ flux showed a deficit when compared to theoretical predictions [35, 36], while this lack was not present in the ν_e flux. Nevertheless, it was only more than 30 years later that the Super-Kamiokande [37] and SNO [38] experiments finally established the existence of neutrino oscillations. The observed deficits could be explained by oscillations of the neutrino of one flavor, ν_α , $\alpha = e, \mu, \tau$, to a different flavor, ν_β . In case of the sun this is $\nu_e \rightarrow \nu_\mu$, in case of the atmospheric neutrinos it is $\nu_\mu \rightarrow \nu_\tau$.

Oscillations between different neutrino flavors are possible if the flavor (or weak interaction) eigenstates, $|\nu_\alpha\rangle$, $\alpha = e, \mu, \tau$, do not coincide with the mass eigenstates, $|\nu_i\rangle$, $i = 1, 2, 3$. The flavor eigenstates can then be expressed as coherent superpositions of the mass eigenstates,

$$|\nu_\alpha\rangle = \sum_i U_{\alpha i}^* |\nu_i\rangle, \quad (2.4)$$

where U is a unitary matrix referred to as the *Pontecorvo-Maki-Nakagawa-Sakata (PMNS)* matrix. A common parametrization of the PMNS matrix is

$$U = \begin{pmatrix} 1 & 0 & 0 \\ 0 & \cos \theta_{23} & \sin \theta_{23} \\ 0 & -\sin \theta_{23} & \cos \theta_{23} \end{pmatrix} \times \begin{pmatrix} \cos \theta_{13} & 0 & \sin \theta_{13} e^{-i\delta} \\ 0 & 1 & 0 \\ -\sin \theta_{13} e^{i\delta} & 0 & \cos \theta_{13} \end{pmatrix} \times \begin{pmatrix} \cos \theta_{12} & \sin \theta_{12} & 0 \\ -\sin \theta_{12} & \cos \theta_{12} & 0 \\ 0 & 0 & 1 \end{pmatrix} \times \begin{pmatrix} e^{i\alpha_1/2} & 0 & 0 \\ 0 & e^{i\alpha_2/2} & 0 \\ 0 & 0 & 1 \end{pmatrix}, \quad (2.5)$$

where θ_{ij} are the three mixing angles, δ is known as the CP-violating Dirac phase, and α_i , $i = 1, 2$, are CP-violating Majorana phases. The latter two are only of relevance if the neutrino is a Majorana particle, that is its own anti-particle. The time evolution of a neutrino created in the flavor eigenstate $|\nu_\alpha\rangle$ is calculated from the mass eigenstates it is composed of. After having travelled the distance L , the neutrino is a superposition of all flavors,

$$|\nu_\alpha(L)\rangle = \sum_i U_{\alpha i}^* e^{-i(m_i^2/2E)L} |\nu_i\rangle, \quad (2.6)$$

where m_i is the mass of the i -th mass eigenstate and E is the average energy of all mass eigenstates. The probability of finding the neutrino in a flavor state $|\nu_\beta\rangle$ after it travelled the distance L is

$$P_{\alpha \rightarrow \beta} = |\langle \nu_\beta | \nu_\alpha(L) \rangle|^2 = \sum_i |U_{\beta i} U_{\alpha i}^*|^2 + 2\text{Re} \sum_{j>i} U_{\beta i} U_{\beta j}^* U_{\alpha i}^* U_{\alpha j} e^{(-i\Delta m_{ij}^2/2E)L}, \quad (2.7)$$

where $\Delta m_{ij}^2 = m_i^2 - m_j^2$ is the squared mass difference between the two mass eigenstates m_i and m_j . Note that oscillations cannot occur for massless neutrinos or for neutrinos with degenerate masses ($\Delta m^2 = 0$). Only mass squared differences can be inferred from oscillation measurements, the absolute mass scale is not accessible for these experiments.

The formalism described above refers to neutrino oscillations in vacuum. In presence of matter, e.g., in the sun, neutrinos undergo scattering processes with W^\pm - and Z^0 -exchange, with the first one being sensitive to the flavor. This alters the oscillation probability. The effect is known as the *Mikheyev-Smirnov-Wolfenstein (MSW) effect* [39, 40]. The large reduction in the flux of the solar neutrinos can only be explained considering also the MSW effect.

All three mixing angles and the two mass differences, Δm_{32}^2 and Δm_{21}^2 , have been determined by experiments with solar, atmospheric, reactor, and accelerator neutrinos. It is not possible to determine the sign of the mass difference Δm_{32}^2 from oscillation measurements, while the MSW effect observed for solar neutrinos gives access to the positive sign of Δm_{21}^2 , establishing $m_2 > m_1$. Therefore, two possible *mass hierarchies* have to be considered when decomposing the mass eigenstates into flavor eigenstates.



Figure 2.1: Schematic of the normal (left) and inverted (right) mass hierarchy. Figure taken from [41].

Considering also the results shown in Table 2.1, the *normal hierarchy* assumes $\Delta m_{32}^2 > 0$, that is $m_1 < m_2 \ll m_3$, while the *inverted hierarchy* describes the case of $\Delta m_{32}^2 < 0$, $m_3 \ll m_1 < m_2$. A schematic of both cases can be seen in Fig. 2.1. If the mass of the lightest neutrino is much larger than the mass differences, the hierarchy is referred to as *quasi-degenerate*, $m_1 \cong m_2 \cong m_3$. The measurement of the CP-violating phase δ and the Majorana phases α_1 and α_2 is beyond experimental reach at the moment. Table 2.1 summarizes the neutrino oscillation parameters derived from a global fit to the current oscillation data.

Table 2.1: Best-fit values of a global analysis of the current oscillation data. All values are taken from [42]. For Δm_{31}^2 , $\sin^2 \theta_{23}$, and $\sin^2 \theta_{13}$ the case of normal hierarchy (inverted hierarchy) is given in the upper (lower) row. For an alternative analysis with comparable results see [43].

parameter	best fit [1σ range]
$\Delta m_{21}^2 (10^{-5} \text{eV}^2)$	7.62 [7.43, 7.81]
$\Delta m_{31}^2 (10^{-3} \text{eV}^2)$	2.55 [2.46, 2.61]
	-2.43 [-2.37, -2.50]
$\sin^2 \theta_{12}$	0.320 [0.303, 0.336]
$\sin^2 \theta_{23}$	0.613 [0.573, 0.635]
	0.600 [0.569, 0.626]
$\sin^2 \theta_{13}$	0.0246 [0.0218, 0.0275]
	0.0250 [0.0223, 0.0276]

2.3 Neutrino Masses

The observation of neutrino oscillations necessitates an extension of the SM accounting for the non-vanishing neutrino mass. In the following, a brief overview on how to

accomodate neutrino masses in the framework of the SM is presented. More details can be found in e.g., [44] and references therein.

Following the SM approach of Yukawa coupling to the Higgs-field to generate particle masses, a Dirac mass term for the neutrino in the Lagrangian is written as

$$\mathcal{L}^D = -m_D \bar{\nu}_R \nu_L + h.c., \quad (2.8)$$

with $m_D = \nu h_\nu$, where ν is the vacuum expectation value of the Higgs field, h_ν the neutrino Yukawa coupling constant, and ν_R and ν_L the right- and left-handed components of the neutrino field, respectively¹. The only addition to the SM is the introduction of the right-handed components of the neutrino fields. They are called *sterile* since they do not participate in the weak interactions.

The Dirac mass term is not the only possibility of introducing a Lorentz invariant neutrino mass term in the Lagrangian. Also the Majorana mass terms

$$\mathcal{L}^L = \frac{1}{2} m_L \bar{\nu}_L^C \nu_L + h.c. \quad (2.9)$$

and

$$\mathcal{L}^R = \frac{1}{2} m_R \bar{\nu}_R^C \nu_R + h.c. \quad (2.10)$$

for ν_L and ν_R have to be considered².

The Majorana mass term for left-handed neutrinos in equation (2.9) is not invariant under SM symmetry transformations. To assure gauge invariance, $m_L = 0$ is required to accomodate it in the SM framework. Thus, the most general neutrino mass Lagrangian becomes

$$\mathcal{L}^{D+M} = \mathcal{L}^D + \mathcal{L}^R = \begin{pmatrix} \bar{\nu}_L^C & \bar{\nu}_R \end{pmatrix} \begin{pmatrix} 0 & m_D \\ m_D & m_R \end{pmatrix} \begin{pmatrix} \nu_L & \nu_R^C \end{pmatrix} + h.c.. \quad (2.11)$$

Of course, (2.9) with $m_L \neq 0$ can enter the Lagrangian, if physics beyond the SM is considered.

A direct consequence of the Majorana mass term in the Lagrangian is that neutrinos are their own anti-particles, $\nu = \bar{\nu}$. Since this is only possible for neutral, colorless particles, neutrinos are the only elementary particles for which such a mass term can enter the Lagrangian.

The smallness of neutrino masses compared to the masses of the other fermions in the SM is a big puzzle. A natural explanation for this phenomenon is provided by the *see-saw mechanism* [45–48]. It requires $m_L = 0$ to conserve SM symmetries and assumes $m_D \ll m_R$. Within the SM, the Dirac mass m_D is limited to the order of the electroweak scale, as it is protected by the SM symmetries. The Majorana mass m_R , on the other hand, is not restricted by the SM. If m_R is generated by new physics beyond the SM, it is protected by the symmetries of these new physics, allowing m_R up to the

¹The adjoint spinor $\bar{\nu}$ of ν is given by $\bar{\nu} = \nu^\dagger \gamma^0$

² $\nu_L^C = \mathcal{C} \bar{\nu}_L^T$ and $\nu_R^C = \mathcal{C} \bar{\nu}_R^T$ are the charge conjugate fields of ν_L and ν_R , respectively

order of the GUT-scale, $10^{14} - 10^{16}$ GeV. These considerations make $m_D \ll m_R$ a rather natural choice. The mass eigenstates m_i , $i = 1, 2$, of equation (2.11) are obtained by diagonalizing the mass matrix. They result to be $m_1 \simeq \frac{m_D^2}{m_R}$ and $m_2 \simeq m_R$. Since the mixing angle is very small, $\tan 2\theta = 2m_D/m_R$, the very light ν_1 is composed mainly of the active ν_L and the heavy ν_2 is composed mainly of the sterile ν_R . The heavier $\nu_2 \simeq \nu_R$ is, the lighter is $\nu_1 \simeq \nu_L$.

2.4 Measurement of the Neutrino Mass

From oscillation measurements, only mass squared differences can be inferred. To determine the absolute neutrino mass scale, three approaches can be followed. Note that the corresponding experiments are complementary, as the measured mass parameter depends on the type of experiment.

Cosmological and astrophysical measurements provide the possibility to estimate the sum of the three neutrino masses, $\sum_{i=1}^3 m_i$. In the early Universe, small density fluctuations were present. The significant thermal velocity of the light neutrinos allowed them to escape from over-dense regions, washing out the structures. The result is visible in the large scale structures we observe today and its extent depends on the neutrino masses. An overview over different methods to extract $\sum_{i=1}^3 m_i$ is given in [49]. Generally, the results depend strongly on the model and on the data combination used in the analysis. The latest result, published by the Planck project [50], yields $\sum_{i=1}^3 m_i < 0.23$ eV [51].

The neutrino mass can be measured directly in decays where one of the decay products is a neutrino. The *effective electron neutrino mass* is defined as $m_{\nu_e} = \sqrt{\sum_i |U_{ei}|^2 m_i^2}$, where the sum runs over all mass eigenstates and U_{ei} are the elements of the PMNS matrix. It influences the energy spectrum of the visible daughter particles around the endpoint energy of the decay. The best limit was determined from tritium decays, $m_{\nu_e} < 2.3$ eV by the Mainz experiment [52] and $m_{\nu_e} < 2.1$ eV by the Troitsk experiment [53]. The KATRIN experiment, currently under construction, is designed to have a sub eV sensitivity [54].

The third class of neutrino mass experiments are those searching for *neutrinoless double beta decay*. They are sensitive to the *effective Majorana neutrino mass*, $\langle m_{\beta\beta} \rangle = |\sum_{i=1}^3 m_i U_{ei}^2|$.

Chapter 3

Double Beta Decay

3.1 Neutrino Accompanied Double Beta Decay

Even-even nuclei are more bound than odd-odd nuclei due to the pairing interaction. Therefore, even-even nuclei exist, whose ground states are energetically lower than those of their odd-odd neighbors, forbidding beta decay, see Fig. 3.1. In this case, it is possible that two neutrons, n , decay simultaneously into two protons, p , two electrons, e^- , and two electron anti-neutrinos, $\bar{\nu}_e$:

$$2\nu\beta\beta : (Z, A) \rightarrow (Z + 2, A) + 2e^- + 2\bar{\nu}_e, \quad (3.1)$$

where Z is the atomic charge and A the mass number. This process is called *neutrino accompanied double beta decay* ($2\nu\beta\beta$). It is shown in Fig. 3.2(a).

With the nuclear matrix element, $M^{2\nu}$, and the phase space factor, $G^{2\nu}(Q_{\beta\beta}, Z)$, the decay rate can be written as

$$\Gamma^{2\nu} = 1/T_{1/2}^{2\nu} = G^{2\nu}(Q_{\beta\beta}, Z) \cdot |M^{2\nu}|^2. \quad (3.2)$$

The phase space factor $G^{2\nu}(Q_{\beta\beta}, Z)$ is very sensitive to the Q-value of the decay, $Q_{\beta\beta}$. It scales with $Q_{\beta\beta}^{11}$ [56, 57].

Neutrino accompanied double beta decay is a lepton number conserving SM process, which does not allow the discrimination between Dirac and Majorana neutrinos. In experiments, the energy of the two electrons is measured, while the two anti-neutrinos escape. The measured energy spectrum is therefore continuous, with a maximum around $Q_{\beta\beta}/3$. An example can be seen in Fig. 3.3.

3.2 Neutrinoless Double Beta Decay

The possibility of *neutrinoless double beta decay* ($0\nu\beta\beta$) was first proposed by Furry in 1939 [59] as a method to gain insight about the Dirac or Majorana nature of the neutrino. In this decay, two neutrons, n , decay simultaneously into two protons, p , and two electrons, e^- , with no emission of electron anti-neutrinos, $\bar{\nu}_e$:

$$0\nu\beta\beta : (Z, A) \rightarrow (Z + 2, A) + 2e^-. \quad (3.3)$$

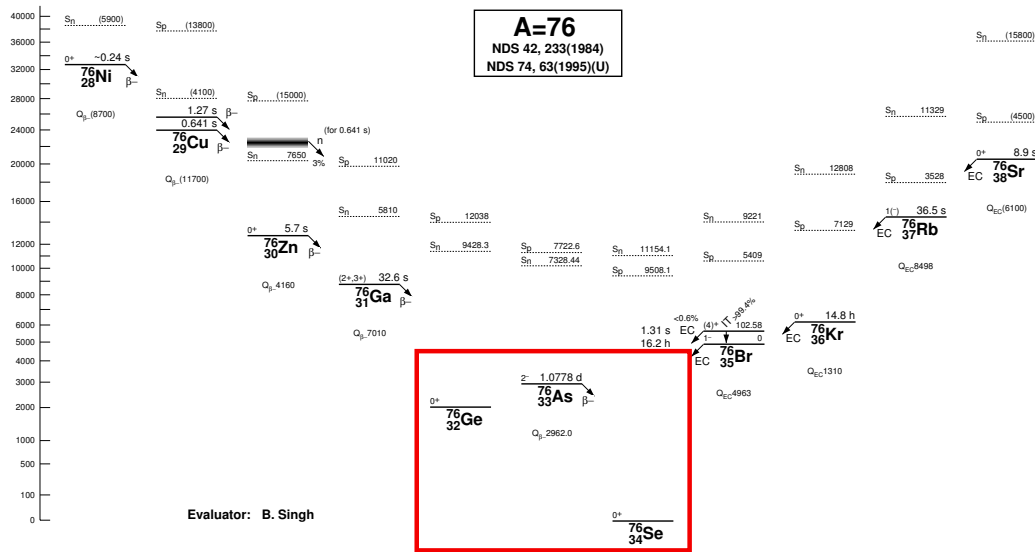


Figure 3.1: Isobars with $A=76$. The mass of ^{76}Ge is less than the mass of ^{76}As , but larger than the mass of ^{76}Se . Single beta decay is energetically forbidden, but double beta decay is allowed. Figure adopted from [55].

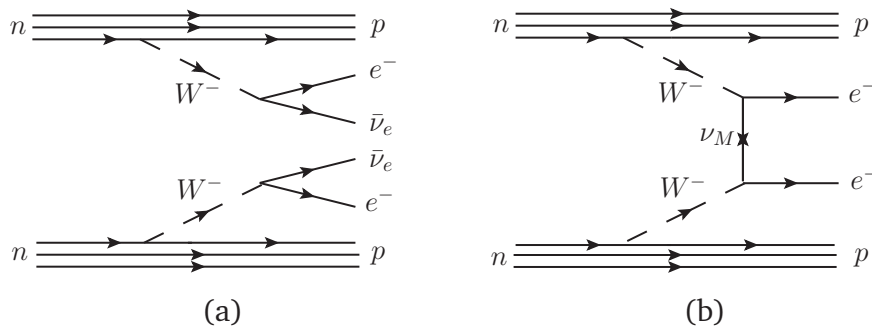


Figure 3.2: Feynman diagram of (a) neutrino accompanied double beta decay ($2\nu\beta\beta$) and (b) neutrinoless double beta decay ($0\nu\beta\beta$).

The experimental signature of $0\nu\beta\beta$ is a peak at $Q_{\beta\beta}$ in the combined energy spectrum of the two emitted electrons, as seen in Fig. 3.3. Since lepton number is violated by two, $\Delta L = 2$, the process is not allowed in the SM and its observation would undoubtedly proof the existence of physics beyond the SM.

As pointed out by the *blackbox* or *Schechter-Valle theorem* [1], the existence of $0\nu\beta\beta$ necessarily requires a Majorana neutrino mass, independent of the decay mechanism. The generated Majorana mass term is, however, only of $\mathcal{O}(10^{-24})\text{eV}$ [60] and thus many orders of magnitude too small to explain the observations of the mass splittings in oscillation experiments. As a consequence, other Majorana or Dirac masses have to contribute to the neutrino mass.

The simplest mechanism leading to $0\nu\beta\beta$ is the exchange of a light Majorana neutrino. This process would allow direct conclusions on the mass and nature of the neutrino. Possible alternative mechanisms, involving heavy Majorana neutrinos,

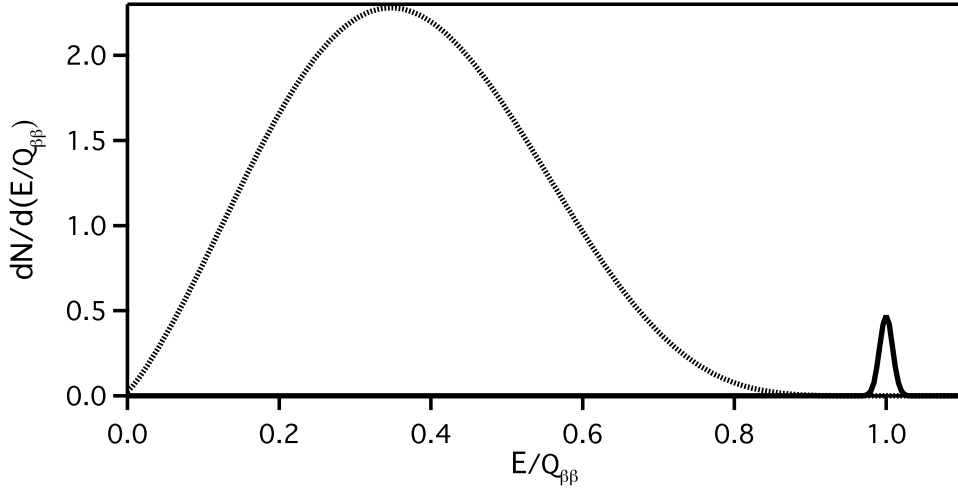


Figure 3.3: Spectra of the sum kinetic energy of the two electrons, E , normalized to the Q -value, $Q_{\beta\beta}$, for neutrino accompanied (dashed line) and neutrinoless (continuous line) double beta decay. Figure taken from [58].

positive chirality currents, and supersymmetric particles, might not allow to draw any conclusions on the dominating neutrino nature and mass scale [61]. All these alternative mechanisms require the introduction of new particles or interactions which are not present in the SM. The rest of this section is dedicated to the case of $0\nu\beta\beta$ via exchange of a light Majorana neutrino. A popular example involving additional particles in the final states, so-called majorons, is presented in Sec. 3.3.

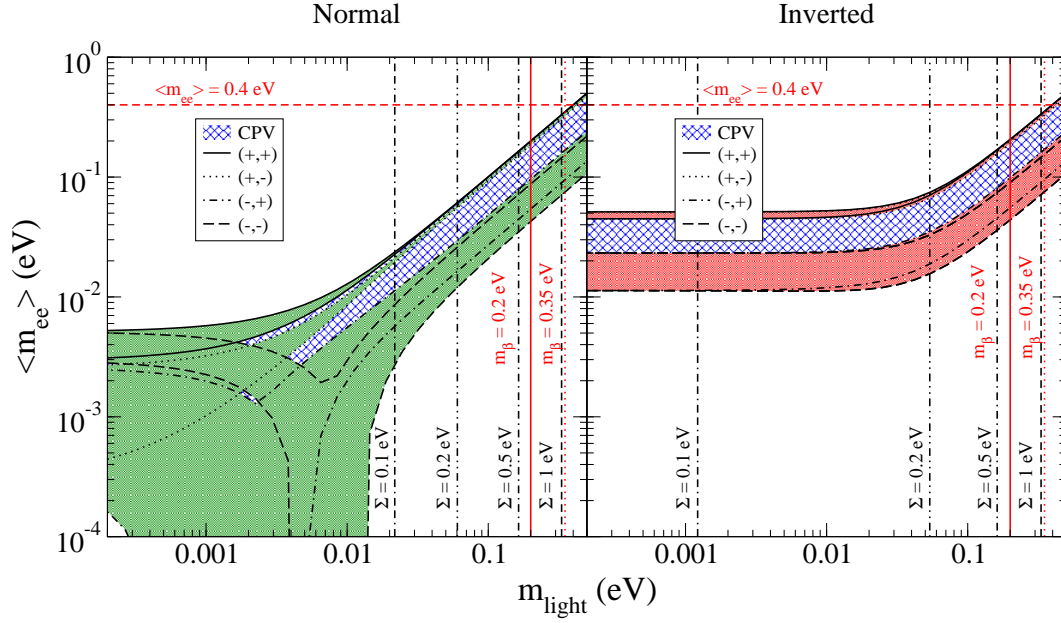
The diagram for $0\nu\beta\beta$ based on light Majorana neutrino exchange is depicted in Fig. 3.2(b). When the neutrino is emitted at one vertex, it has almost total positive helicity. Only a small component of $\mathcal{O}(m_\nu/E)$, where m_ν is the neutrino mass and E the energy, has negative helicity and can be absorbed at the other vertex. The process is only possible, if the neutrino is a massive Majorana particle and the amplitude is proportional to the *effective Majorana neutrino mass*

$$\langle m_{\beta\beta} \rangle = \left| \sum_{i=1}^3 m_i U_{ei}^2 \right|, \quad (3.4)$$

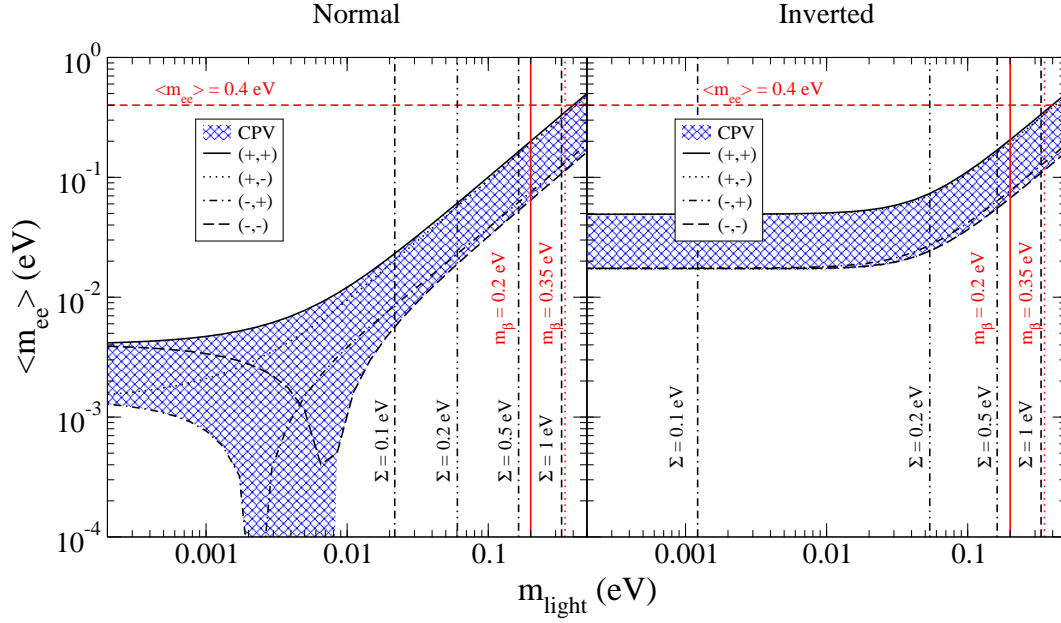
where m_i are the neutrino mass eigenstates and U_{ei} the corresponding PMNS matrix elements, see equation (2.5). The decay rate of $0\nu\beta\beta$ is then given as [62]

$$\Gamma^{0\nu} = 1/T_{1/2}^{0\nu} = G^{0\nu}(Q_{\beta\beta}, Z) \cdot |M^{0\nu}|^2 \cdot \langle m_{\beta\beta} \rangle^2, \quad (3.5)$$

where $T_{1/2}^{0\nu}$ is the half-life of the decay, $G^{0\nu}(Q_{\beta\beta}, Z)$ the phase space factor, which scales with $Q_{\beta\beta}^5$ [63, 64] and depends on the nuclear charge, Z , and $M^{0\nu}$ is the nuclear matrix element. The phase space factor, $G^{0\nu}(Q_{\beta\beta}, Z)$, can be calculated analytically. The nuclear matrix element, $M^{0\nu}$, provides a large source of uncertainty, since the results differ noticeably depending on the nuclear model used for the evaluation. For a discussion see [58] and [63], and references therein.



(a)



(b)

Figure 3.4: Effective Majorana neutrino mass as a function of the lightest neutrino mass for the (a) 3σ -ranges and (b) best-fit values given in Ref. [42] and listed in Table 2.1 for the normal (left) and inverted (right) hierarchy scheme. The blue shaded areas can only be realized for non-trivial CP values. (\pm, \pm) denote different CP conserving situations, corresponding to signs of m_2 and m_3 , relative to positive m_1 . Prospective future values of $\sum_{i=1}^3 m_i = \Sigma$ and $m_{\nu_e} = m_\beta$ are also given. Figure taken from [65].

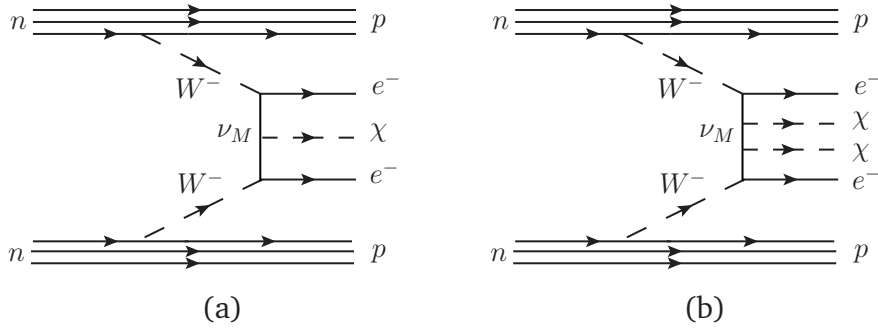


Figure 3.5: Feynman diagram of neutrinoless double beta decay (a) with emission of one majoron ($0\nu\beta\beta\chi$) and (b) emission of two majorons ($0\nu\beta\beta\chi\chi$).

Figure 3.4 shows the effective Majorana neutrino mass as a function of the lightest neutrino mass for the 3σ -range and the best fit values of the oscillation parameters given in Table 2.1. The normal as well as the inverted hierarchy are shown. Since for the normal hierarchy the most massive state has a small contribution due to the small mixing angle, the effective Majorana neutrino mass results to be small. For the inverted hierarchy the contrary holds, and the large contribution of the heavier neutrino states leads to a larger effective Majorana neutrino mass. For the normal hierarchy, the contributions can cancel due to the CP phases, leading to a vanishing effective Majorana neutrino mass.

Note that the existence of sterile neutrinos is not taken into account here. For a discussion of the current situation regarding hints on their existence and their impact on $0\nu\beta\beta$ see elsewhere [65, 66].

3.3 Neutrinoless Double Beta Decay with Majoron Emission

Majorana neutrinos are their own anti-particles and cannot carry an additive quantum number, such as baryon number, B , or lepton number, L . As a consequence, in models with Majorana neutrinos, global $(B - L)$ symmetry is broken. The breaking of the symmetry leads to the existence of a massless Goldstone boson, the *majoron*, χ .

In the original majoron models, the majoron is part of an electroweak singlet [67, 68], doublet [69], or triplet [70]. All models have in common that they predict *neutrinoless double beta decay with majoron emission* ($0\nu\beta\beta\chi$),

$$0\nu\beta\beta\chi : (Z, A) \rightarrow (Z + 2, A) + 2e^- + \chi. \quad (3.6)$$

The corresponding Feynman diagram can be seen in Fig. 3.5(a).

The interactions of the doublet and triplet majorons with the Z^0 boson would give additional contributions to its decay width. Both models could be ruled out by measurements at LEP [26]. The models with a majoron singlet, on the other hand, are still within possibility [71]. Since the coupling strength of the majoron to the

neutrino is proportional to m_ν/M , where m_ν is the neutrino mass and M is the scale of spontaneous lepton number breaking, $M \simeq m_R$, the singlet model needs severe finetuning to obtain an observable rate of $0\nu\beta\beta\chi$.

Supersymmetric models exist that lead to $0\nu\beta\beta\chi$ [72, 73]. Even the emission of two majorons ($0\nu\beta\beta\chi\chi$),

$$0\nu\beta\beta\chi\chi : (Z,A) \rightarrow (Z+2,A) + 2e^- + 2\chi, \quad (3.7)$$

is possible [74]. Figure 3.5(b) shows the Feynman diagram of this decay.

In recent years, a variety of new majoron models has been developed. In this context, *majoron* denotes a massless or very light boson, not necessarily a Goldstone boson, which couples to neutrinos. There are models which foresee majorons carrying leptonic charge, thus assuring lepton number conservation and forbidding $0\nu\beta\beta$. For the case of majorons with $L = -2$, $0\nu\beta\beta\chi$ is expected [75], while $L = -1$ for the majoron leads to $0\nu\beta\beta\chi\chi$ [76]. Also models with a vector majoron are introduced. In these models, the majoron is the longitudinal component of a massive gauge boson emitted in double beta decay [77]. In the framework of the $SU(3)_L \otimes SU(1)_N$ electroweak model, $0\nu\beta\beta\chi$ and $0\nu\beta\beta\chi\chi$ [78] is predicted. Lastly, when considering brane-bulk scenarios in particle physics, the breaking of the standard global $(B-L)$ symmetry by a gauge singlet Higgs field in the bulk leads to extradimensional majorons with a set of Kaluza-Klein modes [79].

Independently of the model, the decay rate for $0\nu\beta\beta\chi$ and for $0\nu\beta\beta\chi\chi$ can be written as

$$\Gamma^{0\nu\chi} = 1/T_{1/2}^{0\nu\chi} = |\langle g_\alpha \rangle|^2 \cdot G_\alpha^{0\nu\chi}(Q_{\beta\beta}, Z) \cdot |M_\alpha^{0\nu\chi}|^2, \quad (3.8)$$

and

$$\Gamma^{0\nu\chi\chi} = 1/T_{1/2}^{0\nu\chi\chi} = |\langle g_\alpha \rangle|^4 \cdot G_\alpha^{0\nu\chi\chi}(Q_{\beta\beta}, Z) \cdot |M_\alpha^{0\nu\chi\chi}|^2, \quad (3.9)$$

respectively, where $|\langle g_\alpha \rangle|$ is the *effective coupling constant*, $|M_\alpha^{0\nu\chi}|$ and $|M_\alpha^{0\nu\chi\chi}|$ are the nuclear matrix elements, $G_\alpha^{0\nu\chi}(Q_{\beta\beta}, Z)$ and $G_\alpha^{0\nu\chi\chi}(Q_{\beta\beta}, Z)$ are the phase space factors, and α denotes the various models. The phase space factors can be parametrized as a function of the Q-value, $Q_{\beta\beta}$, the sum kinetic energy of the two electrons emitted in the decay, E , and the *spectral index*, n ,

$$G_\alpha^{0\nu\chi(\chi)}(Q_{\beta\beta}, Z) \sim (Q_{\beta\beta} - E)^n. \quad (3.10)$$

Normal $2\nu\beta\beta$ has $n = 5$, whereas $0\nu\beta\beta\chi$ can have $n = 1, 2$ or 3 and $0\nu\beta\beta\chi\chi$ can have $n = 3$ or 7 , depending on the model. As a consequence, the energy spectrum of the two emitted electrons allows to distinguish the different models. The energy spectra for all modes of $0\nu\beta\beta\chi$ and $0\nu\beta\beta\chi\chi$ together with the spectrum of $2\nu\beta\beta$ are shown in Fig. 3.6.

Table 3.1 summarizes the main characteristics of the majoron models described above. The first section considers lepton number violating models (I) allowing $0\nu\beta\beta$, whereas in the second section lepton number conserving models (II) are listed, where $0\nu\beta\beta$ is not allowed.

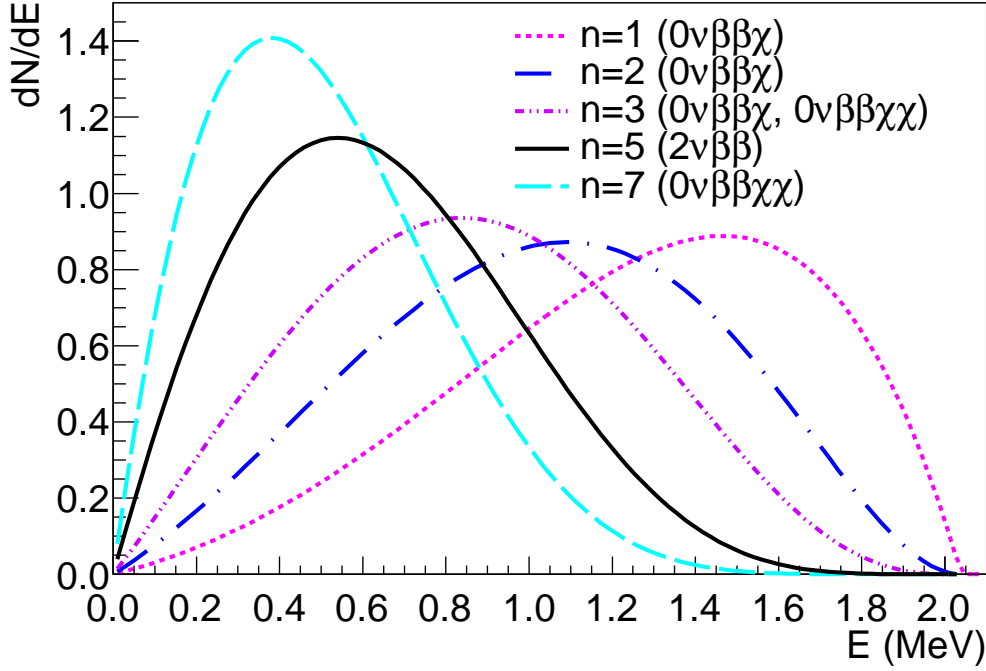


Figure 3.6: Spectra of the sum kinetic energy of the two electrons, E , for $n = 5$ ($2\nu\beta\beta$) and $n = 1, 2, 3, 7$ ($0\nu\beta\beta\chi$ and $0\nu\beta\beta\chi\chi$ modes). The spectra are based on the functions provided in [80,81].

Table 3.1: Summary of different majoron models based on [76, 82, 83]. The first section considers lepton number violating models (I) allowing $0\nu\beta\beta$, while in the second section lepton number conserving models (II) are listed, where $0\nu\beta\beta$ is not allowed. In the second column, the information on whether one majoron, χ , or two majorons, $\chi\chi$, are emitted is given, the third column tells if the majoron is a Goldstone boson, the fourth column provides its lepton number, L , the fifth column gives the spectral index, n , and the last column lists the nuclear matrix elements.

Model	Mode	Goldstone boson	L	n	Matrix element
IB	χ	no	0	1	$M_F - M_{GT}$
IC	χ	yes	0	1	$M_F - M_{GT}$
ID	$\chi\chi$	no	0	3	$M_{Fw^2} - M_{GTw^2}$
IE	$\chi\chi$	yes	0	3	$M_{Fw^2} - M_{GTw^2}$
IF (bulk)	χ	bulk field	0	2	—
IIB	χ	no	-2	1	$M_F - M_{GT}$
IIC	χ	yes	-2	3	M_{CR}
IID	$\chi\chi$	no	-1	3	$M_{Fw^2} - M_{GTw^2}$
IIE	$\chi\chi$	yes	-1	7	$M_{Fw^2} - M_{GTw^2}$
IIF	χ	gauge boson	-2	3	M_{CR}

Chapter 4

Double Beta Decay Experiments

4.1 Direct Searches

4.1.1 Experimental Requirements

The expected number of signal events, N_S , for any double beta process is given by

$$N_S = \varepsilon \cdot f \cdot \frac{M \cdot N_A}{m_A} \cdot (1 - e^{-t \ln(2)/T_{1/2}}), \quad (4.1)$$

where ε is the signal efficiency, f and m_A are the abundance and molar mass of the isotope under study, M is the total source material mass, N_A is Avogadro's number, t the time of measurement, and $T_{1/2}$ is the half-life of the double beta decay. For $t \ll T_{1/2}$, $e^{-t \ln(2)/T_{1/2}}$ can be approximated as $1 + \frac{-t \ln 2}{T_{1/2}}$, resulting in

$$N_S = \varepsilon \cdot f \cdot \frac{M \cdot N_A}{m_A} \cdot \frac{t \cdot \ln 2}{T_{1/2}}. \quad (4.2)$$

From Equation (4.2) it is clear that the sensitivity of a double beta experiment scales linearly with $\varepsilon \cdot f \cdot M \cdot t$ in the absence of background events, N_B .

In the presence of background, for $0\nu\beta\beta$, where the signal is a peak at $Q_{\beta\beta}$, the expected number of background events is

$$N_B = M \cdot BI \cdot \Delta E \cdot t, \quad (4.3)$$

with BI the *background index* in cts/(keV·kg·yr) and ΔE the energy window around $Q_{\beta\beta}$ used for the signal search. The latter is related to the energy resolution. When assuming a large enough background level such that the uncertainty $\sigma_{N_B} \sim \sqrt{N_B}$, the half-life to which an experiment is sensitive can be expressed as [58, 84]

$$T_{1/2}^{0\nu} = \frac{4.16 \cdot 10^{26} \text{yr}}{n_\sigma} \cdot \varepsilon \cdot f \cdot \frac{1}{m_A} \sqrt{\frac{M \cdot t}{BI \cdot \Delta E}}, \quad (4.4)$$

where n_σ is the number of standard deviations corresponding to a given confidence level, C.L.. In the following, the most important factors entering Equation (4.4) are discussed.

Background index, BI The background index plays a decisive role in the reachable sensitivity of an experiment. Various sources of background have to be considered. The radioactive isotopes from the natural decay chains of ^{238}U and ^{232}Th are present in all materials, also in the detector components. Decays, in which α -, β -, and γ -particles at energies above the Q -value of the double beta isotope under study are emitted, lead to background events in the energy *region of interest (ROI)*. Therefore, out of the 35 existing double beta isotopes, only eleven with $Q_{\beta\beta} > 2$ MeV are considered for double beta decay experiments to restrict the contributions from natural radioactivity to a minimum¹. In general, all materials used in the experiments have to be carefully selected and purified. Also radon gas, present in the natural decay chains, is a problem, as it can diffuse through materials and its charged decay products can stick to detector components.

An external source of background are cosmic rays. In order to limit their contribution in the *ROI*, double beta experiments are placed in underground laboratories. In this way, the contribution is limited to muon interactions. Muons can interact directly or via the production of secondary particles, such as neutrons or electromagnetic showers. The direct muon interactions can be vetoed very efficiently, whereas the contributions from secondary particles are reduced by high- Z , radiopure shielding, such as lead, copper, or water. A very powerful tool in reducing the background is the analysis of event topologies, which allows to distinguish background from signal events.

Signal efficiency, ε Double beta processes are very rare, so that a high signal efficiency is crucial. Some double beta isotopes allow the construction of the detector directly from the source material. This guarantees a very high signal efficiency, as the decay products, namely the electrons, are absorbed inside the source itself and event loss is limited to the detector surface.

Isotopic abundance, f The isotopic abundance of the eleven candidate isotopes ranges between 0.187% and 34.5%. Therefore, in many cases isotopic enrichment is inevitable in order to guarantee a reasonable sensitivity.

Source material mass, M Present generation double beta experiments have source masses of the order 10–100 kg. For the future, ton-scale experiments are desired, bringing forth an enormous economical and technological challenge.

Energy window, ΔE A good energy resolution allows to improve the signal-to-noise ratio and is inevitable in reducing the intrinsic background of $2\nu\beta\beta$ events when searching for $0\nu\beta\beta$. Germanium detectors provide the best energy resolution (as low as 0.1%), followed by TeO_2 bolometer crystals ($\approx 0.2\%$).

¹Another argument for the choice of high Q -value isotopes is the strong dependency of the phase space of double beta processes on the Q -value.

Table 4.1: Q-value, $Q_{\beta\beta}$, isotopic abundance, f , half-life of $2\nu\beta\beta$, $T_{1/2}^{2\nu}$, and experimental limits at 90% C.L. for the half-life of $0\nu\beta\beta$, $T_{1/2}^{0\nu}$, for the most interesting double beta decay isotopes. Q-value and isotopic abundance are taken from [61], $T_{1/2}^{2\nu}$ values are taken from [2] for all isotopes but ^{76}Ge and ^{136}Xe .

Isotope	$Q_{\beta\beta}$ (keV)	f (%)	$T_{1/2}^{2\nu}$ (10^{19} yr)	$T_{1/2}^{0\nu}$ (yr) (90% C.L.)
^{48}Ca	4273.7	0.187	$4.4^{+0.6}_{-0.5}$	$5.8 \cdot 10^{22}$ [85]
^{76}Ge	2039.1	7.8	184^{+14}_{-10} [86] ^a	$2.1 \cdot 10^{25}$ [6] $1.9 \cdot 10^{25}$ [4] $1.6 \cdot 10^{25}$ [5]
^{82}Se	2995.5	9.2	9.2 ± 0.7	$3.6 \cdot 10^{23}$ [87]
^{96}Zr	3347.7	2.8	2.3 ± 0.2	$9.2 \cdot 10^{21}$ [88]
^{100}Mo	3035.0	9.6	0.71 ± 0.04	$1.1 \cdot 10^{24}$ [87]
^{116}Cd	2809.1	7.6	2.8 ± 0.2	$1.7 \cdot 10^{23}$ [89]
^{130}Te	2530.3	34.5	68 ± 12	$2.8 \cdot 10^{24}$ [90]
^{136}Xe	2461.9	8.9	$217.2 \pm 1.7(\text{stat}) \pm 6.0(\text{syst})$ [91] $230 \pm 2(\text{stat}) \pm 12(\text{syst})$ [92]	$1.6 \cdot 10^{25}$ [7] $1.9 \cdot 10^{25}$ [8]
^{150}Nd	3367.3	5.6	0.82 ± 0.09	$1.8 \cdot 10^{22}$ [93]

^a See also Appendix B of this work.

4.1.2 Experiments

Several considerations have to be taken into account to maximize the sensitivity in a double beta decay experiment. Table 4.1 lists the most interesting double beta decay isotopes, their Q-value, the natural abundance, the measured half-life of $2\nu\beta\beta$, and limits for the half-life of $0\nu\beta\beta$. The results in the search for $0\nu\beta\beta\chi$ and $0\nu\beta\beta\chi\chi$ are summarized in Table 4.2.

The best limits on the half-life for $0\nu\beta\beta$ have been achieved so far for ^{100}Mo , ^{130}Te , ^{136}Xe , and ^{76}Ge . Note that the limits on the effective Majorana neutrino mass, $\langle m_{\beta\beta} \rangle$, given in the following are reported as provided in the references and different matrix elements might have been used for their calculation. The values for $T_{1/2}^{0\nu}$ from which $\langle m_{\beta\beta} \rangle$ was derived are given in Table 4.1.

The measurement of ^{100}Mo was performed by the NEMO 3 experiment [99]. Thin foils containing the double beta isotopes under study are surrounded by a plane of Geiger cells which allow to track the event topology. The individual particle energies are measured by plastic scintillators read-out with photo multiplier tubes (PMTs). The track reconstruction allows a very low background, $BI \approx 1.2 \cdot 10^{-3}$ cts/(keV · kg · yr) at 3 MeV. The drawback is a reconstruction efficiency for $0\nu\beta\beta$ events of only 13% [100]. The modest energy resolution of (14 – 18)% full width at half maximum (FWHM) at 1 MeV leaves $2\nu\beta\beta$ as the largest background when searching for $0\nu\beta\beta$. The cylindrical detector is divided into 20 independent sectors, which allowed

Table 4.2: Summary of measured lower limits (90% C.L.) on the half-life, $T_{1/2}^{0\nu\chi(\chi)}$, of majoron accompanied decay modes with spectral index $n = 1, 2, 3, 7$. Also the upper limit (90% C.L.) on the neutrino-majoron coupling constant, $\langle g \rangle$, is listed, if provided in the reference.

Isotope	$T_{1/2}^{0\nu\chi(\chi)}$ (10 ²¹ yr) (90% C.L.)				$\langle g \rangle$ (90% C.L.)		
	$n = 1$	$n = 2$	$n = 3$	$n = 7$	$n = 1$	$n = 3$	$n = 7$
	χ	χ	$\chi / \chi\chi$	$\chi\chi$	χ (10 ⁻⁵)	χ (10 ⁻²)/ $\chi\chi$	$\chi\chi$
⁴⁸ Ca [94]	0.72	-	-	-	140	- / -	-
⁷⁶ Ge [4, 95]	64	-	14	6.64	8.1	12 / 3.3	3.3
¹⁰⁰ Mo [83]	27	17	10	0.07	4-18	0.88-2.4 / 1.5	3.2
⁸² Se [83]	15	6.0	3.1	0.5	6.6-19	2.2-6.8 / 2.4	1.3
¹¹⁶ Cd [89, 96]	8	1.7	0.8	0.041	4.6-8.1	- / -	3.9
⁹⁶ Zr [88]	1.9	0.99	0.58	0.11	-	- / -	-
¹⁵⁰ Nd [93]	1.52	0.54	0.22	0.047	6.4-30	- / -	-
¹³⁰ Te [97, 98]	16	-	0.9	-	6-16	- / -	-
¹³⁶ Xe [92]	2.6·10 ³	1.0·10 ³	4.5·10 ²	11	0.8-1.6	1.3 / 0.68	1.2

the measurement of ≈ 9 kg total mass of seven different double beta isotopes with the NEMO 3 detector. The results for ¹⁰⁰Mo lead to a limit for the effective Majorana neutrino mass of $\langle m_{\beta\beta} \rangle < (0.45 - 0.93)$ eV [87].

The search for $0\nu\beta\beta$ of ¹³⁰Te was conducted by the CUORICINO experiment [101]. It consisted of an array of 62 tellurium oxide (TeO₂) bolometers with a total mass of 40.7 kg (10.4 kg of ¹³⁰Te). The crystals were cooled down to 8–10 mK. An energy deposition in the crystals leads to a temperature rise, which was read out with high-resistance germanium thermistors glued to the crystals. An energy deposit of 2530 keV, the Q-value of ¹³⁰Te, lead to an increase in the temperature of $1.77 \cdot 10^{-4}$ K, and a FWHM of (7–9) keV could be reached for this energy. With a background index of about 0.2 cts/(keV · kg · yr) and an exposure of 1.75 kg · yr, a limit on the effective Majorana mass of $\langle m_{\beta\beta} \rangle < (0.30 - 0.71)$ eV [90] could be set.

Two experiments are currently engaged in searching $0\nu\beta\beta$ of ¹³⁶Xe, the KamLAND-Zen experiment [102] and the EXO-200 experiment [103]. KamLAND-Zen operates 13 tons of xenon-loaded liquid scintillator inside a nylon balloon with a diameter of 3 m. This inner balloon is surrounded by an outer balloon with a diameter of 13 m, filled with liquid scintillator, which acts as an active shield. The energy and position of the decay are read out by PMTs. A rather poor energy resolution of 10% at 2.5 MeV, the Q-value of ¹³⁶Xe, is reached. With 89.5 kg · yr, KamLAND-Zen has reached the largest exposure of a double beta isotope up to date. Unfortunately, an unexpected background, most likely due to ^{110m}Ag, deteriorated significantly the sensitivity of the experiment. A scintillator purification campaign in combination with an additional 700 kg of xenon enriched to a level of 90% is expected to improve the sensitivity noticeably in the next months.

The EXO-200 experiment, on the other hand, is a liquid xenon time projection cham-

ber (TPC), filled with 175 kg of liquefied xenon. The ionization as well as the scintillation light signal are measured, allowing for an energy resolution as good as 4% at the Q-value of ^{136}Xe . The cylindrical shape of the TPC allows efficient topological and temporal cuts, reducing the background to $1.5 \cdot 10^{-3}$ cts/(keV · kg · yr). A first result based on 79.4 kg of ^{136}Xe and a seven-month period of data taking was published. Data taking is continuing and more stringent results are expected soon. Combining the results of KamLAND-Zen, $T_{1/2}^{0\nu} > 1.9 \cdot 10^{25}$ yr [8], and of EXO-200, $T_{1/2}^{0\nu} > 1.6 \cdot 10^{25}$ yr [7], a limit of $T_{1/2}^{0\nu} > 3.4 \cdot 10^{25}$ yr is reached and effective Majorana masses as small as $\langle m_{\beta\beta} \rangle < (0.12 - 0.25)$ eV [8] are tested.

The IGEX [104] and Heidelberg-Moscow (HdM) [105] experiments were two experiments searching for $0\nu\beta\beta$ of ^{76}Ge . Both used high-purity germanium (HPGe) detectors enriched to a level of $\approx 86\%$ in ^{76}Ge . The IGEX experiment collected 8.8 kg · yr of data. With a background index of 0.17 cts/(keV · kg · yr) it reached a limit of $\langle m_{\beta\beta} \rangle < (0.33 - 1.35)$ eV [5].

The HdM experiment operated five detectors with a total mass of ≈ 11 kg in copper cryostats with copper, lead, and polyethylene shielding. An excellent energy resolution of 0.2% FWHM was reached. From a data set with a statistical significance of 35.5 kg · yr and a background index of 0.06 cts/(keV · kg · yr) (after pulse shape analysis) $\langle m_{\beta\beta} \rangle < 0.35$ eV [4] was deduced.

A subgroup of the HdM collaboration made a claim of discovery of $0\nu\beta\beta$ of ^{76}Ge with $T_{1/2}^{0\nu} = 1.19_{-0.23}^{+0.37} \cdot 10^{25}$ yr ($\langle m_{\beta\beta} \rangle = (0.2 - 0.6)$ eV) [9], which was later updated to $T_{1/2}^{0\nu} = 2.23_{-0.31}^{+0.44} \cdot 10^{25}$ yr ($\langle m_{\beta\beta} \rangle = (0.29 - 0.35)$ eV) [106]. Inconsistencies in the latter analysis are pointed out in [107]. The combined analysis of the KamLAND-Zen and EXO-200 experiments excludes the claim at 97.5% C.L. [8]. A comparison of two different double beta isotopes, however, has to rely on nuclear matrix element calculations and is therefore strongly model-dependent. A direct, model-independent test was carried out by the GERDA experiment [11] searching for $0\nu\beta\beta$ of ^{76}Ge . The results strongly disfavor the claim and a combined analysis with the IGEX and HdM data yields $\langle m_{\beta\beta} \rangle < (0.2 - 0.4)$ eV [6].

A selection of the most developed next-generation experiments for the search of $0\nu\beta\beta$ is given in Table 4.3.

4.2 Indirect Searches

All experiments presented above employ direct methods for the search of $0\nu\beta\beta$. There are, however, also indirect searches allowing to retrieve information about a possible Majorana neutrino mass and the effective coupling constant of the majoron to the neutrino.

From geochemical measurements, the half-life of ^{128}Te was inferred from measurements of the half-life of ^{130}Te [108]. It was determined to be $(7.7 \pm 0.4) \cdot 10^{24}$ yr. The limit on the Majorana neutrino mass resulted as $\langle m_{\beta\beta} \rangle < (1.1 - 1.5)$ eV and the limit on the effective majoron-neutrino coupling constant for the ordinary majoron

Table 4.3: Most developed next-generation double beta experiments. The sensitivity on the half-life of $0\nu\beta\beta$, $T_{1/2}^{0\nu}$, and the effective Majorana neutrino mass, $\langle m_{\beta\beta} \rangle$, is given at 90% C.L.. Adopted from [2].

Experiment	Isotope	Mass (kg)	Sensitivity (90% C.L.) $T_{1/2}^{0\nu}$ (10^{26} yr)	Sensitivity (90% C.L.) $\langle m_{\beta\beta} \rangle$ (eV)
CUORE	^{130}Te	200	6.5 ¹	0.02-0.05
			2.1 ²	0.035-0.09
GERDA	^{76}Ge	40	2	0.07-0.2
		1000	60	0.01-0.04
MAJORANA	^{76}Ge	30-60	2	0.07-0.2
		1000	60	0.01-0.04
EXO	^{136}Xe	200	0.64	0.1-0.2
		1000	8	0.03-0.06
SuperNEMO	^{82}Se	100-200	1-2	0.04-0.1
KamLAND-Zen	^{136}Xe	400	4.5	0.04-0.08

¹ With $BI = 10^{-3}$ cts/(keV · kg · yr)

² With $BI = 10^{-2}$ cts/(keV · kg · yr)

accompanied decay mode with $n = 1$ resulted as $\langle g \rangle < 3 \cdot 10^{-5}$. However, more recent geochemical measurements suggested an about three times longer half-life of ^{130}Te [109], leading to a longer half-life also for ^{128}Te .

Also from astrophysics, bounds on the coupling between the neutrino and the ordinary majoron can be derived. From the observation of neutrinos from SN1987A it was deduced that a large part of the supernova energy is released via neutrinos. This allows to set a bound on the neutrino-majoron coupling of $\langle g \rangle < (1 - 20) \cdot 10^{-5}$ [110, 111]. From calculations of the effects of a possible majoron decay and scattering in high-density supernova medium it was determined that $\langle g \rangle < 3 \cdot 10^{-7}$ or $\langle g \rangle > 2 \cdot 10^{-5}$ [112]. The first limit is due to the fact that the supernova explosion would be suppressed for strong enough coupling between the neutrino and the majoron, as the supernova energy would be released in majoron emission instead. The second limit was derived considering that for too strong neutrino-majoron coupling the majorons would be trapped inside the supernova medium, so that no conclusion on the coupling could be drawn.

Another way to obtain information about the coupling between the neutrino and the majoron is the search for possible effects of majoron emission in lepton and meson decays. The most recent result from such analyses give $\langle g \rangle^2 < 5.5 \cdot 10^{-6}$ [113].

Chapter 5

Germanium Detectors

Germanium detectors are used to detect particles via their interactions in matter. These interactions are discussed for photons, electrons, positrons, and α -particles. An overview of the working principle of semiconductor detectors in general and the main characteristics of germanium detectors in particular is given. The concept of the signal formation process is presented. Important features for the reduction of background events in the search of $0\nu\beta\beta$ are summarized. A detailed review of germanium detectors can be found in [114] and references therein.

5.1 Interaction of Photons, Electrons, Positrons, and α -particles with Matter

5.1.1 Photons

Radioactive isotopes emit photons in the range from several keV to a few MeV. In this energy range, three processes dominate the interaction of photons with matter. Their cross sections depend on the atomic number of the material and on the photon energy, E_γ :

- In the **photoelectric absorption** process, the photon transfers its entire energy to an atomic shell electron which is ejected from the shell. The kinetic energy, E_{e^-} , of this *photo-electron* is

$$E_{e^-} = E_\gamma - E_b,$$

where E_b is the binding energy of the electron. The remaining vacancy in the shell is filled by electrons from the outer shells and due to the differences in the binding energies characteristic x-rays or Auger electrons are emitted.

- **Compton scattering** is the elastic scattering of a photon off a quasi-free electron, transferring only a part of its energy, ΔE_γ , to the electron. The value of ΔE_γ depends on the scattering angle, Θ . It is largest for $\Theta = 180^\circ$.

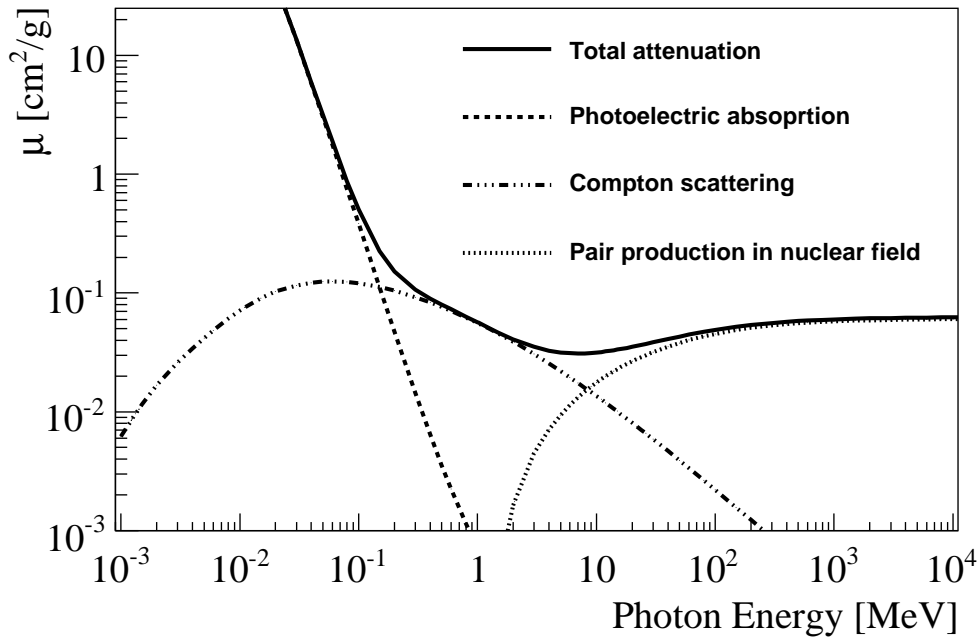


Figure 5.1: Mass attenuation coefficient μ in germanium as a function of the photon energy. Graphic based on [115].

- If the energy of the incident photon exceeds twice the rest mass of the electron, m_e , the photon can create an electron-positron pair in a **pair production** process when in the vicinity of a nucleus. In this process, E_γ is converted to the electron and positron kinetic energies, E_{e^-} and E_{e^+} , and to their rest masses.

The mass attenuation coefficient for photons, $\mu = \frac{N_A}{A} \cdot (\sigma_{\text{photo}} + \sigma_{\text{Compton}} + \sigma_{\text{pair}})$, where N_A is Avogadro's number, A is the mass number and σ_{photo} , σ_{Compton} and σ_{pair} are the cross sections for the respective processes, is shown for germanium in Fig. 5.1. The photoelectric absorption is the dominant process for photon energies up to ≈ 200 keV. For energies between 200 keV and about 8 MeV, Compton scattering has the highest cross section. The photon scatters several times until it is finally absorbed in a photoelectric process. The mean free path of a 1 MeV photon is about 3 cm in germanium.

For higher energies, the pair production process gains more and more importance, until its cross section dominates above an energy of around 8 MeV in germanium. At 2.6 MeV, the energy of the most dominant ^{208}Tl line, its contribution to the total cross section is $\approx 9\%$.

In each of the processes mentioned, energy is transferred to at least one electron, in case of pair production also to a positron.

5.1.2 Electrons, Positrons, and α -particles

There are two main processes that lead to the loss of energy of electrons and positrons traversing matter. High energetic electrons and positrons lose energy mainly radiatively through the *bremsstrahlung* process. *Ionization*, described by the Bethe-Bloch formula [116], is the dominating effect for electrons and positrons with lower energies. In germanium, the ratio of both losses is equal for a particle energy of ≈ 18 MeV [117].

The energy loss mechanisms for electrons and positrons in matter are identical. The behavior of the two particles differs, however, at the end of the track, where positrons annihilate with electrons into two photons with an energy of 511 keV each.

The range of electrons and positrons in matter depends on their energy and the material. The average range for a 1 MeV electron in germanium is about 1 mm [118].

Compared to electrons and positrons, α -particles are much heavier. Bremsstrahlung processes are negligible and all energy is deposited via ionization. The average range for a 5 MeV α -particle in germanium is about $2 \mu\text{m}$.

5.2 Semiconductor Detectors

The characteristics of a solid, and thus also of a semiconductor, are determined by the structure of the crystal lattice, which causes allowed energy bands for the electrons with forbidden states between these bands. For a semiconductor, the gap between the valence and the conduction band, the *bandgap*, is of the order of 1 eV. Electrons can be lifted to the conduction band by thermal excitation or ionizing radiation, leaving a positively charged hole in the valence band. These electrons as well as the holes are called *charge carriers*, as they can move freely throughout the crystal. A fraction of the energy, however, goes into the excitation of phonons. Therefore, the *pair energy*, E_{pair} , the energy needed to create one electron-hole pair, is higher than the bandgap energy. In germanium at 80 K it is 2.95 eV, while the bandgap energy is only 0.7 eV.

Semiconductor materials, like germanium and silicon, are tetravalent. Their atoms form covalent bonds with their four nearest neighboring atoms. In *n*-type material, pentavalent impurities like boron are present. Their fifth valence electrons are only weakly bound, occupying the *donor level* slightly under the conduction band. These electrons are easily thermally excited to the conduction band, creating an abundance of negative charge carriers. In contrast, *p*-type material is doped with trivalent impurities. They are missing one covalent bond, which leads to the formation of the *acceptor level*, which is a little bit above the valence band. When electrons are lifted to these states, they leave holes in the valence band and the net amount of charge carriers remains positive.

A semiconductor detector consists of a *p-n*-junction. Close to the junction, the charge carriers diffuse into the volume where their concentration is lower. The

electrons from the n -region migrate to the p -region and recombine with the holes, resulting in a positive space charge in the n -material and a negative space charge in the p -material from the remaining ions. This *depletion zone* is non-conducting. Any charge carrier created in this volume will be driven out by the electric field resulting from the space charges. If an external potential is applied by connecting the anode to the n -side and the cathode to the p -side (*reverse biasing*), the depletion zone is enlarged. The bias voltage at which the depletion zone extends over the entire detector volume is defined as the *full depletion voltage*.

Semiconductor detectors are fabricated from p -type or n -type material called the *bulk*. There are two types of electrodes, p^+ and n^+ , where the "+" indicates that the net impurity density is much higher than in the bulk material. A p^+ -electrode is produced by boron implantation. Its thickness is of the order of a few tenths of a micrometer. To fabricate an n^+ -electrode, lithium atoms are diffused into the material. This results in a layer with a thickness of several hundred micrometers. The electrodes are metallized with aluminum, allowing the homogeneous application of an external voltage. In n -type bulk material, the p - n -junction is located on the side of the p^+ -electrode. When the full depletion voltage is applied, the depletion zone extends over the entire bulk to the n^+ -electrode. In p -type detectors, the opposite is the case. As the electrodes are conducting, they are not part of the depletion zone. They are thus not sensitive and form a *dead volume*.

5.3 Germanium Detector Properties

5.3.1 Detector Geometries

The largest germanium detectors have cylindrical shapes.

In the (*true*) *coaxial* configuration, the core of the cylinder is (completely) partially removed, so that the inner cylindrical surface provides an electrode. The other electrode is formed by the outer surface.

For *point-contact* and *Broad Energy Germanium (BEGe)* detectors, a small, point-like electrode is situated at the center of the top of the cylinder. The second electrode is formed by the remaining surface.

Figure 5.2 shows examples of p -type detectors with a coaxial and with a BEGe geometry. For both detector schemes, the signal is read out at the p^+ -contact. The n^+ -electrode serves as high-voltage (HV) contact. Small grooves separate the electrodes.

5.3.2 Operating Voltage

Germanium detectors are generally operated with a fully depleted volume. The depleted volume increases with the operating voltage between anode and cathode. Its

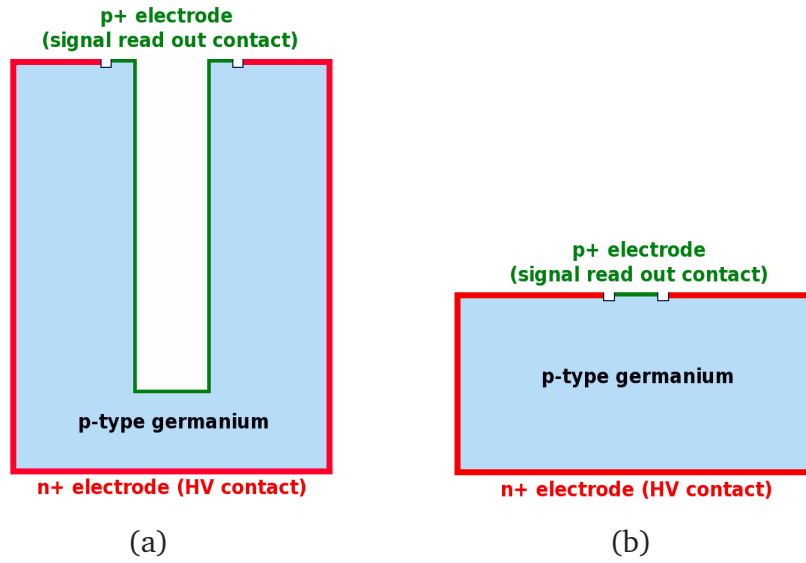


Figure 5.2: Schematic sketch of the vertical sections of a (a) coaxial and of a (b) BEGe detector.

depth, d , is given by [114]

$$d = \left(\frac{2\epsilon_R\epsilon_0V_0}{e\rho_{\text{imp}}} \right)^{1/2}, \quad (5.1)$$

with V_0 being the applied reverse bias voltage, ρ_{imp} the net impurity concentration in the bulk material, e the elementary charge, $\epsilon_R = 16$ the dielectric constant of germanium, and ϵ_0 the vacuum permittivity. The bias voltage, V_0 , cannot be arbitrarily large, because diodes have a finite break-through voltage and cabling and read-out become technically challenging with increasing voltages. Therefore, very pure material is needed for large devices with depletion depths of the order of centimeters. Techniques have been developed to produce High-Purity Germanium (HPGe) with an active impurity concentration below 10^{10} atoms/cm³. Devices with diameters and heights of up to ten centimeters and full depletion voltages of a few kilovolt are produced.

5.3.3 Operating Temperature

Germanium has a very small E_{pair} of only 2.95 eV. At room temperature, a significant fraction of electrons is easily excited to the conduction band, causing a high conductivity of the detector. Applying a bias voltage would lead to a large current through the detector, making its operation as radiation detector impossible. Therefore, the detector has to be cooled. Conventionally, this is done by keeping it in thermal contact with liquid nitrogen through a cooling finger, which establishes a working temperature around 77 K. It has also been shown that the detectors can be directly submerged into the cryoliquid without loss of functionality [119].

5.3.4 Energy Resolution

The energy resolution of germanium detectors, measured in terms of the full width at half maximum (FWHM) of the peak under study, is influenced by three effects.

The first one is the statistical fluctuation in the number of charge carriers created by an incident charged particle of a certain energy, E . This contribution scales with \sqrt{E} . It is called the *Fano term*.

The second factor that determines the energy resolution is the charge collection efficiency. It scales with E .

The last component adding to the broadening of the FWHM is the energy-independent noise contribution from the read-out electronics.

In optimized systems, total energy resolutions of about 2 keV at 1.3 MeV are obtained for coaxial detectors. The distinctively reduced size of the read-out electrode of BEGe detectors leads to a lower capacitance and therefore lower noise level compared to coaxial detectors. At 1.3 MeV, a FWHM of typically 1.75 keV can be reached.

5.4 Signal Formation

5.4.1 Charge Carrier Drift

Photons, electrons, positrons, and α -particles interact inside a semiconductor detector as described in Section 5.1, transferring energy to secondary electrons. These secondary electrons subsequently excite electrons from the valence to the conduction band, hence create electron-hole pairs. The average number of charge carriers produced is proportional to the deposited energy, because E_{pair} is independent of the type of the incident particle and of its energy.

Since a semiconductor detector is operated in reverse bias mode, the electric field in its bulk causes the drift of the electrons and holes in opposite directions towards the electrodes. The electric field can be calculated solving Poisson's equation,

$$\Delta \Phi = -\frac{\rho}{\epsilon_0 \epsilon_R}, \quad (5.2)$$

where Φ is the electric potential, linked to the electric field, \mathbf{E} , via $\mathbf{E} = -\nabla\Phi$, ρ is the space charge density, ϵ_0 is the vacuum permittivity and $\epsilon_R = 16$ is the dielectric constant of germanium. The space charge density, ρ , is determined by the active impurity density, ρ_{imp} , which defines the strength of the electric field inside the detector.

To first order, the drift direction of the electrons (holes) is anti-parallel (parallel) to the electric field lines. The drift velocities grow with rising electric field strength up to a saturation field strength, E_{sat} , which is of the order of 10^2 V/mm for electrons and about a factor three to five larger for holes. Above E_{sat} , the drift velocities remain constant, being of the order of 0.1 mm/ns^1 .

¹At higher order, the effect of the crystal structure has to be taken into account. At the operating temperatures of HPGe detectors of around 100 K, the drift velocities differ for different drift directions

5.4.2 Pulse Shapes

The moving charge carriers induce charges in the electrodes of the detector. For any electrode, the time development of the induced charges, $Q(t)$, follows the *Shockley-Ramo Theorem* [122]. For a moving point charge q that can be found at position $\mathbf{r}(t)$ at time t it is

$$Q(t) = -q \cdot \Phi_{\omega}(\mathbf{r}(t)), \quad (5.3)$$

where Φ_{ω} is the *weighting potential*. In order to determine Φ_{ω} , the Laplace equation,

$$\Delta \Phi = 0, \quad (5.4)$$

has to be solved. The boundary conditions for Φ_{ω} are $\Phi_{\omega} \equiv 1$ on the electrode of interest and $\Phi_{\omega} \equiv 0$ on all other boundaries.

The induced charges are recorded over a time period $t_1 - t_0$ using charge-sensitive preamplifiers. The *pulse* at time t_1 , $P(t_1)$, is proportional to the induced charges in the respective electrode, integrated over the time period,

$$P(t_1) \sim \int_{t_0}^{t_1} Q(t) dt. \quad (5.5)$$

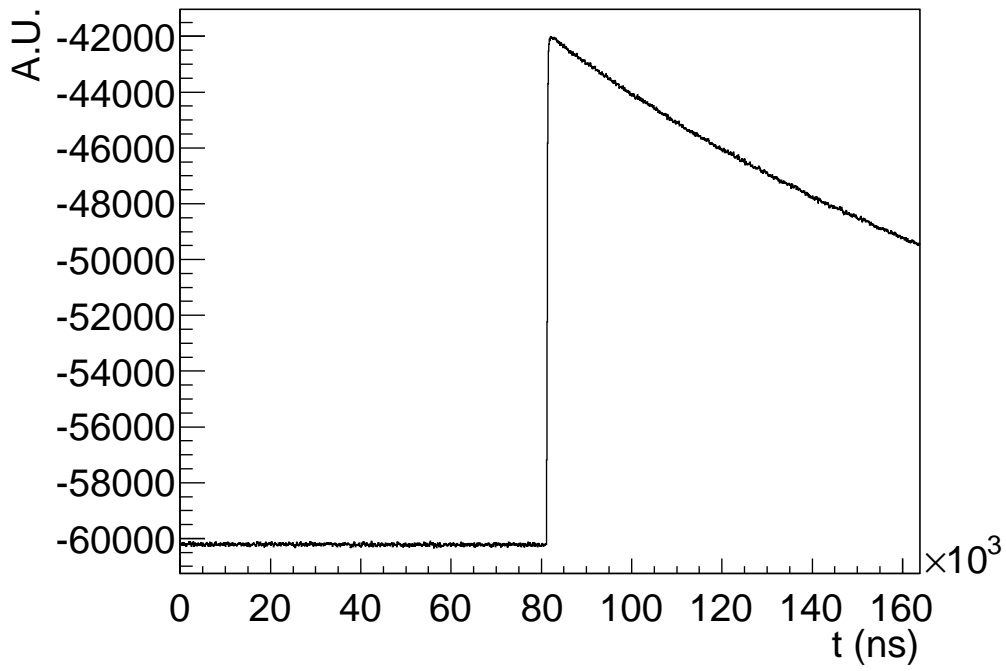
The time development of the functional form of the integrated charges on the electrodes is referred to as the *pulse shape*. Figure 5.3 shows an example of a digitized pulse shape. Typical charge collection times are of the order of a few hundred nanoseconds. In order to assure that the preamplified pulse is proportional to the integral of the induced charge, the decay time of the preamplifier has to be much larger than the charge collection time, typically between 50 and 100 μs .

5.5 Background Rejection

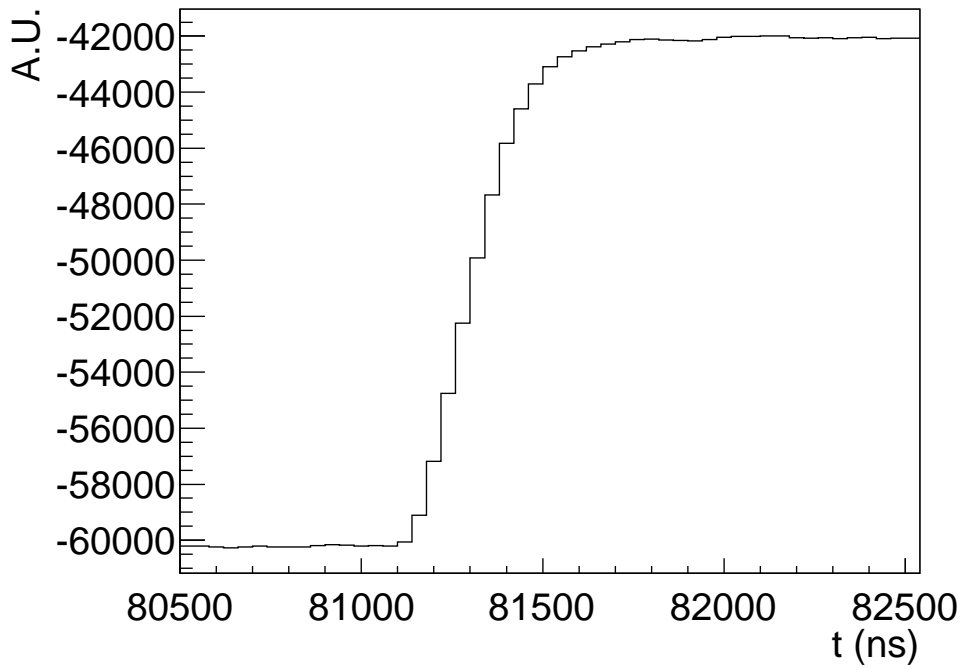
Several techniques have been developed to reject remaining background events in the search for $0\nu\beta\beta$ of ^{76}Ge with germanium detectors. In general, background events have a different topology than $0\nu\beta\beta$ events. Most $0\nu\beta\beta$ events will deposit their energy locally within a sphere with a radius of ≤ 1 mm due to the limited range of electrons in germanium. These are so-called *single-site events (SSE)*. The main background contribution comes from Compton-scattered photons. Their energy deposits are usually separated by centimeters, producing so-called *multi-site events (MSE)*.

When several germanium detectors are arranged in an array, it is thus very unlikely that more than one detector in the array has an energy deposit in the case of a signal event. Therefore, an anti-coincidence cut between different detectors allows for reduction of the background.

(longitudinal anisotropy) and are not always parallel to the electric field (transversal anisotropy) [120, 121]. The drift is only exactly parallel to the field lines, when these are parallel to the crystal axes.



(a)



(b)

Figure 5.3: (a) An example of a digitized pulse shape. (b) A zoom into the rising edge of the pulse shape.

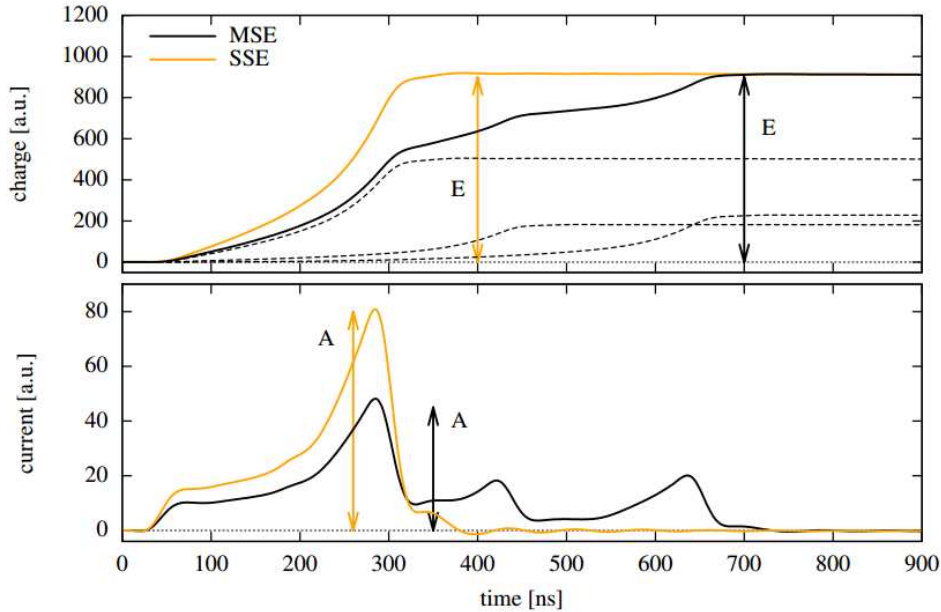


Figure 5.4: In the upper panel, typical charge pulses for a SSE and a MSE in a BEGe detector are shown. In the lower panel, the corresponding current pulses are depicted. At the same energy, E , the amplitude of the current pulse, A , differs for SSE and MSE. Image taken from [128].

Background events can additionally be reduced using *pulse shape analysis (PSA)* [123–125], that is by analyzing the structure of the pulse shapes. This allows to distinguish between different event topologies and thus to discard background events.

The geometry of the BEGe detectors allows an improved PSA compared to coaxial detectors. Thanks to the smallness of the p^+ -contact, the electric field of a BEGe detector has a very peculiar shape. In the top panel of Fig. 5.4, typical charge pulses for a SSE and a MSE in a BEGe detector are depicted. The lower panel shows the first derivative of the charge pulses, the *current pulses*. Very distinct differences between the two event topologies can be observed. At the same event energy, E , determined from the height of the charge pulse, the amplitude of the current pulse, A , differs for SSE and MSE. This leads to the definition of the A/E parameter. An event selection based on A/E has proven to be very effective in distinguishing SSE from MSE and thus lowering significantly the background. Details can be found in [126–129].

Chapter 6

The GERDA Experiment

The *GERmanium Detector Array* (GERDA) [10, 11] is an experiment designed for the search of $0\nu\beta\beta$ of ^{76}Ge with germanium detectors.

From Equation (4.4) it becomes evident that germanium detectors are an attractive option in the search for double beta decay. Being the detector also the source, they guarantee a very high signal efficiency. Germanium can be produced very radio-pure as *high-purity germanium* (HPGe) and thus the intrinsic background is very small. The excellent energy resolution of (0.1 – 0.2) % FWHM at 2039 keV, the Q-value of double beta decay of ^{76}Ge , allows for a good separation between $2\nu\beta\beta$ and $0\nu\beta\beta$ events. Germanium detectors have been used in nuclear physics for a very long time, making it a well established and validated technology.

One of the drawbacks of germanium detectors is the rather low Q-value of ^{76}Ge , leading to substantial external background from natural radioactivity. The natural abundance of ^{76}Ge is only 7.8%, so that costly enrichment is needed. In the future, the scalability to larger masses could prove a problem.

The GERDA experiment adapted the idea of submerging HPGe detectors directly in a cryoliquid [130]. It is operated in two phases.

The data taking for Phase I started in November 2011 and ended in May 2013. With a background of $\approx 10^{-2}$ cts/(keV·kg·yr), 21.6 kg·yr of data were collected. This allowed to set a limit of $T_{1/2}^{0\nu} > 2.1 \cdot 10^{25}$ yr (90% C.L.) on the half-life of $0\nu\beta\beta$ of ^{76}Ge [6].

Phase II is planned to start in 2014. By using a novel detector design, featuring enhanced PSA techniques, and detecting the liquid argon (LAr) scintillation light, it aims at a background level of 10^{-3} cts/(keV·kg·yr). With an exposure of 100 kg·yr, half-lives up to $2 \cdot 10^{26}$ yr can be explored.

6.1 Experimental Setup

The GERDA experiment is located at the INFN Laborati Nazionali del Gran Sasso (LNGS) in Italy. The rock above the laboratory provides in average 3500 m of water equivalent (w.e.) shielding, suppressing the cosmic ray muon flux by a factor 10^6 to 1 muon/($\text{m}^2 \cdot \text{h}$).



Figure 6.1: (a) String of three Phase I detectors in their low mass holders. (b) Three detector strings contained in their minishrouds.

The environmental background component is reduced by graded shielding. The germanium detectors are arranged in four detector strings. Low mass holders are used to minimize the amount of material close to the detectors. Figure 6.1(a) shows such a string with three detectors used in Phase I. The bare germanium detectors are directly submerged in a stainless-steel cryostat with a diameter of 4.2 m, filled with 64 m^3 of liquid argon (LAr). A heatexchanger, located in the top part of the cryostat, prevents the extensive loss of LAr. A copper lining of the steel vessel absorbs its gamma radiation. The cryoliquid provides not only shielding, but also cools down the detectors to their operating temperature. The complete detector array is enclosed in the so-called radon shroud, a copper cylinder with a diameter of 75 cm and a thickness of $30\ \mu\text{m}$. Liquid argon contains the radioactive isotope ^{42}Ar , whose daughter ^{42}K decays to the stable ^{42}Ca . Since this latter decay has a Q-value of 3525.4 keV, it contributes to the background in the *ROI*. In order to minimize this contribution, the attraction of positively charged ^{42}K ions in the detector vicinity has to be reduced. This is achieved by putting the detectors in a field-free configuration, that is by avoiding electrical fields in their proximity. The field-free configuration is provided by closing the electrical field lines originating from the voltage-biased surfaces of the detectors on a thin copper layer closely surrounding each detector string. These so-called minishrouds have a diameter of $\approx 10\text{ cm}$ and are centered on the detector string. They can be seen in Fig. 6.1(b).

In the second phase of GERDA, the cryostat will be equipped with instrumentation



Figure 6.2: An artist's view of the GERDA experiment.

to detect the LAr scintillation light. This will allow a further reduction of the background from ambient radioactivity.

The cryostat is surrounded by a water tank with a diameter of 10 m and a height of 9 m, containing 590 m³ of ultra-pure water. The water serves as shielding from photons and spallation neutrons from outside the water tank. It is equipped with photomultiplier tubes to detect the Čerenkov light of remaining cosmic muons.

On top of the water tank, a class 10 000 clean room is located. The handling of the detectors takes place in class 100 flow-boxes. The detector strings are inserted into the cryoliquid through a lock system. An additional muon veto system is installed on top of the clean room to protect the neck region of the cryostat.

Close to the detectors, only copper and teflon are used, as these materials can be produced with high radio-purity. All materials used to build the experiment were screened to guarantee their radio-purity.

A sketch of the GERDA experiment is depicted in Fig. 6.2.

6.2 Detectors

6.2.1 Phase I Detectors

In the first phase of the GERDA experiment, the reprocessed HPGe detectors of the IGEX [104] and HdM [105] experiments were deployed. All eight detectors were coaxial *p*-type detectors and enriched in ⁷⁶Ge to a level of (85–87)%. An example of one of the detectors can be seen in Fig. 6.3. Together with a natural HPGe detector

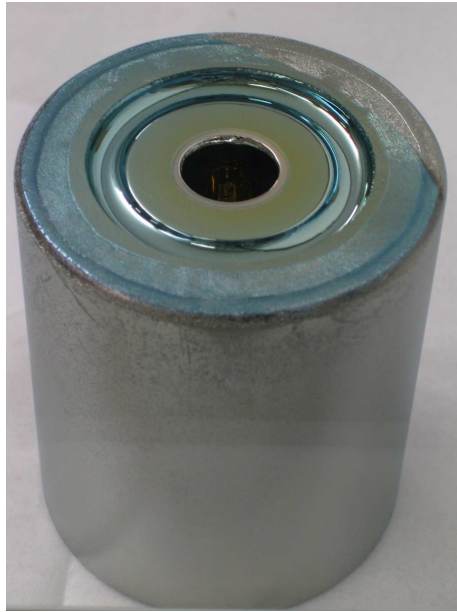


Figure 6.3: Picture of an enriched Phase I coaxial detector.

from the GENIUS-TF experiment [131], they were arranged in three detector strings. Two additional natural GENIUS-TF detectors in a fourth string were later replaced by five Phase II BEGe detectors. Due to high leakage currents, two of the enriched coaxial detectors, ANG1 and RG3, as well as one of the BEGe detectors, GD35C, were not used for data analysis. Table 6.1 summarizes the main characteristics of the detectors used in Phase I.

The detectors were read out at the p^+ -electrode, whereas the n^+ -surface served as HV contact. The applied bias voltage varied between 2 kV and 4.5 kV for the different detectors. Charge-sensitive preamplifiers, custom-designed from low-background material, were operated directly in the LAr at a distance of about 30 cm from the topmost detectors. Coaxial cables with a total length of about 20 m transported the signal to the data acquisition (DAQ). After amplification with a linear amplifier, the pulses were digitized by a 14-bit flash-ADC (FADC). For each event, two traces per channel were stored, one with a trace length of $4 \mu\text{s}$ and a sampling frequency of 100 MHz, the other one with a trace length of $160 \mu\text{s}$ and a sampling frequency of 25 MHz. The decay time of the pulses was $\sim 100 \mu\text{s}$.

6.2.2 Phase II Detectors

In Phase II, additional enriched HPGe detectors will be deployed. For the design, the BEGe detector geometry was chosen. Its improved energy resolution and excellent PSA performance will be crucial in order to reach the sensitivity goals.

To guarantee the extremely low background level needed for Phase II, the production of the new BEGe detectors was carefully planned and carried out. Fast neutrons from the cosmic radiation produce radio-isotopes such as ^{60}Co and ^{68}Ge via spalla-

Table 6.1: Main characteristics of the Phase I detectors: isotopic abundance of ^{76}Ge , f_{76} , diameter, d , height, h , total mass, M , fraction of active mass, f_{act} , and thickness of n^+ dead layer, d_{n^+} . The last column indicates the detectors used for analysis in this work.

Detector	f_{76} (%)	d (mm)	h (mm)	M (g)	f_{act} (%)	d_{n^+} (mm)	used for analysis
Enriched Coaxial Detectors							
ANG1	85.9 (29)	59	68	958	83.0(52)	1.8(5)	–
ANG2	86.6 (25)	80	107	2833	87.1(51)	2.3(7)	✓
ANG3	88.3 (26)	78	93	2391	86.6(57)	1.9(7)	✓
ANG4	86.3 (13)	75	100	2372	90.1(57)	1.4(7)	✓
ANG5	85.6 (13)	79	105	2746	83.1(48)	2.6(6)	✓
RG1	85.5 (15)	78	84	2110	90.4(59)	1.5(7)	✓
RG2	85.5 (15)	78	84	2166	83.1(53)	2.3(7)	✓
RG3	85.5 (15)	79	81	2087	89.5(54)	1.4(7)	–
Enriched BEGe Detectors							
GD32B	87.7(13)	71.89(4)	32.16(12)	717	89.0(27)	0.988(249)	✓
GD32C	87.7(13)	71.99 (1)	33.15(6)	743	91.1(30)	0.809(278)	✓
GD32D	87.7(13)	72.29(2)	32.12 (10)	723	92.3(26)	0.683(235)	✓
GD35B	87.7(13)	76.33(3)	32.10(11)	812	91.4(29)	0.785(270)	✓
GD35C	87.7(13)	74.84(6)	26.32(18)	635	90.6(32)	0.764(265)	–
Natural Coaxial Detectors							
GTF32	7.8(1)	89	71	2321	97(5)	0.4(8)	–
GTF45	7.8(1)	87	75	2312			–
GTF112	7.8(1)	85	100	2965			–

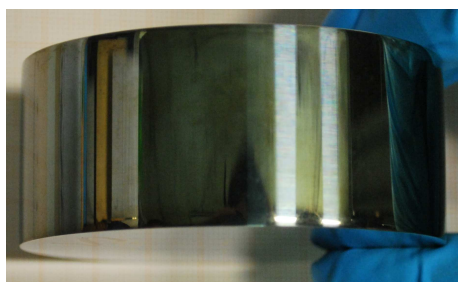


Figure 6.4: Picture of an enriched Phase II BEGe detector.

tion reactions in germanium. The decay of these cosmogenic radio-isotopes mimics the signal events, increasing the internal background. Therefore, the exposure of the germanium to cosmic radiation had to be minimized during the entire production process. To this scope, the material and later the diodes were always transported in a shielded container. At all production sites, underground storages were identified and the germanium was transported between the storage location and the production site on a daily basis. The exposure was rigorously tracked in order to estimate and control the activation.

The steps in the production process of the BEGe diodes were:

- The production of GeO_2 enriched in ^{76}Ge to a level of $\sim 88\%$ at Electrochemical Plant in Zelenogorsk, Krasnojarsk, Russia.
- The metal reduction and zone refinement to obtain 6N grade material at PPM GmbH in Langelsheim, Germany.
- The crystal pulling at Canberra Industries Inc. in Oak Ridge, USA.
- The diode production at Canberra Semiconductors NV in Olen, Belgium.
- The characterization at the HADES underground laboratory in Mol, Belgium [132].
- The contacting at Canberra Semiconductors NV in Olen, Belgium.
- The delivery to the GERDA experimental site at LNGS in Assergi, Italy.

From initially 37.5 kg of enriched GeO_2 , 30 BEGe detectors with a total mass of ~ 20 kg were produced. Figure 6.4 shows one of the newly produced detectors.

The cosmic activation was limited to $\sim 20\text{--}50$ ^{68}Ge nuclei/kg and $\sim 20\text{--}40$ ^{60}Co nuclei/kg, respectively.

As mentioned in Sec. 6.2.1, five of the enriched BEGe detectors could already be operated in the GERDA setup during Phase I.

Chapter 7

GERDA Phase I Data

The GERDA Phase I data taking lasted for almost 19 months and a total of $21.6 \text{ kg} \cdot \text{yr}$ of data was collected with the enriched detectors. The pulse shapes acquired with the GERDA experiment were digitized by the DAQ system and stored for offline processing. In the subsequent data flow, quality cuts were applied and the event energies for each channel were extracted. This chapter recapitulates the offline data treatment. For an extensive description of the data processing, summarized in Sec. 7.1, see [133–138]. Specifics on the calibration procedure, presented in Sec. 7.2, can be found in [139, 140].

After the description of the data treatment, an overview on the GERDA Phase I data taking is presented and the most important parameters are summarized. A first assessment of the background sources present in the experiment is given.

7.1 Data Processing

All steps of the offline processing of the GERDA data were performed within the software framework GELATIO [141]. This ROOT [142] based framework was specifically developed for the GERDA data handling and analysis.

Every time an energy above 100 keV is deposited in at least one of the germanium detectors, two pulse shapes are recorded for each of the detectors present in the setup. One of these traces has a length of $4 \mu\text{s}$ and is digitized with a frequency of 100 MHz, whereas the other one has a length of $160 \mu\text{s}$ and is digitized with a frequency of 25 MHz. For both traces, the rising edge of the pulse is ideally centered on the recorded time window. The high-frequency pulse is typically used for PSA, as details in the rising edge are preserved. The low-frequency pulse is recorded over a 40 times longer time span. This provides the possibility to analyze also the baseline and decay tail of the pulse. All steps described in the following are carried out with the long low-frequency pulse.

The GELATIO software has a modularized structure. Each module is composed of a variety of filters, dedicated to extract information on one particular aspect of the pulse shape. A chain of several modules is used to extract all important parameters

from the traces. After the restoration and analysis of the baseline, the starting point of the rising edge is determined and the number of triggers for each trace is identified. The energy deposited in each detector is extracted from the respective charge pulse by applying an approximate Gaussian filter [133, 143]. Finally, the rise time of the rising edge is determined as the time between 10 % and 90 % of the maximum amplitude of the charge pulse.

In a next step, the quality of the data has to be verified. Non-physical events, such as discharges, cross-talk and pick-up noise events, have to be removed. Figure 7.1(a) shows examples of such pulse shapes. Due to their anomalous shapes they can be rejected by cuts based on the time position of the rising edge, the information from the Gaussian filter, the rise time, and the charge pulse height, which must not exceed the dynamic range of the FADC.

Also, all pile-up and accidental coincidence events are removed from the data set. Example pulses are depicted in Fig. 7.1(b). Pile-up events comprise events in which multiple traces are superposed in the same time window, leading to multiple triggers, as well as events with a slope of the baseline, deriving from the decay tail of a previous pulse outside the time window. Accidental coincidences, on the other hand, describe traces where the rising edge of the pulse is not centered on the recorded time window. Cuts based on the baseline slope, the number of triggers and the position of the rising edge identify both classes of events. The rate of pile-up and accidental coincidence events is negligible in the GERDA data due to an extremely low event rate. The loss due to miss-classification by the quality cuts is $< 0.1\%$ for events with energies above 1 MeV.

By monitoring the pulse shape parameters and their variations over time, data taken in periods with large unstabilities could be removed, assuring always an excellent data quality.

In a last step, all events that come within $8\mu\text{s}$ of a signal of the muon veto are rejected, reducing the background around $Q_{\beta\beta}$ by 7 %.

For all analyses described in this work, only events that survive the detector anti-coincidence cut were considered. This means, that all events with an energy deposit $> 20\text{ keV}$ in more than one detector in the array were not taken into account. While the energy information from ANG1 and RG3 was ignored for this cut, energy deposits in the natural germanium detectors and in GD35C were taken into account. The background reduction around $Q_{\beta\beta}$ is around 15 %. Since $0\nu\beta\beta$ events are of the SSE type, no signal events are lost by this cut.

7.2 Energy Calibration

The energy calibration of the GERDA data is realized using the information from dedicated calibration runs. For these calibration runs, three ^{228}Th sources are brought into the vicinity of the detectors. A detailed description of the calibration system can be found in [144–146].

During normal data taking, the calibration runs were performed every seven to

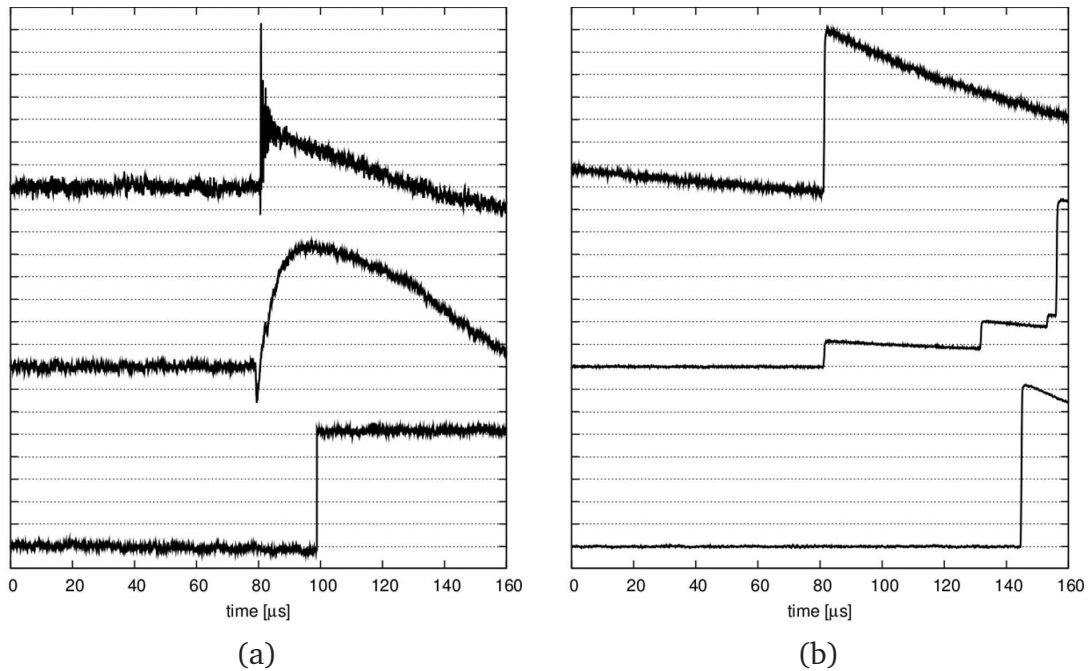


Figure 7.1: (a) Pulses generated by non-physical events. (b) Top: Pile-up event with baseline slope. Middle: Pile-up event with superposition of multiple pulses. Bottom: Accidental coincidence event. Figures adopted from [133].

ten days. The gain stability of the preamplifiers was monitored throughout the entire data taking period by surveying their response to periodical test pulses. Extraordinary calibration runs were performed following instabilities of the gain. The data of the calibration runs was used to extract the calibration curves, that is the functions converting the uncalibrated energy calculated by the Gaussian energy filter into calibrated energy for each detector. Additionally, the calibration data was used to tune the PSA parameters and to check the data quality by monitoring e.g., the positions of the photon peaks and their energy resolution in the recorded ^{228}Th energy spectrum as a function of time.

To save disk space, the calibration data was recorded with a 400 keV threshold, meaning that no event was recorded in which the energy did not exceed 400 keV in at least one detector. The data was processed following the protocol described in Sec. 7.1. All relevant parameters, such as uncalibrated energy, rise time, baseline slope, number of triggers, and time position of the rising edge were extracted and non-physical events as well as pile-up and accidental coincidence events were rejected by the data quality cuts. As a consequence of the higher event rate compared to the physics runs, pile-up and accidental coincidence events constituted up to 15% of all events recorded during the calibration runs. Finally, a muon veto cut and a detector anti-coincidence cut were applied.

For each detector, the uncalibrated energies of the surviving events were filled into a histogram. An example of such an uncalibrated energy spectrum can be seen in Fig. 7.2. All peaks of the spectrum were identified and either matched to known

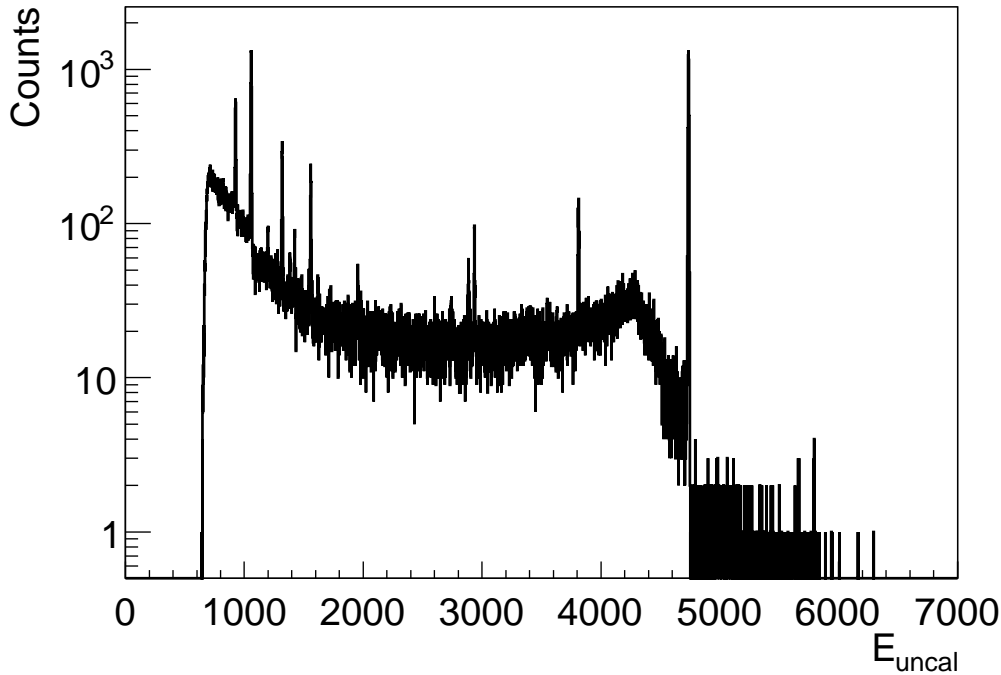


Figure 7.2: Example of an uncalibrated energy spectrum of a single detector recorded during a calibration run with the ^{228}Th sources. All quality cuts have been applied.

photon peaks of the ^{228}Th spectrum or discarded. The selected photon peaks were then fitted with a general fitting function, containing a term for the gaussian peak, a step function, a term describing the low energy tail, and a term describing the linear background. If one of the contributions was not well constrained by the fit or negligible, the fit was repeated without the respective term. Figure 7.3 shows the peak corresponding to the 2.6MeV photon peak for one of the detectors with the best fit function.

In the next step, the peak positions in the uncalibrated spectra obtained from the fits are matched with their literature values. This allows to calculate the *calibration curves* as

$$E_{\text{cal}} = a + b \cdot E_{\text{uncal}} + c \cdot E_{\text{uncal}}^2, \quad (7.1)$$

where E_{cal} is the calibrated energy, E_{uncal} the uncalibrated energy, and a , b , and c are parameters determined from a fit. An example of a calibration curve is shown in Fig. 7.4.

The calibration curves were used to determine the energy deposited in each detector for each event by converting the uncalibrated energy given by the Gaussian filter into calibrated energy. For the physics runs, the curves were applied prospectively, that is a set of calibration curves was valid for all subsequent physics runs until the next calibration run was performed.

The energy resolution, defined as the *full width at half maximum (FWHM)*, was calculated for each photon peak in the calibration spectra. Its energy dependency can

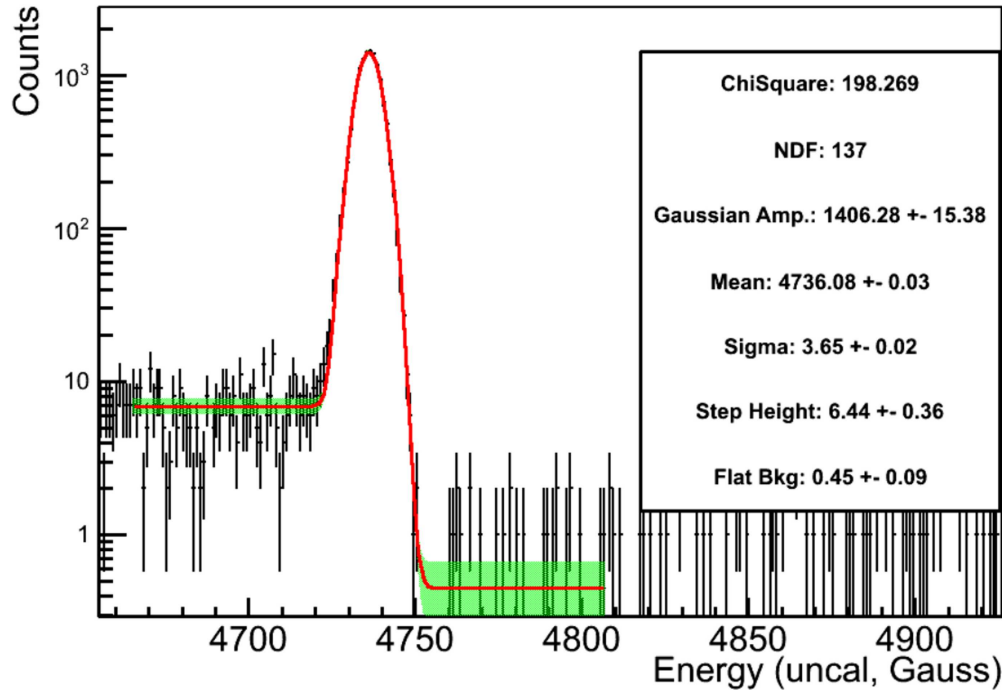


Figure 7.3: Peak corresponding to the 2.6 MeV photon peak with the best fit function. The contributions from the low energy tail and the slope of the linear background are negligible and are therefore omitted in the best fit function. Figure taken from [140].

be expressed as [147]

$$\text{FWHM} = \sqrt{p_0^2 + p_1 \cdot E}, \quad (7.2)$$

with p_1 and p_0 parameters that have to be determined separately for each detector¹. The dependency of the FWHM on the energy for one of the detectors is depicted in Fig. 7.5. Shown is also a fit to the data points with Function (7.2). The peak at 511 keV as well as the *double escape peak (DEP)* at 1593 keV and the *single escape peak (SEP)* at 2104 keV suffer from Doppler-broadening and were excluded from the fit.

The validity of the calibration curves above 2.6 MeV, the highest peak in the calibration spectra, was verified using test pulses as input to the preamplifier. The precision of the calibration curves proved to be better than 10 keV between 3 MeV and 6 MeV.

7.3 Data taking summary

Phase I data taking lasted from November 9, 2011, to May 21, 2013. The measurement live time was calculated from the monitoring test pulses that were inserted into the test input of each detector at a frequency of 0.05 Hz (0.1 Hz before January 2012), that is every 20 s (10 s). For every registered test pulse, 20 s (10 s) are added to the

¹The term proportional to E mentioned in Sec. 5.3.4 is negligible in this case.

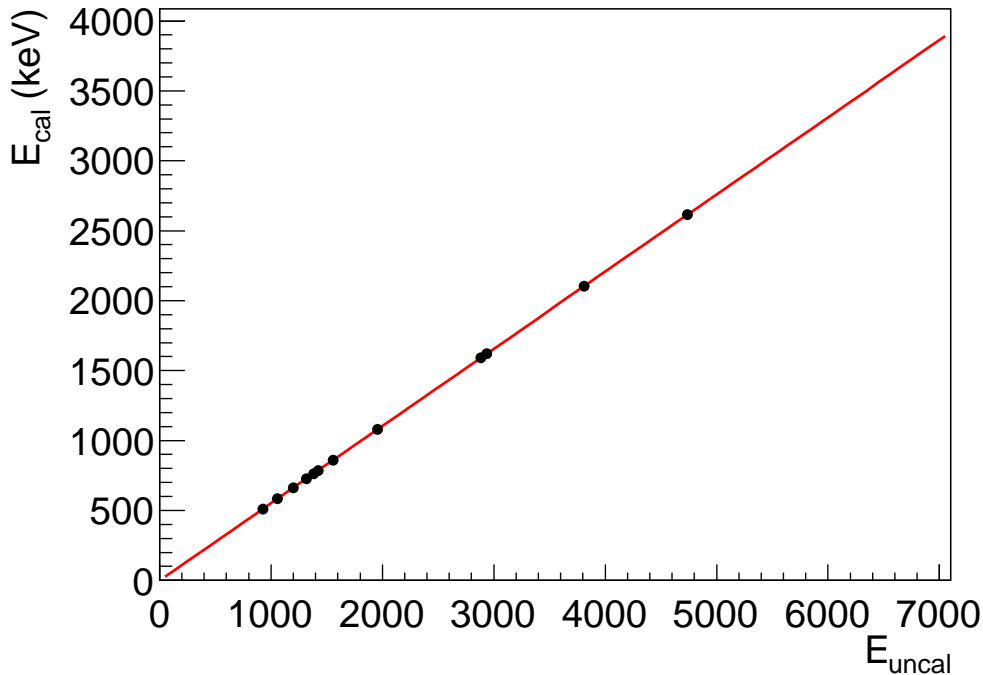


Figure 7.4: True peak positions as a function of the peak positions in the uncalibrated energy spectrum. The calibration curve, plotted in red, is defined as $E_{\text{cal}} = a + b \cdot E_{\text{uncal}} + c \cdot E_{\text{uncal}}^2$, where a , b , and c are determined from a fit. Figure based on [140].

total live time, t_i , of the respective detector, i . RG2, one of the enriched coaxial detectors, showed an increasing leakage current towards the end of the data taking period and was not considered for analysis anymore following March 2013. The data taken between May 31, 2012 and June 15, 2012 was not used for data analysis due to large instabilities of all detectors.

Table 7.1 lists the exposures, \mathcal{E}_i , for all detectors, i , considered for data analysis. They are defined as $\mathcal{E}_i = M_i \cdot t_i$, where M_i is the total mass of detector i . The uncertainty on the exposure was estimated to be $< 0.5\%$. A total of $21.6 \text{ kg} \cdot \text{yr}$ of data was collected with the enriched detectors.

The graph in Fig. 7.6 shows the live time fraction of the enriched detectors over the Phase I data taking period. The gap at the beginning of June 2012 was caused by the exclusion of data due to instabilities. Also the insertion of the BEGe detector string in July 2012 lead to an interruption in the data taking. Clearly seen are the regular short interruptions due to calibration measurements. The overall duty factor was 88.1% . Superposed is the development of the total exposure $\mathcal{E} = \sum_i \mathcal{E}_i$.

From the calibration measurements, the dependency of the FWHM on the energy can be deduced as described in Sec. 7.2. In order to crosscheck the validity of the interpolation, the FWHM at the ^{42}K line at 1524.7 keV estimated from the calibration data was compared to the FWHM derived from a fit to the physics data. For ANG2, ANG4, and GD32D, the FWHM during physics data taking showed a positive offset larger than the 68% uncertainty. As this can be accounted to unobserved gain vari-

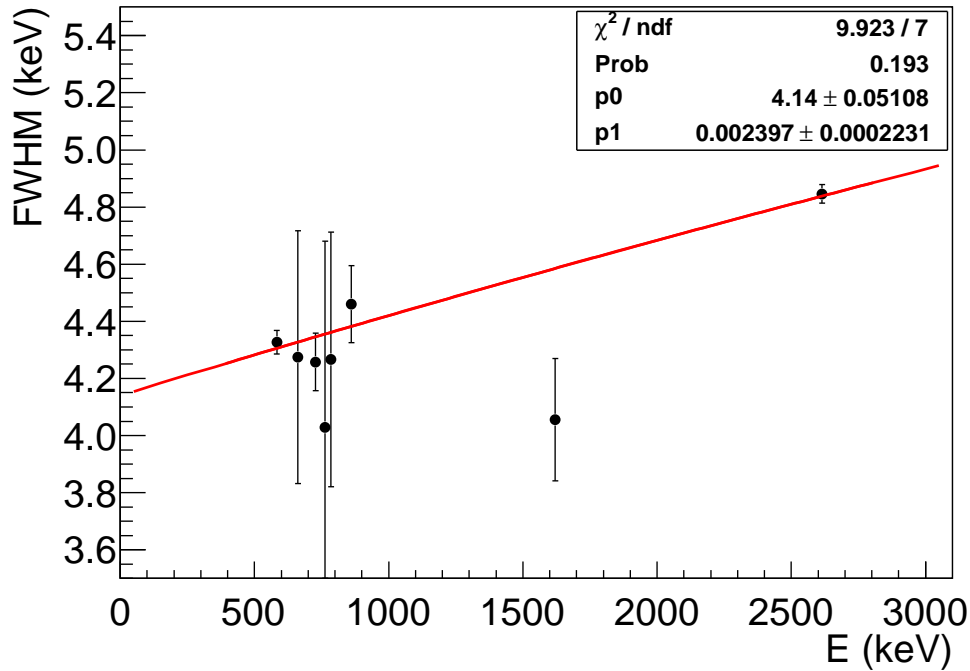


Figure 7.5: FWHM as a function of the energy, E . The data points are fitted with Function (7.2). The Doppler-broadened 511 keV peak, the DEP at 1593 keV, and the SEP at 2104 keV were excluded from the fit. Figure based on [140].

ations, the constant offset of $(1.24 \pm 0.29 \pm 0.02)$ keV, $(0.48 \pm 0.31 \pm 0.05)$ keV, and $(0.94 \pm 0.47 \pm 0.05)$ keV, respectively, had to be added to the FWHM of these three detectors when estimating the energy resolution at a certain energy for the physics data from the calibration data. Table 7.1 lists the estimates for the energy resolution at $Q_{\beta\beta} = 2039$ keV for the single detectors. They were obtained by averaging over the results from all available calibration measurements, weighting the single values with the respective uncertainty, duration of validity for data calibration, and exposure, and corrected for the offset. The statistical uncertainty is larger for ANG2, ANG4, and GD32D due to the uncertainties deriving from the determination of the constant offset from physics data. The systematic uncertainty accounts for the variations deriving from an alternative function to Equation (7.2) and an extraction of FWHM from the sum spectrum of all calibration measurements instead of the weighted sum of the results for the single measurements. The exposure-averaged values for the coaxial and BEGe detectors were (4.8 ± 0.2) keV and (3.2 ± 0.2) keV, respectively.

The energy resolution was stable over the complete Phase I data taking period. This can be seen in Fig. 7.7(a), where the FWHM at 2039 keV of the coaxial detectors is depicted as a function of time. Note that the shown values have not yet been corrected for the constant offset. The fluctuations of the energy resolution remain below 0.2 keV. For the BEGe detectors, the largest variations were about 0.3 keV.

The stability of the gain is demonstrated in Fig. 7.7(b), where the shift of the position of the 2615 keV line for subsequent calibration measurements is depicted for

Table 7.1: Exposure, \mathcal{E} , and FWHM at $Q_{\beta\beta}$, FWHM, for the detectors considered for analysis. The uncertainty on \mathcal{E} was estimated to be $< 0.5\%$. The statistical uncertainty on FWHM was larger for ANG2, ANG4, and GD32D due to the offset correction, which was determined from physics data. Also given are the exposures and exposure-weighted averages of the FWHM for the data sets considering all enriched coaxial detector data (coaxial sum data set), all BEGe detector data (BEGe sum data set), and for the golden and silver data sets, defined in Sec. 7.4.

Detector	\mathcal{E} (kg-yr)	FWHM (keV)
Enriched Coaxial Detectors		
ANG2	3.81	$5.74 \pm 0.29 \pm 0.06$
ANG3	3.21	$4.54 \pm 0.05 \pm 0.13$
ANG4	3.19	$4.91 \pm 0.31 \pm 0.06$
ANG5	3.69	$4.17 \pm 0.04 \pm 0.09$
RG1	2.84	$4.46 \pm 0.07 \pm 0.26$
RG2	2.47	$4.90 \pm 0.06 \pm 0.25$
Coaxial sum	19.2	$4.80 \pm 0.14 \pm 0.13$
Golden	17.9	$4.83 \pm 0.15 \pm 0.13$
Silver	1.3	$4.63 \pm 0.09 \pm 0.22$
Enriched BEGe Detectors		
GD32B	0.55	$2.62 \pm 0.05 \pm 0.07$
GD32C	0.62	$2.63 \pm 0.04 \pm 0.04$
GD32D	0.56	$3.68 \pm 0.47 \pm 0.06$
GD35B	0.67	$3.96 \pm 0.10 \pm 0.07$
BEGe sum	2.4	$3.24 \pm 0.16 \pm 0.06$

the coaxial detectors. The FWHM of the distribution of the shifts, shown in the insert, is 1.3 keV and thus much smaller than the energy resolution. For the BEGe detectors, a FWHM of the gain distribution of 1.0 keV was measured, also well below the energy resolution.

In order to avoid bias, the strategy of a blinded analysis was followed for the Phase I data. All events with an energy deposit between 2019 keV and 2059 keV in one of the detectors, that is within a 40 keV-wide window around $Q_{\beta\beta}$, were stored separately and were not available in the data sets used for analysis. The blinding procedure was applied to all data taken after January 11, 2012. The selection was based on the energy information provided by the FADC. In June 2013, after the end of the Phase I data taking and when all analysis tools needed for the estimation of the half-life of $0\nu\beta\beta$ had been fixed, the complete data was made available for analysis.

Figures 7.8(a) and 7.8(b) show the energy spectra between 20 keV and 7.5 MeV

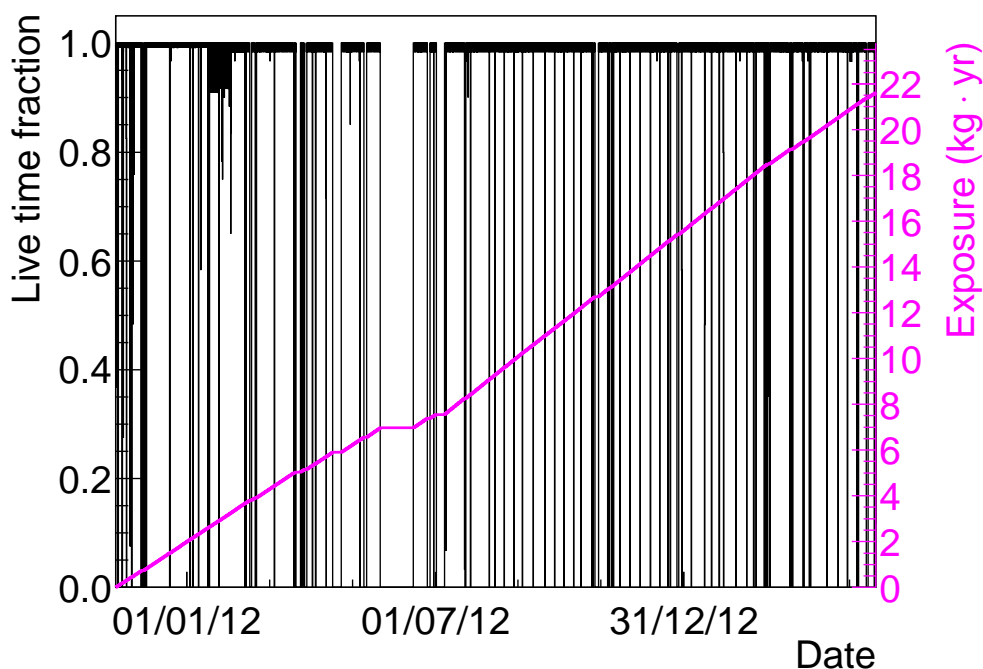


Figure 7.6: Live time fraction and exposure of the enriched detectors in Phase I. The frequent short interruptions were due to the regular calibration measurements.

for the active coaxial (ANG2-ANG5, RG1, RG2) and BEGe (GD32B, GD32C, GD32D, GD35B) detectors, respectively. The data was processed according to the procedure described in Sec. 7.1. The depicted spectra comprise all valid data acquired during Phase I, with a total exposure of 19.2 kg · yr for the coaxial detectors and 2.4 kg · yr for the BEGe detectors. The data sets are referred to as *coaxial sum* and *BEGe sum*, respectively. The green area marks the blinded window. As described in Sec. 7.4, the data of the coaxial detectors was divided in the *golden* and *silver* data set with exposures of 17.9 kg · yr and 1.3 kg · yr, respectively. The corresponding spectra are also shown in 7.8(a). For comparison, the energy spectrum of one of the natural coaxial detectors, GTF112, is depicted in Fig. 7.8(c). Its total exposure was 4.0 kg · yr.

7.4 Background Contributions and Background Index

The energy spectra depicted in Fig 7.8 reveal distinctive characteristics, allowing to draw first conclusions on the present background sources.

The low energy part was dominated by the decay spectrum of ^{39}Ar . This cosmogenically produced radio-isotope decays in the LAr with a half-life of $T_{1/2} = 269$ yr and a Q-value of 565 keV. The decay is pure beta decay without any photon emission. Therefore, the detector geometry and n^+ -surface thickness have a large influence on the shape of the spectrum, explaining the visible differences when comparing the coaxial with the BEGe detector energy spectrum. The activity of ^{39}Ar in natural argon has

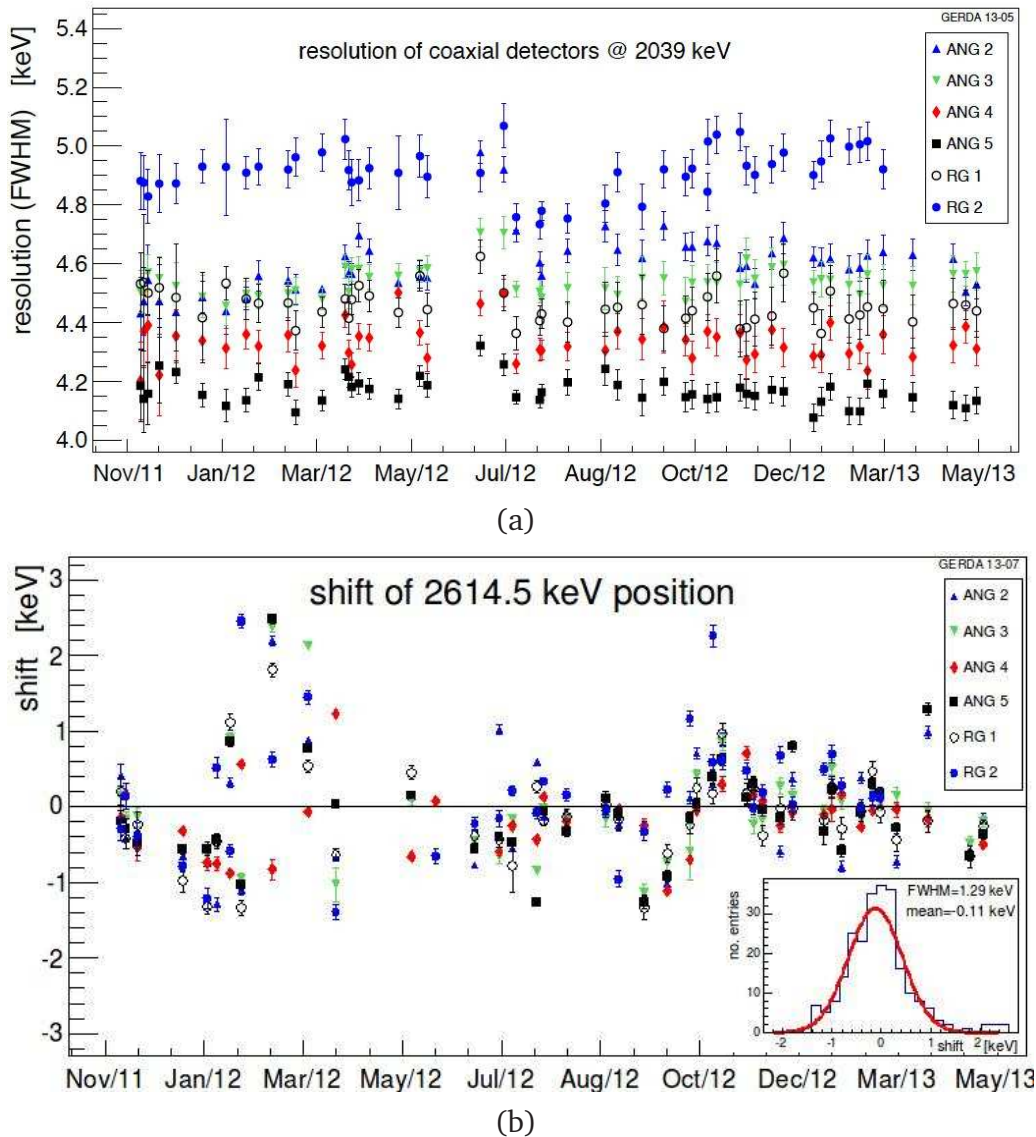
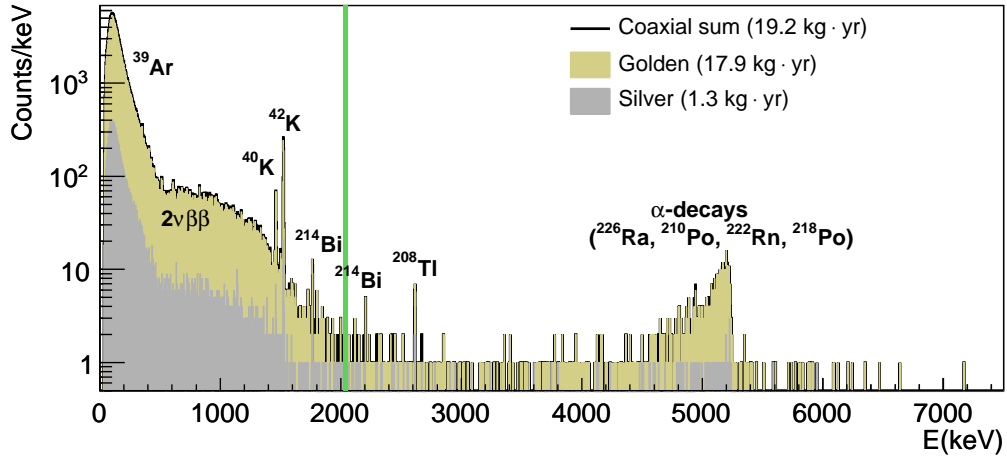


Figure 7.7: (a) The FWHM at 2039 keV for the coaxial detectors as a function of time. Note that the values have not yet been corrected for the constant offset. (b) Shift of the position of the 2615 keV line for subsequent calibration measurements for the coaxial detectors. A FWHM of 1.3 keV was measured for the distribution of the shifts.

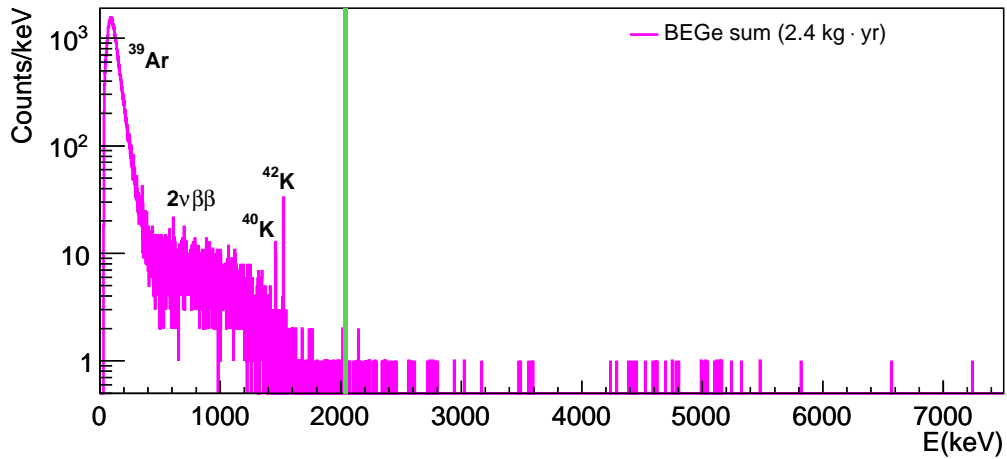
been estimated to be $1.01 \pm 0.02(\text{stat}) \pm 0.08(\text{syst})$ Bq per kg of natural argon [148].

When comparing the energy spectra of the enriched detectors, Fig. 7.8(a) and 7.8(b), with the spectrum of the natural detector, Fig. 7.8(c), it becomes obvious that the dominating contribution between 600 keV and 1500 keV for the enriched detectors derives from the continuum of $2\nu\beta\beta$, while this feature is practically absent for the natural detector.

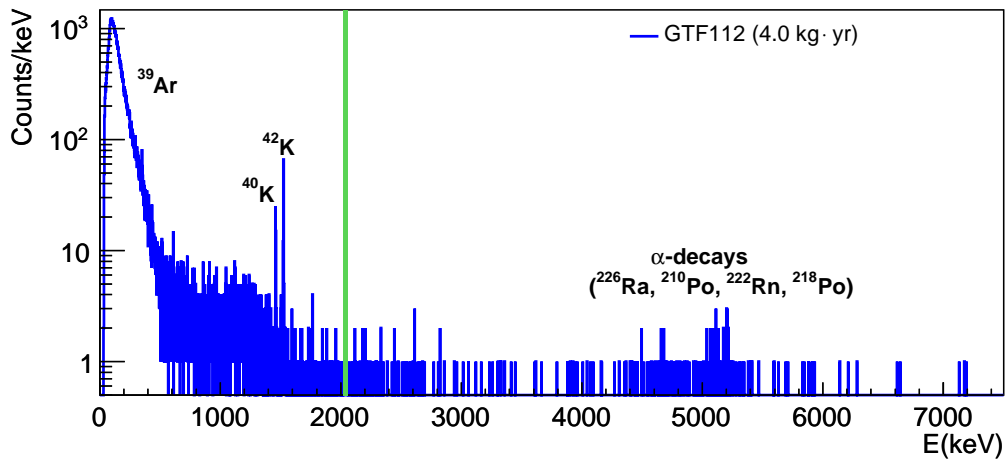
Furthermore, several photon lines can be identified in the depicted spectra. The most prominent ones come from the decays of ^{42}K , ^{40}K , ^{214}Bi , and ^{208}Tl . They are marked in Fig. 7.8. A quantitative analysis of the line intensities is presented in



(a)



(b)



(c)

Figure 7.8: (a) Energy spectra of the enriched coaxial detectors (coaxial sum data set), and the golden and silver data sets. For a definition of the data sets see Sec. 7.4. (b) Energy spectrum of the BEGe detectors (BEGe sum data set). (c) Energy spectrum of the GTF112 detector. All spectra were obtained by processing the data as described in Sec. 7.1. They comprise all valid Phase I data, with a total exposure of $19.2 \text{ kg} \cdot \text{yr}$ for the coaxial detectors ($17.9 \text{ kg} \cdot \text{yr}$ for the golden data set, $1.3 \text{ kg} \cdot \text{yr}$ for the silver data set), $2.4 \text{ kg} \cdot \text{yr}$ for the BEGe detectors, and $4.0 \text{ kg} \cdot \text{yr}$ for GTF112. The green area marks the blinded window.

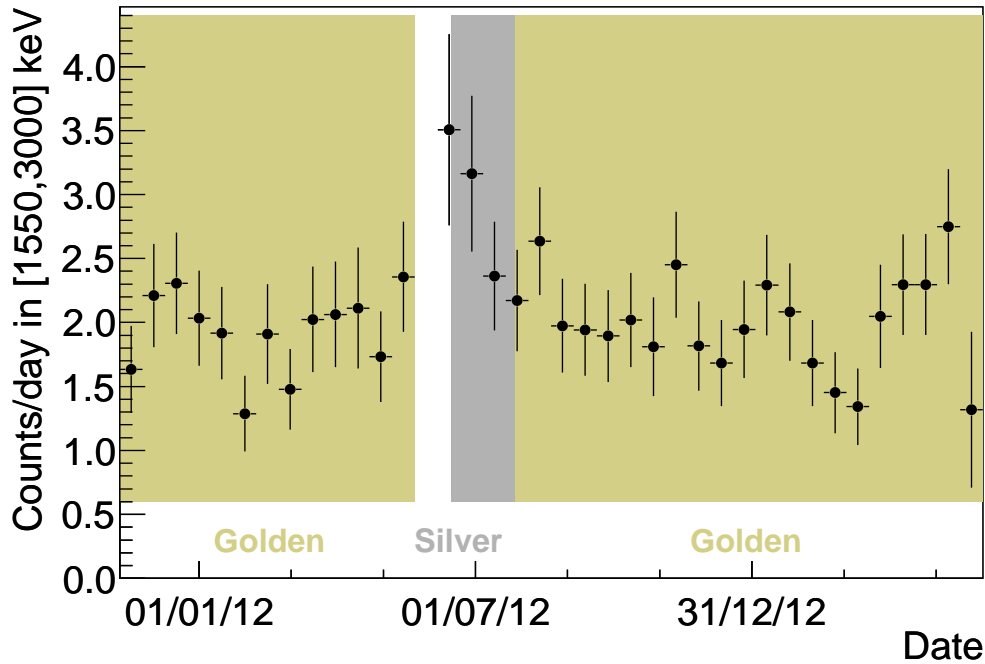


Figure 7.9: Count rate, corrected for the live time fraction, of the coaxial enriched detectors in the range 1550 keV to 3000 keV in time intervals of 15 days as a function of time.

Sec. 7.5.

At energies above 3.5 MeV, contributions from alpha decays are present in the energy spectrum of the enriched coaxial detectors. Several peak-like structures can be distinguished at 4.7 MeV, 5.3 MeV, 5.4 MeV, and 5.9 MeV. They can be attributed to alpha decays from ^{226}Ra , ^{210}Po , ^{222}Rn , and ^{218}Po on or close to the p^+ -surface of the detectors. All four isotopes are found in the natural decay chain of ^{238}U . There are no indications for the presence of isotopes of the ^{232}Th chain in the vicinity of the p^+ -surface of the detectors.

Figure 7.9 shows the count rate, corrected for the live time fraction, of the coaxial enriched detectors in the range 1550 keV to 3000 keV in time intervals of 15 days as a function of time.

The rate was stable within the uncertainties for most part of the data taking. Only for a period following the extraction of the natural detectors in the 1-string arm and the insertion of the BEGe detectors in June/July 2012, the count rate showed an increase larger than 50% compared to the average rate. The rate returned to the usual level after ≈ 30 days. The data from the coaxial detectors could hence be divided into two data sets, as indicated in Fig. 7.9. The *silver* data set contained the data collected with the coaxial detectors during the first ≈ 30 days after the intervention for the detector exchange. The *golden* data set contained all other data collected with the enriched coaxial detectors. The information regarding exposure and energy resolution is given in Table 7.1.

The background index (*BI*) in the *region of interest* (*ROI*) around $Q_{\beta\beta}$ was esti-

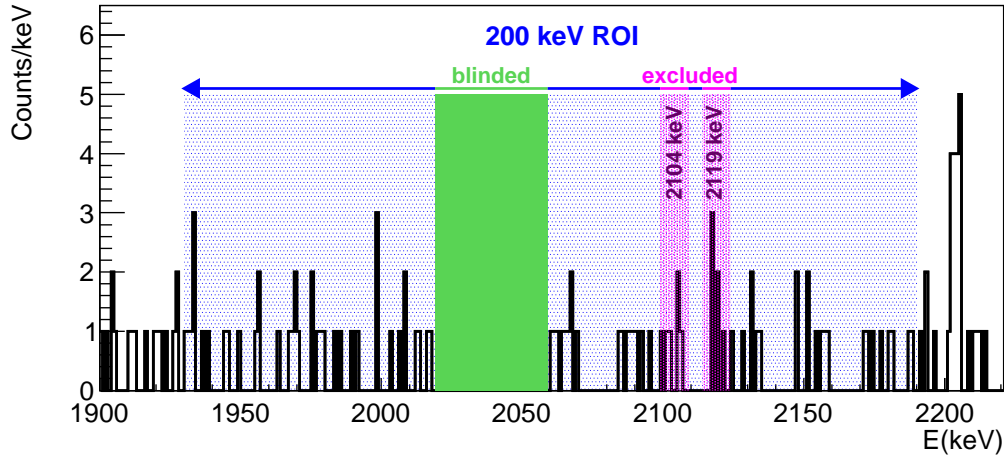


Figure 7.10: Definition of the window used for the determination of the background index, BI . All events between 1930 keV and 2190 keV were counted, excluding the 10 keV windows around the SEP of ^{208}Tl at 2104 keV and the ^{214}Bi photon line at 2119 keV, as well as the 40 keV blinding window around $Q_{\beta\beta}$.

Table 7.2: Background index, BI , for all relevant data sets. The window used for the estimate comprised the range from 1930 keV to 2190 keV, excluding the regions between 2099 keV and 2109 keV and between 2114 keV and 2124 keV, as well as the 40 keV blinded window.

Data set	BI (10^{-2} cts/(keV · kg · yr))
Coaxial sum	$2.1^{+0.3}_{-0.2}$
Golden	$1.8^{+0.3}_{-0.2}$
Silver	$6.5^{+2.0}_{-1.5}$
BEGe sum	$4.4^{+1.2}_{-1.0}$

mated from the energy spectrum between 1930 keV and 2190 keV. The regions between 2099 keV and 2109 keV as well as 2114 keV and 2124 keV were ignored due to possible contributions from the single escape peak (SEP) of ^{208}Tl at 2104 keV and from the 2119 keV photon line from ^{214}Bi , which would have led to an overestimation of the continuous background. Excluding also the 40 keV-wide window around $Q_{\beta\beta}$, where no information on the data was available for the blinded analysis, the total width of the window used for the determination of the BI was 200 keV. Figure 7.10 illustrates the definition of this window. As observable in this figure and shown in Chapter 9 and in [149], the background could be assumed to be flat in the ROI .

The BI was determined by counting all events in the above defined window and normalizing this number to the width of the energy window and the exposure. The results for all enriched coaxial detectors, the golden and silver data sets, and for the BEGe sum data set are listed in Table 7.2.

7.5 Photon Line Intensities

The most prominent photon line for all spectra depicted in Fig. 7.8 is the 1524.7 keV line of ^{42}K , the daughter of ^{42}Ar . The mother isotope, ^{42}Ar , is produced by cosmogenic activation in argon and decays with a Q-value of 599 keV and a half-life of 32.9 yr. The homogeneously distributed ^{42}K ions are transported in the LAr by electric fields and convective flows. They decay with a half-life of 12.4 h via beta decay with a Q-value of 3525.4 keV to the stable ^{42}Ca . In 18% of the cases, ^{42}K decays to an excited level of ^{42}Ca , which de-excites under emission of a 1524.7 keV photon, explaining the observed line in the energy spectrum.

The line at 1460.8 keV derives from the decay of ^{40}K . It decays with a half-life of $1.3 \cdot 10^9$ yr via beta decay and via electron capture and positive beta decay. The Q-values are with 1311.1 keV and 1504.9 keV both well below $Q_{\beta\beta}$.

The beta decay of ^{60}Co leads to two distinct photon lines at 1173.2 keV and 1332.5 keV. The Q-value of the decay is 2823.9 keV and the half-life is 5.3 yr.

Furthermore, the photon lines of several isotopes from the natural decay chains can be recognized in the spectra. The decay chain of ^{232}Th comprises ^{228}Ac with lines at 911.2 keV and 969.0 keV, ^{212}Pb with a line at 238.6 keV, ^{212}Bi with a line at 727.3 keV and ^{208}Tl with lines at 510.8 keV, 583.2 keV, 860.6 keV, and 2614.5 keV. The latter can be easily distinguished in Fig. 7.8(a). The presence of elements of the ^{238}U chain can be deduced from the lines of ^{214}Pb at 295.2 keV and 351.9 keV and lines from ^{214}Bi at 609.3 keV, 768.4 keV, 1120.3 keV, 1238.1 keV, 1764.5 keV, and 2204.2 keV, the latter two again well visible in the spectrum of the coaxial detectors. The half-lives range from a few minutes to several hours and the Q-values vary between 570 keV for ^{212}Pb and 6.2 MeV for ^{212}Bi .

Also a possible contamination by ^{137}Cs might be present.

In order to quantify the background contributions, the line intensities for the mentioned photon lines were determined for the coaxial detectors, the golden and silver data sets, and the BEGe detectors. For each line, the number of events in the signal region, N_{S+B} , was counted in an 8σ -wide window centered on the photon line energy. For σ , the exposure weighted average at $Q_{\beta\beta}$ was used, corresponding to $\sigma = 2.1$ keV for the sum of the coaxial detectors and the golden data set, $\sigma = 1.4$ keV for the sum of the BEGe detectors, and $\sigma = 2.0$ keV for the silver data set.

The number of events due to background, N_B , was estimated from the number of counts in a 16σ -wide window centered on the photon line and excluding the signal region. This resulted in a total range of 8σ for the background counting. Taking into account the Poissonian nature of the processes leading to N_{S+B} and N_B and following a Bayesian approach, the probability distribution for measuring N_{S+B} and N_B is given as

$$P(N_{S+B}, N_B | r_S, r_B) = P(N_{S+B} | r_S, r_B) P(N_B | r_B) = \frac{\lambda^{N_{S+B}} \cdot e^{-\lambda}}{N_{S+B}!} \cdot \frac{\nu^{N_B} \cdot e^{-\nu}}{N_B!}, \quad (7.3)$$

where r_S and r_B are the expected signal and background rate in units of cts/(kg·yr) and $\lambda = \mathcal{E} \cdot (r_S + c_B \cdot r_B)$ and $\nu = \mathcal{E} \cdot r_B$ the expectation values for the number of

events in the signal and background region, respectively, for a data set with exposure \mathcal{E} . The scaling factor, c_B , is equal to unity in case of equally sized signal and background regions. Using the Bayes' theorem, the global posterior probability distribution, $P(r_S, r_B | N_{S+B}, N_B)$, can be expressed as a function of Equation (7.3) and the prior probability distribution functions for r_S and r_B , $P_0(r_S)$ and $P_0(r_B)$, as

$$P(r_S, r_B | N_{S+B}, N_B) = \frac{P(N_{S+B}, N_B | r_S, r_B) P_0(r_S) P_0(r_B)}{\int P(N_{S+B}, N_B | r_S, r_B) P_0(r_S) P_0(r_B) dr_S dr_B}. \quad (7.4)$$

In order to obtain an estimate for r_S , Equation (7.4) has to be marginalized,

$$P(r_S | N_{S+B}, N_B) = \int P(r_S, r_B | N_{S+B}, N_B) dr_B. \quad (7.5)$$

The analysis was carried out using the Bayesian Analysis Toolkit, BAT [150]. For the prior probabilities, $P_0(r_S)$ and $P_0(r_B)$, flat distributions were considered and r_S and r_B were required to be non-negative.

Table 7.3 lists the line intensities, r_S , for all relevant background photon lines for the four data sets. Due to the large background from ^{39}Ar at small energies, only lines above 300 keV were considered in the analysis. For the line intensity, the mode of $P(r_S | N_{S+B}, N_B)$ and the smallest 68% probability interval of the marginalized distribution are given. In case this interval contains zero, the 90% quantile is shown.

As expected, the ^{42}K line was the most intense photon line for all data sets.

For the rate of the 1332.5 keV line of ^{60}Co , only limits can be given for the coaxial and the golden data set. It is expected to be very similar to the rate of the 1173.2 keV line.

The behaviour of the overall count rate between 1550 keV and 3000 keV, depicted in Fig. 7.9, is reflected in the line rates of the isotopes from the ^{232}Th decay chain. For the silver data set, the rates were systematically higher than for the golden data set. The limited statistics did not allow to draw analogous conclusions for the ^{238}U chain isotopes.

The presence of ^{137}Cs was confirmed only for the BEGe detectors.

The line at 511.0 keV is fed by photons from ^{208}Tl decay as well as by the photons resulting from e^+e^- -annihilation. The positrons can be produced by positive beta decay, e.g. for ^{40}K , or by a pair production process.

The smaller rate at the ^{42}K line for the BEGe detectors compared to the coaxial detectors is explained by the smaller size of the BEGe detectors, making full absorption of the 1524.7 keV photons less likely. Due to geometrical differences and diverse diode histories, also for the other photon lines differences in the rates of coaxial and BEGe detectors were expected. The small exposure of the BEGe detectors allowed only upper limits for most line rates and thus no quantitative comparison with the coaxial detectors was possible.

Table 7.3 also shows the corresponding line intensities as measured in the HdM experiment [151]. On average, they are about one order of magnitude higher than the intensities measured in GERDA Phase I.

Table 7.3: Line intensity, r_S , for the most prominent background lines. The mode and smallest interval of 68% probability of the marginalized parameter distribution are given. In case the interval contained zero, the 90% quantile is shown. For comparison, the corresponding line intensities measured in the HdM experiment are shown [151].

Isotope	Energy (keV)	Coaxial sum	Golden	Silver	BEGe sum	HdM
		r_S cts/(kg·yr)	r_S cts/(kg·yr)	r_S cts/(kg·yr)	r_S cts/(kg·yr)	r_S cts/(kg·yr)
^{42}K	1524.7	60.6 [58.8,62.6]	59.6 [57.6,61.5]	75.1 [67.7,83.5]	46.6 [41.7,51.2]	-
^{40}K	1460.8	14.1 [12.9,15.2]	14.5 [13.2,15.6]	14.5 [13.2,15.6]	12.7 [9.6,15.9]	181±2
^{60}Co	1173.2	2.9 [1.3,4.4]	2.5 [0.9,4.0]	5.1 [0.8,9.9]	<8.6	55±1
	1332.5	<1.9	<1.8	5.2 [1.5,9.1]	<6.3	51±1
^{228}Ac	911.2	3.1 [1.1,4.9]	4.0 [1.8,5.9]	<8.9	<8.0	30±2
	969.0	6.7 [4.6,8.5]	5.6 [3.5,7.6]	19.7 [12.2,27.5]	<8.2	18±1
^{212}Bi	727.3	2.3 [0.5,4.1]	<4.7	17.8 [8.7,24.9]	<6.7	8±1
^{208}Tl	583.2	4.0 [1.9,6.2]	3.0 [1.0,5.0]	14.0 [5.9,21.8]	<11.0	36±3
	860.6	<3.1	<3.6	<11.9	<7.0	6±1
	2614.5	1.5 [1.1,1.7]	1.5 [1.1,1.7]	1.2 [0.2,2.4]	0.6 [0.1,1.3]	17±1
^{214}Pb	351.9	9.6 [4.3,14.1]	10.1 [5.0,15.2]	<34.8	13.5 [5.6,22.7]	139±5
^{214}Bi	609.3	8.1 [5.6,10.3]	8.6 [5.9,10.8]	<16.1	12.0 [6.7,18.2]	105±1
	768.4	4.3 [2.1,6.3]	3.6 [1.4,5.5]	16.9 [8.1,23.9]	6.5 [1.6,10.7]	11±1
	1120.3	<2.9	<3.1	<8.9	6.7 [2.5,10.7]	27±1
	1238.1	<2.8	<2.8	<10.7	<6.6	11±1
	1764.5	3.2 [2.7,3.7]	3.3 [2.7,3.7]	2.2 [0.2,4.0]	<2.5	31±1
^{137}Cs	2204.2	0.9 [0.6,1.2]	0.9 [0.6,1.2]	<3.3	1.0 [0.3,1.8]	8±1
^{137}Cs	661.7	<4.6	<5.0	<14.7	7.0 [2.3,11.8]	282±2
e^+e^-						
& ^{208}Tl	511.0	10.4 [7.8,12.8]	10.6 [7.9,13.1]	<20.0	16.5 [10.4,21.9]	30±3

Chapter 8

Monte Carlo Simulation of the GERDA Experiment

The energy spectra acquired during GERDA Phase I and presented in Chapter 7 are composed of various contributions. The decays of a broad variety of radioactive isotopes inside or on the surface of the materials used in the experimental setup as well as in the detectors themselves lead to energy depositions and thus contributed to the final energy spectra. With the help of Monte Carlo (MC) simulations, the energy spectra of the single background contributions were modeled.

8.1 Monte Carlo Description of the GERDA Experiment

The MC simulations were carried out within the GEANT4 [152] based MAGE [153] framework. It comprises a detailed description of the geometry of the GERDA experiment, including cabling, detector holders, minishrouds, and shroud. A schematic of the implementation is shown in Fig. 8.1.

The geometrical information listed in Table 6.1 was taken into account to model each detector used in the GERDA Phase I setup. The p^+ - and n^+ -electrodes were implemented as inactive components of the detectors.

Two different configurations of the detector array were available for the MC campaign. For both cases, the three detector strings containing the eight enriched coaxial detectors and one natural coaxial detector remained unchanged. The fourth string was designed to either contain the two additional natural coaxial detectors used in the first part of Phase I data taking, or the five BEGe detectors inserted in the array in July 2012. In the following, the first configuration will be referred to as *configNAT*, whereas the second one will be referred to as *configBEGE*. In Fig. 8.2(a), *configNAT* is depicted. Figure 8.2(b) shows the BEGe detector string that replaces the string containing the two natural coaxial detectors, when switching to *configBEGE*. Additionally, there was the possibility to replace the detector array by a single detector. For the detector geometry, either ANG3 or GD32B could be chosen. These configurations are labeled *configANG3* and *configGD32B* in the following.

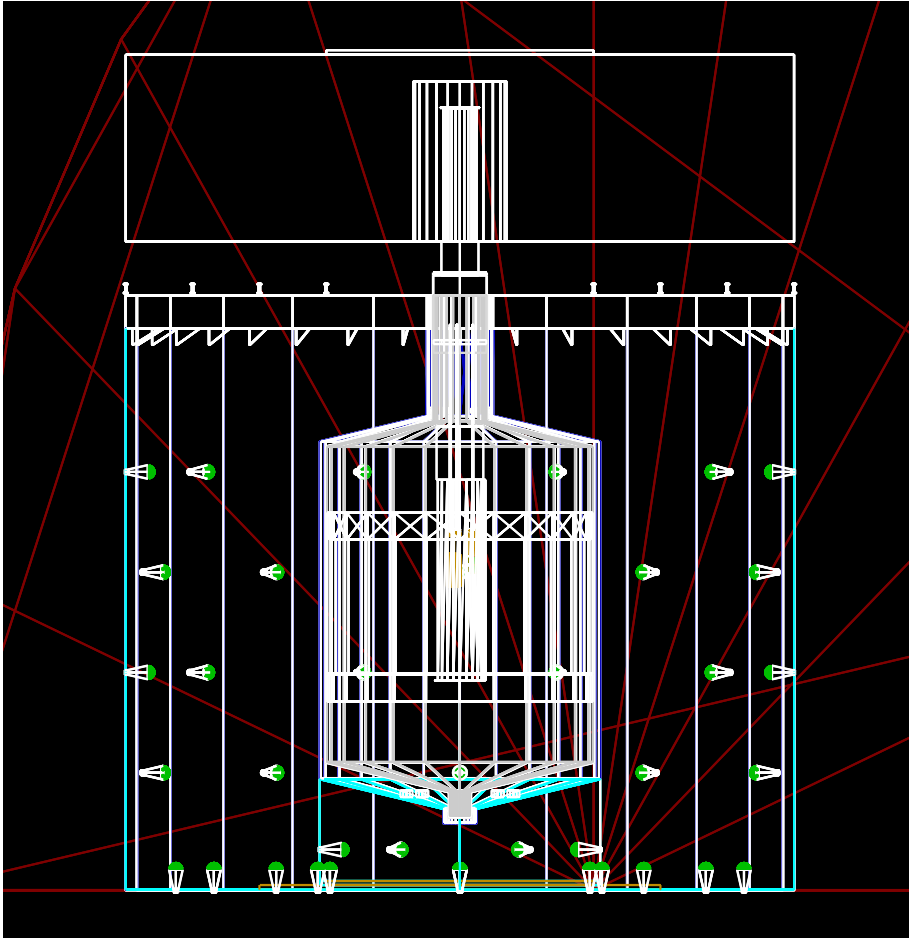


Figure 8.1: Schematic of the MAGE implementation of the GERDA experiment. The water tank, equipped with photomultipliers, and the cryostat can be distinguished. The cylindrical shaped shroud containing the detector array is placed inside the cryostat. On top of the water tank, the cleanroom structure with the lock system is implemented.

8.2 Monte Carlo Event Processing

The output of MAGE is a list of hits with energies E_i for every simulated decay. The energy in a detector, E_{det} , for each event is calculated as $E_{\text{det}} = \sum_i^{\text{det}} E_i$, where the sum runs over all hits of the event in which energy is deposited in the active volume of the respective detector.

In order to account for the energy resolution of each detector, E_{det} was smeared with the resolution obtained during data taking. For this scope, the FWHM as a function of energy, Equation (7.2), was determined for each detector as described in Sec. 7.2. The final curves were obtained by averaging over all valid calibration runs. For each E_{det} , the FWHM was determined from the corresponding detector's curve. The smearing factor to be added to E_{det} was drawn from a Gaussian random distribution centered on zero and with a resolution corresponding to the respective FWHM.

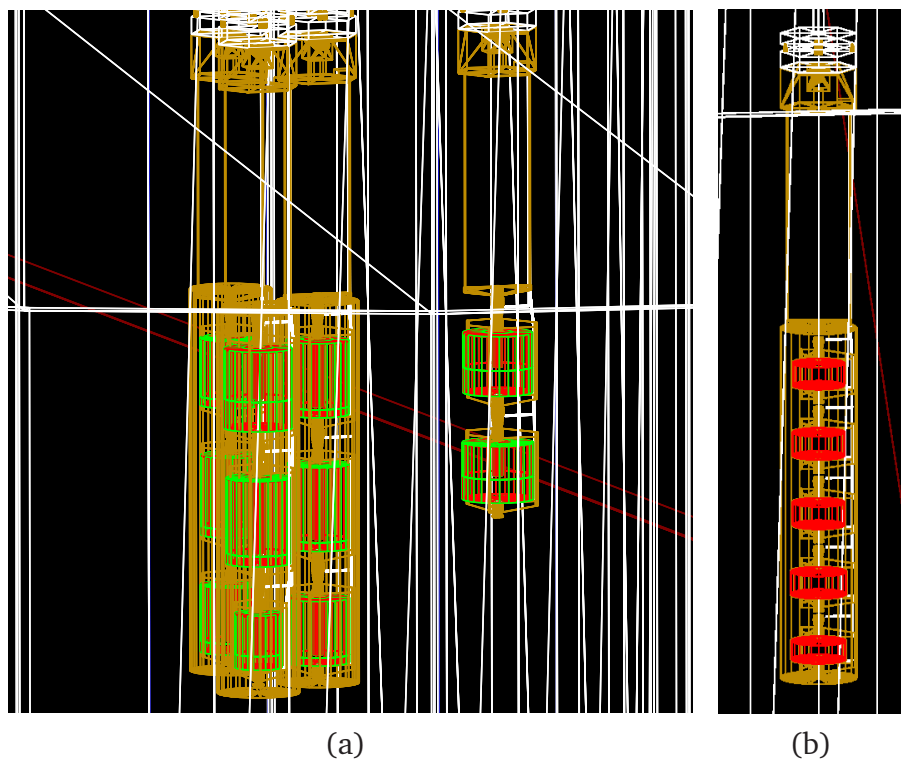


Figure 8.2: (a) The detector array in the *configNAT* configuration. (b) The string containing the five Phase I BEGe detectors. It replaces the two-detector string, when switching from *configNAT* to *configBEGE*. The minishrouds are sketched in brown. No minishroud was present for the string with the two natural detectors.

Figure 8.3 shows an example of the energy spectrum for a single coaxial detector. It was obtained by simulating ^{60}Co decays in the detector holders. During processing, the energy spectrum was smeared and a detector anti-coincidence cut with a threshold of 20 keV was applied. The differences before and after the processing are clearly visible. The energy smearing broadens the photon peaks and the anti-coincidence cut reduces the total number of events contained in the energy spectrum.

A complete set of MC simulations was prepared for the golden and for the BEGe sum data set. For all MC simulations, the effects of the individual detector masses, the active and dead volume fractions of each detector, and the individual detector live time had to be taken into account, when creating the energy spectra corresponding to the data sets. Depending on the simulation mode used, some parameters were already accounted for in the simulations, whereas others had to be introduced during the post-processing. For both data sets, three types of modeling and processing can be distinguished, depending on the nature and position of the simulated source. It has to be noted that for the analyses described in the following chapters, the needed input was the shape of the energy spectra. Therefore, the single detector spectra of each background contribution could be scaled as necessary in order to assure the correct composition of their sum energy spectrum.

Full array Decays of the isotope under examination were simulated in a specific vol-

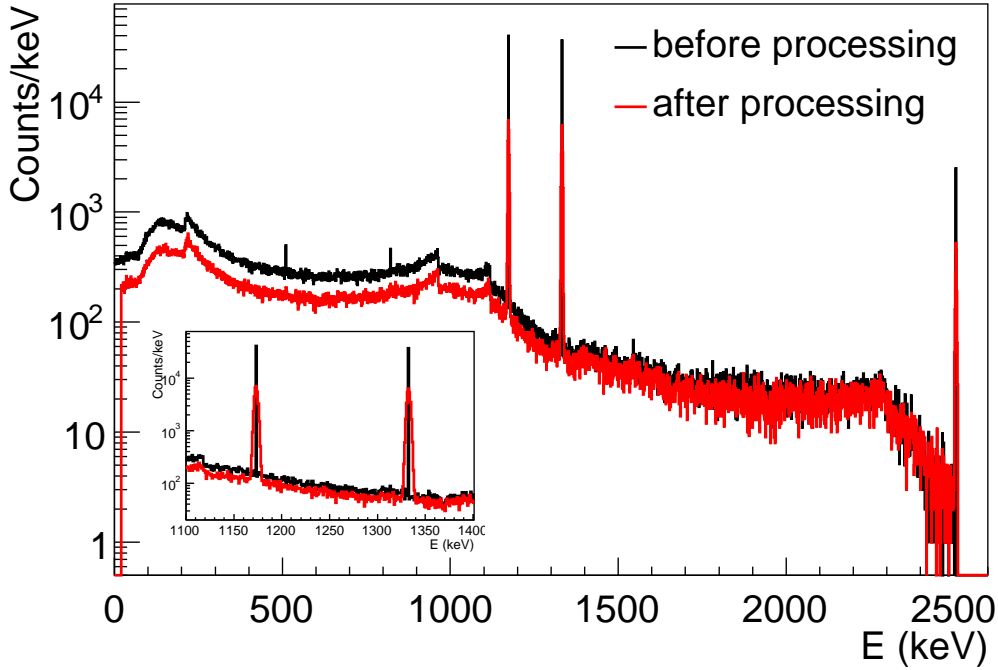


Figure 8.3: Energy spectrum of a single coaxial detector obtained from MC simulation of ^{60}Co decays in the detector holders. The differences before and after processing are clearly visible. The inset shows a zoom into the energy region around the two photon peaks at 1173 keV and 1333 keV.

ume, component, and/or material of the GERDA setup. For the simulations corresponding to the golden (BEGe sum) data set, *configNAT* (*configBEGE*) was used. The single detector energy spectra were smeared and a detector anti-coincidence cut was applied in analogy to the physics data processing, excluding all events with an energy deposit > 20 keV in more than one detector in the array. The energy information from the detectors corresponding to ANG1 and RG3 was not taken into account for this cut. The final energy spectrum, $\phi(E)$, was obtained by scaling the energy spectrum of each detector, $\varphi_j(E)$, with the detector's live time in days, $T_j = 458.3$ for ANG2-ANG5 and RG1, $T_j = 384.6$ for RG2, $T_j = 280.0$ for GD32B, $T_j = 303.4$ for GD32C and GD35B, $T_j = 284.0$ for GD32D, and $T_j = 0$ for all other detectors, and summing up all single detector spectra,

$$\phi(E) = \sum_{j=1}^{N_{det}} T_j \cdot \varphi_j(E), \quad (8.1)$$

with $N_{det} = 11$ for *configNAT* and $N_{det} = 14$ for *configBEGE*.

Single detectors in full array This mode was applied for decays taking place inside the detectors themselves. Again, *configNAT* was used for the simulations referring to the golden data set, whereas those corresponding to the BEGe sum data set were modeled with *configBEGE*. Two simulations were run for each detector

in the array, one simulating the decays in the active part and one simulating the decays in the n^+ -deadlayer of the respective detector. For each simulation, the smearing of the energies and a detector anti-coincidence cut, excluding the energy information from ANG1 and RG3, were applied. The single detector spectra were normalized to the total number of decays simulated to represent the detection efficiency. They were then multiplied by the detector's live time in days and summed up, as described above. For the simulation of N_{act}^α decays in the active part of the detector α , this results in

$$\phi_{act}^\alpha(E) = \sum_{j=1}^{N_{det}} \frac{T_j}{N_{act}^\alpha} \varphi_{act,j}^\alpha(E), \quad (8.2)$$

whereas the simulation of N_{dead}^α decays in the dead part leads to

$$\phi_{dead}^\alpha(E) = \sum_{j=1}^{N_{det}} \frac{T_j}{N_{dead}^\alpha} \varphi_{dead,j}^\alpha(E), \quad (8.3)$$

with $N_{det} = 11$ for *configNAT* and $N_{det} = 14$ for *configBEGE*. The distributions $\varphi_{act,j}^\alpha(E)$ and $\varphi_{dead,j}^\alpha(E)$ represent the energy spectrum in detector j resulting from decays in the active or dead volume of a specific detector α . Consequently, the distributions $\phi_{act}^\alpha(E)$ and $\phi_{dead}^\alpha(E)$ give the total energy spectrum resulting from decays in the active or dead volume of detector α . In the next step, $\phi_{act}^\alpha(E)$ ($\phi_{dead}^\alpha(E)$) was scaled with the active volume fraction, $f_{act,\alpha}$, (dead volume fraction, $(1 - f_{act,\alpha})$) of detector α and the spectra for the active and the dead part were summed,

$$\phi_{tot}^\alpha(E) = f_{act,\alpha} \phi_{act}^\alpha(E) + (1 - f_{act,\alpha}) \phi_{dead}^\alpha(E). \quad (8.4)$$

The spectrum of each detector was then scaled with its total mass, M_α , in units of kg. The final spectrum for each data set was obtained by summing the spectra of all detectors present in the array,

$$\phi(E) = \sum_{\alpha=1}^{N_{det}} M_\alpha \cdot \phi_{tot}^\alpha(E). \quad (8.5)$$

In case of decays of ^{76}Ge , the single spectra were also scaled with the detector's isotopic abundance, $f_{76,\alpha}$,

$$\phi(E) = \sum_{\alpha=1}^{N_{det}} f_{76,\alpha} \cdot M_\alpha \cdot \phi_{tot}^\alpha(E). \quad (8.6)$$

The values for $f_{act,\alpha}$, M_α , and $f_{76,\alpha}$ are reported in Table 6.1.

Single detector In order to reduce the computing expenses for cases, where detector anti-coincidences and minor geometrical differences between the detectors were of secondary importance, the simulations were carried out using *configANG3* and *configGD32B*. In this case, the only processing step that had to be applied was the smearing of the produced energy spectrum.

8.3 Simulated Background Sources

The decays of all radioactive isotopes whose presence was deduced from the Phase I data energy spectra were simulated. As can be seen from Fig. 7.8, the dominating contribution in the energy spectra of the enriched detectors came from $2\nu\beta\beta$ of ^{76}Ge . From the observations made in Sec. 7.4 and from Table 7.3, the background contaminations that had to be considered were radioactive isotopes from the natural decay chains of ^{232}Th and ^{238}U , as well as ^{42}K , ^{40}K , and ^{60}Co decays. Due to its low Q-value of 565 keV, the correct modeling of the ^{39}Ar beta decay spectrum would require an extremely detailed knowledge not only of the detector deadlayer geometry, but more importantly of the trigger efficiency at small energies. As the study of these matters is beyond the scope of this thesis, for all analyses presented in the following, an energy threshold above the Q-value of ^{39}Ar was set and thus the simulation of ^{39}Ar decays was not needed. Since no evidence for the presence of ^{137}Cs was found in the spectra of the coaxial enriched detectors, this source was considered to be negligible and no ^{137}Cs decays were simulated.

Further contributions to the energy spectra could come from muons of the cosmic radiation. It has been shown, however, that the muon rejection efficiency of the muon veto system, $\epsilon_{\mu r}$, is $\epsilon_{\mu r} = 0.991^{+0.003}_{-0.004}$ [154], so that the muon contribution is reduced to a BI of $< 10^{-5}$ cts/(keV · kg · yr) [11].

The background due to neutron interactions was estimated to be of the order of 10^{-5} cts/(keV · kg · yr) [155]. Both contributions are thus negligible and were not considered.

Another possible source of background events were the three 20 kBq ^{228}Th sources used for the calibration measurements. During regular data taking, they were shielded with tantalum plates. Their contribution to the BI was estimated to be $(1.07 \pm 0.04(\text{stat})^{+0.13}_{-0.19}(\text{syst})) \cdot 10^{-4}$ cts/(keV · kg · yr) [146] and was thus negligible in the Phase I data sets. Before the start of Phase I data taking, an additional 20 kBq ^{228}Th calibration source fell to the bottom of the cryostat. Since the contribution to the BI from this source was estimated to be below 10^{-3} cts/(keV · kg · yr), its removal was postponed to after the end of Phase I. It had to be considered for the simulation of the background contaminations in the experimental setup, though.

The contributions from the cryostat and the water tank to the BI have been estimated to be below 10^{-4} cts/(keV · kg · yr) [156]. Therefore, no decays were simulated in these components. However, the contamination of the LAr with isotopes from the ^{238}U chain due to the radon-emanation of the cryostat and lock system materials was taken into account.

The 40 keV region around the Q-value of double beta decay of ^{76}Ge , $Q_{\beta\beta} = 2039$ keV, was blinded over the complete Phase I data taking period. Hence, potential photon peaks from background contributions in this region could not be identified from the data energy spectra. There are three possible candidates whose decays can lead to a line around 2039 keV. The first candidate is neutron capture on ^{76}Ge [155]. The second candidate is the inelastic scattering of neutrons off ^{206}Pb , leading to an ex-

Table 8.1: List of the available screening measurement results of hardware components in the GERDA experiment obtained from gamma ray screening and ^{222}Rn measurements. The activity of the minishroud was derived from ICP-MS measurements assuming secular equilibrium of the ^{238}U chain. The last column gives the estimated BI at $Q_{\beta\beta}$ in units of 10^{-3} cts/(keV · kg · yr) [158, 159]. Table taken from [149].

Component	units	^{40}K	$^{214}\text{Bi}/^{226}\text{Ra}$	^{228}Th	^{60}Co	^{222}Rn	BI
Close sources: up to 2 cm from detectors							
Copper det. support	$\mu\text{Bq}/\text{det}$	<7	<1.3	<1.5			<0.2
PTFE det. support	$\mu\text{Bq}/\text{det}$	6.0 (11)	0.25 (9)	0.31 (14)			0.1
PTFE in array	$\mu\text{Bq}/\text{det}$	6.5 (16)	0.9 (2)				0.1
minishroud	$\mu\text{Bq}/\text{det}$		22 (7)				2.8
Li salt (n^+ -contact)	mBq/kg		17 (5)				≈ 0.003
Medium distant sources: 2 cm to 50 cm from detectors							
CC2 preamps	$\mu\text{Bq}/\text{det}$	600 (100)	95 (9)	50 (8)			0.8
cables and suspension	mBq/m	1.40 (25)	0.4 (2)	0.9 (2)	76 (16)		0.2
Distant sources: further than 50 cm from detectors							
cryostat	mBq					54.7 (35)	<0.7
copper of cryostat	mBq	<784	264 (80)	216 (80)	288 (72)		<0.05
steel of cryostat	kBq	<72	<30	<30	475		
lock system	mBq					2.4 (3)	<0.03
^{228}Th calib. source	kBq		20				<1.0

cited state of this isotope [157], which de-excites under the emission of photons with a discrete energy. The third possibility is the decay of ^{56}Co , which might be present in the material used in the experimental setup. In all three cases, in addition to the photon lines close to $Q_{\beta\beta}$, other strong photon lines outside the blinded region should be visible in the energy spectra. Due to their absence, it was concluded that no such contaminations were present during GERDA Phase I data taking.

8.3.1 Results from Screening Measurements

Valuable information regarding the strength and location of background contaminations was given by the results of the material screening measurements, which had been conducted before installing the respective parts into the GERDA setup. The available results are listed in Table 8.1.

8.3.2 Details of the Simulated Spectra

Based on the screening results and the observations made in Chapter 7, the energy spectra presented in the following were modeled. A summary of all MC simulations described in this section is given in Appendix A.

^{238}U chain

The natural decay chain of ^{238}U is given in Table 8.2.

Table 8.2: Natural decay chain of ^{238}U . Given are the decaying nuclides, the decay mode, the half-life, $T_{1/2}$, the Q-value of the decay, and the decay product. The last column lists all associated gamma rays with an energy above 300 keV and a branching ratio of at least 5%. Horizontal lines indicate, where the secular equilibrium might be broken. Decays with branching ratios below 1% are not listed. Values taken from [55].

Nuclide	mode	$T_{1/2}$	Q-value (keV)	decay product	E_γ (keV)
^{238}U	α	$4.5 \cdot 10^9$ yr	4270.0	^{234}Th	–
^{234}Th	β	24.1 d	273.0	^{234m}Pa	–
^{234m}Pa	β	1.2 min	2195.0	^{234}U	–
^{234}U	α	$2.5 \cdot 10^5$ yr	4858.5	^{230}Th	–
^{230}Th	α	$7.5 \cdot 10^4$ yr	2770.0	^{226}Ra	–
^{226}Ra	α	$1.6 \cdot 10^3$ yr	4870.6	^{222}Rn	–
^{222}Rn	α	3.8 d	5590.3	^{218}Po	–
^{218}Po	α	3.1 min	6114.7	^{214}Pb	–
^{214}Pb	β	26.8 min	1024.0	^{214}Bi	351.9
^{214}Bi	β	19.9 min	3272.0	^{214}Po	609.3
					768.4
					1120.3
					1238.1
					1764.5
					2204.2
^{214}Po	α	164.3 μs	7833.5	^{210}Pb	–
^{210}Pb	β	22.3 yr	63.5	^{210}Bi	–
^{210}Bi	β	5.0 d	1162.1	^{210}Po	–
^{210}Po	α	138.4 d	5407.5	^{206}Pb	–

If the half-life of a decay is of the order of the data taking period or longer, the secular equilibrium can be broken. That means that the decay of the parent nuclide is not necessarily followed by the decay of the long-lived daughter within the run time of the experiment. This divides the decay chain in several sub-chains, as indicated by horizontal lines in the table. The presence of a certain radio-nuclide requires also the presence of all other nuclides from the same sub-chain. No assumptions can be drawn, however, regarding the presence or absence of nuclides from other sub-chains.

The data energy spectra do not indicate the presence of the sub-chains of ^{238}U , ^{234}U , and ^{230}Th . The presence of the ^{226}Ra sub-chain, however, is clearly indicated by the alpha peaks, which are visible in the high-energy part of the spectra. The ^{238}U

chain can break at ^{210}Pb and again at ^{210}Po . The strong peak-like structure around 5.3 MeV that is visible in the energy spectrum of the enriched coaxial detectors, confirms the presence of ^{210}Po . The preceding sub-chain contains only the two beta emitters ^{210}Pb and ^{210}Bi with Q-values of 63.5 keV and 1162.1 keV, respectively, which do not leave traces in the high-energy region and cannot be distinguished via characteristic photon lines. In order to allow a statement about the presence or absence of the isotopes of this sub-chain, an analysis of the time structure of the ^{210}Po decays was carried out. If a ^{210}Pb contamination is present, the ^{210}Po sub-chain is fed by these decays. The half-life of 22.3 yr of ^{210}Pb is much larger than the Phase I run time, whereas the following ^{210}Bi decay has a half-life of only 5.0 d. This would lead to a ^{210}Po decay rate which is approximately constant in time. An initial ^{210}Po contamination and the absence of ^{210}Pb , on the other hand, could be distinguished by an exponentially decreasing ^{210}Po decay rate, with a decay time corresponding to the half-life of ^{210}Po of 138.4 d. A time-dependent analysis of the event rate in the golden data set in the energy region between 3.5 and 5.3 keV, that is in the energy region where ^{210}Po decays are expected, is described in [149, 160]. A fit to the experimental decay rate with a model containing a constant and an exponentially decaying contribution resulted in a rate of (0.6 ± 0.2) cts/d for the constant contribution and (7.9 ± 0.4) cts/d for the decaying contribution. The decay time was determined to be (138.4 ± 0.2) d. The event rate and the best fit model are depicted in Fig. 8.4. The analysis allowed to draw the conclusion that the dominant contribution from ^{210}Po decays derived from an initial ^{210}Po contamination, whereas the contributions due to a contamination with ^{210}Pb were negligible in comparison. A similar analysis of the decay rate of events above 5.3 MeV suggested a constant count rate of (0.09 ± 0.02) cts/d in this energy region. This is in agreement with the assumption that alpha decays of isotopes from the ^{226}Ra sub-chain are the origin of these events, with the half-life of ^{226}Ra being $1.6 \cdot 10^3$ yr. The corresponding graph is shown in Fig. 8.5.

Since α -particles have an attenuation length of the order of a few μm in LAr and in germanium, they can only enter the active detector volume via the p^+ -contact. The presence of peak-like structures indicates that radio-nuclides could be found directly on the p^+ -surface, so that the energy spectrum was not smeared out by energy loss in the LAr. The screening measurements, on the other hand, hinted at the emanation of ^{222}Rn from the cryostat and the lock system into the LAr. Therefore, also decays in the LAr close to the p^+ -electrode had to be taken into account. The thickness of the p^+ -deadlayer is of the order of a few hundred nanometers. In order to model the high-energy part of the spectrum, the spectra originating from all alpha decays in the ^{226}Ra sub-chain, that is the decays of ^{226}Ra , ^{222}Rn , ^{218}Po , and ^{214}Po , were simulated in the **Single detector** mode with *configANG3*. Separate simulations were performed for decays taking place directly on the p^+ -surface and for decays in the LAr close to the p^+ -contact. For the latter, the decays were placed in the LAr inside the bore hole at a maximum distance of 1 mm from the surface. In addition, ^{210}Po decays on the p^+ -contact were simulated. Simulations were carried out for p^+ -layer thicknesses of 100 nm, 200 nm, 300 nm, ..., and 1000 nm.

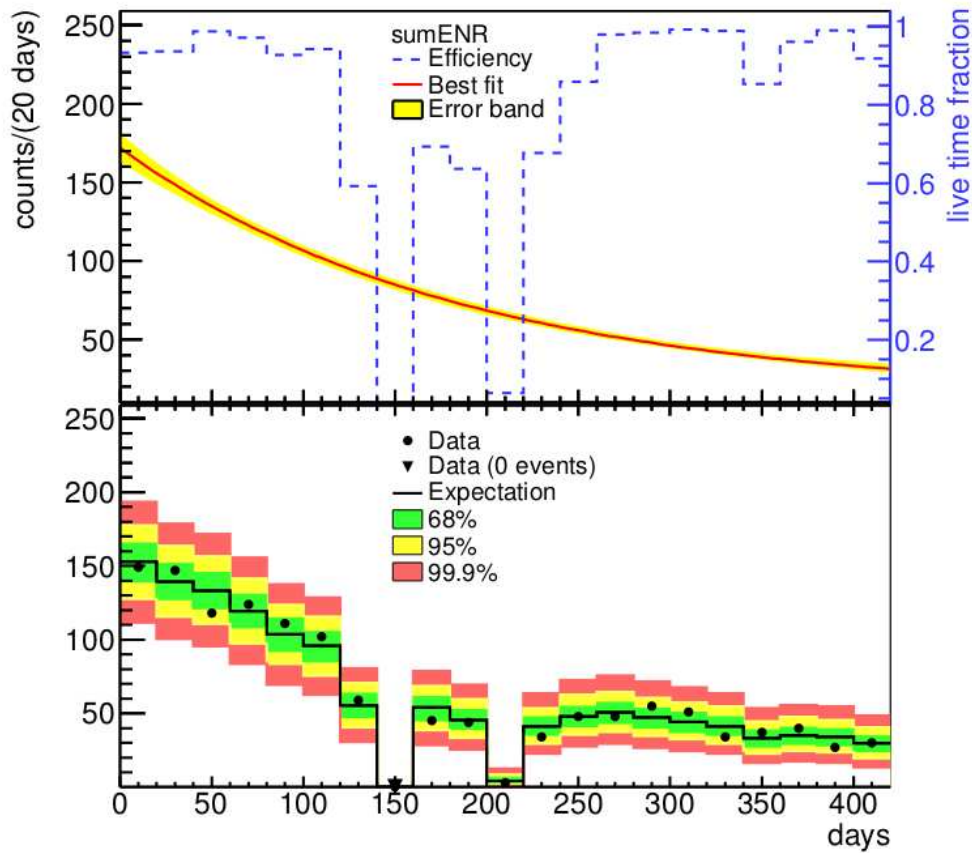


Figure 8.4: Results of a fit to the count rate of events between 3.5 and 5.3 keV for the golden data set with a model accounting for an exponentially decaying and a constant component. In the upper panel, the best fit model with its 68% uncertainty band is shown together with the live time fraction. In the lower panel, the number of observed events is shown as a function of time together with the best fit expectation (after correction for the live time fraction). The smallest intervals of 68%, 95%, and 99.9% probability for the expectation are given as a green, yellow, and red band, respectively [161]. Graph taken from [149].

Figure 8.6 depicts the energy spectra for the simulation of ^{210}Po decays on the p^+ -surface as well as ^{222}Rn decays in the LAr close to the surface for several dead layer thicknesses. The decays taking place on the surface resulted in a peak-like structure with a strong tail towards lower energies. The position of the peak is below the Q-value of the decay and is shifted to smaller energies for increasing thickness of the p^+ -surface. The decays in the LAr volume lead to a spectrum without any peak-like structure, with the maximum energy deposit significantly below the maximum energy released in the decay and decreasing for thicker p^+ -surfaces.

In addition to the alpha decays contributing to the high-energy region of the spectrum, also the relevant beta decays from the ^{238}U chain were simulated. As the absence

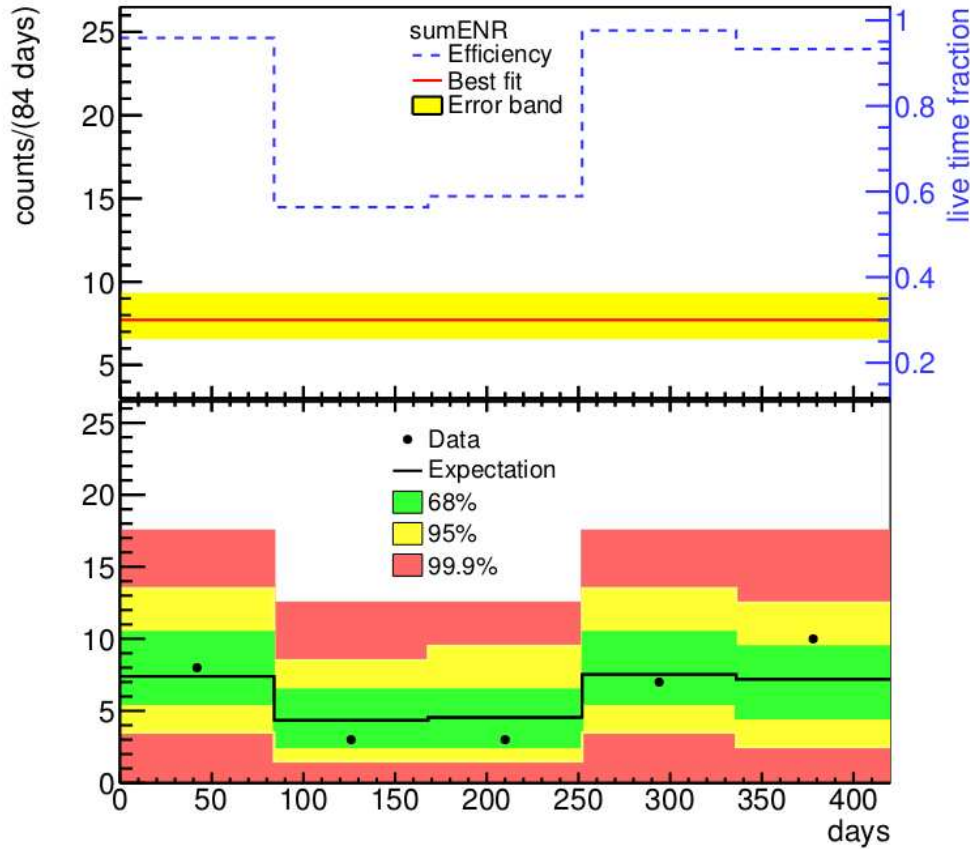


Figure 8.5: Results of a fit to the count rate of events above 5.3 keV for the golden data set with a model accounting for a constant decay rate. In the upper panel, the best fit model with its 68% uncertainty band is shown together with the live time fraction. In the lower panel, the number of observed events is shown as a function of time together with the best fit expectation (after correction for the live time fraction). The smallest intervals of 68%, 95%, and 99.9% probability for the expectation are given as a green, yellow, and red band, respectively. Graph taken from [149].

of a significant contribution from decays of ^{210}Pb and ^{210}Bi had been established, the relevant decays were those of ^{214}Pb and ^{214}Bi . The decays were simulated on the p^+ -surface as well as in the LAr volume inside the entire bore hole, using the **Single detector** mode with *configANG3*. Since the emitted electrons and photons are not sensitive to the changes in the p^+ -layer thickness taken into account for the alpha decays, the beta decays were simulated only for the nominal p^+ -layer thickness of ANG3, 300 nm. For the energy spectra from alpha decays, only the p^+ -deadlayer thickness plays a role, whereas other details of the geometry, like shape and size, do not influence the spectral shape. This is not true for beta decays with emission of photons, where the geometrical shape plays a role in the detection efficiency. Therefore,

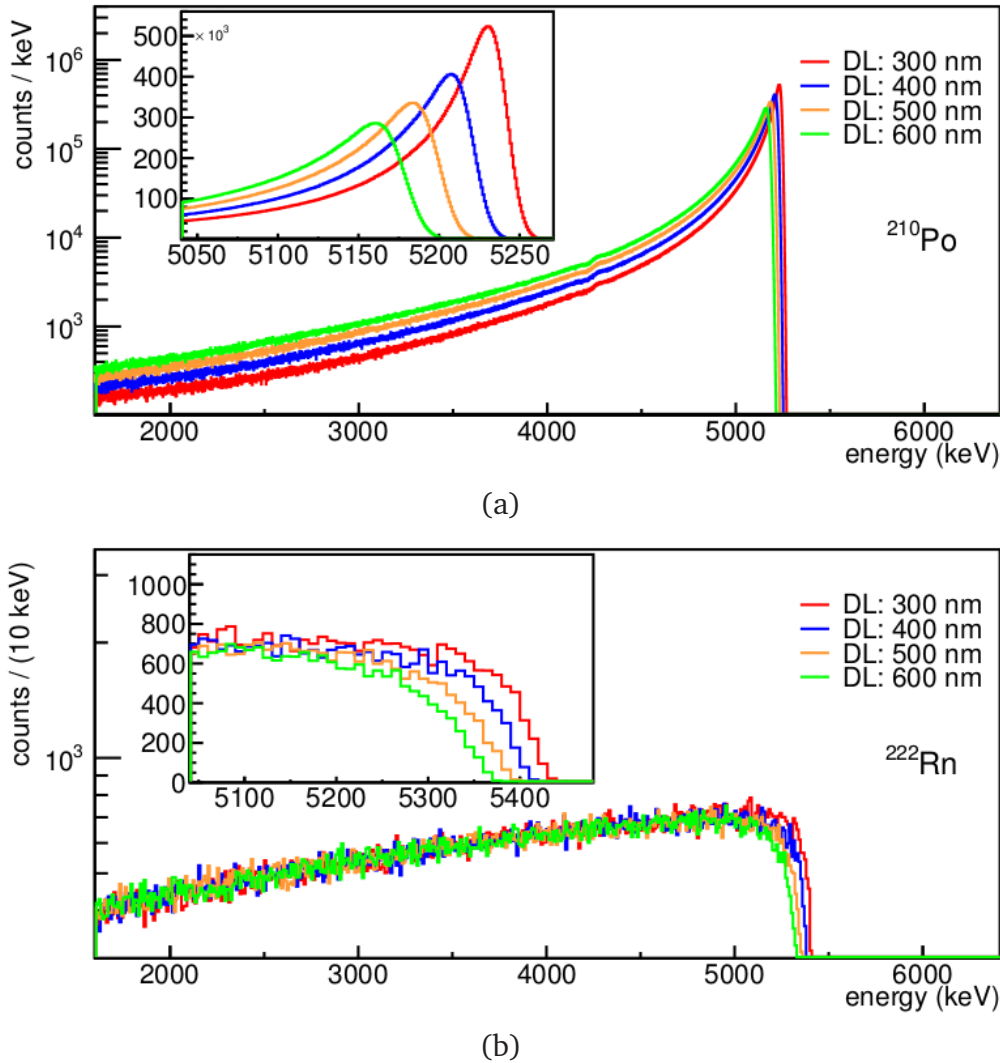


Figure 8.6: (a) Simulated energy spectra for decays of ^{210}Po on the p^+ -surface. (b) Simulated energy spectra for decays of ^{222}Rn in the LAr close to the p^+ -surface. The simulations were carried out for different thicknesses of the p^+ -deadlayer. Figures adopted from [149].

the ^{214}Pb and ^{214}Bi decays were also simulated using the **Single detector** mode with *configGD32B*. The p^+ -layer thickness was set to 600 nm, as suggested by the manufacturer. For the simulation of the decays in LAr, the decays were constrained to a cylindrical volume around the p^+ -contact with a maximum distance of 4 mm from the surface.

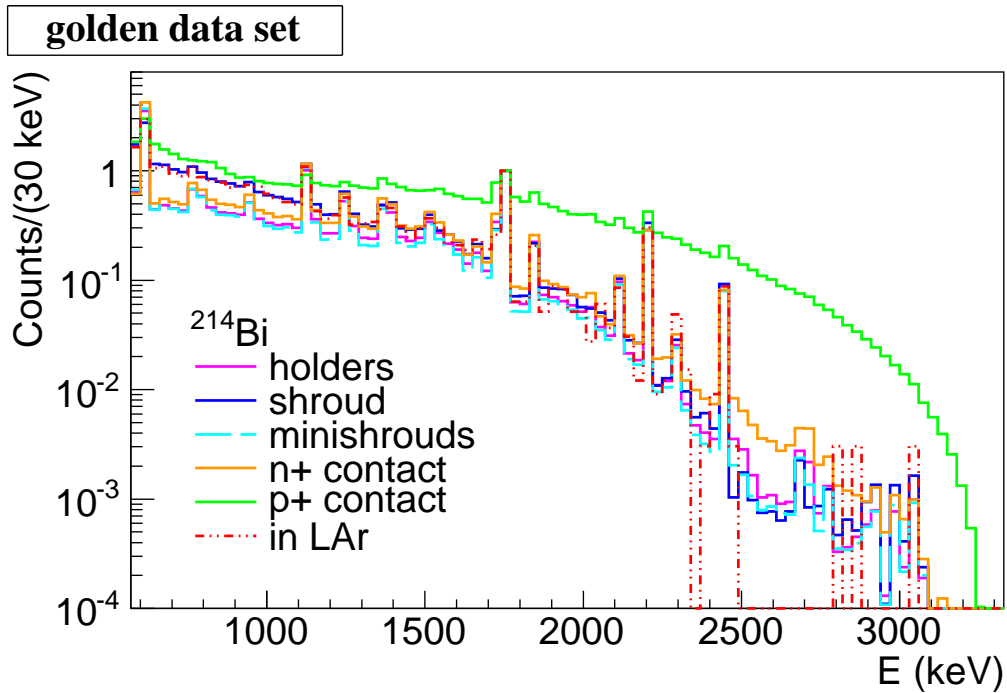
The screening results listed in Table 8.1 suggested the presence of contaminations from the ^{238}U chain not only on and close to the p^+ -surface, but also in other parts of the GERDA setup. The simulations of the alpha decays were omitted for these contributions, as they could not contribute to the energy spectrum due to the reduced range of α -particles. Therefore, it was sufficient to simulate the decays of ^{214}Pb and ^{214}Bi . The energy spectra resulting from the decays of these two isotopes were modeled separately for contaminations in the detector holders, in the minishrouds, and in

the shroud with the **Full array** mode for *configNAT* as well as for *configBEGE*. The energy spectra due to contaminations on the n^+ -surface were simulated with the **Single detector** mode for *configANG3* and *GD32B*, respectively.

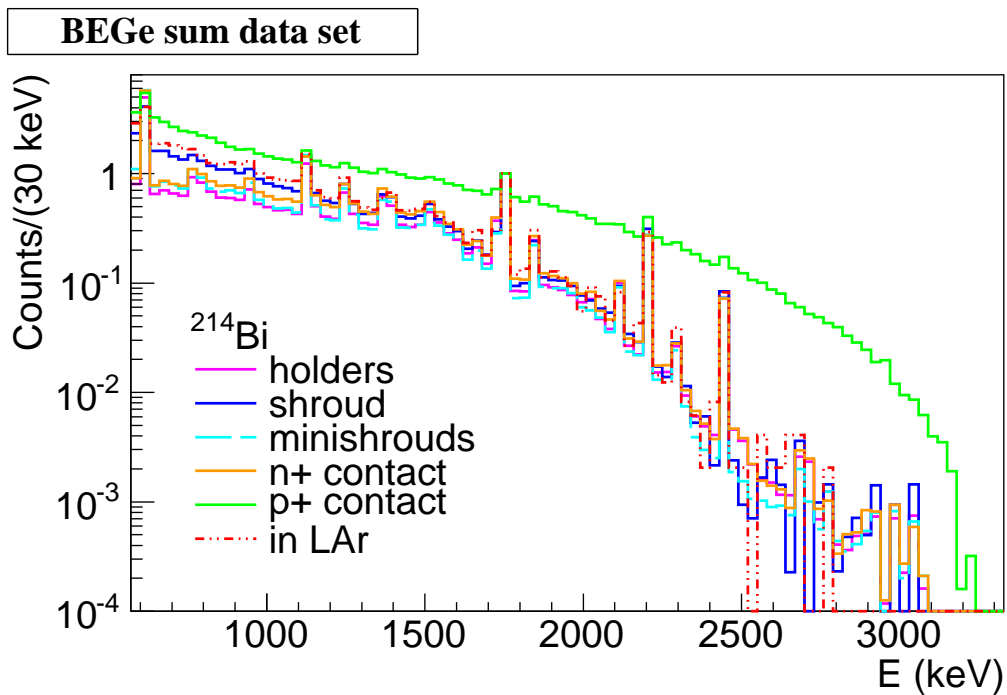
For each source position, the spectra resulting from ^{214}Pb decays and from ^{214}Bi decays were added up to represent the full sub-chain decay spectrum. As the decay of ^{214}Pb is followed in 99.98% of all cases by a decay of ^{214}Bi , no scaling of the spectra had to be performed before adding them.

The electrons released in beta decays have an attenuation length of the order of millimeters. Therefore, significant contributions from these particles to the energy spectrum are expected only from decays close to or on the thin p^+ -surface and to a smaller extent from decays close to or on the n^+ -surface, whose thickness is of the order of the electrons' range. For source distances of more than a few millimeters, the contribution from electrons becomes negligible and all energy depositions in the detectors are due to the photons released in the decays. With increasing distance of the source, the photons become more and more likely to deposit part of their energy via Compton scattering in the matter traversed before reaching the detectors. This leads to reduced contributions at the photon peak energy and increased contributions to the Compton-continuum at energies below the full peak energy.

These observations are confirmed when comparing the ^{214}Bi sub-chain spectra simulated for the different source positions and depicted in Fig. 8.7(a) for the simulations corresponding to the golden data set and in Fig. 8.7(b) for the simulations corresponding to the BEGe sum data set. No significant differences between the two data sets are observed. All spectra were normalized to the number of events in the bin corresponding to the photon peak at 1764.5 keV. The decays at the p^+ -contact lead to a continuous energy spectrum up to the Q-value of the decay and only small photon peaks. The spectrum resulting from the decays on the n^+ -contact, on the other hand, is dominated by strong photon peaks and a small continuous contribution, as most electrons were stopped in the thick deadlayer and did not reach the active part of the detector. The energy spectrum turned out to be very similar to that of other near sources, like the decays taking place in the detector holders and in the minishrouds. In all three cases, the source was at a distance smaller than 2 cm from the detectors, leading to almost identical energy spectra. As expected, the energy spectrum from the decays in the shrouds, located at a distance well above 2 cm but closer than 50 cm, exhibits a lower peak-to-continuum ratio for energies below ≈ 1500 keV. For higher energies, the spectral shape approaches that of the close sources. The energy spectrum resulting from decays in the LAr close to the p^+ -contact resembles this spectrum. Whereas in the first case the amplified continuum is due to photons which lost part of their energy due to Compton-scattering in the surrounding material, in the latter case it is due to the contributions from electrons entering the detector through the thin p^+ -deadlayer. Despite these differences in the origin of the energy depositions, the resulting energy spectra are very similar.



(a)



(b)

Figure 8.7: Simulated energy spectra of the ^{214}Bi sub-chain decays for different source positions corresponding to the (a) golden and (b) BEGe sum data set. All spectra are normalized to the number of events in the bin corresponding to the photon peak at 1764.5 keV.

Table 8.3: Natural decay chain of ^{232}Th . Given are the decaying nuclides, the decay mode, the half-life, $T_{1/2}$, the Q-value of the decay, and the decay product. The last column lists all associated gamma rays with an energy above 300 keV and a branching ratio of at least 5 %. Horizontal lines indicate, where the secular equilibrium might be broken. Decays with branching ratios below 1 % are not listed. Values taken from [55].

Nuclide	mode	$T_{1/2}$	Q-value (keV)	decay product	E_γ (keV)
^{232}Th	α	$1.4 \cdot 10^{10}$ yr	4082.8	^{228}Ra	–
^{228}Ra	β	5.8 yr	45.9	^{228}Ac	–
^{228}Ac	β	6.2 h	2127.0	^{228}Th	911.2 969.0
^{228}Th	α	1.9 yr	5520.1	^{224}Ra	–
^{224}Ra	α	3.7 d	5788.9	^{220}Rn	–
^{220}Rn	α	55.6 s	6404.7	^{216}Po	–
^{216}Po	α	0.1 s	6906.5	^{212}Pb	–
^{212}Pb	β	10.6 h	573.8	^{212}Bi	–
^{212}Bi	$\beta /$	60.6 min	2254.0 /	$^{212}\text{Po} /$	727.3
	α		6207.1	^{208}Tl	
^{212}Po	α	$0.3 \mu\text{s}$	8954.1	^{208}Pb	–
^{208}Tl	β	3.1 min	5001.0	^{208}Pb	510.8 583.2 860.6 2614.5

^{232}Th chain

Table 8.3 shows the natural decay chain of ^{232}Th .

As mentioned in Sec. 7.4, no indication for the presence of radioactive isotopes from the ^{232}Th chain in the vicinity of the p^+ -contact was found in the energy spectra. Therefore, no decays of isotopes from this chain were simulated on or close to the p^+ -surface. As a consequence, the simulation of any of the alpha-decaying isotopes could be omitted. As mentioned before, only the spectrum above 570 keV was analyzed, in order to avoid contributions from ^{39}Ar . The beta-decaying isotopes with a sufficiently high Q-value to give a significant contribution in the energy range above 570 keV are ^{228}Ac , ^{212}Bi , and ^{208}Tl ¹.

Simulations were carried out for all three isotopes for decays taking place in the detector holders as well as in the shroud. Following the discussion for the ^{238}U decay

¹The contributions from ^{212}Pb are negligible above 570 keV due to its small Q-value of 573.8 keV

chain, these two source positions were considered good representatives for the energy spectrum of a close and of a medium distant source. Here, close means a distance of up to 2 cm from the detectors, comprising also possible contaminations in the minishrouds and on the n^+ -surfaces, and medium distant signifies a distance of more than 2 cm, but less than 50 cm.

Investigations in an early phase of the GERDA experiment could not rule out a possible contamination of the heatexchanger, located in the top part of the copper cryostat, with ^{228}Th [162]. Also the possible contribution from the calibration source at the bottom of the cryostat had to be taken into account. These two contaminations from far sources, that is sources at a distance of more than 50 cm, were accounted for by simulating ^{208}Tl decays in the heatexchanger. The contributions from ^{228}Ac and ^{212}Bi could be neglected due to the small energy of the photons released in the decays, which does not allow them to reach the detector array.

For all simulations, the **Full array** mode was used. The simulations for decays in the holders and in the shroud were performed for *configNAT* as well as for *configBEGE*, whereas the simulation of ^{208}Tl on the heatexchanger was carried out only for *configNAT*. This was done to avoid the immense computational effort of the simulation of a distant source in the view that only very small variations in the energy spectrum were expected for a simulation with *configBEGE*.

The decay chain breaks after ^{228}Ac , whereas ^{212}Bi and ^{208}Tl are part of the same sub-chain. For this reason, the spectra of ^{228}Ac were kept separate, whereas those of ^{212}Bi and ^{208}Tl were combined to the total ^{228}Th sub-chain energy spectrum. To this scope, the branching ratio of ^{212}Bi had to be taken into account. The isotope decays with 64.1 % probability via beta decay to ^{212}Po and only in 35.9 % of all cases via alpha decay to ^{208}Tl . Consequently, the spectrum resulting from ^{208}Tl decays had to be down-scaled accordingly before adding it to the spectrum of ^{212}Bi .

The final energy spectra for ^{228}Ac corresponding to the golden and the BEGe sum data sets are depicted in Fig. 8.8(a) and Fig. 8.8(b), respectively, and those for the ^{228}Th sub-chain are shown in Fig. 8.9(a) and Fig. 8.9(b). The first were normalized to the number of events in the bin corresponding to the photon peak at 911.2 keV, and the latter were normalized to the 2614.5 keV photon peak. Similar effects as already noted for the case of the ^{214}Bi sub-chain are observed. Again, the general behavior of the energy spectra simulated to match the golden and the BEGe data sets, respectively, is in very good agreement. For the case of ^{228}Ac , up to an energy of ≈ 1000 keV, the peak-to-continuum ratio is larger for the decays taking place in the holders, that is for the near source, than for the medium distant source. Above this energy, the two spectra become practically indistinguishable. Note that as a result of the normalization at 911.2 keV, for the range above 1000 keV the continuum as well as the peaks seem slightly higher for the medium distant source, but the peak-to-continuum ratio is approximately the same for both source positions. The energy spectra of the simulations of the ^{228}Th sub-chain decays also exhibit a similar structure. Below ≈ 2000 keV, the continuous part of the energy spectrum due to decays in the shroud is enhanced compared to the energy spectrum due to decays in the holders. Between 2000 keV and

2400 keV, the two spectra coincide. Above 2400 keV, that is above the Compton edge of the 2614.5 keV peak, the continuum of the energy spectrum for the medium distant contaminations starts dropping rapidly and is almost absent above the 2614.5 keV photon line, whereas for the close contaminations the continuum decreases much slower and contributions due to the summation of energy deposits of two photons or an electron and a photon are possible also at energies above 3000 keV. The energy spectrum due to decays of ^{208}Tl on the heatexchanger exhibits no peak structures below 2614.5 keV. Also in this case, the continuum decreases steeply around 2400 keV. No contributions to the spectrum above the well pronounced 2614.5 keV peak are observed for the far source.

^{42}Ar

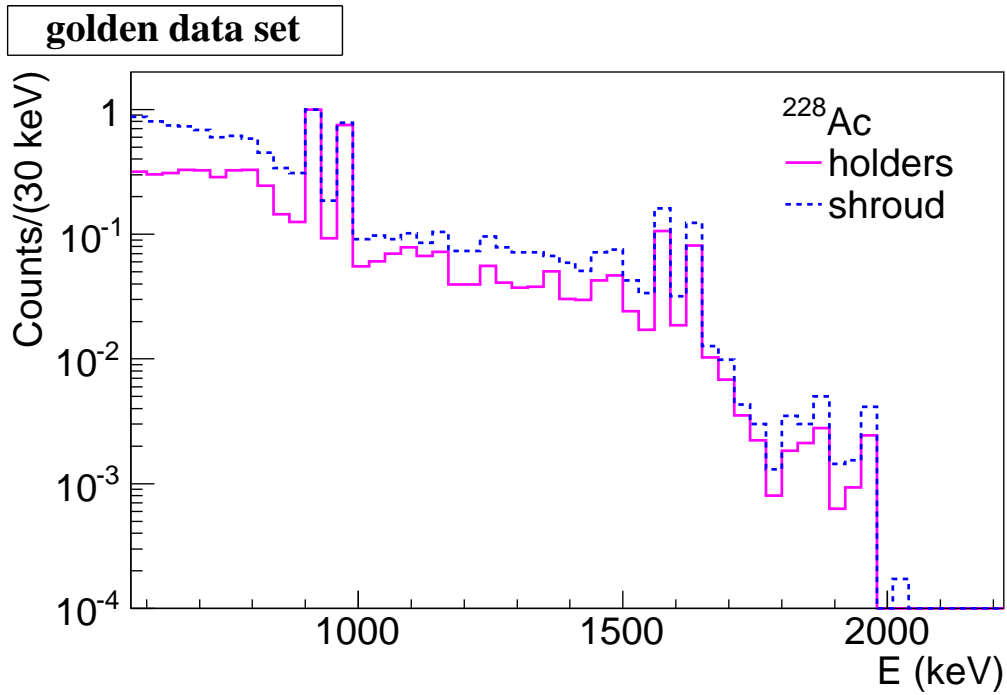
As mentioned in Sec. 7.5, the most prominent photon line in the data spectra derives from the decays of ^{42}K , which follow the decay of ^{42}Ar . The ^{42}Ar isotopes are produced by cosmic activation and are therefore distributed homogeneously in the LAr volume. They decay via beta decay with a Q-value of 599.0 keV and no characteristic photons are emitted. The energy loss in the n^+ -deadlayers reduces the electron energy below the threshold used for analysis. The only possible way to contribute to the energy spectrum above 570 keV would be energy deposits from electrons on the p^+ -surfaces that enter the detector volume without significant energy loss in the LAr surrounding the detectors. However, the fraction of ^{42}Ar isotopes so close to these surfaces was negligible, so that the simulation of ^{42}Ar decays could be omitted.

The situation changes for the daughter isotopes, ^{42}K . As they are produced as ions, they could be transported by electric fields inside the LAr volume until their recombination. The electric fields were due to the high-voltage, which was applied to the detectors. It is thus likely that the ^{42}K concentration in the vicinity of the p^+ -contact was enhanced. The isotopes decay via beta decay with a Q-value of 3525.4 keV. This allowed also the penetration of the thicker n^+ -deadlayer by the released electrons. The field lines closed on the minishrouds, so that no electric fields were present in the remaining part of the cryostat, assuring a homogeneous contribution of the contaminations outside the minishrouds.

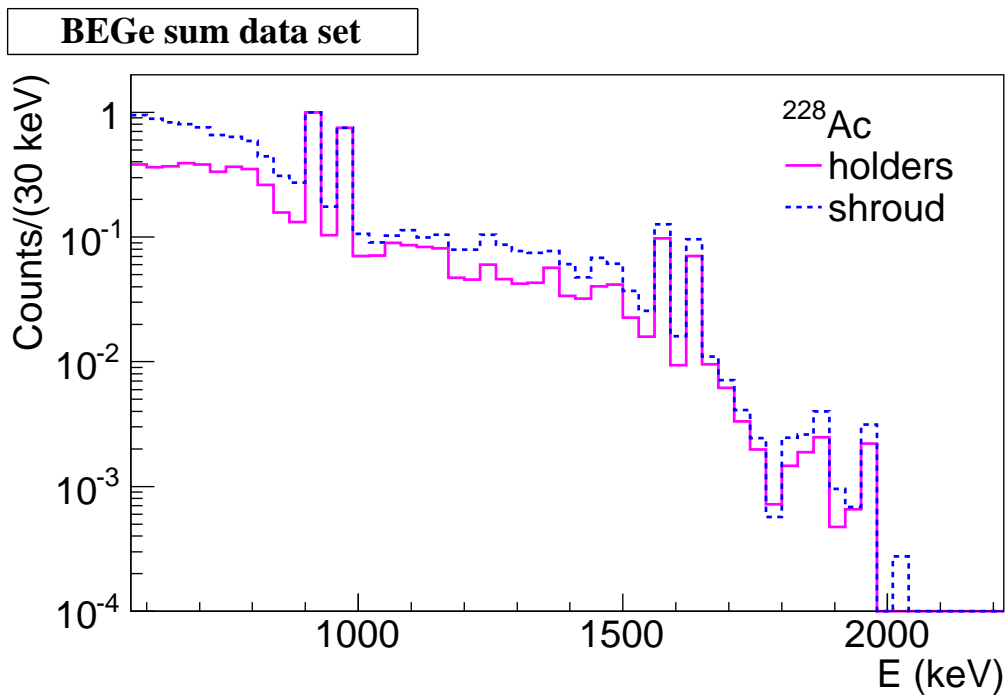
In order to model all possible scenarios, three MC simulations of ^{42}K decays were carried out. In all three cases, the energy spectrum of the particles emitted in the decays was sampled according to the distribution implemented in DECAY0 [163]². This initial decay spectrum served as input to the MAGE framework. All following MC steps, including the propagation of the particles in the GERDA setup with MAGE and the processing of the MC data, were done in the usual way.

The first simulation described the case of a homogenous distribution of ^{42}K inside the LAr. The decays were confined to a cylindrical volume of 6.6 m^3 . The **Full array** mode was used and for the simulations with *configNAT*, the volume was centered on

²The decay of ^{42}K is not Fermi-allowed. Since it is not treated in a specific way in GEANT4, as is done for other isotopes like ^{40}K , it is not simulated properly by GEANT4.



(a)



(b)

Figure 8.8: Simulated energy spectra of ^{228}Ac decays for different source positions corresponding to the (a) golden and (b) BEGe sum data set. All spectra are normalized to the number of events in the bin corresponding to the photon peak at 911.2 keV.

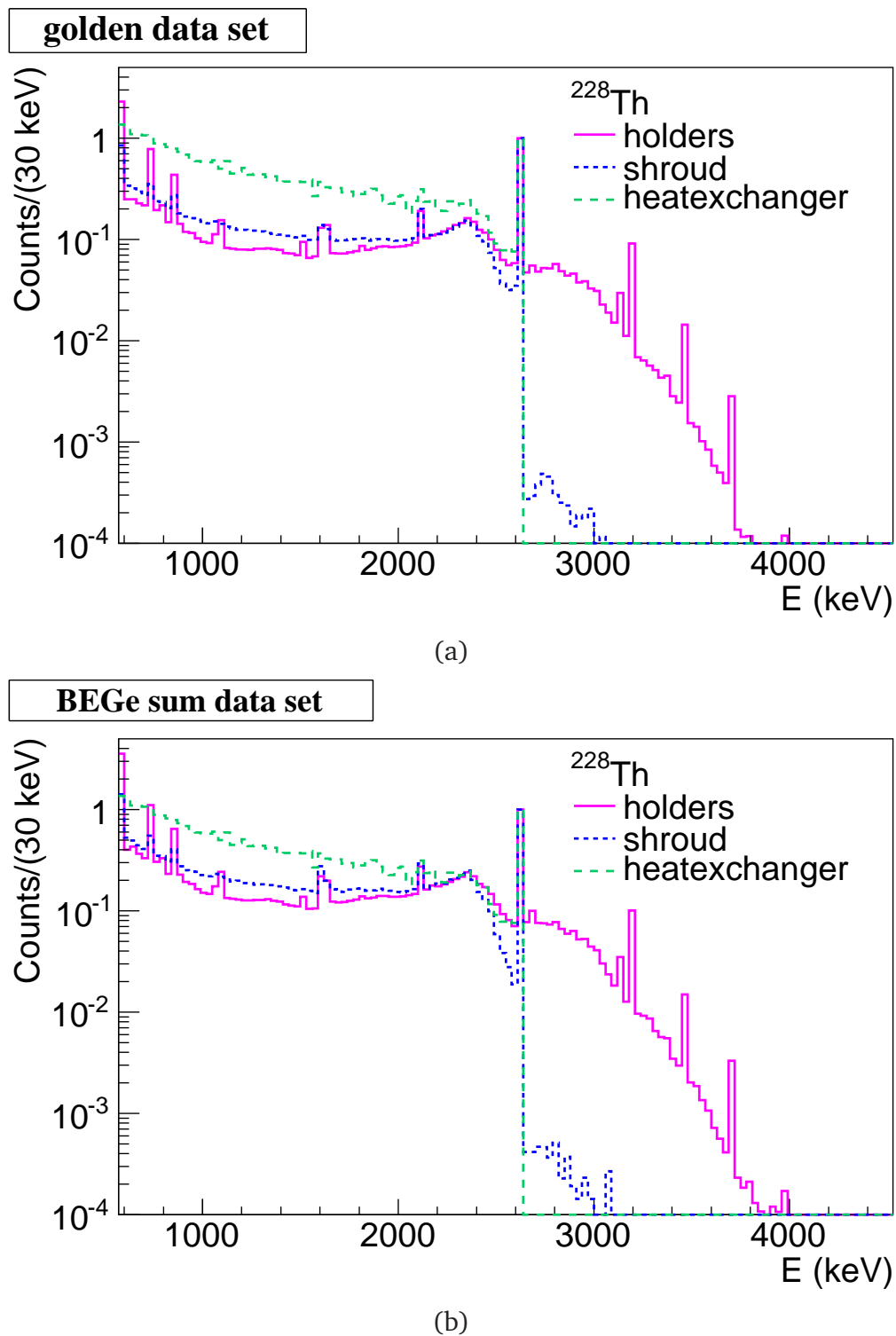


Figure 8.9: Simulated energy spectra of the ^{228}Th sub-chain decays for different source positions corresponding to the (a) golden and (b) BEGe sum data set. All spectra are normalized to the number of events in the bin corresponding to the photon peak at 2614.5 keV. Note that the simulation of decays in the heatexchanger was carried out for *configNAT* in both cases.

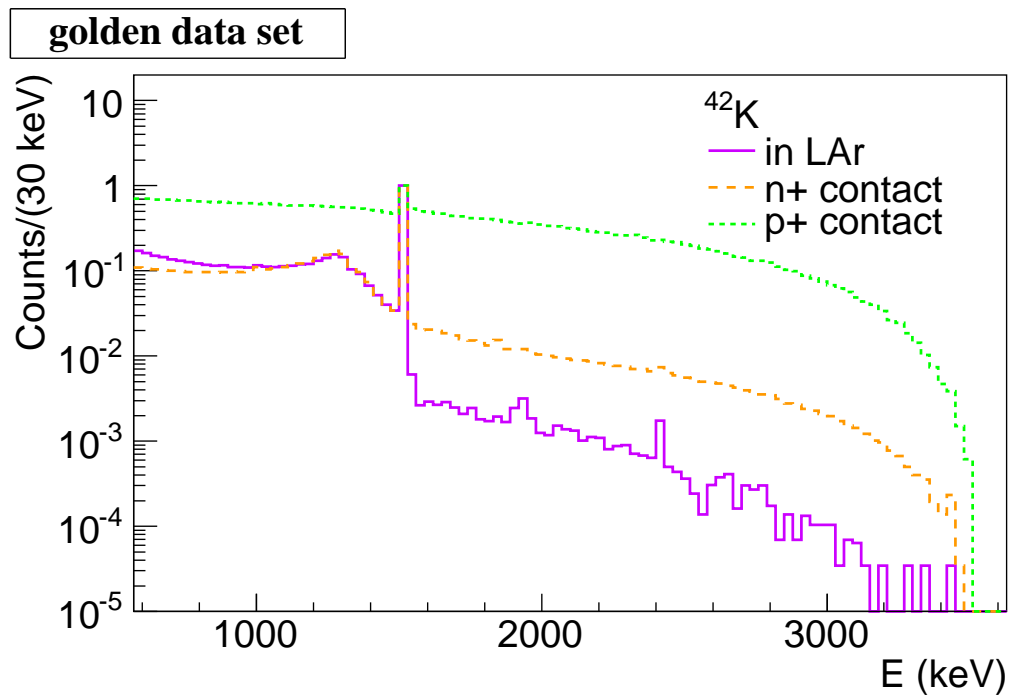
the three strings containing the enriched coaxial detectors, whereas for the simulations with *configBEGE*, it was centered on the string containing the five BEGe detectors.

For the second case, the ^{42}K decays were simulated on the p^+ -surface using the **Single detector** mode for *configANG3* and *GD32B*, respectively.

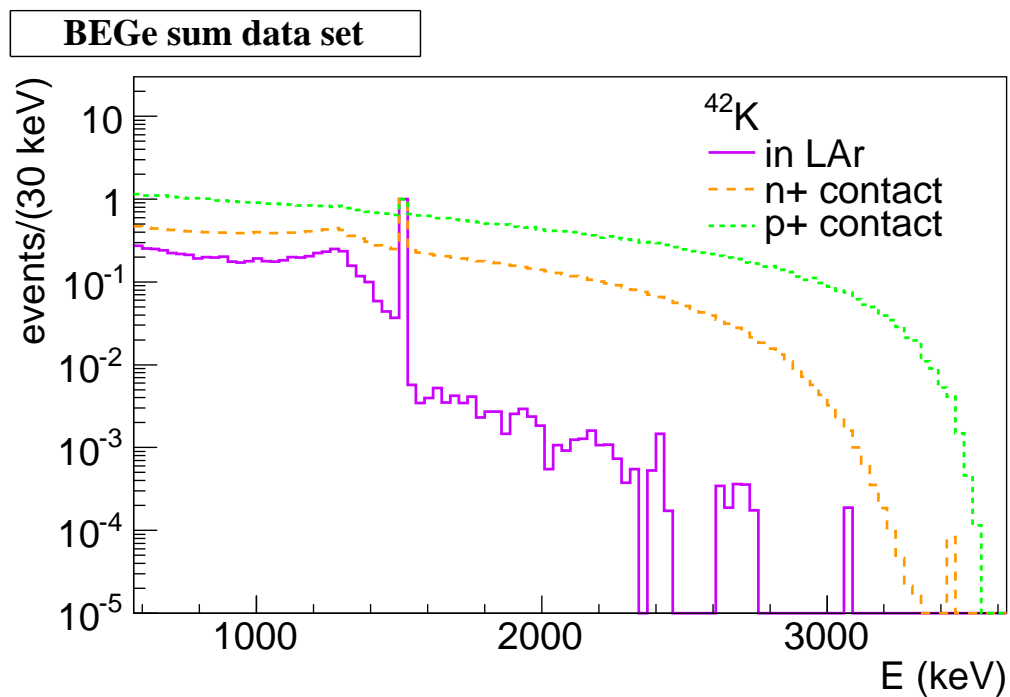
The third case modeled the contributions from contaminations on the n^+ -surface of the detectors. For the golden data set, the simulations were done with *configANG3* in the **Single detector** mode. For the BEGe sum data set, the outcome of recent studies regarding the *transition layer* for point contact detectors [164, 165] was taken into account. The results suggest that only the outermost part of the n^+ -layer is completely insensitive to energy depositions. The transition layer describes a region between this fully dead layer and the fully active volume of the detectors, where partial charge collection takes place. If energy is deposited in this region, the events contribute to the continuum of the energy spectrum in the lower energy region. The transition layer does not play an important role in the case of photon interactions, since these are distributed over the whole detector volume and the transition layer covers only a small fraction. It does, however, have an influence on the energy spectrum for contributions of beta decays on or close to the n^+ -surface, since these deposit their energy throughout the entire n^+ -layer before reaching the active volume. Therefore, separate MC simulations of ^{42}K decays on the n^+ -surface were run for the four active BEGe detectors. For these simulations, the outer 40% of the n^+ -layer, as given in Table 6.1, was considered completely dead, whereas the inner 60% was modeled with a charge collection efficiency increasing linearly from zero until one was reached at the boundary to the active volume. The resulting spectra were then smeared to account for the energy resolution and scaled according to the exposure of the corresponding detector in the BEGe sum data set, before they were added to the total energy spectrum³.

The simulated energy spectra corresponding to the golden and BEGe sum data sets are depicted in Fig. 8.10(a) and Fig. 8.10(b). The energy spectra for the different source positions were normalized to the number of counts in the bin corresponding to the photon peak at 1524.7 keV. For both data sets, the energy spectrum derived from the decays on the p^+ -surface is dominated by the continuum and the photon peak is small compared to the continuum. The spectrum reaches up to the Q-value of the decay. The energy spectra resulting from decays inside the LAr volume exhibit a pronounced photon peak and a large peak-to-continuum ratio. Above the photon peak, the continuum drops by more than one order of magnitude due to the absence of the dominating contribution from Compton-scattered photons. The energy spectra from simulations of ^{42}K decays on the n^+ -surface differ for the two data sets. For the golden data set, below 1000 keV, the peak-to-continuum ratio is slightly smaller than for the case of decays in the LAr, while it becomes equal between 1000 keV and the photon peak energy. Above the photon peak, no sudden drop is observed in the

³Note that this was the only simulation for which the transition layer was modeled. Its effects should also be taken into account when simulating the ^{214}Bi sub-chain decays on the n^+ -surface and the energy spectra from $2\nu\beta\beta$ and $0\nu\beta\beta\chi(\chi)$, which will be described below. However, a dedicated analysis was still ongoing at the time of writing of this thesis and therefore only partial results could be taken into account.



(a)



(b)

Figure 8.10: Simulated energy spectra of ^{42}K decays for different source positions corresponding to the (a) golden and (b) BEGe sum data set. All spectra are normalized to the number of events in the bin corresponding to the photon peak at 1524.7 keV.

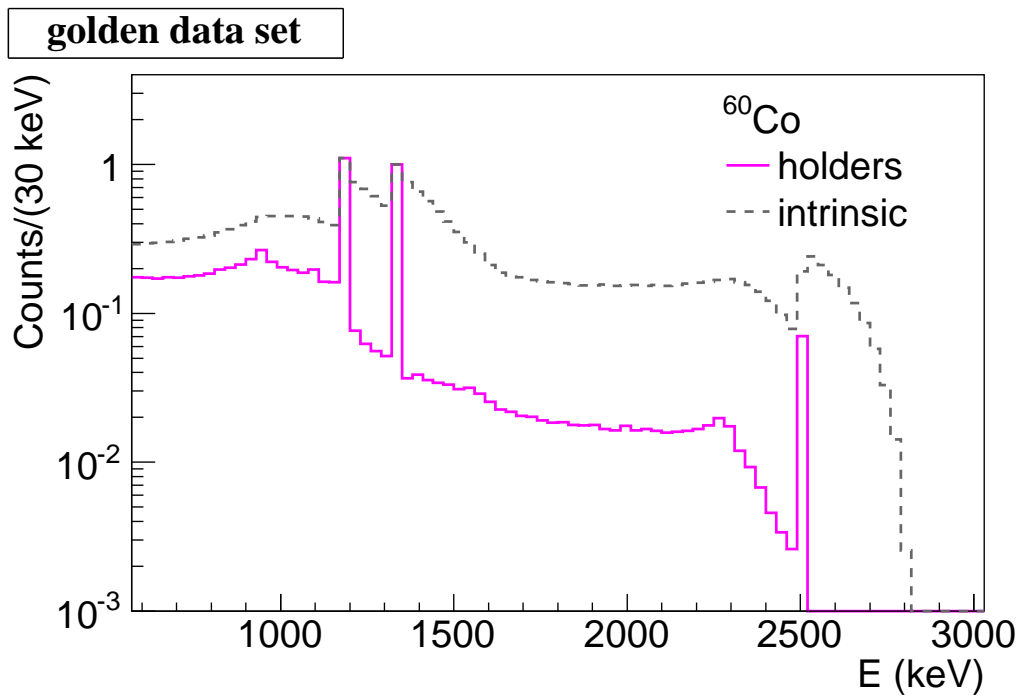
continuum, since the spectrum is dominated by electrons. For the BEGe sum data set, the case is different. The peak-to-continuum ratio is much smaller in the energy spectrum from decays on the n^+ -electrode than in the energy spectrum from decays in the LAr. The explanation for this is two-fold. Firstly, the average thickness of the n^+ -layer for the coaxial detectors was ≈ 2 mm (the detector used for the simulation, ANG3, has a deadlayer thickness of 1.9 mm, which corresponds to the average of the detectors contributing to the golden data set). The deadlayer thickness of the BEGe detectors, on the contrary, was below 1 mm for all detectors. Therefore, the contribution of the electrons to the total energy spectrum is enhanced in the BEGe sum data set, reducing the peak-to-continuum ratio significantly. Secondly, the partially active transition layer lead to an increase of the spectrum at lower energies, again reducing the peak-to-continuum ratio in the region below the photon line.

^{60}Co

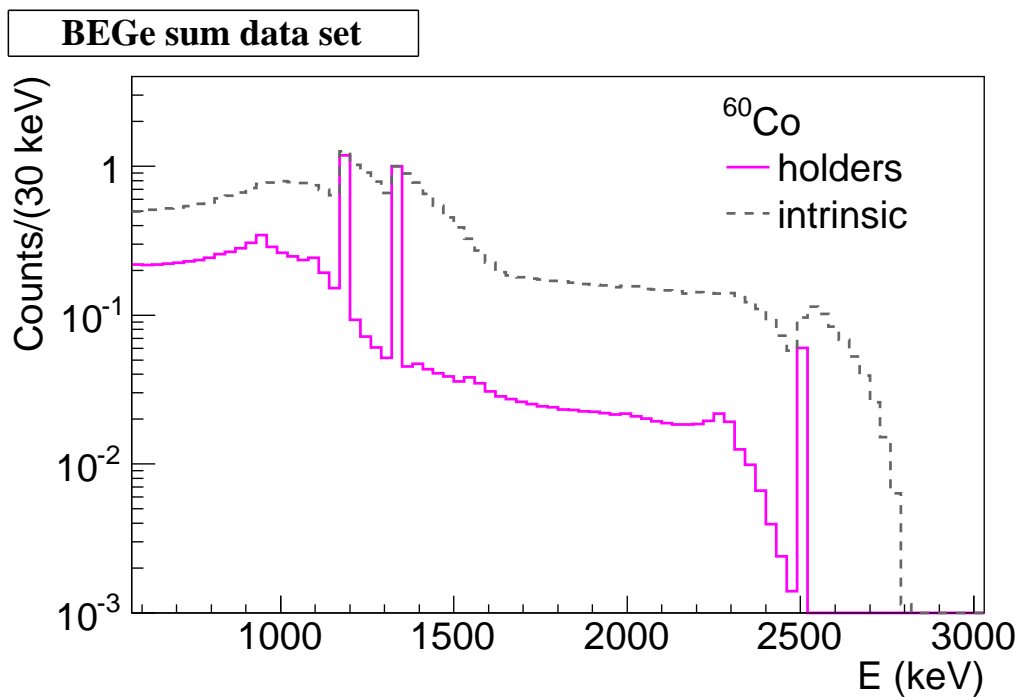
The beta decays of ^{60}Co had to be taken into account as a natural contamination in the materials used in the GERDA experiment. Based on the observations made above, the energy spectra of a near and a medium distant ^{60}Co source were not expected to show large differences. From the small line intensities at the ^{60}Co photon peaks, listed in Table 7.3, it was deduced that the limited statistics in the data would not allow a distinction between near and medium distant sources. Hence, ^{60}Co decays were simulated only in the detector holders, with the resulting energy spectrum being representative for all ^{60}Co contaminations in the experimental setup external to the detectors. The simulations were performed for both *configNAT* and *configBEGE* in the **Full array** mode.

Another source of ^{60}Co was located inside the detectors themselves. The radioisotopes are produced inside the germanium via spallation reactions, when the detectors are exposed to cosmic rays. Due to the half-life of ^{60}Co of 5.3 yr, contributions to the energy spectrum are expected also after several years of underground storage of the detectors. The decays were simulated for both *configNAT* and *configBEGE* using the **Single detectors in full array** mode.

Figures 8.11(a) and 8.11(b) depict the simulated energy spectra corresponding to the golden and the BEGe sum data set, respectively. They were normalized to the number of events in the bin corresponding to the energy of the photon peak at 1332.5 keV. For the decays in the holders of the detectors, the energy spectra exhibit very clear photon peaks. Also the summation peak at 2505.7 keV is clearly visible. In the case of the decays taking place inside the detectors, the peak-to-continuum ratio is much smaller, as the dominant contribution to the energy spectra comes from the electrons emitted in the decay. The peak structures are washed out, with large tails to the high energy side.



(a)



(b)

Figure 8.11: Simulated energy spectra of ^{60}Co decays for different source positions corresponding to the (a) golden and (b) BEGe sum data set. All spectra are normalized to the number of events in the bin corresponding to the photon peak at 1332.5 keV.

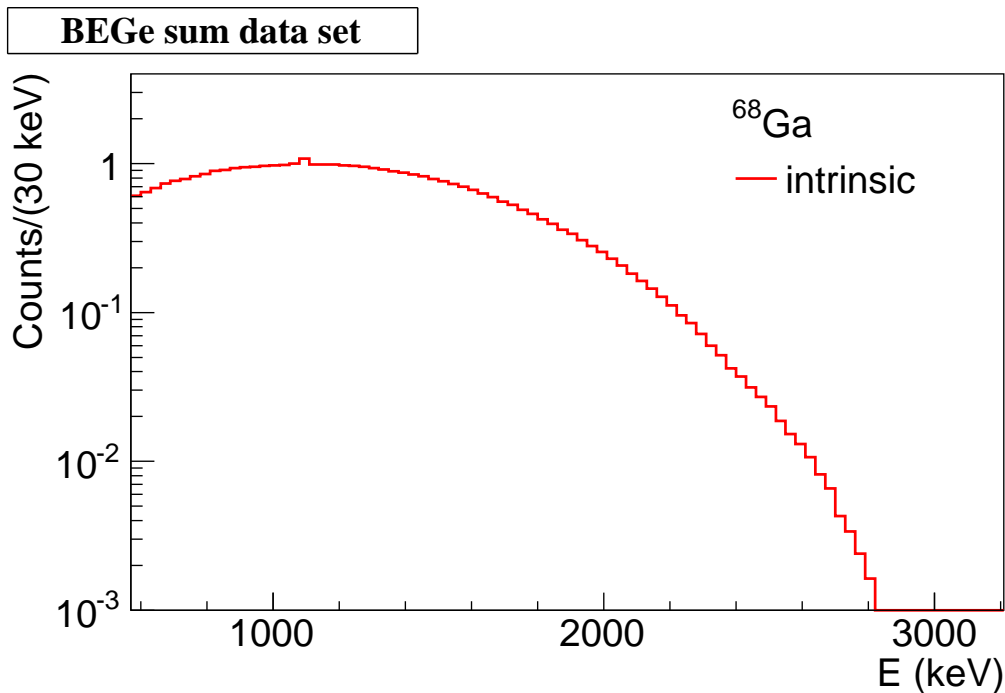


Figure 8.12: Simulated energy spectrum of ^{68}Ga decays inside the germanium detectors of the BEGe sum data set. The spectrum is normalized to the number of events in the bin corresponding to the photon peak at 1077.4 keV.

^{68}Ge

In analogy to the production of ^{60}Co via cosmic activation, also the unstable ^{68}Ge is produced inside the germanium detectors when they are exposed to cosmic radiation. The isotopes decay with a half-life of 270 d via electron capture (EC). The Q-value is with 106.0 keV well below the analysis threshold and therefore the decays did not have to be simulated. However, the daughter of ^{68}Ge , ^{68}Ga , decays with a short half-life of 67.6 min via EC and positive beta decay. The Q-value is 2921.1 keV. The coaxial enriched detectors had been stored underground for several years before their use in the GERDA experiment. Therefore, it was assumed that the majority of the ^{68}Ge produced during their exposure to cosmic radiation during production and refurbishing had decayed and no contributions to the energy spectrum were expected from this radio-isotope. A possible contamination had to be taken into account for the BEGe detectors, though, since they had been produced only months before their insertion into the experiment. The decays of ^{68}Ga inside the BEGe detectors was simulated in the **Single detectors in full array** mode for *configBEGE* only.

The resulting energy spectrum is shown in Fig. 8.12. It was normalized to the number of events in the the bin corresponding to the photon peak at 1077.4 keV. The spectrum is continuous with only a small peak structure at 1077.4 keV.

^{40}K

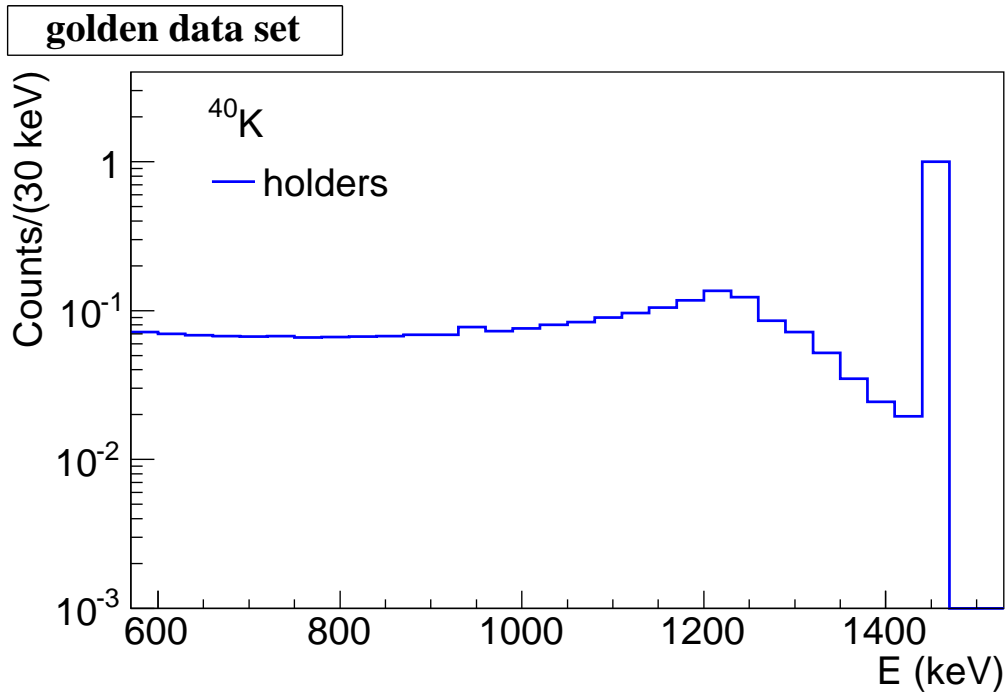
The screening results listed in Table 8.1 suggested the presence of ^{40}K in several components of small and medium distance in the experimental setup. These isotopes decay via beta decay with a Q-value of 1311.1 keV or via EC and positive beta decay with a Q-value of 1504.9 keV. The half-life is $1.3 \cdot 10^9$ yr. In both cases, the released energy is below the Q-value of double beta decay of ^{76}Ge . This means, that the energy spectrum due to ^{40}K decays falls in the energy region, which was dominated by the $2\nu\beta\beta$ spectrum. This limited the sensitivity to small variations in the shape of the energy spectrum, as expected for different source positions. Therefore, ^{40}K decays were simulated only in the holders of the detectors and the resulting energy spectrum was used as a representative for all ^{40}K contaminations in the setup.

The energy spectra were modeled in the **Full array** mode for *configNAT* and *configBEGe*. They are shown in Fig. 8.13(a) and Fig. 8.13(b), respectively. They were normalized to the number of events in the bin corresponding to the 1460.8 keV photon line.

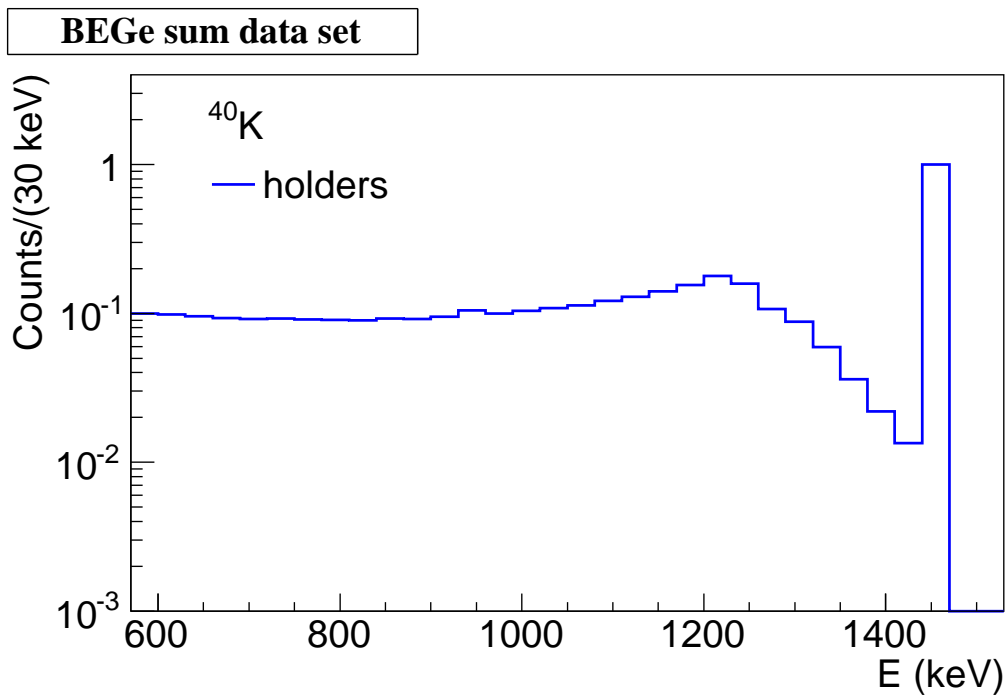
 ^{76}Ge

The energy depositions from $2\nu\beta\beta$ of ^{76}Ge dominate the energy spectra for both the golden and the BEGe sum data sets up to an energy of ≈ 1800 keV. In addition to the $2\nu\beta\beta$ energy spectra, also the spectra for $0\nu\beta\beta\chi(\chi)$ were simulated for all spectral indices predicted by theory, $n = 1, 2, 3,$ and 7 . The initial energy spectrum of the particles released in the decay was sampled with DECAY0 according to the distributions given in [80, 81]. The propagation of the particles in the GERDA setup was carried out with MAGE. For the simulations, the **Single detectors in full array** mode was used. Simulations were performed for *configNAT* as well as for *configBEGe*.

All spectra are depicted in Fig. 8.14(a) and Fig. 8.14(b) for the golden and the BEGe sum data set, respectively. The scaling of the spectra corresponds to the output of the processing of the **Single detectors in full array** mode. Since for all cases the energy is deposited exclusively by electrons and Bremsstrahlung photons, the spectra are all continuous. They correspond to the spectra shown in Fig. 3.6.



(a)



(b)

Figure 8.13: Simulated energy spectra of ^{40}K decays in the detector holders corresponding to the (a) golden and (b) BEGe sum data set. All spectra are normalized to the number of events in the bin corresponding to the photon peak at 1460.8 keV.

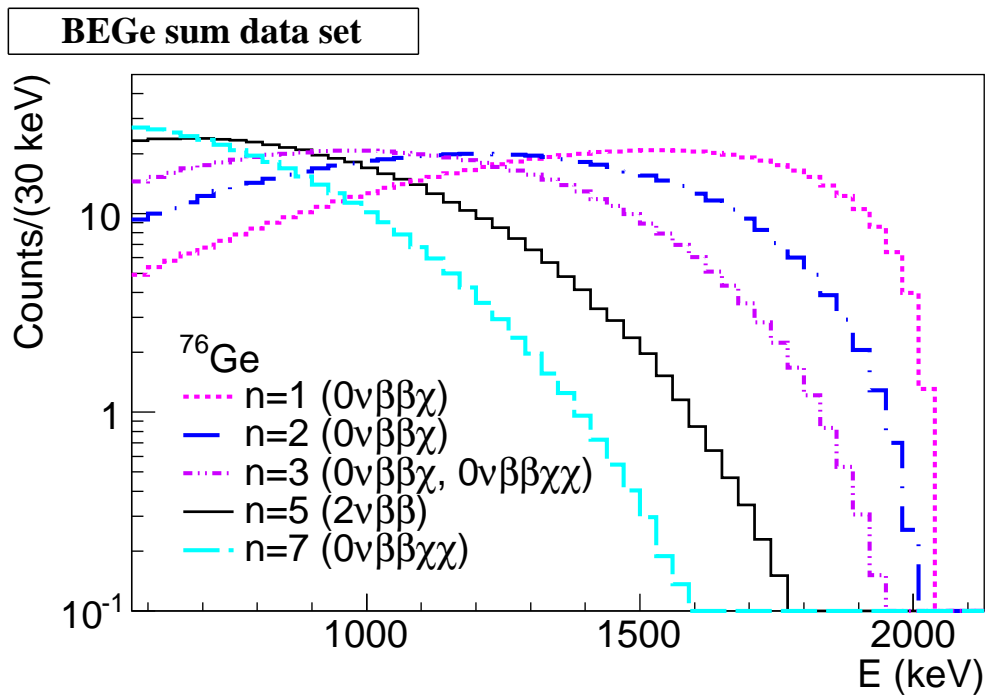
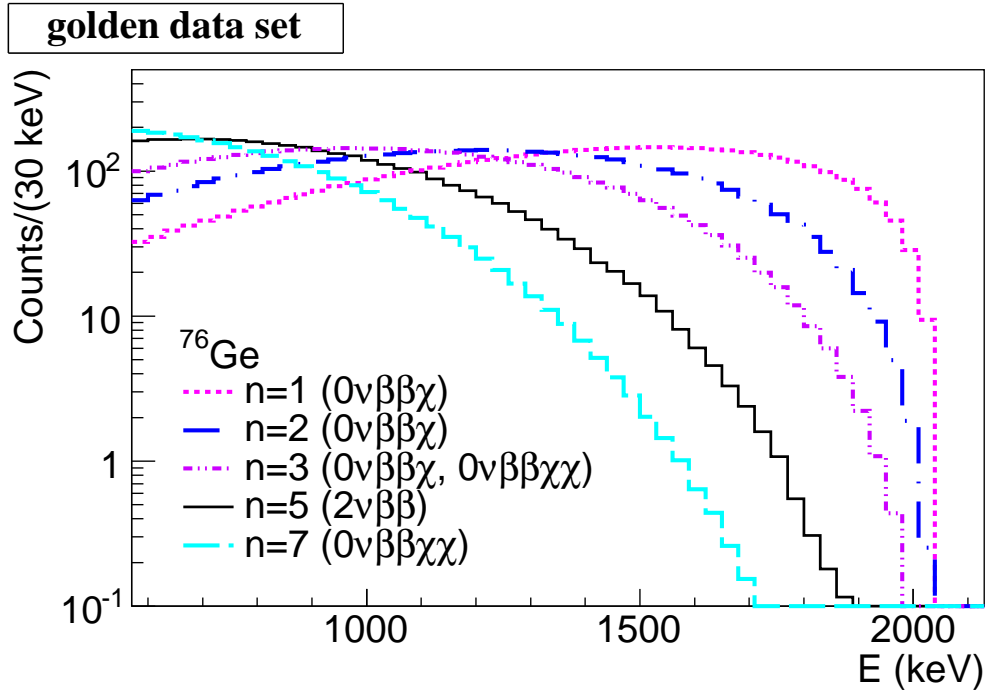


Figure 8.14: Simulated energy spectra of $2\nu\beta\beta$ and $0\nu\beta\beta\chi(\chi)$ for ^{76}Ge corresponding to the (a) golden and (b) BEGe sum data set. All spectra are normalized according to the processing of the **Single detectors in full array** simulation mode.

Chapter 9

Background Model for the GERDA Phase I Data

The simulated energy spectra described in Chapter 8 were used to decompose the GERDA Phase I data spectra into their single contributions. The data sets defined in Sec. 7.4 were examined separately. Complete background models were obtained for the golden and for the BEGe sum data set. The limited exposure of the silver data set of only $1.3 \text{ kg} \cdot \text{yr}$ did not allow a quantitative analysis. However, its background composition was assumed to be similar to that of the golden data set. The increase in the event rate, shown in Fig. 7.9, can be connected to an increase in the number of isotopes from the natural decay chains of ^{232}Th and ^{238}U in the detector vicinity following the opening of the lock system and the extraction and insertion of detector strings. The background models for the golden and the BEGe sum data sets allowed to examine in detail the spectral shape and the composition of the background around $Q_{\beta\beta}$.

9.1 Statistical Analysis Method

The statistical data analysis was performed using a binned maximum likelihood approach. The spectra obtained from the MC simulation described in Chapter 8 were added to compose a model containing all possible contributions. The expected number of events in the i -th bin of the model spectrum, λ_i , can then be written as the sum of all M contributions from the single components, c , in the i -th bin, λ_i^c ,

$$\lambda_i = \sum_{c=1}^M \lambda_i^c. \quad (9.1)$$

With n_i describing the number of events in the i -th bin of the measured data spectrum, the likelihood, $P(\mathbf{n}|\boldsymbol{\lambda})$, for the observed data spectrum, \mathbf{n} , given a certain model, $\boldsymbol{\lambda}$, can then be written as the product of the probabilities of the single bins, $P(n_i|\lambda_i)$,

$$P(\mathbf{n}|\boldsymbol{\lambda}) = \prod_i P(n_i|\lambda_i) = \prod_i \frac{e^{-\lambda_i} \lambda_i^{n_i}}{n_i!}. \quad (9.2)$$

With Bayes' theorem, the global posterior probability distribution, $P(\boldsymbol{\lambda}|\mathbf{n})$, describing the probability of the model given the data, can be expressed as

$$P(\boldsymbol{\lambda}|\mathbf{n}) = \frac{P(\mathbf{n}|\boldsymbol{\lambda})P_0(\boldsymbol{\lambda})}{\int P(\mathbf{n}|\boldsymbol{\lambda})P_0(\boldsymbol{\lambda})d\boldsymbol{\lambda}}, \quad (9.3)$$

where $P_0(\boldsymbol{\lambda})$ describes the prior probability of the parameters,

$$P_0(\boldsymbol{\lambda}) = \prod_{c=1}^M P_0(\boldsymbol{\lambda}^c). \quad (9.4)$$

Information about a single model component, $\boldsymbol{\lambda}^c$, can be extracted by marginalizing Equation (9.4) with respect to $\boldsymbol{\lambda}^c$,

$$P(\boldsymbol{\lambda}^c|\mathbf{n}) = \int_{1 \neq c} \dots \int_{M \neq c} P(\boldsymbol{\lambda}|\mathbf{n}) d\boldsymbol{\lambda}^{1 \neq c} \dots d\boldsymbol{\lambda}^{M \neq c}, \quad (9.5)$$

that is by integrating the global posterior probability distribution over all model components except the one in question.

The fit was carried out using the Bayesian Analysis Toolkit BAT [150]. All model spectra aside the one from the simulation of $2\nu\beta\beta$ of ^{76}Ge were normalized to unity, so that

$$\lambda_i^c = \mathcal{N}^c \int_{\Delta E_i} \phi^{c,\text{norm}}(E) dE, \quad (9.6)$$

with $\phi^{c,\text{norm}}(E)$ the normalized simulated energy spectrum of the component c and $\int_{\Delta E_i} \phi^{c,\text{norm}}(E) dE$ the fraction of the energy spectrum in the i -th bin. The parameter \mathcal{N}^c , which was determined in the fit, represents the total number of events of the component c in the fit window.

The spectrum deriving from the simulation of $2\nu\beta\beta$ was treated in a different manner. Not the number of events was determined in the fit, but instead the half-life of the decay, $T_{1/2}^{2\nu}$. For a single detector, j , $T_{1/2}^{2\nu}$ is connected to the number of $2\nu\beta\beta$ events in the i -th bin, $\lambda_{i,j}^{2\nu}$, via

$$\lambda_{i,j}^{2\nu} = \frac{k}{T_{1/2}^{2\nu}} M_j f_{76,j} T_j \cdot [f_{\text{act},j} \varepsilon_{\text{act},j} \mathcal{F}_{\text{act},i,j}^{2\nu} + (1 - f_{\text{act},j}) \varepsilon_{\text{dead},j} \mathcal{F}_{\text{dead},i,j}^{2\nu}], \quad (9.7)$$

with

$$\mathcal{F}_{\text{act},i,j}^{2\nu} = \int_{\Delta E_i} \varphi_{\text{act},j}^{2\nu,\text{norm}}(E) dE \quad (9.8)$$

and

$$\mathcal{F}_{\text{dead},i,j}^{2\nu} = \int_{\Delta E_i} \varphi_{\text{dead},j}^{2\nu,\text{norm}}(E) dE. \quad (9.9)$$

M_j denotes the total detector mass, T_j the live time of the detector, $f_{76,j}$ its isotopic abundance in ^{76}Ge , and $f_{\text{act},j}$ the active volume fraction of the detector. The detection

efficiencies for $2\nu\beta\beta$ taking place in the active and in the deadlayer part of the detector are given by $\varepsilon_{act,j}$ and $\varepsilon_{dead,j}$, respectively. The corresponding normalized energy distributions derived from the simulations are denoted $\varphi_{act,j}^{2\nu,\text{norm}}$ and $\varphi_{dead,j}^{2\nu,\text{norm}}$. The constant factor k is defined as $k = (\ln(2)N_A)/m_{76}$, where N_A is Avogadro's number and $m_{76} = 75.95$ g/mol is the molar mass of ^{76}Ge .

For the case of more than one detector, a decay inside a detector can lead to an energy deposit in the detector itself, but also to an energy deposit in one of the other detectors. If the energy deposit in the detector where the decay took place is below the threshold for the anti-coincidence cut, the event contributes to the energy spectrum with the energy deposited in the other detector. Therefore, when determining the total energy spectrum resulting from decays in one of the detectors, the contributions from all detectors in the array have to be taken into account. With $\mathcal{F}_{act,i,j}^{\alpha,2\nu}$ ($\mathcal{F}_{dead,i,j}^{\alpha,2\nu}$) giving the content of the i -th bin of the normalized energy distribution recorded with detector j for $2\nu\beta\beta$ taking place in the active (dead) volume of detector α and $\varepsilon_{act,j}^\alpha$ ($\varepsilon_{dead,j}^\alpha$) the corresponding detection efficiency, the content of the i -th bin in the combined energy spectrum of all N_{det} detectors in the array for decays taking place in the active and dead part of detector α becomes

$$\lambda_i^{\alpha,2\nu} = \frac{k}{T_{1/2}^{2\nu}} M_\alpha f_{76,\alpha} \cdot \left[f_{act,\alpha} \sum_{j=1}^{N_{det}} T_j \varepsilon_{act,j}^\alpha \mathcal{F}_{act,i,j}^{\alpha,2\nu} + (1 - f_{act,\alpha}) \sum_{j=1}^{N_{det}} T_j \varepsilon_{dead,j}^\alpha \mathcal{F}_{dead,i,j}^{\alpha,2\nu} \right]. \quad (9.10)$$

Summing up the simulations of decays in all N_{det} detectors, this results in the final model spectrum for $2\nu\beta\beta$,

$$\lambda_i^{2\nu} = \sum_{\alpha=1}^{N_{det}} \lambda_i^{\alpha,2\nu}. \quad (9.11)$$

The **Single detectors in full array** mode described in Sec. 8.2 incorporates almost all steps described in Equations (9.10) and (9.11). When using the final energy spectrum provided by this processing mode, $\phi^{2\nu}(E)$, it follows that

$$\lambda_i^{2\nu} = \frac{k}{T_{1/2}^{2\nu}} \int_{\Delta E_i} \phi^{2\nu}(E) dE. \quad (9.12)$$

For the fitting procedure, this was rewritten as

$$\lambda_i^{2\nu} = \frac{k_0}{t_{1/2}} \int_{\Delta E_i} \phi^{2\nu}(E) dE. \quad (9.13)$$

The factor $k_0 = (\ln(2) \cdot N_A)/(m_{76} \cdot 10^{21} \cdot 365 \text{ d}) = 15.06 (\text{kg} \cdot \text{d})^{-1}$ gives the decay rate of 1 kg of germanium enriched to 100% in ^{76}Ge for $T_{1/2}^{2\nu} = 10^{21}$ yr. The parameter determined in the fit was $t_{1/2}$, which represents $T_{1/2}^{2\nu}$ in units of 10^{21} yr.

For the fit, a Markov Chain Monte Carlo (MCMC) run with 10^7 iterations was performed. At each step, a complete set of fit parameters was available.

For each parameter, the fitting procedure returned its best-fit value, defined by the mode of the global posterior probability distribution. This will be referred to as

the *global mode* in the following. The *best-fit model* was composed by scaling the individual normalized components according to their global mode and adding up the single contributions. The contribution from $2\nu\beta\beta$ was calculated using the global mode for $t_{1/2}$ and Equation (9.13).

In order to obtain the marginalized distributions, for each parameter a histogram was filled containing its value at each step of the MCMC run. After normalization to the number of entries in the histogram, this represents the marginalized posterior distribution for the respective parameter [166]. The marginalized distribution for the total model was obtained by summing up the individual contributions at each step, again converting $t_{1/2}$ into the number of counts, filling each sum value in a histogram and normalizing the histogram to the number of entries.

From the marginalized posterior distributions, the *marginalized mode*, *smallest 68% interval*, and *90% quantile* for the individual parameters and the total model could be calculated.

For predictions in a sub-range of the fit window, the MC energy spectra were used to scale the individual parameters according to the fraction of events contained in the sub-range. Again, the best-fit expectation for the total model was obtained by summing the scaled global modes of all single contributions. For the marginalized distributions, the histograms were filled with the value at each step of the MCMC run after scaling it to the sub-range. The marginalized distribution for the total model in the sub-range was composed by the sum of the individual contributions in the sub-range at each step.

9.2 Background Model for the Golden Data Set

The background model for the golden data set was developed in two steps. First, the high energy region was analyzed and the model describing the contributions from alpha decays in the energy spectrum was defined. The alpha model served as input for the second step, that is for the development of the complete background model, describing the whole energy spectrum above the Q-value of ^{39}Ar . The development of the alpha model for the golden data set, summarized in the following, is described in detail in [149] and [160]. It was performed with a subset of the golden data set with a total exposure of $15.4 \text{ kg} \cdot \text{yr}$.

Regarding the description of the full energy spectrum, a similar approach to the one presented in these works was adopted. However, some changes were introduced to the statistical analysis and to the composition of the model. The development of the background model for the full energy spectrum used the total exposure of the golden data set of $17.9 \text{ kg} \cdot \text{yr}$.

9.2.1 High Energy Region

The high energy region was defined as the region between 3500 keV and 7500 keV. All but one of the Q-values of the beta decays that are expected to contribute to the

energy spectrum are below this region. Therefore, neither the photons nor the electrons from these decays can lead to energy depositions in this region. The only beta decaying isotope with a Q-value higher than this threshold is ^{208}Tl with a Q-value of 5001 keV. However, in 99% of all cases it decays to an excited state of ^{208}Pb , which de-excites releasing a 2614.5 keV photon. The electron energy is therefore reduced to below 3500 keV and the contributions to the energy spectrum above this threshold are negligible. The region between 3500 keV and 7500 keV is thus strongly dominated by the energy depositions from alpha decays.

As mentioned in Sec. 8.3 and visible from Fig. 8.6, the thickness of the p^+ -deadlayer has a strong influence on the shape of the energy spectrum induced by alpha decays on and close to this contact. The high number of events at the ^{210}Po peak allowed an estimate of this critical parameter. A fit to the data was performed in the energy range between 4850 keV and 5250 keV, which is dominated by the decay spectrum of ^{210}Po on the p^+ -surface. The model comprised the energy spectra of the simulations of ^{210}Po decays on the p^+ -surface for deadlayer thicknesses 100 nm, 200 nm, ..., 1000 nm. The prior probabilities of the ten parameters were chosen flat, meaning that they were allowed to vary freely in the fit. The resulting deadlayer model was a combination of the contributions for a deadlayer thickness of 300 nm, 400 nm, 500 nm, and 600 nm, respectively, while the contributions from all other energy spectra were negligible. This deadlayer model was adapted for the analysis of the high-energy region and all energy spectra were composed accordingly.

In order to define the alpha model, the region between 3500 keV and 7500 keV was divided into 80 bins with a width of 50 keV each. The fit model comprised the contributions from ^{210}Po on the p^+ -contact, as well as the contributions from the alpha decays of the ^{226}Ra sub-chain, that is from ^{226}Ra , ^{222}Rn , ^{218}Po , and ^{214}Po , on the p^+ -surface as well as in the LAr close to the p^+ -surface. No prior assumptions apart from the non-negativity of the number of events were taken into account for the intensity of the single components. Following the method described in Sec. 9.1, the number of expected events in the fit range for each component was determined from the fit. Figure 9.1 depicts the best-fit model with its individual contributions for the 15.4 kg·yr subset of the golden data set. The data energy spectrum is drawn for comparison. It can be seen that the agreement between data and model is very good. A model without the contributions from the decays in LAr could not succeed in describing the data that well. This confirmed the assumption of a contamination of the LAr with the isotopes of the ^{226}Ra sub-chain.

Table 9.1 lists the number of expected counts in the complete energy spectrum from 100 keV to 7500 keV for each component in the model. The numbers were estimated from the MC energy spectra, using the modes and the smallest 68% probability interval of the marginalized posterior distributions. In case the latter contained zero, the 90% quantile was quoted.

For the decays on the p^+ -surface, a systematic decrease in the number of events at each step of the decay chain can be observed. An explanation is the recoil of the mother nucleus with ≈ 100 keV. This can detach the nucleus from the surface. As a

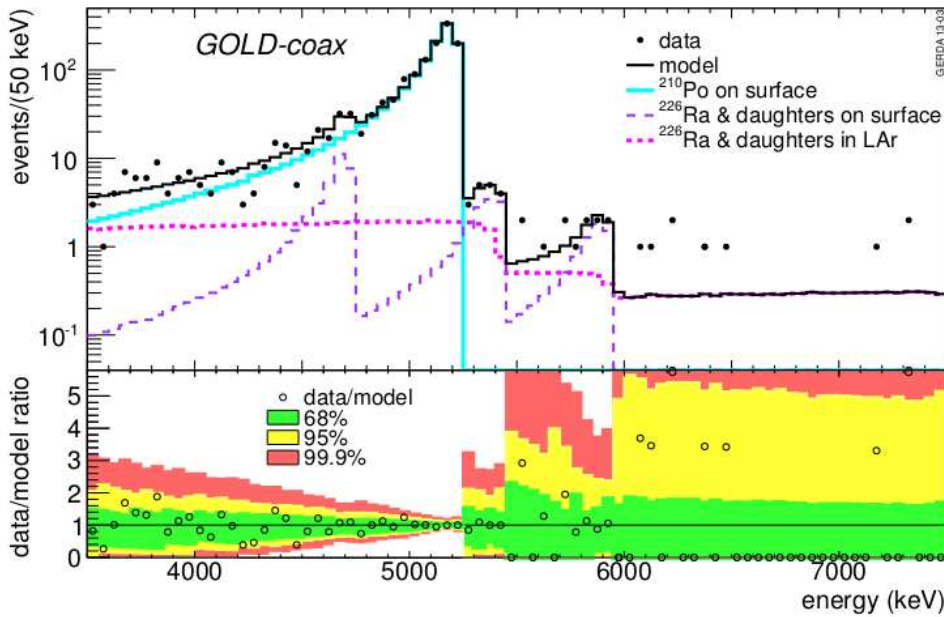


Figure 9.1: Best-fit model and individual components for the alpha model of the $15.4 \text{ kg} \cdot \text{yr}$ subset of the golden data set. The data energy spectrum is also drawn. The lower panel shows the ratio of data and model and the smallest intervals of 68% (green), 95% (yellow), and 99.9% (red) probability for the model expectation. Figure taken from [149].

consequence, the detection efficiency for the subsequent alpha decay is reduced due to the small range of these particles in matter. For the decays in LAr, mostly limits could be derived from the fit. Nevertheless, a systematic decrease after each step in the decay chain seems to be present also in this case.

9.2.2 Full Background Model

Definition of the Model

The full background model was determined by a fit to the energy spectrum of the golden data set in the energy range between 570 keV and 7500 keV. The full data set with an exposure of $17.9 \text{ kg} \cdot \text{yr}$ was used. The analysis was performed with the blinded energy spectrum, meaning that no information was provided about the contributions between 2019 keV and 2059 keV. Accordingly, also from the MC energy spectra all events with an energy deposit in this range were omitted for the fit.

The range was divided into bins with a width of 30 keV.

The ingredients to the model were the following:

Alpha model The alpha model determined previously was used as one component of the full model. The composition of the alpha model was fixed according to the best-fit model determined by the fit to the high-energy region. The resulting energy spectrum was treated analogously to the other background components.

Table 9.1: Number of expected events in the whole energy range from 100 keV to 7500 keV for each component of the alpha model for the 15.4 kg · yr subset of the golden data set. The numbers were estimated from the MC energy spectra, using the modes and the smallest 68 % probability intervals of the marginalized distributions of the parameters. In case the interval contained zero, the 90 % quantile is quoted. Table adapted from [149].

Isotope	Location	Number of counts
^{210}Po	p^+ -surface	1355 [1310,1400]
^{226}Ra	p^+ -surface	51 [36,65]
^{222}Rn	p^+ -surface	25 [18,33]
^{218}Po	p^+ -surface	14 [9,19]
^{214}Po	p^+ -surface	<10
^{226}Ra	LAr	<159
^{222}Rn	LAr	<64
^{218}Po	LAr	<30
^{214}Po	LAr	20 [10,29]

It was normalized to unity and the number of events from alpha decays in the energy spectrum was a free parameter in the fit with a flat prior probability distribution.

^{214}Bi sub-chain close sources In order to describe the contributions from decays of the ^{214}Bi sub-chain at a distance below 2 cm from the detectors, the energy spectrum resulting from simulations of decays in the detector holders was used. From the observations made in Sec. 8.3, it was assumed that this spectrum represented well the characteristics of a close source. The information collected in the screening measurements and listed in Table 8.1 was used as input to the prior probability. From the measured activities and resulting *BI* estimates and using the MC spectra, the expected number of counts in the complete fit range due to decays of the ^{214}Bi sub-chain was calculated. It resulted to be 746 events for the golden data set. Since not for all close components results from screening measurements were available, other contaminations than the ones listed in Table 8.1 might have been present. The estimated number was therefore considered the minimum number of events expected from close ^{214}Bi sub-chain sources. Accordingly, the prior probability was chosen to be flat above 746 and zero below.

^{214}Bi sub-chain medium distant sources The energy spectrum deduced from decays in the shroud was chosen as a representative for the energy spectrum corresponding to ^{214}Bi sub-chain contaminations at a medium distance, that is at distances above 2 cm and below 50 cm. Analogously to the case of the close sources, the minimum number of events expected in the energy spectrum was

determined from the screening measurement results. Consequently, the flat prior probability required a minimum of 88 events.

²¹⁴Bi sub-chain on p⁺-contact The presence of ²¹⁴Bi sub-chain contaminations on the p⁺-contact is a direct consequence of the presence of ²²⁶Ra on this surface. Therefore, the results from the alpha model provide a strong prior knowledge on the number of events expected from ²¹⁴Bi sub-chain decays on the p⁺-surface. Every decay of ²²⁶Ra is expected to be followed by a decay of ²¹⁴Pb and by a decay of ²¹⁴Bi. The reduction in the number of events of subsequent decays in the sub-chain observed for the alpha model is not expected to play a significant role here, since the range of β-particles is much larger and is thus not noticeably affected by the recoil of the mother nucleus. Using the detection efficiency for ²²⁶Ra decays of 44.3% determined from MC and the estimated number of events from ²²⁶Ra on the p⁺-contact as given in Table 9.1 for a live time of 384.6 d, the activity was determined to be $(3.4 \pm 1.0) \mu\text{Bq}$. Considering the detection efficiencies of ²¹⁴Bi and ²¹⁴Pb in the fit window, 61% and 8%, and the live time of the data set, 458.3 d, this results in an expectation of 93 ± 27 counts due to decays from the ²¹⁴Bi sub-chain on the p⁺-surface. The prior probability for this parameter was defined as a Gaussian distribution with the mean and standard deviation given by the expected number of events and the uncertainty interval.

²²⁸Ac close sources In analogy to the case of the ²¹⁴Bi sub-chain, the simulated spectrum of decays of ²²⁸Ac in the holders was chosen to represent the energy spectrum from close sources in the model. As the ²³²Th decay chain might be broken after ²²⁸Ac, the screening measurements could not be used to deduce prior knowledge on the expected contributions. Therefore, a flat prior was used for this parameter.

²²⁸Ac medium distant sources Again following the example of the ²¹⁴Bi sub-chain, the simulated spectrum of ²²⁸Ac decays in the shroud was used to describe the contributions to the energy spectrum deriving from medium distant ²²⁸Ac sources in the experimental setup. The prior distribution was flat.

²²⁸Th sub-chain close sources The spectrum of the ²²⁸Th sub-chain decays in the holders was used to model the contributions from all close sources of ²²⁸Th sub-chain decays. Also in this case, screening measurements allowed to constrain the flat prior probability distribution. From the estimates of the BI and the measured activities, a lower limit of seven expected events was determined. The limit is weaker than in the case of ²¹⁴Bi sub-chain, since less screening measurements were performed for the case of the ²²⁸Th sub-chain.

²²⁸Th sub-chain medium distant sources The spectrum of the medium distant ²²⁸Th sub-chain contaminations was represented by the decays in the shroud. The lower limit of the flat prior distribution for the expected number of events determined from the screening measurements was 46 counts.

- ²²⁸Th sub-chain distant sources** For the ²²⁸Th sub-chain, also a distant source position had to be considered in the model to represent the contributions from the calibration source on the bottom of the cryostat and from the heat-exchanger. The simulation of decays on the heat-exchanger was used to describe the resulting energy spectrum. The prior probability for the fit parameter was flat.
- ⁶⁰Co external sources** As mentioned in Sec. 8.3, the spectrum of ⁶⁰Co decays in the holders was chosen to represent the contributions from all ⁶⁰Co decays in the experimental setup external to the germanium detectors. Due to this simplification, the results from the screening measurements could not be used as input to the fit and the prior distribution was chosen to be flat.
- ⁶⁰Co internal source** The ⁶⁰Co isotopes inside the germanium detectors are the result of cosmic activation during the exposure of the detectors to cosmic rays. The critical time for the activation is the time that the germanium and later the detectors spent above ground after the zone refinement of the germanium. In [167], an estimate of the activity in June 2009 is given for each coaxial Phase I detector. For the cosmogenic production, a rate of 4 nuclei/(kg · d) was assumed [168]. From these activities, A_0 , the activities in November 2011, that is at the beginning of Phase I, were calculated as $A = A_0 e^{-\lambda t}$, with $t = 2.33$ yr and $\lambda = \ln(2)/T_{1/2} = \ln(2)/5.27$ yr. To estimate the number of decays recorded by the detectors, for each detector the total data taking period was divided into bins of $\Delta t = 15$ d and the live time fraction for each of these bins i , $f_{live,i}$, was calculated. Using the actual activity at the time corresponding to the center of the i -th bin, $A_i = A_0 e^{-\lambda(i \cdot \Delta t - (\Delta t/2))}$, and the detection efficiency determined from MC for a detection in any of the detectors considered for the golden data set, ε , the number of expected events in each bin for a specific detector was determined as $A_i \cdot \varepsilon \cdot f_{live,i} \cdot \Delta t$. All contributions were summed up over the data taking period. The contributions from the decays in the active and in the dead part of each detector were calculated separately and scaled accordingly before they were added. Adding the contributions from all detectors, a total of 40 events was expected due to the decay of ⁶⁰Co inside the detectors. The prior distribution was chosen flat until 40 and zero above.
- ⁴⁰K external sources** The contributions to the energy spectrum from decays of ⁴⁰K in the experimental setup were represented by the spectrum resulting from ⁴⁰K decays in the holders, as stated in Sec. 8.3. This rendered the use of the results from the screening measurements impossible. Therefore, a flat prior was used in the fit.
- ⁴²K in LAr** For the case of ⁴²K decays homogeneously distributed in the LAr volume, no prior knowledge was present. The prior distribution for the parameter was flat.
- ⁴²K on p⁺-contact** Also for the decays of ⁴²K on the p⁺-surface, a flat prior distribution was used.

^{42}K on n^+ -contact The prior distribution was chosen to be flat also for the case of ^{42}K decays on the n^+ -surface.

$2\nu\beta\beta$ A crucial ingredient to the model is the contribution from $2\nu\beta\beta$. In this case, not the number of events in the fit window, but the half-life of the decay in units of 10^{21} yr, $t_{1/2}$, was the parameter determined in the fit, as shown in Sec. 9.1. The prior for $t_{1/2}$ was chosen flat between one and three, corresponding to $T_{1/2}^{2\nu}$ between $1 \cdot 10^{21}$ yr and $3 \cdot 10^{21}$ yr. Since both the lower and upper limit were far away from the previous result given in Table 4.1, the prior probability was uninformative.

For all cases, where no explicit lower limit of the parameter range is given, this was set to zero, so that the number of events in the analyzed range of the spectrum was required to be non-negative.

Fit Results

A fit was performed according to the procedure described in Sec. 9.1. The global fit provided the posterior probability distribution for the 16-dimensional parameter space. The p -value calculated according to the procedure described in [169] was 0.07. Both the measured spectrum and the best-fit model contained 35847 events in the complete range between 570 keV and 7500 keV. Figures 9.2 and 9.3 depict the best-fit model for the energy region between 570 keV and 1800 keV and between 1800 keV and 3500 keV, respectively. The individual model contributions were scaled according to their global modes. The measured energy spectrum for the golden data set is also drawn. In the lower panels, the ratio of the data and the best-fit model is shown. The smallest intervals containing 68%, 90%, and 99.9% probability for the ratio assuming the best-fit parameters are indicated with a green, yellow, and red band. From the 42 points in the ratio plot for the lower energy region, 26 are contained in the 68% probability interval, 39 in the 95% probability interval, and all 42 in the 99.9% probability interval. This corresponds very well to the theoretical expectations of 28.6, 39.9, and 42.0, respectively. Also for the higher energy region, the fluctuations match the expectations. From the 57 points, 35 are contained in the 68% interval, 55 in the 95% interval, and 57 in the 99.9% interval, whereas the expectations are 38.8, 54.1, and 56.9, respectively. This good agreement between observation and expectation confirms that the model describes the data very well.

From the 35847 counts in the fit range, 72% were accounted to $2\nu\beta\beta$ and only 28% derived from the various background contaminations. Nevertheless, the characteristic photon peaks allowed to clearly identify the contributions from the different background isotopes.

The energy spectra resulting from decays of the same isotope at different positions have to be distinguished by the differences in the peak-to-continuum ratio. For some of the contaminations, the variation of the peak-to-continuum ratio between two source positions considered in the model was so small that the individual contributions could

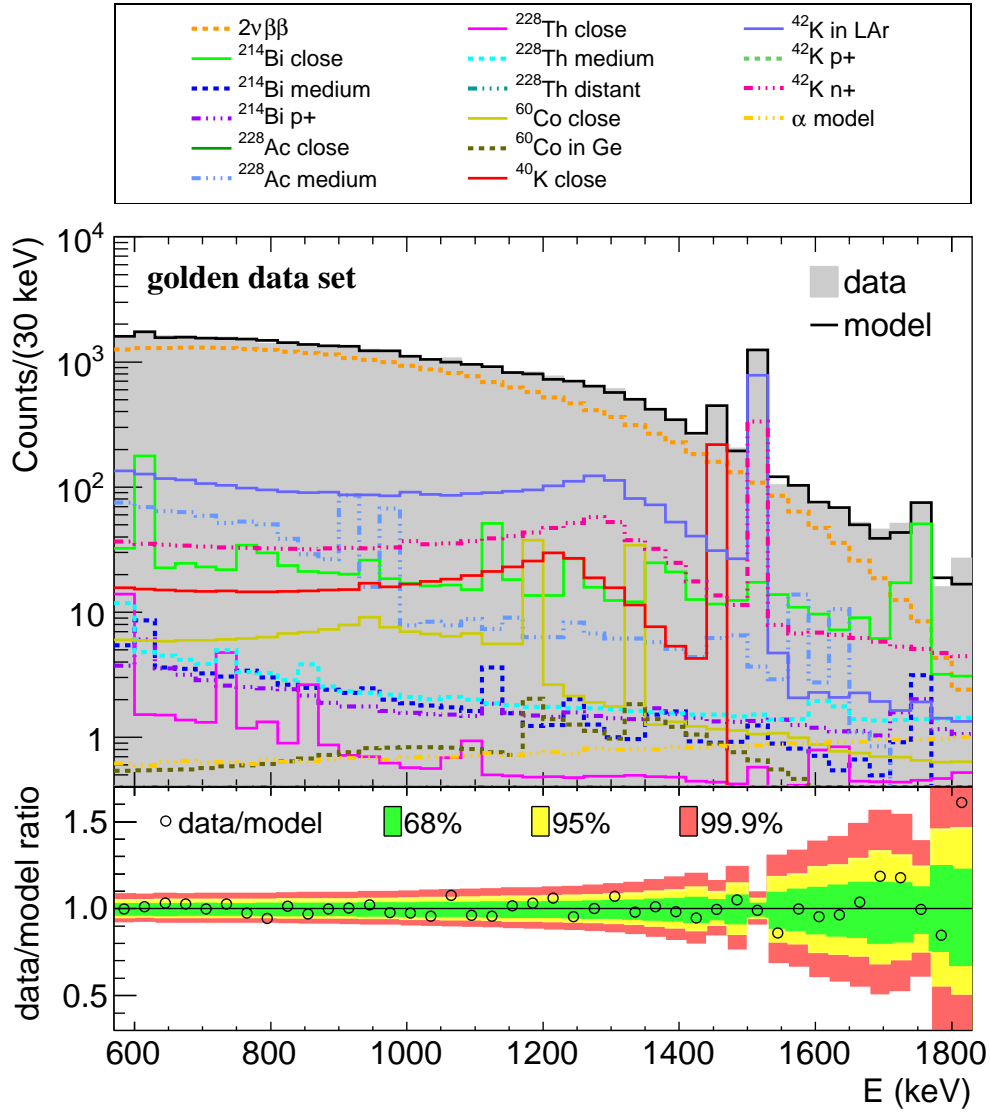


Figure 9.2: Best-fit model and data energy spectrum for the energy region from 570 keV to 1800 keV for the golden data set. The individual model components scaled according to their global mode are also drawn. The lower panel shows the ratio of data and model and the smallest intervals of 68% (green), 95% (yellow), and 99.9% (red) probability for the ratio assuming the best-fit parameters.

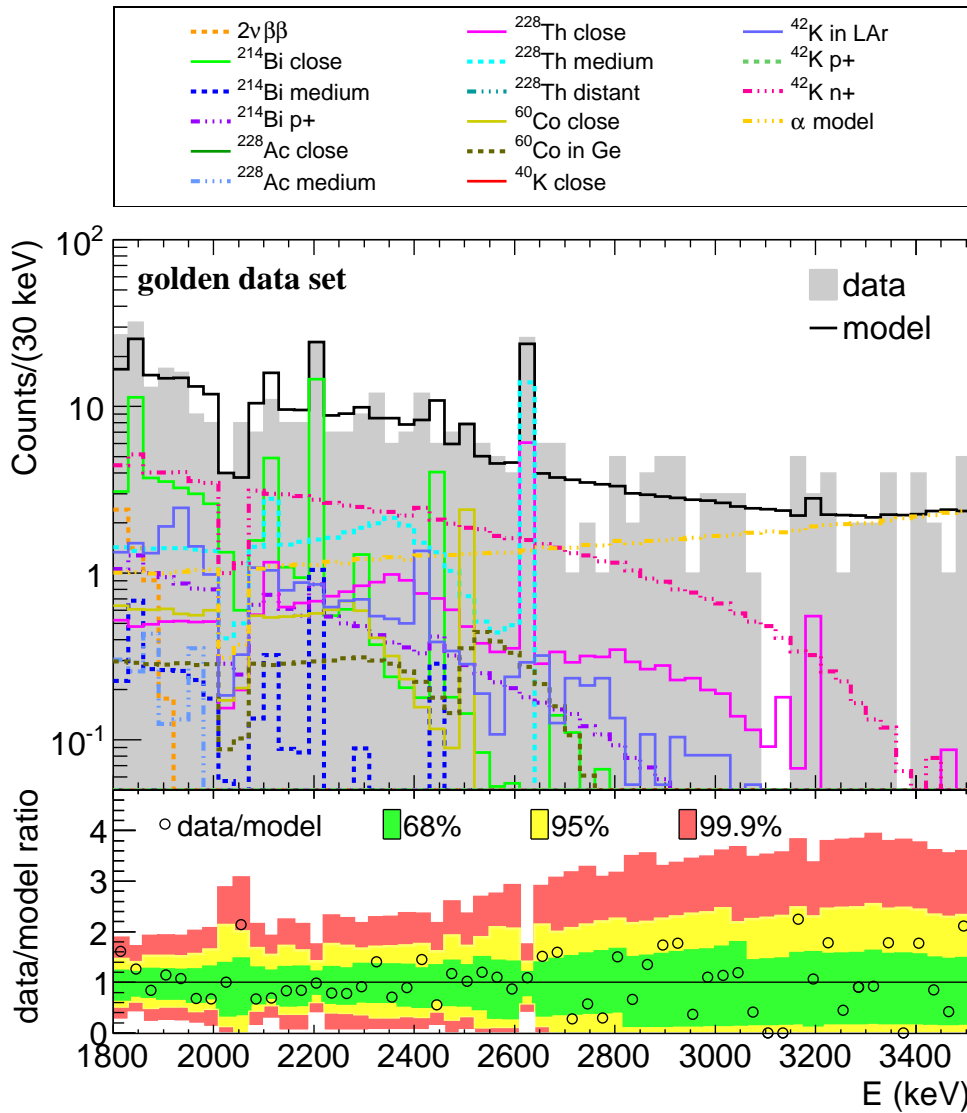


Figure 9.3: Best-fit model and data energy spectrum for the energy region from 1800 keV to 3500 keV for the golden data set. The individual model components scaled according to their global mode are also drawn. The lower panel shows the ratio of data and model and the smallest intervals of 68% (green), 95% (yellow), and 99.9% (red) probability for the ratio assuming the best-fit parameters.

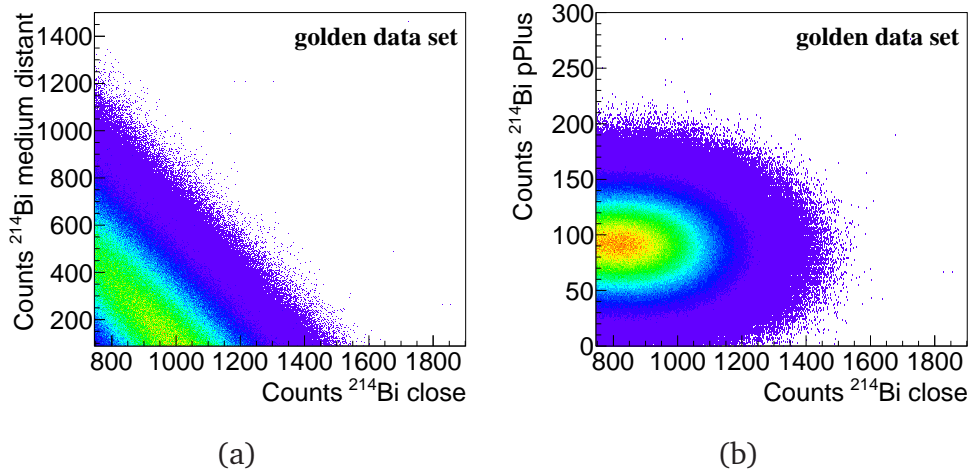


Figure 9.4: (a) Number of counts in the fit range attributed to ^{214}Bi sub-chain decays of medium distant sources against number of counts in the fit range attributed to ^{214}Bi sub-chain decays of close sources. (b) Number of counts in the fit range attributed to ^{214}Bi sub-chain decays on the p^+ -contact against number of counts in the fit range attributed to ^{214}Bi sub-chain decays of close sources. Every histogram entry corresponds to one step of the MCMC used for the fitting procedure.

not be identified unambiguously. Therefore, dependencies were present between some of the parameters describing the contributions from the same isotope at different locations. Figure 9.4(a) shows the number of counts in the fit range attributed to ^{214}Bi sub-chain decays of medium distant sources against the number of counts attributed to ^{214}Bi sub-chain decays of close sources for every step of the MCMC run. Clearly, dependencies between the two parameters were present. Figure 9.4(b), on the other hand, shows the number of counts in the fit range attributed to ^{214}Bi sub-chain decays on the p^+ -surface against the number of counts attributed to ^{214}Bi sub-chain decays of close sources. Due to the larger variations in the shape of the two energy spectra, they could be distinguished in the fit and no dependencies were observed. A strong dependency was also found between ^{42}K on the p^+ -contact and on the n^+ -contact. In addition, the energy spectra deriving from ^{228}Th sub-chain decays of close sources, medium distant sources, and far sources were not completely independent in the fit. The good agreement of the model with the data spectrum confirms the validity of the total fit model. However, the mentioned dependencies have to be kept in mind when interpreting the results for individual model components.

The mode and smallest 68% probability interval for the half-life of $2\nu\beta\beta$, derived from the marginalized posterior distribution, give

$$T_{1/2}^{2\nu} = 1.94 [1.91, 1.97] \cdot 10^{21} \text{ yr.} \quad (9.14)$$

This is in agreement with a previous determination based on a subset of the golden data set, described in detail in Appendix B.

The Background Model at $Q_{\beta\beta}$

The upper panel of Fig. 9.5 shows the region around $Q_{\beta\beta}$ for the best-fit model and its individual components after the revision of the MC blinding procedure together with the data spectrum.

The model was used to estimate the total BI and the individual contributions from all model components in the region around $Q_{\beta\beta}$. To this scope, the number of expected counts from each contribution and from the total model was determined in the ± 5 keV-window around $Q_{\beta\beta}$. This was done for the global as well as for the marginalized posterior probability distributions, following the procedure described in Sec. 9.1. The BI expectation was obtained by normalizing the number of counts to the width of the window, 10 keV, and to the exposure, 17.9 kg · yr. The results for the individual model components and the total BI are listed in Table 9.2.

The region was dominated by the contributions from ^{214}Bi sub-chain decays, ^{228}Th sub-chain decays, ^{42}K decays, and alpha decays from the ^{238}U decay chain.

The total BI in the 10 keV-window around $Q_{\beta\beta}$ estimated from the best-fit model was $20.3 \cdot 10^{-3}$ cts/(keV · kg · yr). The marginalized posterior distribution for the total model is shown in Fig 9.6. Its mode was found to be $21.0 \cdot 10^{-3}$ cts/(keV · kg · yr), with the smallest 68% probability interval extending from $19.8 \cdot 10^{-3}$ cts/(keV · kg · yr) to $22.2 \cdot 10^{-3}$ cts/(keV · kg · yr).

Stability of the Background Model at $Q_{\beta\beta}$

Some parameters that are known only within an uncertainty enter the model via the MC simulations or the priors. In order to evaluate their effect on the final model composition and the BI predictions, the analysis was repeated several times taking into account these uncertainties. The main results of the following discussion are summarized in Table 9.3.

Uncertainty on screening measurement results The influence of the uncertainty on the activities used as prior input for the contributions from the ^{214}Bi and ^{228}Th sub-chain decays of close and medium distant sources was estimated. This was done by rerunning a separate fit for each possible change in the fit parameter ranges, as calculated from the uncertainties on the activity measurements for ^{214}Bi and ^{228}Th in Table 8.1. No change was observed for any of the background components.

Active volume fraction (n^+ -deadlayer thickness) Another uncertainty that had to be considered was the uncertainty on the active volume fractions of the detectors, f_{act} . This affects several model components in different ways. For the contributions from internal sources, like $2\nu\beta\beta$ and ^{60}Co decays in the germanium, the fractions of decays taking place in the active and in the dead volume of the detectors change. The uncertainties on f_{act} , listed in Table 6.1, are of the order of a few percent. Therefore, the effect can be approximated as linear and can be taken into account by rescaling the contributions from the active and

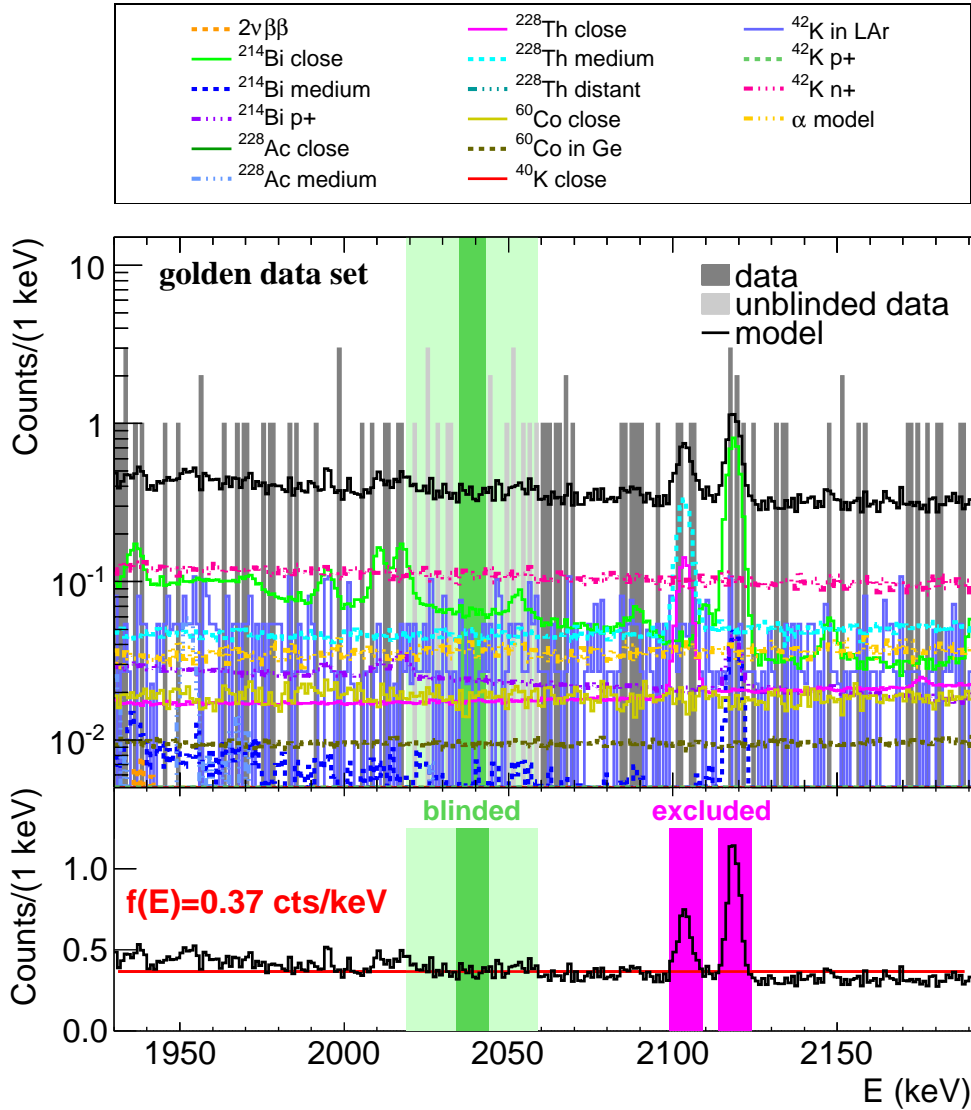


Figure 9.5: Best-fit model and data energy spectrum between 1930 keV and 2190 keV for the golden data set. The individual model components, scaled according to their global modes, are also drawn. The light grey data spectrum indicated as *unblinded* was made available after the background model determination and was thus not used for the analysis. The remaining 10 keV blinded window is marked in green. The lower panel shows a fit with a constant to the best-fit model. The 10 keV-windows around the SEP of ^{208}Tl at 2104 keV and the ^{214}Bi photon line at 2119 keV were excluded from the fit.

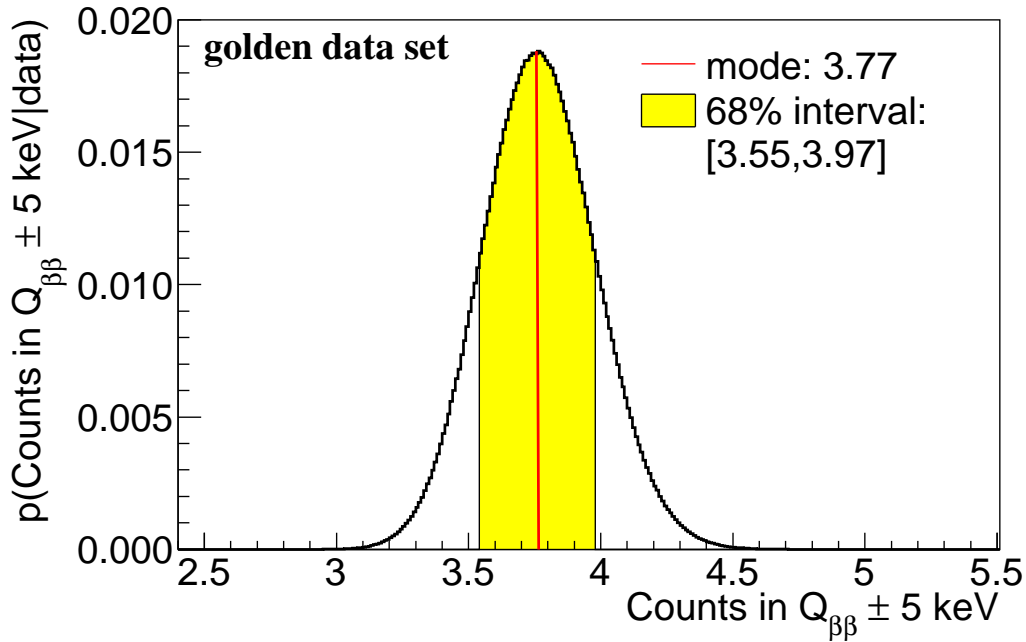


Figure 9.6: Marginalized posterior probability distribution for the expected number of counts in the 10 keV-window around $Q_{\beta\beta}$ for the golden data set. The mode and smallest 68% interval are marked.

the dead parts of the detectors. Altered spectra were produced for $2\nu\beta\beta$ and internal ^{60}Co decays by following the steps for the post-processing of the **Single detectors in full array** mode, but using the upper or lower limits for f_{act} for all detectors. The analysis was then performed with the lower and the upper limit spectra, respectively. Note that this overestimates the effect, as the maximum uncertainty is considered for each detector and no distinction is made between the correlated and the uncorrelated part of the uncertainty, see Table B.1. Nevertheless, the background model composition was not affected by this change.

Energy spectra dominated by contributions from photons are not expected to vary significantly for small variations of the active volume fraction. However, the spectrum deriving from ^{42}K decays on the n^+ -surface is likely to be altered, as a higher or lower number of electrons reaches the active volume of the detectors for decreasing or increasing deadlayer thicknesses. Simulations of ^{42}K decays on the n^+ -surface were performed for the cases of maximal and minimal deadlayer thickness of ANG3 and the analysis was repeated by replacing the standard ^{42}K spectrum by the spectra of the two extreme cases. While for the case of the upper limit of the deadlayer thickness the results remained unchanged, the case of the lower limit lead to some differences in the model composition and the BI expectation. The global mode of the total BI increased by $0.5 \cdot 10^{-3}$ cts/(keV · kg · yr), and the marginalized mode and upper and lower limit of the smallest 68% interval grew by $0.4 \cdot 10^{-3}$ cts/(keV · kg · yr). Also

Table 9.2: Estimates of the BI from the background model in a 10 keV-window around $Q_{\beta\beta}$. Listed are the results for the total model and all individual model components whose spectrum extends up to the window. The global modes, as well as the modes and smallest 68% interval of the marginalized distributions are given. In case the 68% interval contains zero, the 90% quantile of the marginalized distribution is shown. All values are given in units of 10^{-3} cts/(keV · kg · yr).

Isotope	Source position	Global mode	Marg. mode	68% interval/ 90% quantile
alpha model	p^+ -surface	2.1	2.1	[2.0,2.1]
^{214}Bi chain	close	3.6	2.9	[2.6,3.4]
^{214}Bi chain	medium distant	0.3	0.3	[0.3,1.2]
^{214}Bi chain	p^+ -surface	1.3	1.3	[0.9,1.7]
^{228}Th chain	close	1.0	0.8	[0.1,1.4]
^{228}Th chain	medium distant	2.6	0.8	[0.8,2.3]
^{228}Th chain	distant	-	-	<3.3
^{60}Co	close	1.0	1.0	[0.5,1.5]
^{60}Co	in Ge	0.5	-	<0.5
^{42}K	LAr	1.7	2.2	[1.9,2.4]
^{42}K	p^+ -surface	-	-	<4.9
^{42}K	n^+ -surface	6.2	-	<5.5
Total		20.3	21.0	[19.8,22.2]

the composition of the background model changed slightly. For the contributions from the ^{228}Th sub-chain, the global mode for close sources rose by $1.1 \cdot 10^{-3}$ cts/(keV · kg · yr), whereas the contribution due to decays of medium distant sources fell by $1.2 \cdot 10^{-3}$ cts/(keV · kg · yr). This change was not observed for the marginalized modes and limits. A variation in the composition of the contributions from ^{42}K decays was present for both the global mode and the values from the marginalized probability distributions. For the global mode, the BI due to decays in the LAr and on the p^+ -contact increased by $0.5 \cdot 10^{-3}$ cts/(keV · kg · yr) and $1.6 \cdot 10^{-3}$ cts/(keV · kg · yr), respectively, and the contribution from decays on the n^+ -surface decreased by $1.4 \cdot 10^{-3}$ cts/(keV · kg · yr). This change was only partly reflected in the values of the marginalized distributions. The marginalized modes of ^{42}K decays in the LAr increased by $1.1 \cdot 10^{-3}$ cts/(keV · kg · yr), which was also reflected in the boundaries of the 68% probability interval. The contribution from decays on the p^+ -surface not only lead to an upper limit as before, but resulted in $2.2 \cdot 10^{-3}$ cts/(keV · kg · yr), with a 68% smallest interval of $[0.4, 4.0] \cdot 10^{-3}$ cts/(keV · kg · yr). The contribution from decays on the n^+ -surface

Table 9.3: Results of the stability tests for the total BI prediction at $Q_{\beta\beta}$ for the golden data set. Given are the changes of the global and the marginalized mode of the total BI in the ± 5 keV-window around $Q_{\beta\beta}$, $\Delta BI_{\text{global}}$ and ΔBI_{marg} , in units of 10^{-3} cts/(keV · kg · yr). All variations of the marginalized mode remained within the smallest 68% probability interval. The last two columns indicate, if the global or marginalized mode of any of the individual contributions to the model varied.

Item	$\Delta BI_{\text{global}}$	ΔBI_{marg}	Model composition varied	
			global	marg.
Screening results	–	–	–	–
Active volume fraction				
for internal sources	–	–	–	–
for ^{42}K on n^+ -surface	+0.5	+0.4	✓	✓
Enrichment fraction	–	–	–	–
Source positions	+1.6 –0.2	+0.2 –0.1	✓	✓
Binning	–0.1	–0.1	✓	✓

remained unchanged.

Enrichment fraction The implications of the uncertainty on the enrichment fractions, f_{76} , were also estimated. This only affects the spectrum deriving from ^{76}Ge decays, that is the energy spectrum of $2\nu\beta\beta$. As described for the case of the uncertainty on the active volume, the post-processing of the simulated energy spectra was repeated using the upper and lower limit of f_{76} for each detector and the analysis was performed with the altered energy spectra. Again, this presents the extreme case of all detectors having systematically lower or higher enrichment fractions, and thus overestimates the effect. Neither the total BI nor the composition of the model were affected by the change.

Source positions For the fit model, the locations of the contaminations were classified as close, medium distant, and far sources, and their energy spectra were approximated with the energy spectra from decays in the holders, the shroud, and the heatexchanger, respectively. In order to evaluate the influence of a change in the location of the decays on the BI prediction, the fit was repeated for several variations in the location of the ^{214}Bi sub-chain sources. The effect is expected to be of the same order or smaller for model components different from the ^{214}Bi sub-chain. The fit was repeated by replacing the energy spectrum of ^{214}Bi sub-chain decays in the holders by the one of decays in the mini-shrouds and also by the one of decays close to the n^+ -surface. The energy spectrum resulting from decays in the shroud was replaced by the one of decays in the LAr. For the case of decays in the mini-shrouds representing the close source, the global mode of the total BI increased by $1.6 \cdot 10^{-3}$ cts/(keV · kg · yr). The increase in the marginalized

distribution was smaller, the mode grew by $0.2 \cdot 10^{-3}$ cts/(keV · kg · yr), whereas the boundaries of the smallest 68 % interval grew by $0.1 \cdot 10^{-3}$ cts/(keV · kg · yr). For the close source being represented by decays on the n^+ -surface, the total BI decreased by $0.2 \cdot 10^{-3}$ cts/(keV · kg · yr) for the global mode and by $0.1 \cdot 10^{-3}$ cts/(keV · kg · yr) for the marginalized mode and limits. The variation of the medium distant source from shroud to LAr lead to an increase of the BI of $0.3 \cdot 10^{-3}$ cts/(keV · kg · yr) for the global mode and of $0.2 \cdot 10^{-3}$ cts/(keV · kg · yr) for the values deriving from the marginalized distribution. The global mode of the ^{214}Bi sub-chain close source contribution rose by $0.6 \cdot 10^{-3}$ cts/(keV · kg · yr) for the case of the mini-shroud spectrum replacing the holder spectrum and for the case of the LAr spectrum replacing the shroud spectrum. It remained unchanged for the case of the n^+ -surface spectrum replacing the holder spectrum. The global mode of the contribution of the medium distant ^{214}Bi sub-chain decays grew by $0.8 \cdot 10^{-3}$ cts/(keV · kg · yr) when the holder spectrum was replaced with the mini-shrouds spectrum and by $0.6 \cdot 10^{-3}$ cts/(keV · kg · yr) when it was replaced with the n^+ -surface spectrum. It increased by $1.0 \cdot 10^{-3}$ cts/(keV · kg · yr) for the case of decays in the LAr representing the medium distant source. The global modes of the BI contributions from ^{42}K in the LAr and on the n^+ -surface increased by $0.6 \cdot 10^{-3}$ cts/(keV · kg · yr), respectively, when the holder spectrum was replaced by the mini-shrouds spectrum. In contrast, the modes from the marginalized probability distributions did not undergo large changes in any of the cases. The contribution from close source ^{214}Bi sub-chain decays was affected most, when the holder spectrum was replaced by the mini-shroud spectrum. In this case, it decreased by $0.4 \cdot 10^{-3}$ cts/(keV · kg · yr). All other changes in any of the marginalized modes for any of the variations turned out to be below $0.3 \cdot 10^{-3}$ cts/(keV · kg · yr). The limits of the smallest 68 % intervals reflected this behavior.

Binning For the fitting procedure, a binwidth of 30 keV was chosen for all energy spectra. In order to test the stability of the fit, the analysis was repeated using different binwidths. The energy resolution of the detectors was ≈ 4.5 keV around $Q_{\beta\beta}$ and the energy calibration was precise within 10 keV in the alpha region of the energy spectra. Therefore, the finest binning allowing for a meaningful fit is 10 keV. For a binwidth above 50 keV, the structures of the photon peaks are washed out and the quality of the fit is reduced drastically. A binning coarser than 50 keV is therefore not expected to give a useful result. The effect of different binnings was thus estimated by repeating the fitting procedure once with 10 keV bins and once with 50 keV bins. In both cases, the global as well as the marginalized mode and the corresponding limits for the total BI decreased by $0.1 \cdot 10^{-3}$ cts/(keV · kg · yr). Several changes were observed for the global mode of the single model components. For the case of 50 keV bins, the contribution from close ^{214}Bi sub-chain decays fell by $1.0 \cdot 10^{-3}$ cts/(keV · kg · yr), whereas that from medium distant sources rose by $1.5 \cdot 10^{-3}$ cts/(keV · kg · yr). For ^{228}Th sub-chain decays, the contribution from close sources increased by

$1.1 \cdot 10^{-3}$ cts/(keV · kg · yr) and the contribution from medium distant sources decreased by $1.8 \cdot 10^{-3}$ cts/(keV · kg · yr). The BI due to ^{42}K decays on the n^+ -surface was lower by $1.9 \cdot 10^{-3}$ cts/(keV · kg · yr). The changes for the case of 10 keV bins were smaller. Again, the contribution from close ^{214}Bi sub-chain decays decreased, this time by $0.9 \cdot 10^{-3}$ cts/(keV · kg · yr), whereas that from medium distant sources increased by $1.3 \cdot 10^{-3}$ cts/(keV · kg · yr). Also in this case, the contribution from ^{42}K decays on the n^+ -surface fell by $1.5 \cdot 10^{-3}$ cts/(keV · kg · yr). All other variations remained below $0.5 \cdot 10^{-3}$ cts/(keV · kg · yr). The values deriving from the marginalized distributions turned out to be stabler. The largest variation of the marginalized modes of the individual contributions was observed for the case of ^{214}Bi sub-chain decays from medium distant sources for a binning of 10 keV. The marginalized mode increased by $0.5 \cdot 10^{-3}$ cts/(keV · kg · yr). All other variations did not exceed $0.3 \cdot 10^{-3}$ cts/(keV · kg · yr).

In summary, a variation within their uncertainties of the prior limits on the ^{214}Bi and ^{228}Th sub-chain contributions and of the enrichment fractions did not affect the background model. Considering the change in the energy spectrum of ^{42}K on the n^+ -contact for the lower limit of the n^+ -deadlayer thickness derived from the uncertainty on the active volume fractions resulted in an increase of the total BI by $0.5 \cdot 10^{-3}$ cts/(keV · kg · yr) for the global mode and $0.4 \cdot 10^{-3}$ cts/(keV · kg · yr) for the marginalized mode. For a variation of the close and medium distant source positions, a maximum increase of the total BI by $1.6 \cdot 10^{-3}$ cts/(keV · kg · yr) for the global mode and $0.2 \cdot 10^{-3}$ cts/(keV · kg · yr) for the marginalized mode and a maximum decrease of $0.2 \cdot 10^{-3}$ cts/(keV · kg · yr) for the global and of $0.1 \cdot 10^{-3}$ cts/(keV · kg · yr) for the marginalized mode was observed. A change in the width of the bins lead to a decrease of $0.1 \cdot 10^{-3}$ cts/(keV · kg · yr) for both the global and marginalized mode both for smaller and wider bins. All variations of the marginalized mode of the total BI remained well within the 68% uncertainty interval.

In all cases where a change in the total BI was observed, also the composition of the background model was altered. Especially the contributions from ^{214}Bi sub-chain decays, ^{228}Th sub-chain decays, and ^{42}K surface decays were affected. All changes of individual contributions remained below $2.0 \cdot 10^{-3}$ cts/(keV · kg · yr). Generally, the global mode was more affected by changes than the values deriving from the marginalized posterior distributions¹.

As shown in Fig. 9.5, a part of the data energy spectrum contained in the 40 keV blinded window was made available for analysis after the determination of the background model had been finalized. Only the 10 keV-window around $Q_{\beta\beta}$ was kept blinded. The partial unblinding allowed to check the consistency of the background model with the data. In the unblinded 30 keV-window, 16 events were detected, whereas the best-fit model predicted 11.6 events. The expectation from the marginal-

¹The result for $T_{1/2}^{2\nu}$ resulted to be stable for all described variations of the fitting procedure, excluding the change in the enrichment fractions and the change of the active volume fractions. These lead to differences of $\pm 0.04 \cdot 10^{21}$ yr and $\pm 0.12 \cdot 10^{21}$ yr, respectively, for the mode of the marginalized posterior distribution.

ized distribution was 12.0 counts, with a smallest 68% interval of [11.5, 12.7]. The probability to detect 16 events or more given the expectation of 12.0 events is 16%.

The lower panel of Fig. 9.5 shows a fit with a constant to the background model in the window between 1930 keV and 2190 keV. The 10 keV-windows around the SEP of ^{208}Tl at 2104 keV and the ^{214}Bi photon line at 2119 keV were excluded from the fit. A fit with a first order polynomial resulted in a difference $< 1\%$ for the total number of expected counts in the window.

The fact that the energy spectrum is nearly constant in the window around $Q_{\beta\beta}$ allows to estimate the BI directly from the data, as described in Sec. 7.4. The events in the data energy spectrum between 1930 keV and 2190 keV were counted, excluding the two 10 keV-windows around 2104 keV and 2119 keV and the 40 keV of the previously blinded window, and normalized to the width of the energy window and the exposure. The resulting BI is $17.6^{+2.5}_{-2.2} \cdot 10^{-3}$ cts/(keV·kg·yr). Including the unblinded 30 keV of the previously blinded window leads to a BI of $18.5^{+2.3}_{-2.2} \cdot 10^{-3}$ cts/(keV·kg·yr). The model prediction is in agreement with both results.

9.3 Background Model for the BEGe Sum Data Set

The exposure of the BEGe sum data set was only 13% of the exposure of the golden data set. Also, the detection efficiency for the full energy peaks is reduced for the BEGe detectors with respect to the coaxial detectors due to their lower mass, diminishing the possibility to identify unequivocally the photon lines present in the energy spectrum. Therefore, the results presented in the following have to be regarded more from a qualitative rather than a quantitative point of view.

The general approach for the development of the full background model for the BEGe data set followed the strategy described for the golden data set. After the determination of the alpha model for the high-energy region of the spectrum, the full background model was developed.

9.3.1 High Energy Region

As discussed in Sec. 9.2.1, the energy spectrum above 3500 keV is dominated by the energy deposits of alpha decays. The energy spectrum of the BEGe data set is depicted in Fig. 7.8(b). Only a small number of counts was recorded for the alpha region and no peaklike structures were observed. Therefore, a determination of the deadlayer model, as described for the golden data set, was not possible. The energy spectra resulting from simulations with a p^+ -deadlayer thickness of 600 nm, the nominal deadlayer thickness of the BEGe detectors, were used for the analysis. As mentioned in Sec. 8.3, the MC simulations of the alpha decaying isotopes performed with *configANG3* can be used also to describe the BEGe high-energy spectrum, since the spectral shape due to alpha decays is influenced only by the p^+ -deadlayer thickness and not by other geometrical details of the detectors. The region from 3500 keV to 7500 keV was divided into 80 bins with a width of 50 keV each. From the small number of events in the BEGe

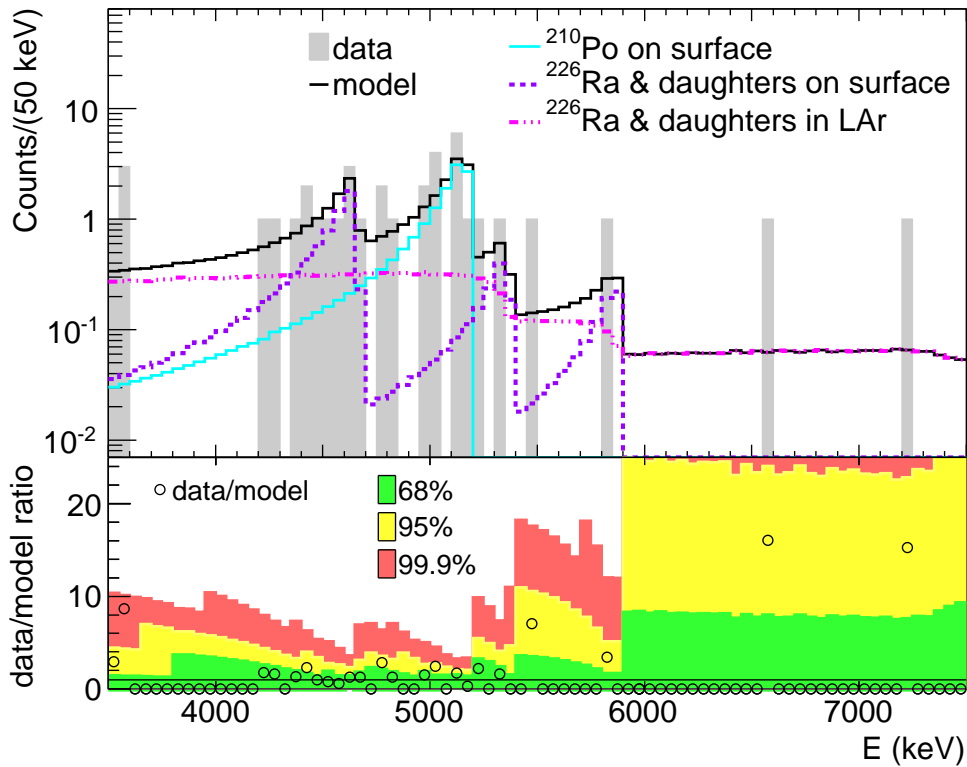


Figure 9.7: Best-fit model and individual components for the alpha model for the BEGe sum data set. The data energy spectrum is also drawn. The lower panel shows the ratio of data and model and the smallest intervals of 68% (green), 95% (yellow), and 99.9% (red) probability for the model expectation.

sum data set above 3500 keV, no conclusions could be drawn regarding potential additional or missing contributions to the alpha spectrum compared to the golden data set. Hence, the contributions to the alpha model considered for the fit were the same that had been taken into account for the golden data set. They comprised the decays of ^{210}Po and the alpha decays of the ^{226}Ra sub-chain (^{226}Ra , ^{222}Rn , ^{218}Po , ^{214}Po) on the p^+ -contact, as well as the alpha decays of the ^{226}Ra sub-chain in the LAr close to the p^+ -contact. The prior probabilities were uninformative with the only requirement of non-negative number of events. The best-fit alpha model for the BEGe sum data set is shown in Fig. 9.7 together with the data spectrum. The single contributions were scaled according to the global modes of the posterior probability.

An estimate of the number of expected events for each component in the full energy range between 100 keV and 7500 keV was extracted using the marginalized posterior distributions and the MC energy spectra for the full energy region. The modes and smallest 68% intervals are given in Table 9.4. For cases where the 68% probability range extended down to zero, the 90% quantile is listed. This is the case for all but two components of the model. It seems that the contamination with ^{210}Po isotopes

Table 9.4: Number of expected events in the whole energy range from 100 keV to 7500 keV for each component of the alpha model for the BEGe sum data set. The numbers were estimated from the MC energy spectra, using the modes and the smallest 68 % probability intervals of the marginalized distributions of the parameters. In case the interval contained zero, the 90 % quantile is quoted.

Isotope	Location	Number of counts
^{210}Po	p^+ -surface	14.0 [9.4,19.4]
^{226}Ra	p^+ -surface	6.1 [2.2,10.2]
^{222}Rn	p^+ -surface	<7.1
^{218}Po	p^+ -surface	<4.8
^{214}Po	p^+ -surface	<4.3
^{226}Ra	LAr	<51.2
^{222}Rn	LAr	<28.6
^{218}Po	LAr	<20.4
^{214}Po	LAr	<12.0

was much reduced compared to the coaxial detectors². Note that not only the smaller exposure, but also the much reduced size of the p^+ -surface as well as differences in the production process and diode history have to be taken into account for an interpretation of the alpha model. Therefore, differences between the coaxial and the BEGe detectors were expected.

9.3.2 Full Background Model

Definition of the Model

The full background model was composed analogously to the background model of the golden data set. The energy spectrum from decays of ^{68}Ga in the germanium was added as an additional contribution. Due to the short time period that had elapsed since the production and transport of the detectors until their operation in the GERDA experiment, this contribution could not be considered negligible as had been the case for the coaxial detectors. Again, the model was defined for the energy region between 570 keV and 7500 keV and in the MC spectra the events between 2019 keV and 2059 keV were removed to imitate the data blinding procedure.

A binwidth of 30 keV was chosen.

The following model components and prior information entered the fit:

²Not all coaxial detectors showed the same high level of contamination with ^{210}Po . The detectors ANG2-ANG5, which were inherited from the HdM experiment, exhibited a much larger count rate around 5.3 keV than the detectors RG1 and RG2, originating from the IGEX experiment. For further information see [149].

- Alpha model** The composition of the alpha model was fixed according to the best-fit model resulting from the fit to the high-energy region. The total number of alpha events in the fit range was a free parameter. No prior information was taken into account.
- ²¹⁴**Bi sub-chain close sources** The energy spectrum from decays in the holders was used to represent this component. As described for the golden data set, the results from the screening measurements, listed in Table 8.1, were used to derive a minimum number of events expected from this source in the fit range. Therefore, the prior probability was chosen to be flat above 107 and zero below.
- ²¹⁴**Bi sub-chain medium distant sources** The energy spectrum due to decays in the shroud was used to describe the contributions from medium distant ²¹⁴Bi sub-chain sources. The flat prior required at least 13 counts in the fit window, as derived from the results of the screening measurements.
- ²¹⁴**Bi sub-chain on p⁺-contact** Following the reasoning for the golden data set, the activity of ²¹⁴Bi sub-chain isotopes on the p⁺-surface is directly related to the activity of ²²⁶Ra on the p⁺-surface. From the number of events attributed to ²²⁶Ra decay in the alpha model, the detection efficiency of 44.3%, and the average live time of the BEGe detectors of 300 d, the activity of ²²⁶Ra on the p⁺-surface was calculated to be $(0.5 \pm 0.3) \mu\text{Bq}$. The detection efficiencies of ²¹⁴Bi and ²¹⁴Pb in the fit window were determined to be 41% and 4%. As a result, a total of 6 ± 3 events due to ²¹⁴Bi sub-chain decays on the p⁺-surface was expected in the fit range. The information was used to define the mean and standard deviation of the Gaussian prior probability distribution.
- ²²⁸**Ac close sources** The energy spectrum resulting from decays on the holders and a non-informative prior were used for this contribution.
- ²²⁸**Ac medium distant sources** The contribution was represented by the spectrum deriving from decays on the shroud. The prior probability was flat.
- ²²⁸**Th sub-chain close sources** Also in this case, a minimum number of events due to close sources of ²²⁸Th sub-chain decays, represented by the spectrum of decays in the holders, was derived from the screening measurements. As a consequence, the flat prior distribution required at least one event in the fit range.
- ²²⁸**Th sub-chain medium distant sources** The decays in the shroud were used to model the contributions from medium distant ²²⁸Th sub-chain decays. Usage of the screening results allowed to set a lower limit of six counts for the flat prior.
- ²²⁸**Th sub-chain distant sources** The energy spectrum deriving from decays of ²⁰⁸Tl in the heatexchanger simulated for the *configNAT* setup was used also for the BEGe background model. No prior information was available, hence a flat distribution was chosen.

- ^{60}Co external sources** The simulation of ^{60}Co decays in the holders was used as a representative of all contributions from ^{60}Co decays external to the detectors. This did not allow to use the screening results to constrain the fit parameter. Hence, an uninformative prior was chosen.
- ^{60}Co internal source** An estimate of the number of produced ^{60}Co isotopes inside the germanium detectors can be calculated knowing the exposure history of the germanium following the zone refinement. This allowed to extract the activity of each BEGe detector at the time of insertion into the GERDA setup [170]. Following the approach described for the golden data set, the total number of events in the analyzed data spectrum was estimated for periods of 15 d, respectively, taking into account each detector's live time fraction and the actual activity for each detector in this period. Summing up all contributions for the complete data taking period allowed to set an upper limit of four events for the flat prior distribution.
- ^{68}Ga internal source** Also in this case, the upper limit on the number of events could be estimated from the exposure history of the germanium detectors to cosmic radiation. The relevant time that has to be taken into account for the activation calculations is the time period spent above ground by the detectors following the isotope separation, that is the enrichment process. For the cosmogenic production, a rate of 1 nuclei/(kg · d) was assumed [168]. An analogous procedure as described for the case of the ^{60}Co internal source was applied, using the estimated activities for each detector at the time of insertion into the experiment [170] and the half-life of ^{68}Ga , $T_{1/2} = 270.8$ d. A maximum contribution of 50 events was determined. The prior distribution was flat up to this number and zero above.
- ^{40}K external sources** The energy spectrum from ^{40}K decays in the holders was used to represent all possible contributions from ^{40}K . Again, this generalization made it impossible to use the information from the screening measurements. Hence, a non-informative prior was used for the fit.
- ^{42}K in LAr** Also for the parameter describing the number of events that can be accounted to ^{42}K decays in the LAr, a flat prior was chosen.
- ^{42}K on p^+ -contact** No input information was available for this component, thus a flat prior was used also in this case.
- ^{42}K on n^+ -contact** Again, no prior knowledge about the number of expected events was available, necessitating an uninformative prior.
- $2\nu\beta\beta$** Following the example of the golden data set, the prior probability distribution on the fit parameter $t_{1/2}$, which gives the half-life of $2\nu\beta\beta$ in units of 10^{21} yr, was constant between one and three.

For all components where no lower limit of the parameter range was specified above, this was set to zero to assure a non-negative number of events for each contribution.

Fit Results

The background model comprised 16 parameters describing the number of events from the background components other than $2\nu\beta\beta$ and one parameter for the half-life of $2\nu\beta\beta$. The global posterior distribution as well as the marginalized posterior probabilities were determined with the fitting procedure described in Sec. 9.1. The p -value resulted to be 0.42. The best-fit model is shown together with the data energy spectrum in Fig. 9.8 and 9.9 for the energy ranges between 570 keV and 1800 keV and between 1800 keV and 3500 keV, respectively. The best-fit model contains 5032 events, exactly matching the number of counts observed in the data spectrum. The lower panels depict the ratio of the observed and expected number of events. For the lower energy range, the interval of 68% probability contains 35, that of 95% probability contains 40, and that of 99.9% contains all of the 42 ratio points. This is in good agreement with the expectations of 28.6, 39.9, and 42.0, respectively. Also for the higher energy range, the fluctuations remain within expectations with 44, 54, and 57 ratio points matching the theoretical values of 38.8, 54.1, and 56.9 for the 68%, 95%, and 99.9% probability intervals for a total of 57 points.

As shown already for the golden data set, dependencies were present between some of the fit parameters. These were even stronger for the BEGe sum data set, due to the smaller number of events in the measured energy spectrum. In the fit, no clear distinction was possible between the energy spectra of ^{214}Bi sub-chain decays from close and medium distant sources. This was the case also for the two source positions of ^{228}Ac and for all three source positions of the ^{228}Th sub-chain decays. Strong dependencies were observed also between the parameters describing the contributions from ^{42}K on the n^+ -contact and on the p^+ -contact.

The half-life of $2\nu\beta\beta$ was determined from the marginalized posterior distribution of $t_{1/2}$. It resulted in

$$T_{1/2}^{2\nu} = 2.10 [2.02, 2.19] \cdot 10^{21} \text{ yr.} \quad (9.15)$$

It agrees within 2σ with the results from the golden data set and those presented in Appendix B.

The Background Model at $Q_{\beta\beta}$

Figure 9.10 shows the data spectrum and the best-fit model with its individual contributions in the 260 keV-window around $Q_{\beta\beta}$.

The background contributions expected from the individual model components and from the total model in an 8 keV-window around $Q_{\beta\beta}$ are listed in Table 9.5. As already observed for the case of the golden data set, the dominating contributions are accounted to decays of the ^{214}Bi and ^{228}Th sub-chains, the alpha decays from the ^{238}U chain, and ^{42}K decays. Compared to the coaxial detectors, the contributions from ^{42}K decays on the detector surfaces were considerably higher. Note that the fit parameters

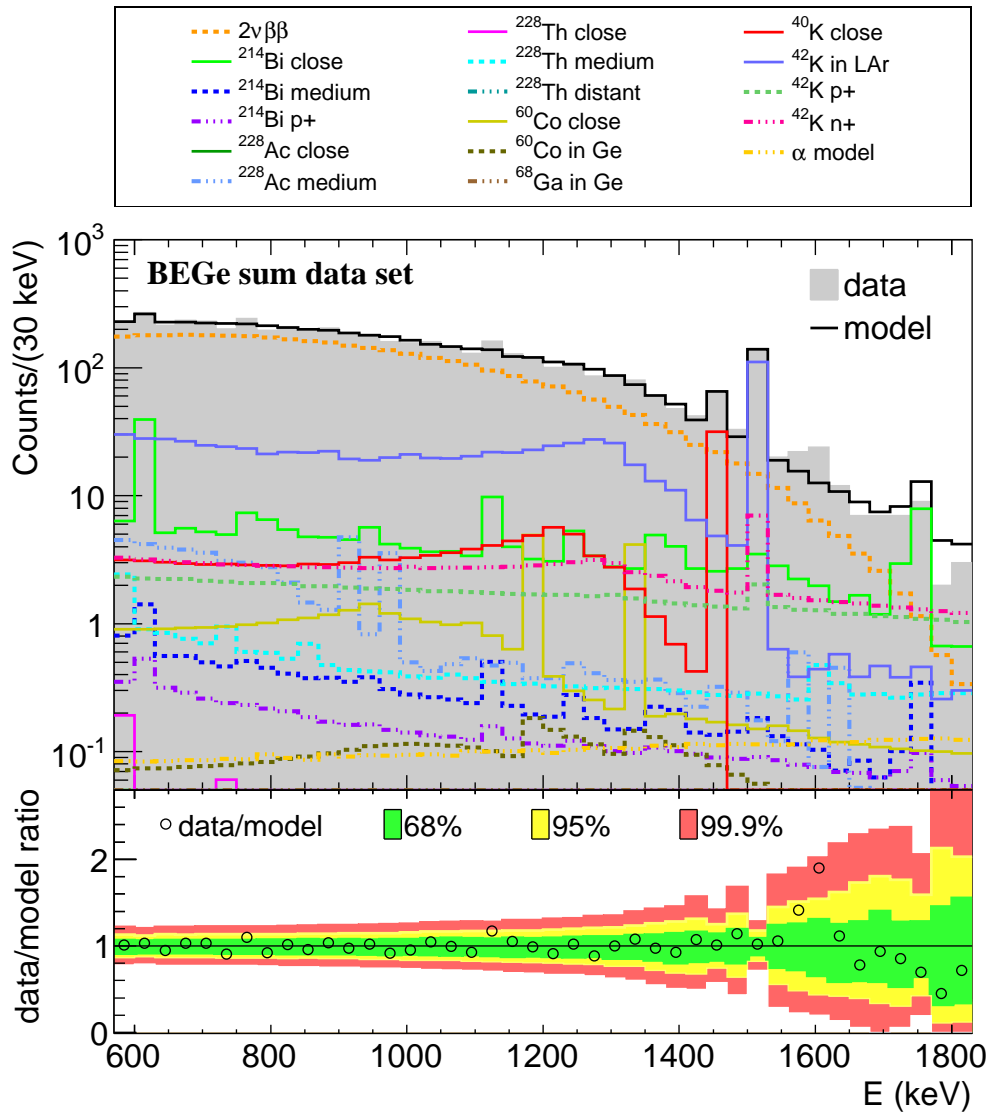


Figure 9.8: Best-fit model and data energy spectrum for the energy region from 570 keV to 1800 keV for the BEGe sum data set. The individual model components scaled according to their global mode are also drawn. The lower panel shows the ratio of data and model and the smallest intervals of 68% (green), 95% (yellow), and 99.9% (red) probability for the ratio assuming the best-fit parameters.

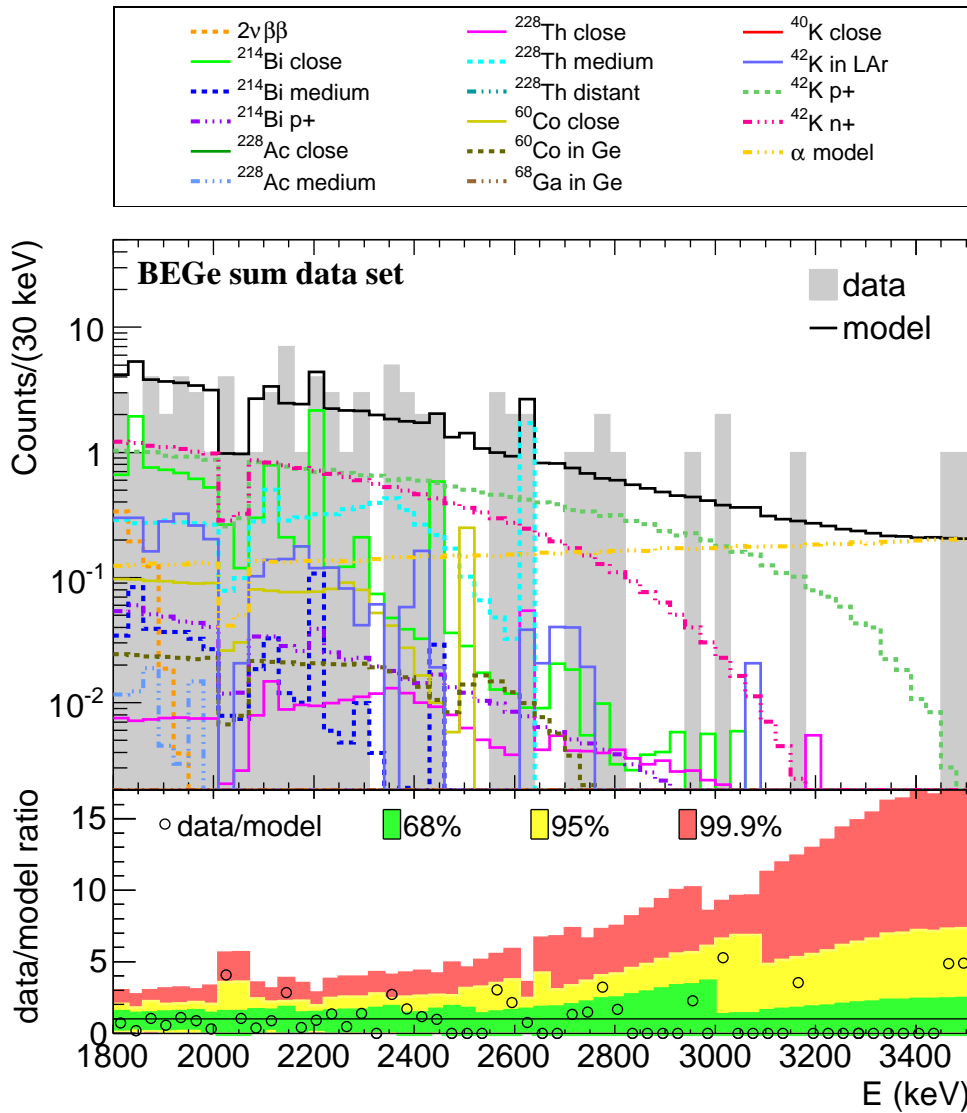


Figure 9.9: Best-fit model and data energy spectrum in the energy region from 1800 keV to 3500 keV for the BEGe data set. The individual model components scaled according to their global mode are also drawn. The lower panel shows the ratio of data and model and the smallest intervals of 68% (green), 95% (yellow), and 99.9% (red) probability for the ratio assuming the best-fit parameters.

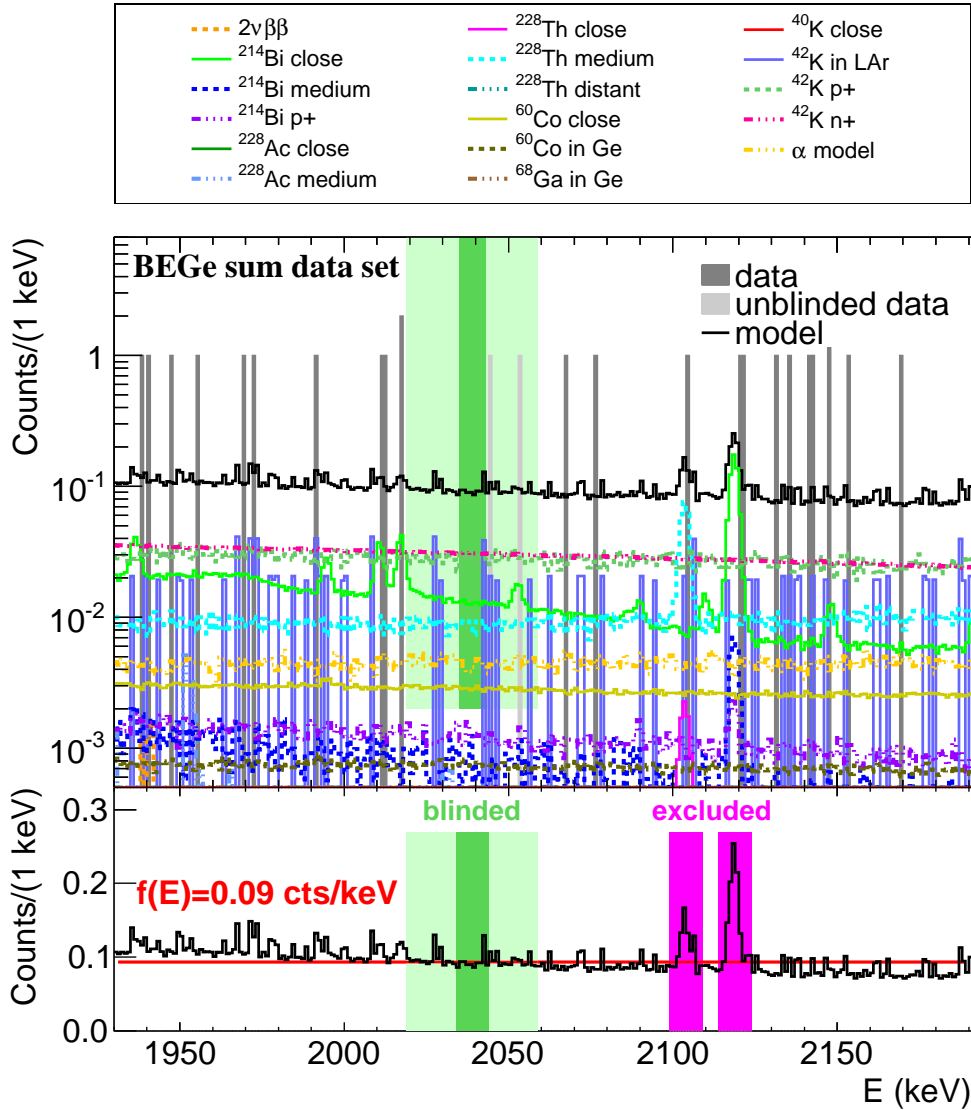


Figure 9.10: Best-fit model and data energy spectrum between 1930 keV and 2190 keV for the BEGe data set. The individual model components scaled according to their global mode are also drawn. The light grey data spectrum indicated as *unblinded* was made available after the background model determination and was thus not used for the analysis. The remaining 8 keV blinded window is marked in green. The lower panel shows a fit with a constant to the best-fit model. The 10 keV-windows around the SEP of ²⁰⁸Tl at 2104 keV and the ²¹⁴Bi photon line at 2119 keV were excluded from the fit.

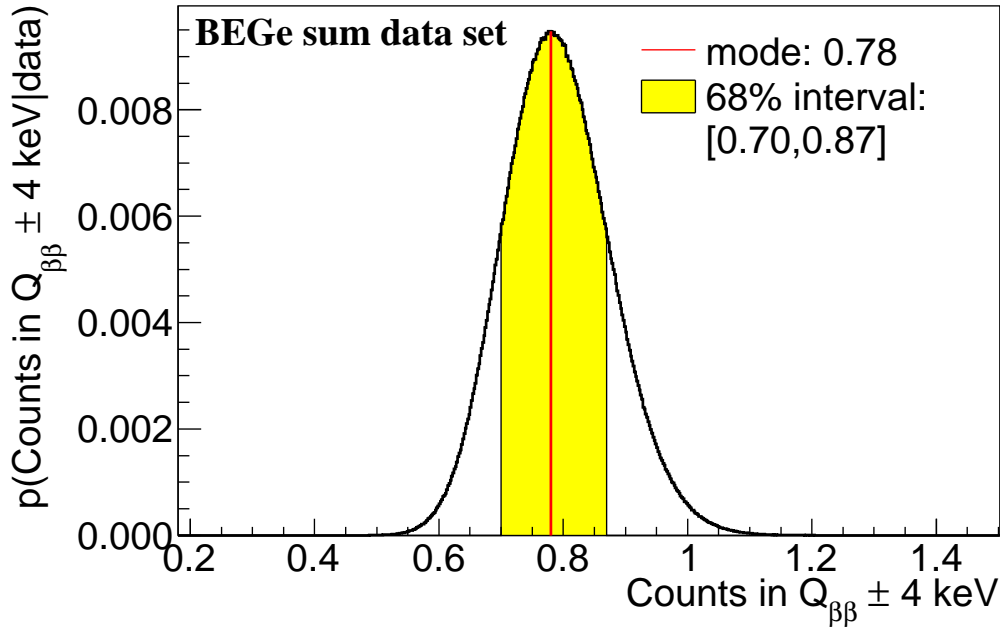


Figure 9.11: Marginalized posterior probability distribution for the expected number of counts in the 10 keV-window around $Q_{\beta\beta}$ for the BEGe sum data set. The mode and smallest 68 % interval are marked.

for the decays of ^{42}K on the p^+ -surface and on the n^+ -surface were highly dependent, so that the sum of both contributions has to be considered. For the best-fit model, these two components constitute 62% of the total BI around $Q_{\beta\beta}$. Most likely this large difference between the BEGe detectors and the coaxial detectors can be ascribed to decays happening on the n^+ -surface. For the coaxial detectors, the thickness of the Li-diffused deadlayer is about twice that of the BEGe detectors, so that for the latter more electrons released in the decay of ^{42}K reach the active volume and thus contribute to the energy spectrum.

The total BI in the 8 keV-window, estimated from the best-fit model, was $40.0 \cdot 10^{-3}$ cts/(keV·kg·yr). The marginalized distribution, shown in Fig. 9.11, gave a mode of $40.6 \cdot 10^{-3}$ cts/(keV·kg·yr) and a smallest 68 % interval of $[36.5, 45.2] \cdot 10^{-3}$ cts/(keV·kg·yr).

Stability of the Background Model at $Q_{\beta\beta}$

The effect of the uncertainties on the priors and MC simulations on the model predictions around $Q_{\beta\beta}$ were evaluated from crosschecks analogous to those performed for the golden data set. The main results can be found in Table 9.6.

Uncertainty on screening measurement results The activities that were used to define the priors for the parameters of the close and medium distant ^{214}Bi and ^{228}Th sub-chain contributions were known only within an uncertainty. While the total

Table 9.5: Estimates of the BI from the background model in a 8keV-window around $Q_{\beta\beta}$. Listed are the results for the total model and all individual model components whose spectrum extends up to the window. The global modes, as well as the modes and smallest 68% interval of the marginalized distributions are given. In case the 68% interval contains zero, the 90% quantile of the marginalized distribution is shown. All values are given in units of 10^{-3} cts/(keV · kg · yr).

Isotope	Source position	Global mode	Marg. mode	68% interval/ 90% quantile
alpha model	p^+ -surface	1.8	1.8	[1.5,2.1]
^{214}Bi chain	close	5.4	3.2	[2.7,5.1]
^{214}Bi chain	medium distant	0.3	0.3	[0.3,2.7]
^{214}Bi chain	p^+ -surface	0.5	0.5	[0.2,0.8]
^{228}Th chain	close	0.1	0.1	[0.1,3.0]
^{228}Th chain	medium distant	3.7	0.8	[0.8,4.2]
^{228}Th chain	distant	-	-	<8.4
^{60}Co	close	1.2	-	<4.2
^{60}Co	in Ge	0.3	-	<0.3
^{68}Ga	in Ge	-	-	<3.6
^{42}K	LAr	2.0	2.1	[1.9,2.3]
^{42}K	p^+ -surface	11.8	5.1	[0.5,10.5]
^{42}K	n^+ -surface	12.9	-	<16.4
Total		40.0	40.6	[36.5,45.2]

BI remained unchanged, using the lower limit for the ^{214}Bi sub-chain activity of medium distant sources lead to an increase by $0.4 \cdot 10^{-3}$ cts/(keV · kg · yr) of the marginalized mode and upper limit and an increase by $0.2 \cdot 10^{-3}$ cts/(keV · kg · yr) of the lower limit for the contribution from close source ^{214}Bi sub-chain decays. The contribution from medium distant ^{214}Bi sub-chain decays did not change. The marginalized mode for ^{42}K decays on the p^+ -surface grew by $1.4 \cdot 10^{-3}$ cts/(keV · kg · yr). This increase was not observed for the 68% interval limits. The 90% quantile of the contribution from ^{42}K decays on the n^+ -surface fell by $0.5 \cdot 10^{-3}$ cts/(keV · kg · yr).

Active volume fraction (n^+ -deadlayer thickness) In order to study the influence of the uncertainty on f_{act} for the BEGe detectors, alternative energy spectra were produced for $2\nu\beta\beta$, internal ^{60}Co decays, and for the internal ^{68}Ga decays, taking into account the upper and lower limits for f_{act} for each detector. The global modes of the single contributions as well as of the to-

Table 9.6: Results of the stability tests for the total BI prediction at $Q_{\beta\beta}$ for the BEGe sum data set. Given are the changes of the global and the marginalized mode of the total BI in the ± 4 keV-window around $Q_{\beta\beta}$, $\Delta BI_{\text{global}}$ and ΔBI_{marg} , in units of 10^{-3} cts/(keV · kg · yr). All variations of the marginalized mode remained within the smallest 68% probability interval. The last two columns indicate, if the global or marginalized mode of any of the individual contributions to the model varied.

Item	$\Delta BI_{\text{global}}$	ΔBI_{marg}	Model composition varied	
			global	marg.
Screening results	–	–	–	✓
Active volume fraction				
for internal sources	–	+0.3	–	✓
for ^{42}K on n^+ -surface	–0.4	+0.5	✓	✓
Enrichment fraction	–	–	–	✓
Source positions	+1.1 –0.5	+1.1	✓	✓
Binning	+1.3 –0.5	+1.3 –1.2	✓	✓

tal BI did not change. The marginalized mode of the total BI increased by $0.3 \cdot 10^{-3}$ cts/(keV · kg · yr) for both maximal and minimal active volume. The limits of the smallest 68% interval remained unaltered. For both the case of minimum and maximum f_{act} , the marginalized mode of ^{42}K on the p^+ -contact increased. The change was $0.6 \cdot 10^{-3}$ cts/(keV · kg · yr) for minimal active volumes and $0.8 \cdot 10^{-3}$ cts/(keV · kg · yr) for maximal active volumes. The change in the limits of the 68% intervals was smaller, it was $0.2 \cdot 10^{-3}$ cts/(keV · kg · yr) for both the lower and the upper limit in both cases.

The effect from changes in the energy spectrum of ^{42}K decays on the n^+ -contact following variations of the deadlayer thickness was estimated using the energy spectra from simulations with deadlayer thicknesses of 1.0 mm and 0.7 mm, respectively. These values correspond to the mass-weighted average upper and lower limits for the four BEGe detectors used for analysis. The transition layer was modeled as described in 8.3.2. For the case of reduced deadlayer thickness (0.7 mm), the total BI of the best-fit model did not change. The mode of the marginalized distribution for the total BI increased by $0.4 \cdot 10^{-3}$ cts/(keV · kg · yr), whereas the limits remained stable. In the best-fit model, the contribution from ^{42}K decays on the p^+ -surface was reduced by $2.1 \cdot 10^{-3}$ cts/(keV · kg · yr), whereas that of ^{42}K decays on the n^+ -surface increased by the same amount. Regarding the marginalized results, the only alteration was observed for the case of ^{42}K decays on the p^+ -surface. The 68% interval extended down to zero, so that only an upper limit of $14.7 \cdot 10^{-3}$ cts/(keV · kg · yr) could be given. For the case of maximal deadlayer thickness (1.0 mm), the global mode of the total BI decreased by $0.4 \cdot 10^{-3}$ cts/(keV · kg · yr). The mode of the marginalized distribution

increased by $0.5 \cdot 10^{-3}$ cts/(keV · kg · yr), but no change was observed for the limits of the smallest 68% interval. For the global modes of ^{42}K on the surfaces, an effect contrary to that of the case of thinner deadlayer was observed. This time, more events were attributed to ^{42}K on the p^+ -contact, the contribution rose by $2.6 \cdot 10^{-3}$ cts/(keV · kg · yr), whereas that of decays on the n^+ -contact diminished by $3.2 \cdot 10^{-3}$ cts/(keV · kg · yr). Regarding the marginalized distributions, a change was observed for ^{42}K on the p^+ -surface. The mode grew by $0.3 \cdot 10^{-3}$ cts/(keV · kg · yr) and the lower and upper limit of the 68% probability interval increased by $1.1 \cdot 10^{-3}$ cts/(keV · kg · yr) and $1.4 \cdot 10^{-3}$ cts/(keV · kg · yr). The 90% quantile derived for the contribution from decays of ^{42}K on the n^+ -surface fell by $1.2 \cdot 10^{-3}$ cts/(keV · kg · yr).

Enrichment fraction Analogously to what explained for the golden data set, the $2\nu\beta\beta$ energy spectrum was reproduced to represent the two extreme cases of maximal and minimal f_{76} for each detector. This did not affect the total BI predictions. The only change in the model composition was found for the marginalized mode of ^{42}K on the p^+ -surface, which increased by $1.2 \cdot 10^{-3}$ cts/(keV · kg · yr).

Source positions The influence of varying source position was again studied using the case of ^{214}Bi sub-chain decays. The energy spectrum of the decays in the holders representing the close source was exchanged by that of decays in the mini-shrouds and by that of decays on the n^+ -surface. For the medium distant source, usually represented by the spectrum of decays in the shroud, the energy spectrum due to decays in the LAr was used. The global as well as the marginalized mode of the total BI rose by $1.1 \cdot 10^{-3}$ cts/(keV · kg · yr) for the case of decays in the mini-shrouds representing the close source. This increase was reflected also in the limits of the 68% interval, which increased by $0.7 \cdot 10^{-3}$ cts/(keV · kg · yr). On the contrary, when the spectrum from decays on the n^+ -surface was used as close source spectrum, a decrease of $0.5 \cdot 10^{-3}$ cts/(keV · kg · yr) was observed for the global mode of the total BI . The marginalized mode and limits did not change. No change in the total BI of the best-fit model was observed when the energy spectrum due to decays in the shroud was replaced by that of decays in the LAr. However, the marginalized mode of the total BI increased by $1.0 \cdot 10^{-3}$ cts/(keV · kg · yr) and the limits of the smallest interval increased by $0.3 \cdot 10^{-3}$ cts/(keV · kg · yr). Regarding the composition of the spectrum around $Q_{\beta\beta}$, several changes could be noted. The global mode describing the decays of ^{42}K on the p^+ -surface decreased by $0.9 \cdot 10^{-3}$ cts/(keV · kg · yr), whereas that of ^{42}K on the n^+ -surface increased by $2.4 \cdot 10^{-3}$ cts/(keV · kg · yr) when the spectrum from decays in the mini-shroud was used. The marginalized mode of ^{42}K on the p^+ -surface, on the other hand, grew by $0.9 \cdot 10^{-3}$ cts/(keV · kg · yr). The corresponding lower limit did not change, whereas the upper limit increased by $0.3 \cdot 10^{-3}$ cts/(keV · kg · yr). The 90% quantile of ^{42}K on the n^+ -surface followed the trend of the global mode, it increased by $0.8 \cdot 10^{-3}$ cts/(keV · kg · yr). The opposite behaviour was observed when using

^{214}Bi sub-chain decays on the n^+ -surface as the close source representative. The global mode of ^{42}K on the p^+ -surface increased by $1.2 \cdot 10^{-3}$ cts/(keV · kg · yr) and that of ^{42}K on the n^+ -surface diminished by $2.9 \cdot 10^{-3}$ cts/(keV · kg · yr). Again, in the first case, the marginalized mode showed the opposite trend, decreasing by $0.7 \cdot 10^{-3}$ cts/(keV · kg · yr), while the limits remained unchanged. For the case of ^{42}K on the n^+ -surface, the behaviour of the global mode was followed, the 90% quantile decreased by $0.5 \cdot 10^{-3}$ cts/(keV · kg · yr). In addition, the contributions due to ^{214}Bi close source events rose by $0.9 \cdot 10^{-3}$ cts/(keV · kg · yr) for the global mode, by $0.5 \cdot 10^{-3}$ cts/(keV · kg · yr) for the marginalized mode, and by $0.6 \cdot 10^{-3}$ cts/(keV · kg · yr) for the upper limit of the smallest 68% interval. For the alternative position of the medium distant ^{214}Bi sub-chain source, the marginalized mode for ^{214}Bi sub-chain close source decays increased by $0.8 \cdot 10^{-3}$ cts/(keV · kg · yr), the lower limit increased by $0.2 \cdot 10^{-3}$ cts/(keV · kg · yr), and the upper limit by $0.4 \cdot 10^{-3}$ cts/(keV · kg · yr). The marginalized mode for the ^{42}K on the p^+ -surface contribution rose by $1.1 \cdot 10^{-3}$ cts/(keV · kg · yr). No change was observed for the limits of this contribution. The quantile describing the contributions from ^{42}K on the n^+ -surface decreased by $0.7 \cdot 10^{-3}$ cts/(keV · kg · yr).

Binning Several changes were observed when studying the model stability for different binwidths. The total *BI* rose by $1.3 \cdot 10^{-3}$ cts/(keV · kg · yr) (global mode and values from marginalized distribution) for the smaller bins, whereas the global mode fell by $0.5 \cdot 10^{-3}$ cts/(keV · kg · yr) and the marginalized mode and 68% interval limits fell by $1.2 \cdot 10^{-3}$ cts/(keV · kg · yr) for the wider bins. The global modes of the single contributions were affected by large changes. For the 10 keV binning, the contribution from close source ^{214}Bi sub-chain decays decreased by $1.4 \cdot 10^{-3}$ cts/(keV · kg · yr). The composition of ^{228}Th sub-chain contributions changed significantly. The close source contribution grew by $1.7 \cdot 10^{-3}$ cts/(keV · kg · yr), whereas the medium distant source contribution was reduced by $2.7 \cdot 10^{-3}$ cts/(keV · kg · yr). The largest contribution came from the before absent distant source with $4.0 \cdot 10^{-3}$ cts/(keV · kg · yr). Also the ^{68}Ga decays gave an increased contribution of $3.9 \cdot 10^{-3}$ cts/(keV · kg · yr). The contributions of ^{42}K on the p^+ -surface and n^+ -surface fell by $3.0 \cdot 10^{-3}$ cts/(keV · kg · yr) and $1.5 \cdot 10^{-3}$ cts/(keV · kg · yr), respectively. The values deriving from the marginalized posterior distributions turned out to be much stabler. The only significant changes of the marginalized mode were observed for ^{42}K on the p^+ -contact, which decreased by $1.3 \cdot 10^{-3}$ cts/(keV · kg · yr) and for close source ^{214}Bi , which decreased by $0.4 \cdot 10^{-3}$ cts/(keV · kg · yr). The lower limit of the ^{42}K contamination on the p^+ -surface decreased by $0.3 \cdot 10^{-3}$ cts/(keV · kg · yr). All other lower limits of the smallest 68% interval remained unchanged. The upper limits of the close and medium distant ^{214}Bi sub-chain sources decreased by $0.8 \cdot 10^{-3}$ cts/(keV · kg · yr) and $0.5 \cdot 10^{-3}$ cts/(keV · kg · yr), respectively. The upper limit of ^{42}K on the p^+ -surface increased by $0.2 \cdot 10^{-3}$ cts/(keV · kg · yr). Also for the alpha model, a change was observed. The upper limit of the smallest 68% interval rose by $0.7 \cdot 10^{-3}$ cts/(keV · kg · yr). The 90% quantile on the

contribution from ^{42}K on the n^+ -contact grew by $2.2 \cdot 10^{-3}$ cts/(keV · kg · yr). For the external ^{60}Co contamination, a mode of $1.5 \cdot 10^{-3}$ cts/(keV · kg · yr) and a smallest 68% interval of $[0.4, 2.5] \cdot 10^{-3}$ cts/(keV · kg · yr) were found, whereas in the standard fit only an upper limit of $4.2 \cdot 10^{-3}$ cts/(keV · kg · yr) was determined. Also for the fit using 50 keV-wide bins, the global modes of the individual components were affected by notable changes. The ^{214}Bi sub-chain close source contamination was reduced by $2.7 \cdot 10^{-3}$ cts/(keV · kg · yr). The ^{228}Th sub-chain contributions of close and medium distant sources increased by $4.7 \cdot 10^{-3}$ cts/(keV · kg · yr) and $0.4 \cdot 10^{-3}$ cts/(keV · kg · yr), respectively. No contribution due to external ^{60}Co was present in the best-fit model, whereas the ^{68}Ga contribution increased by $4.1 \cdot 10^{-3}$ cts/(keV · kg · yr). There were no events attributed to ^{42}K on the p^+ -surface, but the contribution from ^{42}K on the n^+ -surface grew by $5.7 \cdot 10^{-3}$ cts/(keV · kg · yr). The absence of a contribution from ^{42}K on the p^+ -surface was reflected also in the results from the marginalized parameter distribution. Only the 90% quantile could be determined for this contamination. It resulted to be $11.6 \cdot 10^{-3}$ cts/(keV · kg · yr). The 90% quantile for ^{42}K on the n^+ -surface was reduced by $1.7 \cdot 10^{-3}$ cts/(keV · kg · yr). A decrease of $0.3 \cdot 10^{-3}$ cts/(keV · kg · yr) was observed for the marginalized mode of close source ^{214}Bi sub-chain decays. While the lower limit of this contribution increased by $0.2 \cdot 10^{-3}$ cts/(keV · kg · yr), the upper limit decreased by $0.6 \cdot 10^{-3}$ cts/(keV · kg · yr). For ^{228}Th sub-chain contributions, the upper limits of the 68% probability interval due to close and medium distant sources increased by $1.5 \cdot 10^{-3}$ cts/(keV · kg · yr) and $1.8 \cdot 10^{-3}$ cts/(keV · kg · yr), respectively. The 90% quantile for the contribution from far sources increased by $2.0 \cdot 10^{-3}$ cts/(keV · kg · yr).

Summarizing, it can be said that a change of the prior limits on ^{214}Bi and ^{228}Th sub-chain decays did not change the total BI prediction, but provoked small changes in the model composition. The same was the case for a variation of the enrichment fractions of the detectors within their uncertainties. Changing the active volume fractions within their uncertainties, when processing the energy spectra for the internal sources produced an increase in the marginalized mode of the total BI of $0.3 \cdot 10^{-3}$ cts/(keV · kg · yr) as well as an increase in the contribution from ^{42}K on the p^+ -contact. Using the upper limit of the n^+ -deadlayer thickness for the simulation of ^{42}K on the n^+ -surface decreased the global mode of the total BI by $0.4 \cdot 10^{-3}$ cts/(keV · kg · yr) and increased the marginalized mode of the total BI by $0.5 \cdot 10^{-3}$ cts/(keV · kg · yr). The contributions from ^{42}K on the p^+ -surface and on the n^+ -surface were affected for both the case of maximum and minimum deadlayer thickness. Variations of the source locations for close and medium distant ^{214}Bi sub-chain decays lead to a maximum increase of $1.1 \cdot 10^{-3}$ cts/(keV · kg · yr) for the global and the marginalized mode of the total BI . The maximum decrease for the global mode was $0.5 \cdot 10^{-3}$ cts/(keV · kg · yr), whereas no decrease was observed for the marginalized mode. Again, the contributions from ^{42}K surface decays changed noticeably. Also the results obtained for ^{214}Bi sub-chain events were altered. The largest

changes in the background model were observed for the variations of the width of the bins of the energy spectra. The reason for this lies in the small number of events contained in the data energy spectrum for the BEGe sum data set and the consequently enhanced effects due to the binning. For the 10 keV-bins, the expected fluctuations for the single bins were very large. For the 50 keV-bins, the already small photon-peaks were completely washed out, making the identification of background sources and the distinction between similar spectra even more difficult. The modes of the total BI rose by $1.3 \cdot 10^{-3}$ cts/(keV · kg · yr) for the case of smaller bins and fell by $0.5 \cdot 10^{-3}$ cts/(keV · kg · yr) (global mode) and $1.2 \cdot 10^{-3}$ cts/(keV · kg · yr) (marginalized mode) for the case of wider bins. In both cases, a substantial change in the best-fit model composition was present, involving almost all model components. The unstabilities in the composition of the background model for the BEGe sum data set were considerably higher than for the golden data set. Nevertheless, the maximal variations of the total BI did not exceed $1.3 \cdot 10^{-3}$ cts/(keV · kg · yr) and thus remained well within the uncertainty interval³.

Also for the BEGe sum data set, the blinding of the data in the 40 keV-window around $Q_{\beta\beta}$ was partly removed after the definition of the background model had been finalized. Due to the better resolution of the BEGe detectors compared to the coaxial detectors, it was possible to open a 32 keV-window for analysis, leaving blinded only the 8 keV-window around $Q_{\beta\beta}$, without risking to enter the $0\nu\beta\beta$ signal region. The unblinded window contained two counts, whereas the background model expectation was 3.1 counts (global and marginalized mode), with a smallest 68 % probability interval of [2.8, 3.5]. The probability to observe two counts considering the model prediction was 22 %.

As shown for the case of the golden data set, also for the BEGe sum data the background in the ROI can be approximated by a constant. This becomes evident from the fit shown in the lower panel of Fig. 9.10, where a constant was used to describe the model in the energy window between 1930 keV and 2190 keV, excluding the two background peaks at 2104 keV and 2119 keV. An analogous fit was performed using a first order polynomial. The expected number of events in the window turned out to be in agreement within $< 1\%$ for both fit results. Therefore, also for the BEGe sum data set, the BI at $Q_{\beta\beta}$ was estimated from the number of events in the data spectrum between 1930 keV and 2190 keV, excluding the 10 keV-windows around the background peaks and the 40 keV-window around $Q_{\beta\beta}$. The result is $43.8^{+11.7}_{-9.5} \cdot 10^{-3}$ cts/(keV · kg · yr). When the unblinded 32 keV-region is added, the BI results in $41.3^{+10.4}_{-8.4} \cdot 10^{-3}$ cts/(keV · kg · yr). The model prediction at $Q_{\beta\beta}$ agrees very well with both results.

³The result for $T_{1/2}^{2\nu}$ changed by $+0.08 \cdot 10^{21}$ yr, when using 50 keV-bins and by $-0.06 \cdot 10^{21}$ yr, when using 10 keV-bins. The variations with varying f_{act} and varying f_{76} were $\pm 0.07 \cdot 10^{21}$ yr and $\pm 0.02 \cdot 10^{21}$ yr, respectively. The effect due to the change in the energy spectrum of ^{42}K on the n^+ -surface for variations in the deadlayer thicknesses was estimated to be $\pm 0.01 \cdot 10^{21}$ yr. Also the alternative positions of the ^{214}Bi sub-chain decays provoked a maximal change of $\pm 0.01 \cdot 10^{21}$ yr on $T_{1/2}^{2\nu}$.

9.4 Summary

Background models were developed for both the golden and the BEGe sum data sets. They describe the full energy region between 570 keV and 7500 keV. Several cross-checks were carried out to test the stability of the results under changes in the conditions of the fit used to define the models. The predictions for the total BI around $Q_{\beta\beta}$ deduced from the models resulted to be stable within their uncertainties. With the help of the background models it was shown that the background in the 260 keV-window around $Q_{\beta\beta}$ could be described as a constant, when the two known photon peaks at 2104 keV and 2119 keV were excluded from the analysis. This legitimated the determination of the BI as anticipated in Sec. 7.4 and used in Chapter 11 for the analysis of $0\nu\beta\beta$. Eventhough no background model could be developed for the silver data set, it was assumed that also in this case the background in the window around $Q_{\beta\beta}$ was approximately constant, since its background composition was assumed to be similar to that of the golden data set, with additional contributions from the natural decay chains of ^{232}Th and ^{238}U , see also Sec. 7.5. Counting the events in the 230 keV-window between 1930 keV and 2190 keV (excluding the 10 keV-windows around 2104 keV and 2119 keV and the still blinded 10 keV-window around $Q_{\beta\beta}$) gives $BI = 63.4^{+18.0}_{-14.3}$ for the silver data set.

Chapter 10

Neutrino Accompanied Double Beta Decay and Neutrinoless Double Beta Decay with Majoron Emission in GERDA Phase I

The half-life of $2\nu\beta\beta$ was measured using the golden and BEGe sum data sets. The analysis employed the background models described in Chapter 9. Also, a search for $0\nu\beta\beta\chi(\chi)$ was performed, leading to improved lower limits on $T_{1/2}^{0\nu\chi(\chi)}$ of ^{76}Ge for all possible decay modes (spectral index $n = 1, 2, 3$ and 7).

10.1 Statistical Analysis Method

The analysis was based on a similar statistical approach as that used for the development of the background models and described in Sec. 9.1. The information from the golden and the BEGe sum data set was combined in one fit, while keeping their energy spectra separate. The combined likelihood, $P(\mathbf{n}^{\text{gold}}, \mathbf{n}^{\text{BEGe}} | \boldsymbol{\lambda}^{\text{gold}}, \boldsymbol{\lambda}^{\text{BEGe}})$, for the observed data spectra of the golden data set, \mathbf{n}^{gold} , and the BEGe sum data set, \mathbf{n}^{BEGe} , given the models $\boldsymbol{\lambda}^{\text{gold}}$ and $\boldsymbol{\lambda}^{\text{BEGe}}$, could then be written as the product of the individual probabilities for the two data sets,

$$P(\mathbf{n}^{\text{gold}}, \mathbf{n}^{\text{BEGe}} | \boldsymbol{\lambda}^{\text{gold}}, \boldsymbol{\lambda}^{\text{BEGe}}) = \prod_i P(n_i^{\text{gold}} | \lambda_i^{\text{gold}}) \cdot \prod_j P(n_j^{\text{BEGe}} | \lambda_j^{\text{BEGe}}), \quad (10.1)$$

with n_i^{gold} (n_i^{BEGe}) the number of events in the i -th bin of the measured data spectrum for the golden (BEGe sum) data set. The expected number of events in the i -th bin of the golden and the BEGe sum data set, λ_i^{gold} and λ_i^{BEGe} , could be expressed as the sum of their single model contributions, c , for the total of M^{gold} and M^{BEGe} contributions, respectively,

$$\lambda_i^{\text{gold}} = \sum_{c=1}^{M^{\text{gold}}} \lambda_i^{\text{gold}, c} \quad (10.2)$$

and

$$\lambda_i^{\text{BEGe}} = \sum_{c=1}^{M^{\text{BEGe}}} \lambda_i^{\text{BEGe},c}. \quad (10.3)$$

Also in this case, the posterior probability distribution, $P(\boldsymbol{\lambda}^{\text{gold}}, \boldsymbol{\lambda}^{\text{BEGe}} | \mathbf{n}^{\text{gold}}, \mathbf{n}^{\text{BEGe}})$, was determined from a fit performed within the BAT framework [150]. The marginalized posterior distributions for the single parameters, $P(\lambda_i^{\text{gold},c} | \mathbf{n}^{\text{gold}}, \mathbf{n}^{\text{BEGe}})$ and $P(\lambda_i^{\text{BEGe},c} | \mathbf{n}^{\text{gold}}, \mathbf{n}^{\text{BEGe}})$, were obtained as described in Sec. 9.1.

The fit contained $(M^{\text{gold}} - 2) + (M^{\text{BEGe}} - 2)$ parameters for all contributions other than $2\nu\beta\beta$ and $0\nu\beta\beta\chi(\chi)$, allowing for independent contributions to the energy spectrum of the golden and BEGe sum data set. They were defined according to Equation (9.6) as

$$\lambda_i^{\text{gold},c} = \mathcal{N}^{\text{gold},c} \int_{\Delta E_i} \phi^{\text{gold},c,\text{norm}}(E) dE, \quad (10.4)$$

and

$$\lambda_i^{\text{BEGe},c} = \mathcal{N}^{\text{BEGe},c} \int_{\Delta E_i} \phi^{\text{BEGe},c,\text{norm}}(E) dE, \quad (10.5)$$

with $\phi^{\text{gold},c,\text{norm}}(E)$ and $\phi^{\text{BEGe},c,\text{norm}}(E)$ the normalized simulated energy spectra of the component c for the golden and BEGe sum data set, respectively, and $\int_{\Delta E_i} \phi^{\text{gold},c,\text{norm}}(E) dE$ and $\int_{\Delta E_i} \phi^{\text{BEGe},c,\text{norm}}(E) dE$ the fraction of the energy spectrum in the i -th bin.

One common parameter, $t_{1/2}^{2\nu}$, described the contributions due to $2\nu\beta\beta$ for both the golden and the BEGe sum data set. For the i -th bin, this resulted in

$$\lambda_i^{\text{gold},2\nu} = \frac{k_0}{t_{1/2}^{2\nu}} \int_{\Delta E_i} \phi^{\text{gold},2\nu}(E) dE \quad (10.6)$$

and

$$\lambda_i^{\text{BEGe},2\nu} = \frac{k_0}{t_{1/2}^{2\nu}} \int_{\Delta E_i} \phi^{\text{BEGe},2\nu}(E) dE, \quad (10.7)$$

respectively, in analogy to Equation (9.13).

A fit using these $(M^{\text{gold}} - 2) + (M^{\text{BEGe}} - 2) + 1$ parameters without the possibility of a contribution from $0\nu\beta\beta\chi(\chi)$ decay was performed to determine $T_{1/2}^{2\nu}$.

When studying the possible contributions from majoron accompanied decay modes, a separate fit was performed for each spectral index. Hence, one additional parameter, $\text{inv}_-t_{1/2}^{0\nu\chi(\chi)}$, was considered, again in common for the two datasets. It was defined as the inverse of the half-life of the respective majoron accompanied mode in units of 10^{21} yr. Following the definitions for $T_{1/2}^{2\nu}$ in Sec. 9.1, the contributions in the i -th bin due to $0\nu\beta\beta\chi(\chi)$ for the golden data set could then be written as

$$\lambda_i^{\text{gold},0\nu\chi(\chi)} = \text{inv}_-t_{1/2}^{0\nu\chi(\chi)} \cdot k_0 \int_{\Delta E_i} \phi^{\text{gold},0\nu\chi(\chi)}(E) dE, \quad (10.8)$$

whereas that of the BEGe sum data set were defined as

$$\lambda_i^{\text{BEGe}, 0\nu\chi(\chi)} = \text{inv_}t_{1/2}^{0\nu\chi(\chi)} \cdot k_0 \int_{\Delta E_i} \phi^{\text{BEGe}, 0\nu\chi(\chi)}(E) dE. \quad (10.9)$$

The energy distributions $\phi^{\text{gold}, 0\nu\chi(\chi)}$ and $\phi^{\text{BEGe}, 0\nu\chi(\chi)}(E)$ were those deriving from the simulations and post-processing of the majoron accompanied decay mode in question for the golden and the BEGe sum data set, respectively.

10.2 Fit Results

The fit range extended from 570 keV to 7500 keV for both the golden and the BEGe sum data set. This maximized the information available in the fit in order to fix the background contributions. The data spectra after unblinding were used, containing also the events in the 40 keV-window around $Q_{\beta\beta}$. The total fit range was divided into 231 bins of 30 keV width each. The background contributions considered in the fit models for the golden and the BEGe sum data sets were those described in Sec. 9.2.2 and 9.3.2, that is the alpha model, ^{214}Bi sub-chain decays from close and medium distant sources as well as on the p^+ -surface, ^{228}Ac close and medium distant sources, ^{228}Th sub-chain decays from close, medium distant, and distant sources, ^{60}Co external and internal sources, ^{40}K external sources, and ^{42}K decays in the LAr, on the p^+ -contact, and on the n^+ -contact. For the BEGe sum data set, an additional parameter describing the contribution from ^{68}Ga internal decays was needed. This accounted to 15 parameters for the golden data set and 16 parameters for the BEGe sum data set. All prior probabilities were defined in analogy to the background model analysis.

In addition, the parameter $t_{1/2}^{2\nu}$, in common to the data sets, was used to describe the contributions from $2\nu\beta\beta$ in the energy spectra. Its prior distribution was chosen flat between zero and five, corresponding to $T_{1/2}^{2\nu}$ between zero and $5 \cdot 10^{21}$ yr. Since both values are very distant from the results of previous measurements, see Table 4.1, this prior probability could be considered uninformative.

The parameter $\text{inv_}t_{1/2}^{0\nu\chi(\chi)}$ was used to estimate the contributions from majoron accompanied decay. A separate fit was performed for each decay mode $n = 1, 2, 3$ and 7, with $\text{inv_}t_{1/2}^{0\nu\chi(\chi)}$ in common to the golden and the BEGe sum data set. The prior probability distribution was chosen flat between zero and one, meaning that $T_{1/2}^{0\nu\chi(\chi)}$ was required to be greater than 10^{21} yr. Since this is well below the limits deduced from previous measurements, see Table 4.2, the prior could be regarded as uninformative.

Note that the statistical analysis was dominated by the golden data set, which had a more than seven times larger exposure than the BEGe sum data set.

10.2.1 Measurement of $T_{1/2}^{2\nu}$

In order to determine $T_{1/2}^{2\nu}$, a fit was performed considering only the $(M^{\text{gold}} - 2) = 15$ parameters for the golden data set background contaminations, the $(M^{\text{BEGe}} - 2) = 16$

parameters for the BEGe sum data set background contaminations, and one parameter for the half-life of $2\nu\beta\beta$ without any contribution from any of the majoron accompanied modes, resulting in a total of 32 parameters. The best-fit models for the golden and the BEGe data sets in the energy range between 570 keV and 2040 keV are shown in Fig. 10.1 together with the data spectra. The contributions from the total model, the background model, defined as the total model without the contributions from $2\nu\beta\beta$, and the $2\nu\beta\beta$ energy spectra scaled according to the global modes are also depicted. Also indicated is the smallest 68% probability interval for the total model expectation. The models contain a total of 35902.3 events for the golden data set and 5062.1 events for the BEGe sum data set, whereas the data energy spectra contain 35868 and 5035 events, respectively. This good agreement between data and model is confirmed also by the good p -value of 0.13.

The energy spectrum in the region between 570 keV and 1800 keV is dominated by $2\nu\beta\beta$, whereas above this energy the contributions from $2\nu\beta\beta$ are negligible. MC simulations show that the probability for a $2\nu\beta\beta$ decay in the active volume of the detectors to deposit an energy above 1800 keV is $< 0.02\%$. According to the best-fit model prediction, 74.6% of the total spectrum between 570 keV and 1800 keV of the golden data set can be accounted to $2\nu\beta\beta$. For the BEGe data set, the fraction of $2\nu\beta\beta$ events in this range was 73.2%. Thus, for both data sets a signal-to-background ratio of $\approx 3 : 1$ was reached.

The half-life of $2\nu\beta\beta$ was determined from the marginalized posterior distribution for $t_{1/2}^{2\nu}$, shown in Fig. 10.2. From the marginalized mode and smallest 68% probability interval for $t_{1/2}^{2\nu}$, which represents $T_{1/2}^{2\nu}$ in units of 10^{21} yr, the half-life of $2\nu\beta\beta$ was found to be

$$T_{1/2}^{2\nu} = 1.96 [1.93, 1.99] \cdot 10^{21} \text{ yr.} \quad (10.10)$$

Note that the statistical uncertainty of this result, unlike the one presented in Appendix B, does not yet contain the uncertainties on f_{76} and f_{act} . Instead, these had to be taken into account when estimating the systematical uncertainty. It does, however, already contain the uncertainty related to the background sources, as all possible sources and source positions were considered in the fit model.

10.2.2 Limits for $T_{1/2}^{0\nu\chi(\chi)}$

The fits performed to search for the decay modes with majoron emission accounted for an additional parameter, $\text{inv_}t_{1/2}^{0\nu\chi(\chi)}$, and thus contained a total of 33 parameters. Separate fits were performed for the four modes.

The global model for the case of spectral index $n = 1$ is shown in Fig. 10.3 together with the data energy spectra for both the golden and the BEGe sum data sets. The contributions from the background contaminations, the combined spectra from the background contaminations and $2\nu\beta\beta$, and from $2\nu\beta\beta$ only are drawn separately. The corresponding figures for the cases $n = 2, 3$ and 7 are depicted in Fig. C.1, C.3, and C.5 in Appendix C.

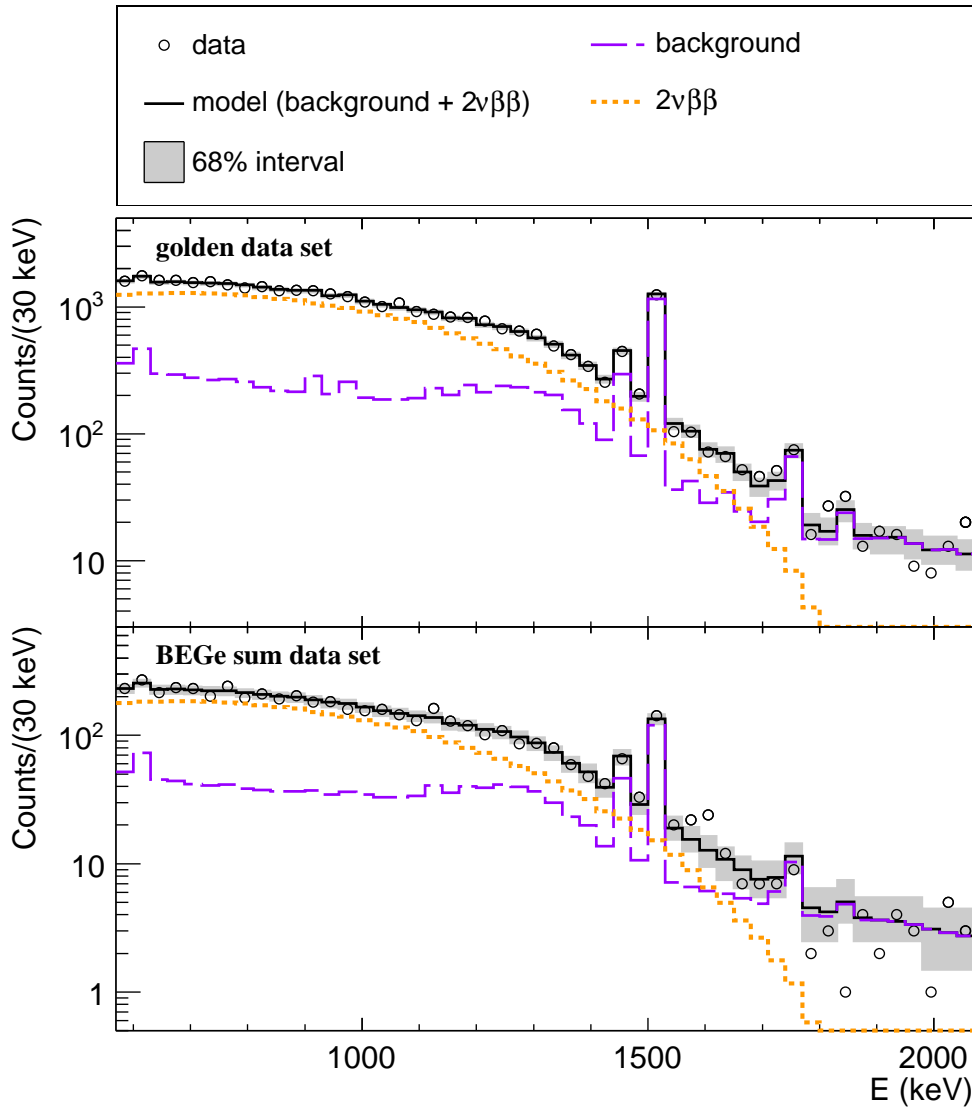


Figure 10.1: Best-fit model and data energy spectrum for the golden and the BEGe sum data set. The contributions from $2\nu\beta\beta$ and the background contributions are shown separately. The smallest interval of 68% probability for the model expectation is indicated in grey.

The 35868 events in the data spectrum of the golden data set were matched with 35834.0, 35794.7, 35841.5, and 35795.8 events in the best-fit model for $n = 1, 2, 3$ and 7 , respectively. Of those events, 54.5, 234.0, 384.9, and 9.7, respectively, were attributed to $0\nu\beta\beta\chi(\chi)$ for the four modes. For the BEGe sum data set, the best-fit models contained 5081.4, 5061.8, 5046.4, and 5049.6 counts, respectively, for the 5035 measured events. In this case, 7.8, 33.6, 55.1, and 1.4 events were considered as deriving from $0\nu\beta\beta\chi(\chi)$. Note that for the depicted best-fit models, the possible contributions from $0\nu\beta\beta\chi(\chi)$ were not considered. The p -values of 0.13 for $n = 1$ and $n = 7$, 0.14 for $n = 2$, and 0.12 for $n = 3$ confirm the good agreement between the data and the models.

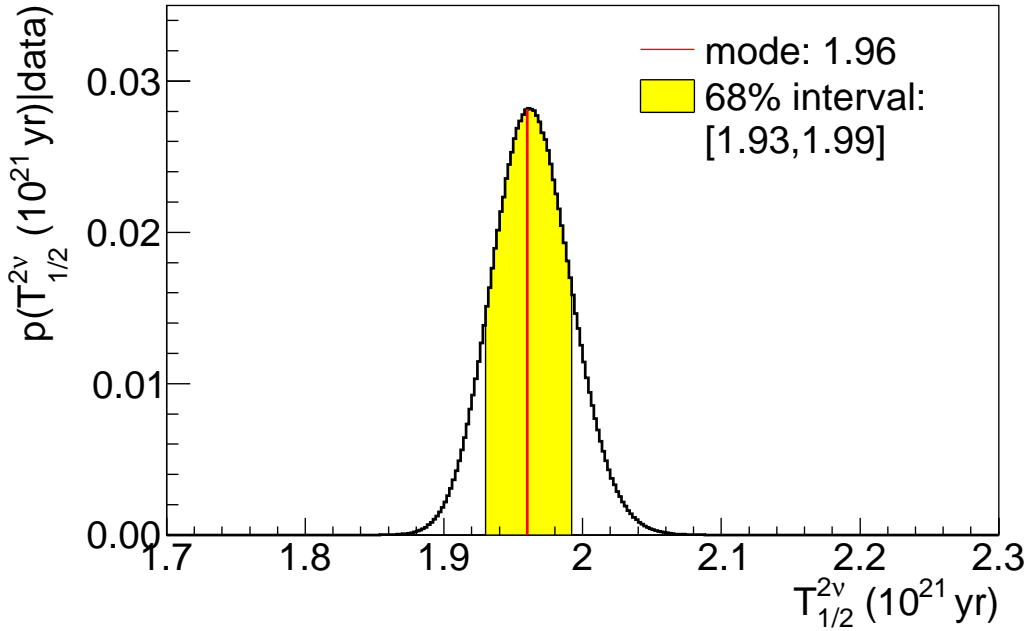


Figure 10.2: Marginalized posterior probability distribution $P(t_{1/2}^{2\nu}|\mathbf{n})$ for the parameter $t_{1/2}^{2\nu}$, which represents $T_{1/2}^{2\nu}$ in units of 10^{21} yr. The mode and smallest interval of 68 % probability are marked.

The half-life of $2\nu\beta\beta$, determined from the marginalized posterior distributions of $t_{1/2}^{2\nu}$, resulted in $T_{1/2}^{2\nu} = 1.96 \cdot 10^{21}$ yr for $n = 1$, $T_{1/2}^{2\nu} = 1.97 \cdot 10^{21}$ yr for $n = 2$, $T_{1/2}^{2\nu} = 1.98 \cdot 10^{21}$ yr for $n = 3$, and $T_{1/2}^{2\nu} = 1.99 \cdot 10^{21}$ yr for $n = 7$. Hence, it remained within the statistical uncertainties of Equation (10.10) for all four cases.

The information about the half-life of $0\nu\beta\beta\chi(\chi)$ was extracted from the marginalized posterior distributions of $\text{inv}_{-}t_{1/2}^{0\nu\chi(\chi)}$. As an example, Fig. 10.4 shows the marginalized distribution for $n = 1$. The corresponding marginalized posterior distributions for the cases $n = 2, 3$ and 7 have similar shapes. They are shown in Fig. C.2, C.4, and C.6 in Appendix C.

As expected, for all four cases the smallest 68 % interval extended down to zero, corresponding to $T_{1/2}^{0\nu\chi(\chi)} = \infty$. Therefore, only lower limits on the half-life could be given for all four modes. They were obtained from the 90 % quantiles of the marginalized posterior distributions. These were 0.00229, 0.00523, 0.01066, and 0.02895 for $n = 1, 2, 3$ and 7 , respectively. For the mode with spectral index $n = 1$, this converts into

$$T_{1/2}^{0\nu\chi} > 4.36 \cdot 10^{23} \text{ yr.} \quad (10.11)$$

For $n = 2$, a lower limit of

$$T_{1/2}^{0\nu\chi} > 1.91 \cdot 10^{23} \text{ yr} \quad (10.12)$$

was determined. The analysis of the decay mode with $n = 3$ resulted in

$$T_{1/2}^{0\nu\chi(\chi)} > 0.94 \cdot 10^{23} \text{ yr.} \quad (10.13)$$

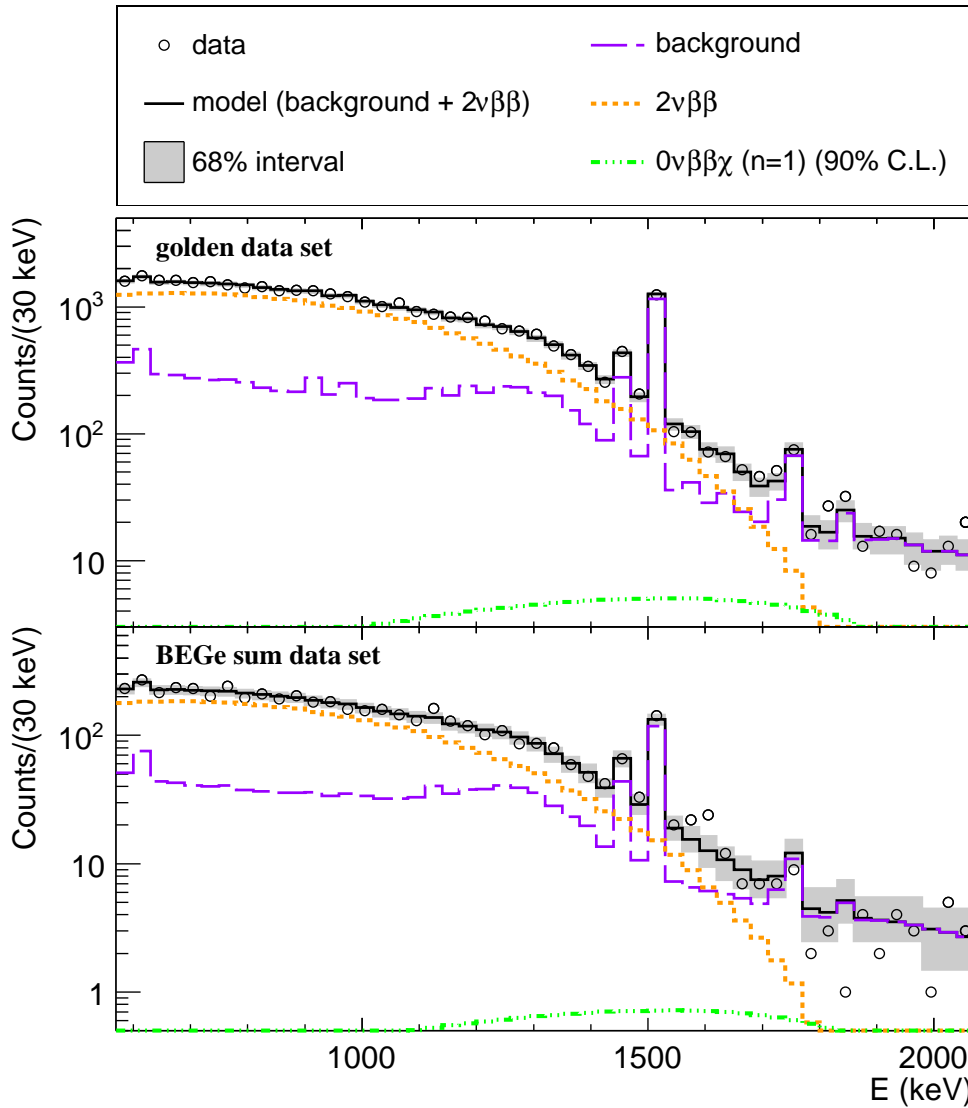


Figure 10.3: Best-fit model and data energy spectrum for the golden and the BEGe sum data set for the case of spectral index $n = 1$. The contributions from $2\nu\beta\beta$ and the background contributions are shown separately. The best-fit model does not contain the contributions from $0\nu\beta\beta\chi$. The smallest interval of 68% probability for the model expectation is indicated in grey. Also shown is the upper limit for $0\nu\beta\beta\chi$ with $n = 1$ as determined from the 90% quantile of the marginalized posterior probability for $\text{inv-}t_{1/2}^{0\nu\chi(\chi)}$.

The result for $n = 7$ was

$$T_{1/2}^{0\nu\chi(\chi)} > 0.35 \cdot 10^{23} \text{ yr.} \quad (10.14)$$

Note that these results do not yet account for systematic uncertainties.

For the mode with $n = 1$, 95% of all decays in the active volume of a coaxial or BEGe detector lead to an energy deposit in the range analyzed in the fit. For the case of $n = 2$, the detection efficiency was reduced to 91%, and for the mode with $n = 3$,

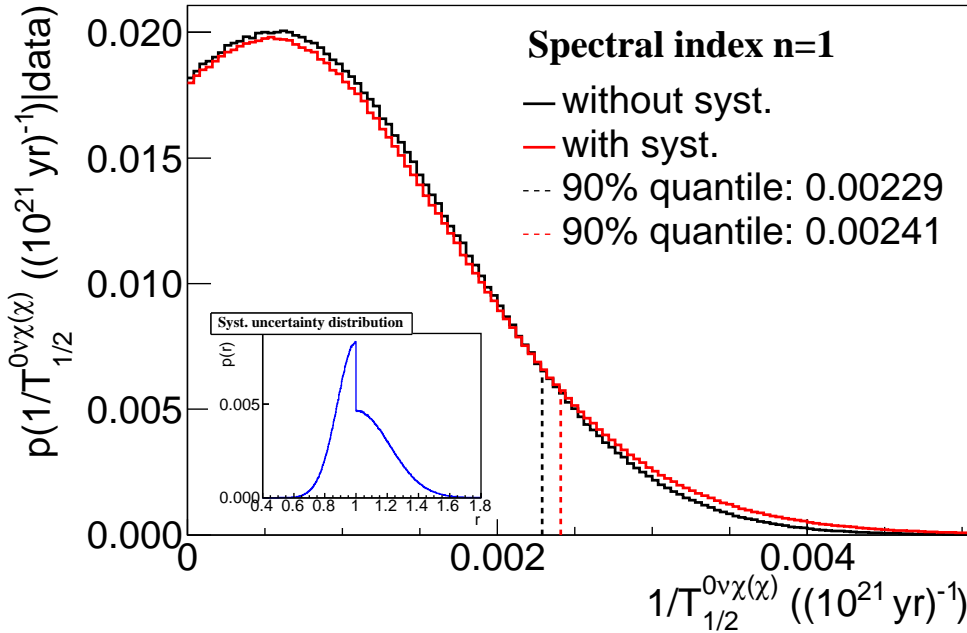


Figure 10.4: Marginalized posterior probability distribution $P(\text{inv}_t_{1/2}^{0\nu\chi(\chi)} | \mathbf{n})$ for the parameter $\text{inv}_t_{1/2}^{0\nu\chi(\chi)}$, which represents $1/T_{1/2}^{0\nu\chi(\chi)}$ in units of $(10^{21} \text{ yr})^{-1}$ for the case of spectral index $n = 1$. The 90 % quantile is marked. Also drawn is the posterior probability distribution after folding in the systematic uncertainty distribution, shown in the inset, and the resulting 90 % quantile.

the detection efficiency dropped to 84 %. The energy spectrum for the $0\nu\beta\beta\chi\chi$ mode with $n = 7$ exhibits a maximum around 400 keV and thus below the analysis range. The detection efficiency in the analysis window was reduced to 49 %. Even more importantly, the background for $0\nu\beta\beta\chi(\chi)$ in the experiment was distinctly higher for lower energies, as the region up to 1800 keV was dominated by the $2\nu\beta\beta$ spectrum. Therefore, the higher the spectral index, that is the more the energy spectrum of $0\nu\beta\beta\chi(\chi)$ was shifted towards lower energies, the more the sensitivity was reduced. This explains why the strongest limit was determined for the mode with $n = 1$. With increasing spectral indices, the limits get weaker. As expected, for the mode with $n = 7$, the sensitivity was the smallest, since the entire energy spectrum lies in the region dominated by $2\nu\beta\beta$.

10.3 Systematic Uncertainties

In order to estimate the systematic uncertainty on the results for $T_{1/2}^{2\nu}$ and $T_{1/2}^{0\nu\chi(\chi)}$, several aspects had to be taken into account. They were grouped into the three categories *fit model*, *MC simulation*, and *data acquisition and selection*. The contributions to the total systematic uncertainty on $T_{1/2}^{2\nu}$ and $T_{1/2}^{0\nu\chi(\chi)}$ are summarized in Table 10.1.

10.3.1 Fit Model

Several parameters that enter the fit model via the MC simulations or the prior probabilities were known only within an uncertainty. In Sec. 9.2.2 and 9.3.2 it was shown, how these uncertainties affect the background model around $Q_{\beta\beta}$. In the following, their impact on the result for $T_{1/2}^{2\nu}$ and the limits on $T_{1/2}^{0\nu\chi(\chi)}$ will be discussed.

The fit model containing the contributions from the mode with $n = 1$ was chosen as a representative and all possible variations of the input parameters were studied for this case. They were then applied also to the other fit models. Due to the similarity of the fit models, it is reasonable to assume that the results for $n = 1$ were good approximations also for the cases of $n = 2, 3$ and 7 , as well as for the case of $2\nu\beta\beta$ only.

Regarding the fit model, the following sources of uncertainty were considered:

Uncertainty on screening measurement results The results from the screening measurements listed in Table 8.1 were used to set lower limits on the number of events expected from close and medium distant sources of the ^{214}Bi and ^{228}Th sub-chain decays. The lower limits were recalculated taking into account the maximum and minimum activity for each source and a fit was run for each possible change in the prior probability of the corresponding model components for the golden and the BEGe data set. The result for $t_{1/2}^{2\nu}$ remained unchanged for all variations. The 90% quantile for $\text{inv-}t_{1/2}^{0\nu\chi(\chi)}$ showed its maximal increase of 0.5%, when the lower limit for the activity of the ^{214}Bi sub-chain medium distant sources was used for the fit. The maximal decrease of 1.3% was observed for the case of the upper limit for the activity of close sources of the ^{214}Bi sub-chain.

Binning For the standard fit, a bin width of 30 keV was used. As mentioned in Sec. 9.2.2, the smallest and largest meaningful sizes for the bins were 10 keV and 50 keV. The fit was repeated for both bin widths in order to estimate the impact. A small change was observed for $t_{1/2}^{2\nu}$. For the larger bin size, it increased by 0.5% and it decreased by the same amount for the smaller bin size. The change in the 90% quantile for $\text{inv-}t_{1/2}^{0\nu\chi(\chi)}$ was much more pronounced. Whereas only a 2.6% growth was observed for the case of 10 keV bins, the value increased by 16.1% for the case of 50 keV bins. This large increase can be explained by the fact that peak structures were washed out for such a coarse binning. For $2\nu\beta\beta$, this did not affect the results in a decisive manner due to the large signal-to-background ratio. For $0\nu\beta\beta\chi(\chi)$, on the other hand, the sensitivity dropped, as the possibility to distinguish between the energy spectra of the background components and the $0\nu\beta\beta\chi(\chi)$ energy spectrum was reduced.

Active volume fraction (n^+ -deadlayer thickness) The uncertainties on the active volume fractions entered the model in several ways. On the one hand, the MC energy spectra for all internal sources, that is for $2\nu\beta\beta$, $0\nu\beta\beta\chi(\chi)$, ^{60}Co , and ^{68}Ga , were affected, as the fraction of decays taking place in the active and

dead part of the detectors changes with changing f_{act} . For the coaxial detectors, the total uncertainty on f_{act} was $\approx 6\%$, whereas for the BEGe detectors, it was $\approx 3\%$, as can be seen from Table 6.1. Both the uncertainties of the coaxial as well as of the BEGe detectors were sufficiently small to allow a linear approach. The post-processing of the concerned model components was repeated using the upper and lower limit for f_{act} , respectively, for each detector. The fit was repeated twice, once by replacing the standard energy spectra with those for the upper limit and once by replacing them with those for the lower limit. The change in $t_{1/2}^{2\nu}$ was $+5.6\%$ for the first case and -5.6% for the latter case, and thus of the same order as the uncertainties on f_{act} . This was not surprising, since $T_{1/2}^{2\nu}$ depends directly on f_{act} . The larger uncertainty of the coaxial detectors dominated the total uncertainty due to their larger exposure. An analogous effect was observed for $\text{inv}_-t_{1/2}^{0\nu\chi(\chi)}$, which also varied by $\pm 5.6\%$. Note that for each detector the maximum uncertainty was considered and no distinction was made between correlated and uncorrelated contributions, see Table B.1. Therefore, this approach gives a rather conservative estimate of the effect on $T_{1/2}^{2\nu}$ and $T_{1/2}^{0\nu\chi(\chi)}$.

The uncertainty on the active volume fraction also plays a role for the shape of the energy spectrum due to ^{42}K decays on the n^+ -surface. Larger f_{act} means thinner n^+ -deadlayer and thus the possibility of an increased contribution from the electrons to the spectrum. For smaller f_{act} and thicker n^+ -deadlayer, their contributions are expected to be reduced. The effect of this change was estimated by repeating the analysis using alternative MC spectra for ^{42}K on the n^+ -surface. For the golden data set, the spectra from MC simulations with the upper and lower limit for f_{act} of ANG3 were used. For the BEGe sum data set, the results of simulations of a BEGe detector with deadlayer thicknesses corresponding to the mass weighted average upper and lower limit for the BEGe detectors, 1.0 mm and 0.7 mm, were used. As described in 8.3.2, a transition layer was considered for the BEGe detectors. The result for $t_{1/2}^{2\nu}$ did not change at all when using the alternative spectra for ^{42}K on the n^+ -surface. The result for $\text{inv}_-t_{1/2}^{0\nu\chi(\chi)}$ changed by $+0.9\%$ for the case of thicker deadlayer and by -5.7% for the case of thinner deadlayer.

The total uncertainty on $t_{1/2}^{2\nu}$ due to the uncertainty on the size of the active volume was $\pm 5.6\%$. The total uncertainty on the 90% quantile for $\text{inv}_-t_{1/2}^{0\nu\chi(\chi)}$ was obtained by summing the single contributions in quadrature, resulting in a total of $^{+5.7}_{-8.0}\%$.

Enrichment fraction The effect of the uncertainty on the enrichment fraction, f_{76} , was estimated in a similar manner as that of the active volume fraction. The only components affected were $2\nu\beta\beta$ and $0\nu\beta\beta\chi(\chi)$. Again, their post-processing was repeated for the cases of maximal and minimal f_{76} for all of the detectors and the resulting spectra were used instead of the standard spectra for the fit model.

The result for $t_{1/2}^{2\nu}$ was altered by $\pm 2.0\%$ for the two cases, whereas the result for $\text{inv-}t_{1/2}^{0\nu\chi(\chi)}$ varied by $\pm 1.7\%$. Also in this case, the estimate can be regarded as a conservative estimate of the systematic uncertainty.

Source positions The source positions were characterized as close, medium distant, and distant, and represented by decays in the holders, the shroud, and the heat-exchanger, respectively. The impact of a change in the representative source positions was estimated for the ^{214}Bi sub-chain decays. For other background components, the effect was expected to be of the same size or smaller. For variations of the close source position, the fit was repeated twice, once replacing the energy spectra from ^{214}Bi sub-chain decays in the holders with those from decays in the mini-shrouds and once by replacing them with those from decays close to the n^+ -surface. In order to estimate the change for variations in the medium distant source position, the fit was repeated with the energy spectra from ^{214}Bi sub-chain decays in the LAr replacing those of the decays in the shroud.

The result for $t_{1/2}^{2\nu}$ did not change for any of the alterations of the model.

The result for $\text{inv-}t_{1/2}^{0\nu\chi(\chi)}$ increased by 12.6% for the case of the decays in the mini-shrouds representing the close source. For the case of the decays on the n^+ -surface representing the close source it decreased by 8.3% . The change in the position of the medium distant source only lead to a small decrease by 1.3% .

Transition layer As discussed in Sec. 8.3.2, for the simulations of ^{42}K on the n^+ -surface of the BEGe detectors, a transition layer was taken into account. The partial charge collection in a part of the deadlayer is also expected to affect the energy spectra from $2\nu\beta\beta$ and $0\nu\beta\beta\chi(\chi)$ by enhancing the number of events in the low energy region. Dedicated studies and simulations were still ongoing during the writing of this thesis, so that no final results could be considered. For a first estimate of the effect, simulations were carried out for GD32D [165] with the same transition layer model that was used for the case of ^{42}K on the n^+ -surface. The outer 40% of the n^+ -layer were assumed completely dead, whereas for the inner 60% a linearly increasing charge collection was considered. A comparison with the simulations for the case of 100% dead n^+ -layer suggested an increase in the detection efficiency in the energy window considered for the fit of 1.7% for $2\nu\beta\beta$ and of 2.0% for $0\nu\beta\beta\chi(\chi)$. As the effect is energy-dependent, the shape of the energy spectra was slightly changed. The increase in efficiency was more pronounced in the low-energy region and decreased with growing energy. In general, an increase in efficiency would lead to a decrease in the half-life estimate. However, due to the change in the spectral shape, also an increase in the half-life is possible as the contribution of $2\nu\beta\beta$ or $0\nu\beta\beta\chi(\chi)$ to the total model might be reduced in the fit, leading to a smaller number of attributed events. The impact of the presence of a transition layer on the final fit results was estimated by recalculating $t_{1/2}^{2\nu}$ and the 90% quantile for $\text{inv-}t_{1/2}^{0\nu\chi(\chi)}$ for a variation of the number of $2\nu\beta\beta$ events by $\pm 1.7\%$ and for a variation of the

number of $0\nu\beta\beta\chi(\chi)$ events by $\pm 2.0\%$ in the BEGe sum data set. The number of events in the golden data set remained unchanged. Both the result for $t_{1/2}^{2\nu}$ and the result for $\text{inv-}t_{1/2}^{0\nu\chi(\chi)}$ varied by $\pm 0.5\%$. No results are available regarding the existence of a transition layer in coaxial detectors. Due to the similarity of the production process it is likely that also in this case such a region of partial charge collection is present. However, the history of the coaxial detectors used in the experiment was different from that of the BEGe detectors. Also, their n^+ -layers were systematically thicker as they grow over time. These differences did not allow to draw any conclusions on the transition layer effects for the coaxial detectors and thus no estimate of the size of a related uncertainty could be included in this analysis.

The total systematic uncertainty deriving from the fit model was determined by summing up in quadrature all individual contributions. For the half-life of $2\nu\beta\beta$, this turned out to be $\pm 6.0\%$. For the limit on the half-life of $0\nu\beta\beta\chi(\chi)$ it amounted to $+21.3\%$ / -11.7% .

As mentioned above, for the case of the active volume and the enrichment fractions, the systematic uncertainty was determined in a rather conservative way. The maximal effect of the single contributions was determined and the final uncertainty was calculated by summing up in quadrature these contributions. A less cautious estimate of the systematic uncertainty could be provided by the use of a sampling method. The fit would have to be repeated many times. For each of the sources of uncertainty listed above, a probability distribution would have to be provided. For every fit, random numbers would be drawn for all sources of uncertainty according to these distributions. This would then be used to define the input to the fit. Correlations could be accounted for by the definition of the probability distributions. The marginalized posterior distributions for $t_{1/2}^{2\nu}$ and $\text{inv-}t_{1/2}^{0\nu\chi(\chi)}$ derived from each individual fit would be summed up to the final posterior probability distributions for $t_{1/2}^{2\nu}$ and $\text{inv-}t_{1/2}^{0\nu\chi(\chi)}$. As these final posterior distributions would already incorporate not only the statistical but also the systematic uncertainties, they would provide directly access to the final results. However, this approach is very time-consuming and could not be implemented in the time-frame of this thesis. It will be adopted for a future iteration of this analysis. Estimates based on the results presented in Appendix B suggest a reduction of the systematic uncertainties on $t_{1/2}^{2\nu}$ and $\text{inv-}t_{1/2}^{0\nu\chi(\chi)}$ of the order of $(1 - 2)\%$ of the mode and 90% quantile, respectively, if the systematic uncertainty is determined with the alternative method.

10.3.2 MC Simulation

The sources of uncertainty due to the MC simulation were two-fold.

MC geometry The setup of the GERDA experiment was implemented in the MC framework. However, some small details might not be accounted for. One example is the implementation of the detectors, which does not take into account the

rounding of the detector corners. This leads to a 0.6% difference in the total mass of the coaxial detectors, when comparing MC to the real experiment. Furthermore, some variations in the dimensions or placement of experimental components might be present. An extensive study on the impact of these imprecisions had been carried out for the analysis described in Appendix B. The uncertainty on $T_{1/2}^{2\nu}$ had been evaluated to be 1.0%. This was assumed to be a good estimate also for the uncertainty on $T_{1/2}^{0\nu\chi(\chi)}$.

MC tracking This item considered the uncertainties on cross-sections and final states, which are relevant for the simulated particle interactions with matter. They mainly affect the propagation of photons and thus have a larger effect on the background components than on the simulation of $2\nu\beta\beta$ and $0\nu\beta\beta\chi(\chi)$. From validations of the GEANT4 particle tracking for electromagnetic processes in the energy range relevant for γ -ray spectroscopy [171–173], this uncertainty was deduced to be 2%.

10.3.3 Data Acquisition and Selection

The uncertainty due to data acquisition and selection was expected to be very small. As possible sources, the calculation of the live time as well as reconstruction and trigger efficiencies had to be considered. Another uncertainty arises from the fact that unphysical events might be present in the data sets. In total, the impact of this component was expected to be not larger than 0.5% for both $T_{1/2}^{2\nu}$ as well as for $T_{1/2}^{0\nu\chi(\chi)}$.

10.3.4 Total Systematic Uncertainty

Systematic uncertainty on $T_{1/2}^{2\nu}$

The single contributions to the systematic uncertainty for $t_{1/2}^{2\nu}$ are listed in Table 10.1. The precision of the measurement was limited by the uncertainty on the active volume fractions of the coaxial detectors. Eventhough the systematic uncertainty might be slightly reduced, if determined with the alternative method described above, this uncertainty will still be the limiting factor. This fact provides the possibility to improve the precision of the measurement of $T_{1/2}^{2\nu}$ without the need to accumulate new data sets, but simply by performing more precise measurements of the active mass fractions of the coaxial detectors.

The total systematic uncertainty was obtained by summing in quadrature the individual contributions. For $t_{1/2}^{2\nu}$, this lead to $\pm 6.4\%$, corresponding to a systematic uncertainty of $\pm 0.13 \cdot 10^{21}$ yr on $T_{1/2}^{2\nu}$.

Systematic uncertainty on the limits for $T_{1/2}^{0\nu\chi(\chi)}$

The total systematic uncertainty on the 90% quantile for $\text{inv-}t_{1/2}^{0\nu\chi(\chi)}$, obtained by summing in quadrature the single contributions listed in Table 10.1, turned out to

Table 10.1: Systematic uncertainties on $T_{1/2}^{2\nu}$ and the 90 % quantile for $1/T_{1/2}^{0\nu\chi(\chi)}$, which are not included in the fitting procedure.

Item	Uncertainty on $T_{1/2}^{2\nu}$ (%)	Uncertainty on $1/T_{1/2}^{0\nu\chi(\chi)}$ (% on 90 % quantile)
Screening results	–	+0.5 –1.3
Binning	± 0.5	+16.1
Active volume fraction	± 5.6	+5.7 –8.0
Enrichment fraction	± 2.0	± 1.7
Source positions	–	+12.6 –8.3
Transition layer	± 0.5	± 0.5
Total fit model	± 6.0	+21.3 –11.7
MC geometry	± 1.0	± 1.0
MC tracking	± 2.0	± 2.0
Total MC simulation	± 2.2	± 2.2
Data acquisition and selection	± 0.5	± 0.5
Total systematic uncertainty	± 6.4	+21.4 –12.0

be ${}_{-12.0}^{+21.4}\%$. Again, as already seen for the case of $T_{1/2}^{2\nu}$, the uncertainty on the active volume fractions was a major contribution to the total uncertainty on the limits for $T_{1/2}^{0\nu\chi(\chi)}$. However, in this case it was not the dominating uncertainty. Instead, the largest source of uncertainty was the composition of the fit model and the individual background contributions. This becomes obvious from the fact that the most important changes in the result were observed for the case of a fit with increased bin size for the energy spectra and for changes in the position of the background sources.

As already mentioned above, for the case of large bin size, the power to distinguish between background components and the $0\nu\beta\beta\chi(\chi)$ spectrum was reduced significantly. This was due to the fact that structures deriving from photon peaks in the background spectra were washed out, leading to an ambiguity between the background and the $0\nu\beta\beta\chi(\chi)$ spectra.

Variations in the source position of a background source, on the other hand, lead to small changes in the shape of the corresponding energy spectrum. A little relative variation of one of the background contributions can have a large impact on the contribution from $0\nu\beta\beta\chi(\chi)$ due to its small size compared to the background contributions. This effect was also observed for the variation in the ${}^{42}\text{K}$ spectrum from decays on the n^+ -surface for minimum deadlayer thickness, which provoked a large change in the result for $T_{1/2}^{0\nu\chi(\chi)}$.

In summary, the most important restriction of the sensitivity to $0\nu\beta\beta\chi(\chi)$ derived from the uncertainties on the background composition. Therefore, in order to reach a

significant improvement in future analyses, the background needs to be known with an even higher precision, necessitating a complete and detailed screening campaign of all components used in the experimental setup. Also, an increase of the exposure and a decrease of the BI would allow to improve the precision of the measurement. The latter might be achieved by the use of PSA methods, which would have to be implemented also for the MC simulations.

In order to take into account the systematic uncertainty when determining the final results for the limits on $T_{1/2}^{0\nu\chi(\chi)}$, the distribution describing the systematic uncertainties had to be folded in the posterior probability distributions for $\text{inv-}t_{1/2}^{0\nu\chi(\chi)}$. This distribution was composed by two normal distributions with widths corresponding to the positive and negative part of the systematic uncertainty, respectively. The asymmetric function is shown in the inset in Fig. 10.4. The mean value of the distribution was $\mu = 1$. In order to fold this function in the posterior probability distribution of $\text{inv-}t_{1/2}^{0\nu\chi(\chi)}$, for each entry in the posterior distribution (that is for the result for $\text{inv-}t_{1/2}^{0\nu\chi(\chi)}$ at each step of the MCMC), p , a random number, r , was drawn from the systematic uncertainty distribution. A new histogram was filled with the product $p \cdot r$. This represented the final posterior probability distribution, comprising the statistical and systematic uncertainties. The final result for $\text{inv-}t_{1/2}^{0\nu\chi(\chi)}$, from which the limit on $T_{1/2}^{0\nu\chi(\chi)}$ was deduced, was determined as the 90% quantile of this distribution. For the mode with $n = 1$, this final distribution is depicted in Fig. 10.4. For the cases of $n = 2, 3$ and 7 , the same systematic uncertainty distribution was used. Their final posterior probability distributions are shown in Appendix C.

10.4 Final Results and Discussion

10.4.1 Results for $2\nu\beta\beta$

The final result for the measurement of $T_{1/2}^{2\nu}$ of ${}^{76}\text{Ge}$ was determined to be

$$T_{1/2}^{2\nu} = (1.96 \pm 0.03_{\text{fit}} \pm 0.13_{\text{syst}}) \cdot 10^{21} \text{ yr} = (1.96 \pm 0.13) \cdot 10^{21} \text{ yr}, \quad (10.15)$$

combining the fit and systematic uncertainty in quadrature.

Due to the extremely low background level in the GERDA experiment, allowing a signal-to-background ratio of 3 : 1, the half-life of $2\nu\beta\beta$ of ${}^{76}\text{Ge}$ was measured with a precision unprecedented by previous experiments [4]. A total exposure of $20.3 \text{ kg} \cdot \text{yr}$ was sufficient to reduce the fit error to 1.5%.

Figure 10.5 shows a summary of the most recent measurements of $T_{1/2}^{2\nu}$. Shown are nine measurements from experiments prior to the GERDA experiment and two weighted averages. Clearly, a trend towards longer half-life over time is visible. This is likely due to the always improving signal-to-background ratio, which lessens the impact of the chosen background model. Also shown are the results of the official GERDA analysis presented in Appendix B and of the present analysis. Both results are

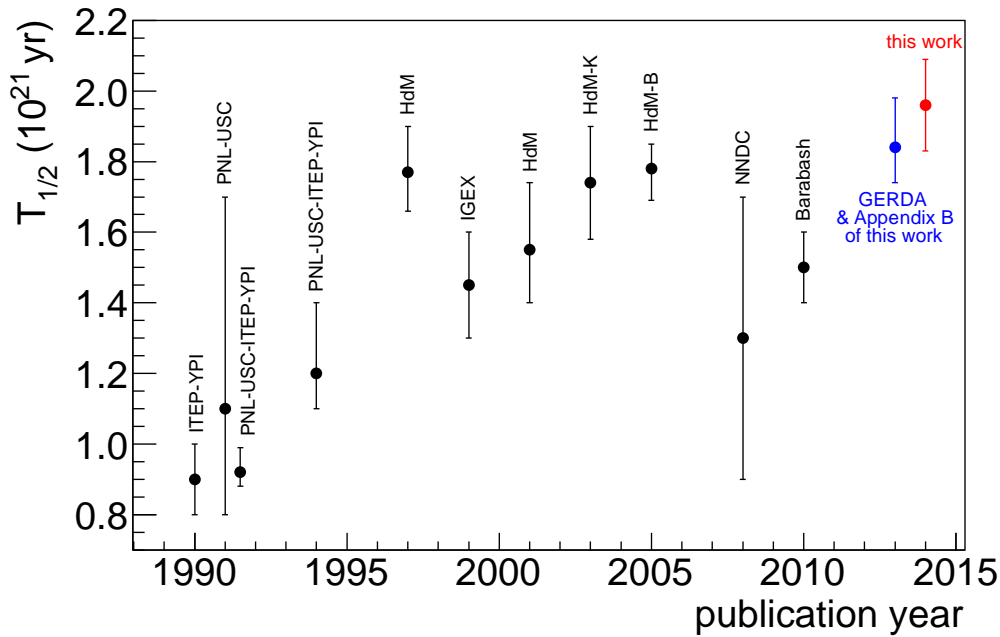


Figure 10.5: Results of measurements of $T_{1/2}^{2\nu}$ of ^{76}Ge as a function of the publication year. Shown are the results from ITEP-YPI [174], PNL-USC (natGe) [175], PNL-USC-ITEP-YPI [176, 177], HdM [4, 105] and IGEX [178, 179], from the re-analysis of the HdM data by Klapdor-Kleingrothaus et al. [180] (HdM-K) and by Bakalyarov et al. [181] (HdM-B). The NNDC-recommended value [182] and the global weighted average evaluated by Barabash [183] are also shown. The first result from GERDA Phase I data, published in [86] and described in Appendix B, and the result from the analysis described in this chapter are also given. Graphic based on [86].

in good agreement. Due to the small exposure of the data set, the systematic uncertainty of the former result had been dominated by possible unidentified background sources. The larger exposure of the present analysis allowed the determination of a complete background model. The uncertainty due to the model contributions was already comprised in the fit uncertainty and much reduced compared to the previous case. As the larger data set allowed to clearly establish the presence of the formerly only suspected additional background sources, the result for $T_{1/2}^{2\nu}$ was higher. This had been anticipated by the estimate of the systematic uncertainty in the first analysis.

Using Equation (3.2) and the phase space factors calculated in [184], the nuclear matrix element deriving from the new result for $T_{1/2}^{2\nu}$, given in Equation (10.15), was calculated. It resulted in $|M^{2\nu}| = (0.129 \pm 0.004) \text{MeV}^{-1}$. The nuclear matrix element can also be estimated from charge exchange reactions. The most recent studies for $(d, ^2\text{He})$ result in $(0.159 \pm 0.023) \text{MeV}^{-1}$ [185], whereas the analysis of the reaction $(^3\text{He}, t)$ gives $(0.23 \pm 0.07) \text{MeV}^{-1}$ [186]. Both results seem to be slightly higher than the one deduced in this work. All values agree within 2σ .

Table 10.2: Results for the limits on $T_{1/2}^{0\nu\chi(\chi)}$ of ^{76}Ge for the majoron models introduced in Sec. 3.3. Also given are the resulting limits on the effective coupling constants, $\langle g \rangle$. All limits correspond to the 90% quantiles. For the case of $n = 1$, the nuclear matrix element, $M^{0\nu\chi(\chi)}$, from [187–193] and the phase space factor, $G^{0\nu\chi(\chi)}$, from [56] were used for the calculation of $\langle g \rangle$. The given range covers the variations of $M^{0\nu\chi(\chi)}$ in these works. For $n = 3$ and 7, $\langle g \rangle$ was determined using the matrix elements and phase space factors from [82]. The results for $0\nu\beta\beta\chi\chi$ ($n = 3, 7$) account for the uncertainty on $M^{0\nu\chi(\chi)}$.

Model	Mode	n	$T_{1/2}^{0\nu\chi(\chi)}$ (10^{23} yr)	$M^{0\nu\chi(\chi)}$	$G^{0\nu\chi(\chi)}$ (yr^{-1})	$\langle g \rangle$
IB	χ	1	> 4.15	(2.30 – 5.82)	$5.86 \cdot 10^{-17}$	$< (3.5 - 8.8) \cdot 10^{-5}$
IC	χ	1	> 4.15	(2.30 – 5.82)	$5.86 \cdot 10^{-17}$	$< (3.5 - 8.8) \cdot 10^{-5}$
ID	$\chi\chi$	3	> 0.89	$10^{-3\pm 1}$	$6.32 \cdot 10^{-19}$	$< 2.1^{+4.4}_{-1.4}$
IE	$\chi\chi$	3	> 0.89	$10^{-3\pm 1}$	$6.32 \cdot 10^{-19}$	$< 2.1^{+4.4}_{-1.4}$
IF (bulk)	χ	2	> 1.82	–	–	–
IIB	χ	1	> 4.15	(2.30 – 5.82)	$5.86 \cdot 10^{-17}$	$< (3.5 - 8.8) \cdot 10^{-5}$
IIC	χ	3	> 0.89	0.16	$2.07 \cdot 10^{-19}$	$< 4.6 \cdot 10^{-2}$
IID	$\chi\chi$	3	> 0.89	$10^{-3\pm 1}$	$6.32 \cdot 10^{-19}$	$< 2.1^{+4.4}_{-1.4}$
IIE	$\chi\chi$	7	> 0.33	$10^{-3\pm 1}$	$1.21 \cdot 10^{-18}$	$< 2.2^{+4.9}_{-1.4}$
IIF	χ	3	> 0.89	0.16	$2.07 \cdot 10^{-19}$	$< 4.6 \cdot 10^{-2}$

10.4.2 Results for $0\nu\beta\beta\chi(\chi)$

The lower limits on $T_{1/2}^{0\nu\chi(\chi)}$ were determined from the 90% quantiles of the posterior probability distributions for $\text{inv-}t_{1/2}^{0\nu\chi(\chi)}$ after folding in the systematic uncertainties. The final results are listed in Table 10.2 for the different majoron models introduced in Sec. 3.3.

The limits on $T_{1/2}^{0\nu\chi(\chi)}$ presented here are the most stringent limits obtained to date for ^{76}Ge . The limits for $n = 1$ and $n = 3$ were improved by more than a factor six [4], the limit for $n = 7$ was improved by a factor five [95] compared to previous measurements. The limit for the mode with $n = 2$ was measured for the first time.

From the lower limits on $T_{1/2}^{0\nu\chi(\chi)}$, the upper limits on the effective neutrino-majoron coupling constants $\langle g \rangle$ for the models with $n = 1, 3$ and 7 were calculated using Equations (3.8) and (3.9). The matrix element for the case of $n = 1$, $M_F - M_{GT}$, was taken from [187–193], whereas the phase space factor, $G^{0\nu\chi}$, was that of [56]. The matrix element M_{CR} for the case of $0\nu\beta\beta\chi$ with $n = 3$ and $M_{Fw^2} - M_{GTw^2}$ for the cases of $0\nu\beta\beta\chi\chi$ with $n = 3$ and $n = 7$, as well as the corresponding phase space factors were taken from [82]. The results for the upper limits on $\langle g \rangle$ are also shown in Table 10.2.

The coupling constants allow a comparison with other isotopes. The best limits

on $0\nu\beta\beta\chi(\chi)$ decay of isotopes other than ^{76}Ge have been obtained for ^{100}Mo [83] and ^{136}Xe [92], as shown in Table 4.2. When comparing with the case of ^{100}Mo , it becomes obvious that the limits on $T_{1/2}^{0\nu\chi(\chi)}$ determined in the present analysis were about one order of magnitude more stringent, for the case of $n = 7$ even two orders of magnitude. However, due to the differences in the matrix elements and the phase space factors, the resulting limits on $\langle g \rangle$ from ^{100}Mo and ^{76}Ge are comparable. The limits for $\langle g \rangle$ derived from ^{136}Xe result to be a factor two to five lower due to the higher limits that had been measured for $T_{1/2}^{0\nu\chi(\chi)}$.

Chapter 11

Neutrinoless Double Beta Decay in GERDA Phase I

The energy spectrum in the *ROI* around $Q_{\beta\beta}$ was analyzed for the golden, silver, and BEGe sum data set. Two different statistical approaches were adopted for the analysis. One envisaged the counting method described in [194], the other one used the spectral fit method presented in [166]. For both methods, no indications for contributions from $0\nu\beta\beta$ were found and lower limits on $T_{1/2}^{0\nu}$ of ^{76}Ge were established.

11.1 Statistical Analysis Method

When analyzing the data spectrum in the *ROI* around $Q_{\beta\beta}$, two different hypotheses can be made. In the first case, hypothesis H , one assumes that all counts are due exclusively to background processes and that $0\nu\beta\beta$ does not contribute to the spectrum. In the second case, hypothesis \bar{H} , the assumption is made that the contributions in the energy spectrum derive from background sources as well as from $0\nu\beta\beta$. In a first step, it has to be determined which hypothesis is preferred by the data. If the probability of \bar{H} is larger than a predefined threshold, in a second step an estimate of $T_{1/2}^{0\nu}$ can be given. In the opposite case, a lower limit can be set.

For the analysis of the GERDA Phase I data, different statistical approaches are possible. In the following, an analysis using the counting method described in [194], as well as an analysis using a binned maximum likelihood fit as suggested in [166] are presented. The former method will be referred to as *Counting Method*, whereas the latter approach will be referred to as *Spectral Fit*.

11.1.1 Counting Method

When adapting the counting method, the number of observed events in a small window around $Q_{\beta\beta}$, the *region of interest (ROI)*, is counted. Assuming the validity of H , the probability to observe x_d events in the *ROI* for data set d when ξ_d events are

expected from background, $P(x_d|\xi_d, H)$, is

$$P(x_d|\xi_d, H) = \frac{e^{-\xi_d} \xi_d^{x_d}}{x_d!}. \quad (11.1)$$

If instead \bar{H} is assumed to hold, the probability to observe x_d events has to be calculated taking into account not only the number of expected background events, ξ_d , but also the number of expected signal events, that is events due to $0\nu\beta\beta$, ω_d ,

$$P(x_d|\xi_d, \omega_d, \bar{H}) = \frac{e^{-(\xi_d+\omega_d)} (\xi_d + \omega_d)^{x_d}}{x_d!}. \quad (11.2)$$

For the case of D data sets, the combined likelihoods, $P(\mathbf{x}|\xi, H)$ and $P(\mathbf{x}|\xi, \omega, \bar{H})$, for the set of observed counts $\mathbf{x} = (x_1, x_2, \dots, x_D)$ and the sets of expected counts for the background, $\xi = (\xi_1, \xi_2, \dots, \xi_D)$, and for the signal, $\omega = (\omega_1, \omega_2, \dots, \omega_D)$, are obtained as the product of the individual probabilities for the single data sets,

$$P(\mathbf{x}|\xi, H) = \prod_{d=1}^D P(x_d|\xi_d, H) \quad (11.3)$$

and

$$P(\mathbf{x}|\xi, \omega, \bar{H}) = \prod_{d=1}^D P(x_d|\xi_d, \omega_d, \bar{H}). \quad (11.4)$$

Using Bayes' theorem, the probability for H given the observations \mathbf{x} becomes

$$P(H|\mathbf{x}) = \frac{P(\mathbf{x}|H)P_0(H)}{P(\mathbf{x}|H)P_0(H) + P(\mathbf{x}|\bar{H})P_0(\bar{H})} \quad (11.5)$$

and the probability for \bar{H} given \mathbf{x} becomes

$$P(\bar{H}|\mathbf{x}) = \frac{P(\mathbf{x}|\bar{H})P_0(\bar{H})}{P(\mathbf{x}|H)P_0(H) + P(\mathbf{x}|\bar{H})P_0(\bar{H})}, \quad (11.6)$$

with the prior probabilities $P_0(H)$ and $P_0(\bar{H})$ for H and \bar{H} , respectively. It holds that $P(H|\mathbf{x}) + P(\bar{H}|\mathbf{x}) = 1$, as well as $P_0(H) + P_0(\bar{H}) = 1$. The probabilities $P(\mathbf{x}|H)$ and $P(\mathbf{x}|\bar{H})$ are obtained by integrating over all possibilities for the expected number of background or background and signal events, respectively,

$$P(\mathbf{x}|H) = \int P(\mathbf{x}|\xi, H)P_0(\xi) d\xi \quad (11.7)$$

and

$$P(\mathbf{x}|\bar{H}) = \int \left[\int P(\mathbf{x}|\xi, \omega, \bar{H})P_0(\xi) d\xi \right] P_0(\omega) d\omega. \quad (11.8)$$

In Chapter 9 it was shown, that for all GERDA Phase I data sets the background in the ROI could be approximated by a constant. In this case, the number of expected

background events, ξ_d , for data set d can be expressed as the product of the exposure of the data set, \mathcal{E}_d , its background index, BI_d , and the width of the window in which the events were counted, ROI_d ,

$$\xi_d = \mathcal{E}_d \cdot BI_d \cdot ROI_d. \quad (11.9)$$

The parameters determined in the fit were the background indices, BI_d .

In general, the number of observed $0\nu\beta\beta$ events, $N_{obs}^{0\nu}$, is connected to the half-life via

$$T_{1/2}^{0\nu} = \frac{\ln(2) \cdot N_A}{m_{76}} \cdot \frac{1}{N_{obs}^{0\nu}} \cdot \mathcal{E} \cdot \epsilon, \quad (11.10)$$

with Avogadro's number N_A , $m_{76} = 75.95$ g/mol the molar mass of ^{76}Ge , \mathcal{E} the exposure, and ϵ the total signal detection efficiency. Therefore, for the fitting procedure, the number of expected signal events for data set d , could be expressed as

$$\omega_d = \text{inv}_-t_{1/2}^{0\nu} \cdot \kappa_0 \cdot \mathcal{E}_d \cdot \langle \epsilon \rangle_d \cdot \epsilon_{PSA,d} \cdot \epsilon_{ROI,d}, \quad (11.11)$$

with $\text{inv}_-t_{1/2}^{0\nu}$ the inverse of the half-life of $0\nu\beta\beta$ in units of 10^{25} yr and $\kappa_0 = (\ln(2) \cdot N_A)/(m_{76} \cdot 10^{25} \text{ yr}) = 0.549$ (kg·yr) $^{-1}$ the decay rate due to $0\nu\beta\beta$ for 1 kg of germanium enriched to 100 % in ^{76}Ge for $T_{1/2}^{0\nu} = 10^{25}$ yr. The detection efficiency, $\langle \epsilon \rangle_d$, accounts for the active volume fractions, the enrichment fractions, and the efficiencies for detecting the full energy peak. The efficiency factor $\epsilon_{PSA,d}$ gives the signal acceptance after the application of pulse shape analysis (PSA) methods, and $\epsilon_{ROI,d}$, defined as

$$\epsilon_{ROI,d} = \int_{Q_{\beta\beta} - ROI_d/2}^{Q_{\beta\beta} + ROI_d/2} \frac{1}{\sqrt{2\pi}\sigma_d} e^{-\frac{(E - Q_{\beta\beta})^2}{2\sigma_d^2}} dE, \quad (11.12)$$

is a function of ROI_d and $\sigma_d = 1/(2\sqrt{2\ln(2)}) \cdot \text{FWHM}_d$ and corrects the expected number of signal events for the fraction of events expected outside the ROI . The parameter determined in the fit was $\text{inv}_-t_{1/2}^{0\nu}$, which was in common to all D data sets.

Using the above, the combined likelihood for the case that \bar{H} is true, defined in Equation (11.4), can be expressed as a function of $\text{inv}_-t_{1/2}^{0\nu}$ and the set of background indices $\mathbf{BI} = (BI_1, BI_2, \dots, BI_D)$,

$$P(\mathbf{x}|\xi, \omega, \bar{H}) = P(\mathbf{x}|\mathbf{BI}, \text{inv}_-t_{1/2}^{0\nu}, \bar{H}). \quad (11.13)$$

In the following, the condition \bar{H} has been dropped from all expressions, as its validity is implicit. With Bayes' theorem, the global posterior probability can be written as

$$P(\mathbf{BI}, \text{inv}_-t_{1/2}^{0\nu}|\mathbf{x}) = \frac{P(\mathbf{x}|\mathbf{BI}, \text{inv}_-t_{1/2}^{0\nu})P_0(\mathbf{BI})P_0(\text{inv}_-t_{1/2}^{0\nu})}{\int \left[\int P(\mathbf{x}|\mathbf{BI}, \text{inv}_-t_{1/2}^{0\nu})P_0(\mathbf{BI}) d\mathbf{BI} \right] P_0(\text{inv}_-t_{1/2}^{0\nu}) d\text{inv}_-t_{1/2}^{0\nu}}. \quad (11.14)$$

Marginalization with respect to $\text{inv}_-t_{1/2}^{0\nu}$,

$$P(\text{inv}_-t_{1/2}^{0\nu}|\mathbf{x}) = \int P(\mathbf{BI}, \text{inv}_-t_{1/2}^{0\nu}|\mathbf{x}) d\mathbf{BI}, \quad (11.15)$$

allows to extract an estimate for $\text{inv}_-t_{1/2}^{0\nu}$ in case \bar{H} is more likely than H . For the contrary case, Equation (11.15) can be used to extract a lower limit on $\text{inv}_-t_{1/2}^{0\nu}$.

11.1.2 Spectral Fit

The statistical analysis adopted in case of a spectral fit is a binned maximum likelihood approach similar to the one described in Sec. 9.1. If H holds, the probability $P(\mathbf{n}_d|\boldsymbol{\lambda}_d, H)$ for the observed data spectrum, \mathbf{n}_d , for data set d given a certain expectation for the background spectrum, $\boldsymbol{\lambda}_d$, can be written as the product of the probabilities of the single bins, $P(n_{i,d}|\lambda_{i,d}, H)$,

$$P(\mathbf{n}_d|\boldsymbol{\lambda}_d, H) = \prod_i P(n_{i,d}|\lambda_{i,d}, H) = \prod_i \frac{e^{-\lambda_{i,d}} \lambda_{i,d}^{n_{i,d}}}{n_{i,d}!}. \quad (11.16)$$

The expected number of events in the i -th bin of the background spectrum for data set d is denoted with $\lambda_{i,d}$, whereas $n_{i,d}$ is the number of events in the i -th bin of the measured spectrum of data set d . For the case in which \bar{H} is valid, also contributions from $0\nu\beta\beta$ have to be taken into account. With \mathbf{v}_d the expectation for the signal spectrum in data set d and $v_{i,d}$ the expected number of signal events in the i -th bin, the conditional probability for the data becomes

$$P(\mathbf{n}_d|\boldsymbol{\lambda}_d, \mathbf{v}_d, \bar{H}) = \prod_i P(n_{i,d}|\lambda_{i,d}, v_{i,d}, \bar{H}) = \prod_i \frac{e^{-(\lambda_{i,d}+v_{i,d})} (\lambda_{i,d} + v_{i,d})^{n_{i,d}}}{n_{i,d}!}. \quad (11.17)$$

When the information of D data sets is combined, the likelihoods $P(\mathbf{N}|\boldsymbol{\Lambda}, H)$ and $P(\mathbf{N}|\boldsymbol{\Lambda}, \boldsymbol{\Upsilon}, \bar{H})$ for the set of data spectra $\mathbf{N} = (\mathbf{n}_1, \mathbf{n}_2, \dots, \mathbf{n}_D)$ and the sets of expected background and signal spectra, $\boldsymbol{\Lambda} = (\boldsymbol{\lambda}_1, \boldsymbol{\lambda}_2, \dots, \boldsymbol{\lambda}_D)$ and $\boldsymbol{\Upsilon} = (\mathbf{v}_1, \mathbf{v}_2, \dots, \mathbf{v}_D)$, are calculated as the product of the individual probabilities,

$$P(\mathbf{N}|\boldsymbol{\Lambda}, H) = \prod_{d=1}^D P(\mathbf{n}_d|\boldsymbol{\lambda}_d, H) \quad (11.18)$$

and

$$P(\mathbf{N}|\boldsymbol{\Lambda}, \boldsymbol{\Upsilon}, \bar{H}) = \prod_{d=1}^D P(\mathbf{n}_d|\boldsymbol{\lambda}_d, \mathbf{v}_d, \bar{H}). \quad (11.19)$$

With Bayes's theorem and given a set of measured energy spectra, \mathbf{N} , the probability for H can be calculated as

$$P(H|\mathbf{N}) = \frac{P(\mathbf{N}|H)P_0(H)}{P(\mathbf{N}|H)P_0(H) + P(\mathbf{N}|\bar{H})P_0(\bar{H})}, \quad (11.20)$$

whereas the probability for \bar{H} is defined by

$$P(\bar{H}|\mathbf{N}) = \frac{P(\mathbf{N}|\bar{H})P_0(\bar{H})}{P(\mathbf{N}|H)P_0(H) + P(\mathbf{N}|\bar{H})P_0(\bar{H})}. \quad (11.21)$$

Also in this case, the prior probabilities and the posterior probabilities, respectively, sum up to unity, $P_0(H) + P_0(\bar{H}) = 1$ and $P(H|\mathbf{N}) + P(\bar{H}|\mathbf{N}) = 1$. The probabilities

$P(\mathbf{N}|H)$ and $P(\mathbf{N}|\bar{H})$ are determined by the integral over all possible configurations for Λ and Υ ,

$$P(\mathbf{N}|H) = \int P(\mathbf{N}|\Lambda, H)P_0(\Lambda) d\Lambda \quad (11.22)$$

and

$$P(\mathbf{N}|\bar{H}) = \int \left[\int P(\mathbf{N}|\Lambda, \Upsilon, \bar{H})P_0(\Lambda) d\Lambda \right] P_0(\Upsilon) d\Upsilon. \quad (11.23)$$

The analysis was confined to the window between 1930 keV and 2190 keV and the ± 5 keV regions around the background peaks at 2104 keV and 2119 keV were excluded from the analysis. Approximating the spectral shape of the background in this range with a constant, as suggested in Chapter 9, leads to

$$\lambda_{i,d} = \mathcal{E}_d \cdot BI_d \cdot \Delta E_{i,d} \quad (11.24)$$

for the number of expected background events in the i -th bin of data set d , with \mathcal{E}_d the exposure of the data set, BI_d its background index, and $\Delta E_{i,d}$ the width of the i -th bin. The background indices, BI_d , were the parameters determined in the fit.

With Equation (11.10) and the definitions of Equation (11.11), the number of expected signal events in the i -th bin of data set d can be written as

$$\nu_{i,d} = \text{inv}_{-t_{1/2}^{0v}} \cdot \kappa_0 \cdot \mathcal{E}_d \cdot \langle \varepsilon \rangle_d \cdot \varepsilon_{PSA,d} \cdot \int_{\Delta E_{i,d}} f_d^{0v}(E) dE. \quad (11.25)$$

The normalized functional form of the signal shape, $f_d^{0v}(E)$, is given by a Gaussian peak with standard deviation $\sigma_d = 1/(2\sqrt{2\ln(2)}) \cdot \text{FWHM}_d$ and mean $\mu = Q_{\beta\beta}$,

$$f_d^{0v}(E) = \frac{1}{\sqrt{2\pi}\sigma_d} e^{-\frac{(E-\mu)^2}{2\sigma_d^2}} \quad (11.26)$$

and $\int_{\Delta E_{i,d}} f_d^{0v}(E) dE$ gives the fraction of the signal spectrum in the i -th bin of data set d . The parameter $\text{inv}_{-t_{1/2}^{0v}}$, in common to all data sets, was determined in the fit.

In analogy to Equation (11.13), the above defined expressions for $\lambda_{i,d}$ and $\nu_{i,d}$ can be used to express $P(\mathbf{N}|\Lambda, \Upsilon, \bar{H})$ from Equation (11.19) in terms of $\text{inv}_{-t_{1/2}^{0v}}$ and the set of background indices, $\mathbf{BI} = (BI_1, BI_2, \dots, BI_D)$,

$$P(\mathbf{N}|\Lambda, \Upsilon, \bar{H}) = P(\mathbf{N}|\mathbf{BI}, \text{inv}_{-t_{1/2}^{0v}}, \bar{H}). \quad (11.27)$$

Omitting the explicit writing of \bar{H} , the global posterior probability is defined as

$$P(\mathbf{BI}, \text{inv}_{-t_{1/2}^{0v}}|\mathbf{N}) = \frac{P(\mathbf{N}|\mathbf{BI}, \text{inv}_{-t_{1/2}^{0v}})P_0(\mathbf{BI})P_0(\text{inv}_{-t_{1/2}^{0v}})}{\int \left[\int P(\mathbf{N}|\mathbf{BI}, \text{inv}_{-t_{1/2}^{0v}})P_0(\mathbf{BI}) d\mathbf{BI} \right] P_0(\text{inv}_{-t_{1/2}^{0v}}) d\text{inv}_{-t_{1/2}^{0v}}}. \quad (11.28)$$

Integrating over all possibilities for \mathbf{BI} gives the marginalized posterior probability distribution for $\text{inv}_{-}t_{1/2}^{0\nu}$,

$$P(\text{inv}_{-}t_{1/2}^{0\nu}|\mathbf{N}) = \int P(\mathbf{BI}, \text{inv}_{-}t_{1/2}^{0\nu}|\mathbf{N}) d\mathbf{BI}. \quad (11.29)$$

From this, an estimate or lower limit for $\text{inv}_{-}t_{1/2}^{0\nu}$ can be deduced for the case that H or \bar{H} is valid, respectively.

11.1.3 Common Definitions

The fitting procedures for both the counting method and the spectral fit were performed within the Bayesian analysis toolkit BAT [150]. The data was divided into three data sets, the golden, the silver, and the BEGe sum data set, as defined in Sec. 7.4.

For both statistical methods, in a first step hypothesis H was adopted, and in a second step the validity of \bar{H} was assumed.

In case of the counting method, the prior probabilities on BI_d were defined as Poissonian distributions with mean according to the background index after the application of PSA, BI_d^{PSA} , given in Table 11.2. For the spectral fit, the information from the background region was used in the fit. This did not allow a Poissonian prior based on the knowledge about BI_d^{PSA} , since in this case the same information would have been used twice, once for the fit and once for the definition of the prior probabilities. Therefore, for the spectral fit, uninformative prior probabilities on BI_d , defined as flat distributions between zero and 1 cts/(keV · kg · yr), were chosen.

For $\text{inv}_{-}t_{1/2}^{0\nu}$, a flat prior distribution between zero and ten was chosen, corresponding to $T_{1/2}^{0\nu} > 10^{24}$ yr. Since previous measurements suggest lower limits on $T_{1/2}^{0\nu}$ well above 10^{24} yr [4, 5], the prior distribution could be regarded as uninformative.

In order to determine, which of the two hypotheses was more likely, the *Bayes' factor* (BF) was used. It allows to measure the plausibility of one hypothesis compared to another based on the observed data. For the counting method, the Bayes' factor is defined as

$$BF = \frac{P(\mathbf{x}|\bar{H})}{P(\mathbf{x}|H)}, \quad (11.30)$$

with $P(\mathbf{x}|H)$ and $P(\mathbf{x}|\bar{H})$ given by Equations (11.7) and (11.8).

For the spectral fit, it is determined by

$$BF = \frac{P(\mathbf{N}|\bar{H})}{P(\mathbf{N}|H)}, \quad (11.31)$$

with $P(\mathbf{N}|H)$ and $P(\mathbf{N}|\bar{H})$ defined in Equations (11.22) and (11.23). In practice, the BF was calculated directly using a function provided by BAT. The prior probabilities for the two hypotheses were assumed equal, $P_0(H) = P_0(\bar{H}) = 0.5$, for both statistical approaches.

Using the scale given by Harold Jeffreys [195], if $BF < 1$, the data clearly supports hypothesis H , whereas for $BF > 100$, there is decisive evidence for the validity of \bar{H} .

As an *a priori* criterion for the present analysis it was decided, that for $BF < 1$, \bar{H} would be rejected and a lower limit for $T_{1/2}^{0\nu}$ had to be determined. For $BF > 100$, on the other hand, \bar{H} would be accepted and an estimate for the value of $T_{1/2}^{0\nu}$ was calculated. For $1 \leq BF \leq 100$, the data would not allow a decisive conclusion.

After the validity of either one of the two hypotheses was established for both statistical approaches, the half-life or lower limit on the half-life of $0\nu\beta\beta$ had to be estimated from the marginalized posterior probability distribution of $\text{inv}_-t_{1/2}^{0\nu}$, defined by Equation (11.15) and (11.29), respectively. As explained in Section 9.1, the marginalized posterior probability distributions were obtained by normalizing the frequency distributions of $\text{inv}_-t_{1/2}^{0\nu}$ to the number of Markov Chain Monte Carlo (MCMC) steps used to obtain the fit results. From these distributions, the marginalized mode and smallest interval of 68% probability was calculated for the case that \bar{H} was valid. For the case that \bar{H} could not be confirmed, the 90% quantile was determined.

11.2 Pulse Shape Analysis

As mentioned in Chapter 5, a reduction of the background can be achieved by means of pulse shape analysis (PSA). Such PSA algorithms were developed for the coaxial and the BEGe detectors employed in the first phase of the GERDA experiment and used for the search for $0\nu\beta\beta$ described in the following. The PSA methods are described in detail in [125] and references therein. Their main characteristics and results are summarized here.

Note that all PSA algorithms were developed prior to the unblinding of the data in order to avoid biasing and no changes were applied after the unblinding procedure. All PSA methods aim at the separation of multi-site events (MSE) from single-site events (SSE), as in the search for $0\nu\beta\beta$ the signal events are almost exclusively of the SSE type, whereas most background events are due to Compton-scattered photons and therefore of the MSE type. It is important to take care that the reduction of the background does not go at the expense of a large reduction in the signal efficiency, as this could lead to a reduced sensitivity.

11.2.1 PSA for the BEGe detectors

In Sec. 5.5 it was pointed out, that an event selection based on the parameter A/E , that is the ratio between the amplitude of the current pulse, A , and the deposited energy, E , has shown very good results when aiming at separating SSE from MSE. The distribution of A/E for SSE in the bulk of a detector can be approximated by a Gaussian distribution, where the width is dominated by the energy resolution. For MSE, A/E is typically smaller, since they consist of more than one current pulse, with the individual current pulses separated in time, see Fig. 5.4. This leads to a smaller amplitude and

therefore smaller A/E . Also particles penetrating through the n^+ -layer are characterized by a small A/E . Events that take place close to the p^+ -surface, on the other hand, exhibit an unusually large current amplitude and can therefore be identified by their large A/E . It has to be noted that energy losses due to Bremsstrahlung of the electrons emitted in double beta decays can reduce the current amplitude of such events, whereas double beta decays close to the p^+ -surface are characterized by increased A . This leads to a low-side and high-side tail, respectively, in the A/E distributions for $2\nu\beta\beta$ and $0\nu\beta\beta$ events, so that a cut based on the width of the Gaussian distribution will always lead to an acceptance efficiency lower than one.

The PSA method and performance for the BEGe detectors was developed based on the calibration runs performed with ^{228}Th while recording the BEGe sum data set, see Sec. 7.2. For each detector, A/E was calculated for all events with an energy of ≈ 1593 keV, corresponding to the double escape peak (DEP) of the 2.6 MeV peak of ^{208}Tl . Due to the event topology, the DEP is expected to be constituted by a large fraction of SSE. The A/E distributions of these events featured a Gaussian peak, dominated by SSE, with a tail towards lower A/E , populated by MSE. Small corrections had to be applied to account for time shifts of the mean of the Gaussian distributions and energy dependencies of A/E , before combining the distributions of the single detectors. The standard deviation of the Gaussian part of the distribution, $\sigma_{A/E}$, was determined from a fit with a Gaussian function. For convenience, the distributions were rescaled in order to have unity as the mean of the Gaussian distribution. The distribution of A/E was also analyzed for the events in the Compton continuum between 1.0 MeV and 1.3 MeV in the calibration data. The $\sigma_{A/E}$ determined from this analysis was in agreement with the result for the DEP. Figure 11.1(a) shows the distribution of A/E for the events in the Compton continuum.

The applicability of the results to the physics data was verified by repeating the analysis with the events between 1.0 MeV and 1.3 MeV, that is in the region dominated by $2\nu\beta\beta$, in the BEGe sum data set. The results agreed very well with those derived from calibration data.

The selection cut was tuned in order to maximize the background reduction, while keeping a good signal efficiency. All events with $A/E < 2\sigma_{A/E}$ or $A/E > 4\sigma_{A/E}$ were rejected as background events. The cut on the high-side could be chosen twice wider than that on the low-side due to the much lower occurrence and the better separation from the Gaussian distribution of the events on the p^+ -surface.

The acceptance efficiency for SSE after the application of PSA was estimated from the DEP survival fraction and MC simulations of $0\nu\beta\beta$. It was determined to be $\varepsilon_{PSA} = 0.92 \pm 0.02$. The uncertainty was due to the statistical uncertainty on the DEP survival fraction, the uncertainty from the energy dependence of A/E , the differences in the derived selection criteria between the analysis based on calibration data and the analysis based on the BEGe sum data set, and the differences between the survival fraction measured for the DEP and that derived by means of a MC simulation of $0\nu\beta\beta$ that included modelling of the pulse shapes.

An estimate of the survival fraction for $2\nu\beta\beta$ events was deduced from the events

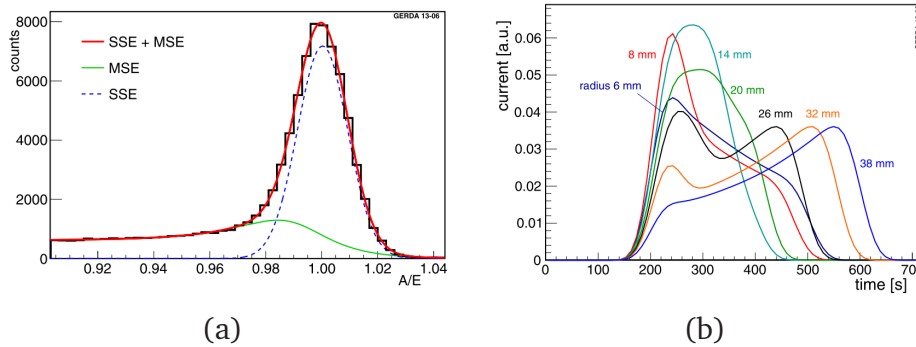


Figure 11.1: (a) Distribution of A/E for the Compton continuum between 1.0 MeV and 1.3 MeV in the BEGe calibration data. (b) Simulated current pulses of SSE in a coaxial detector for interaction positions between the n^+ -surface (radius 38 mm) and the bore hole (radius 6 mm). Both graphics taken from [125].

between 1.0 MeV and 1.45 MeV in the BEGe sum data set, taking into account the survival probabilities for the different classes of events other than $2\nu\beta\beta$ and the background composition in this range, as given in [149]. A comparison with ϵ_{PSA} gave good agreement.

The selection cut was applied to the BEGe sum data set in the window used to define the background, that is between 1930 keV and 2190 keV, excluding the ± 5 keV regions around the background peaks at 2104 keV and 2119 keV and the ± 4 keV blinded window around $Q_{\beta\beta}$. Only three of the 23 events in the window survived the selection, resulting in $BI_{\text{BEGe}}^{PSA} = 5.4^{+5.2}_{-2.9} \cdot 10^{-3}$ cts/(keV · kg · yr). The reduction was consistent with the expectation, which was calculated taking into account the survival probabilities for different event types and the background composition in the window.

11.2.2 PSA for the coaxial detectors

The geometrical differences of the coaxial detectors with respect to the BEGe detectors lead to distinct differences in the weighting potential, which defines the pulse shapes, see Sec. 5.4.2, so that a larger part of the volume is relevant for the current signal. In Fig. 11.1(b), simulated current pulses of SSE are shown for different interaction positions. A variety of different shapes can be distinguished. Therefore, a selection based on A/E is not useful in distinguishing between SSE and MSE. Instead, an analysis with an artificial neural network (ANN) was performed, which used the information of the rising part of the charge pulses. After subtraction of the baseline, smoothing with an 80 ns moving window, and normalization of the pulse height, the times of 1%, 3%, ..., 99% of total pulse height were determined via linear interpolation and used as input to the ANN. The data taking period was divided into three periods, corresponding to the data taking for the golden data set before the period of the silver data set, the period of the silver data set, and the part of the golden data set that was recorded after the period of the silver data set. All steps of the analysis were performed separately for the three periods. The training of the ANN was achieved

using the data from the ^{228}Th calibration runs performed during the respective data taking period. Events corresponding to the DEP served as representatives of the SSE, whereas the MSE were represented by events from the 1621 keV peak of ^{212}Bi . For each charge pulse, the ANN returned a qualifier, that is a number between 0 and 1, with 0 representing a MSE and 1 representing a SSE. The selection cut based on the qualifier was defined such that 90% of the events in the DEP survived the cut. The method was cross-checked by applying it to the data of the golden and silver data sets in different energy regions and comparing the resulting qualifier distributions to expectations.

The acceptance efficiency was assumed to be equal for $0\nu\beta\beta$ events and the events in the DEP. In order to verify the validity of this assumption, the PSA was applied to the events between 1.0 MeV and 1.3 MeV in the golden and silver data sets, that is in the region dominated by $2\nu\beta\beta$. Assuming a background composition according to the results presented in [149] and the survival fraction for Compton events equal to that determined for the 1621 keV peak in the calibration data, the survival efficiency for $2\nu\beta\beta$ events was calculated. It was in good agreement with that determined for DEP events. Applying the PSA to the events in the calibration data close to the Compton edge of the 2.6 MeV peak of ^{208}Tl at 2.4 MeV, a region enhanced in SSE, allowed to establish the absence of an energy dependency of the survival efficiency. The total uncertainty on the acceptance efficiency was estimated from the deviations from 90% for the $2\nu\beta\beta$ and Compton edge events. The final result was determined to be $\varepsilon_{PSA} = 0.90^{+0.05}_{-0.09}$.

When the PSA was applied to the data in the background window, that is between 1930 keV and 2190 keV, excluding the ± 5 keV regions around the background peaks at 2104 keV and 2119 keV and the ± 5 keV blinded window around $Q_{\beta\beta}$, in the golden data set 45 of the 77 events survived the selection, whereas in the silver data set 9 of 19 events remained. The corresponding BI are $BI_{\text{golden}}^{PSA} = 10.9^{+1.9}_{-1.6} \cdot 10^{-3}$ cts/(keV·kg·yr) and $BI_{\text{silver}}^{PSA} = 30.1^{+13.7}_{-9.8} \cdot 10^{-3}$ cts/(keV·kg·yr).

Two alternative PSA methods were developed for the coaxial detectors. The first was a likelihood analysis based on eight input variables calculated from the height of the charge pulse at different times. The training of the method was performed using the events in the Compton edge of the 2.6 MeV peak in the calibration data as representatives for SSE and the events between 2.45 MeV and 2.57 MeV, that is above the Compton edge and below the full energy peak as representatives for MSE. The two samples were used to define likelihood functions for the signal and the background. For each analyzed pulse, the method returned a qualifier defined by these two likelihoods.

The second alternative method selected the events according to a parameter that combined the A/E information and the asymmetry of the current pulse, defined by the difference when integrating the part left and right of A , respectively.

All events that were removed by the ANN in the 230 keV window described above were also removed by at least one of the alternative methods. In 90% of the cases, the events were removed by all three PSA methods.

11.3 Input Parameters

The expected number of signal and background events, defined in Equations (11.11) and (11.9) for the counting method and in Equations (11.25) and (11.24) for the spectral fit, are expressed as functions of several efficiency parameters and the exposures of the data sets. For the case of the counting method, also the width of the ROI has to be specified. In the following, the values relevant for the fitting procedures are described. All detector parameters needed for their evaluation are summarized in Table 11.1. Table 11.2 lists all final results for the input parameters used in the analyses.

Exposure, \mathcal{E}_d The exposures for the individual detectors i in a data set were determined as described in Sec. 7.3 from the product of the total detector mass, M_i , and the detector's live time in the data set, $t_{i,d}$, $\mathcal{E}_{i,d} = M_i \cdot t_{i,d}$. Summing these individual contributions gave the total exposure for the data set, $\mathcal{E}_d = \sum_i \mathcal{E}_{i,d}$.

Energy resolution, FWHM_d In order to calculate the average energy resolution for data set d , FWHM_d , the exposures of the single detectors were taken into account. For details refer to Sec. 7.2 and 7.3.

Detection efficiency, $\langle \varepsilon \rangle_d$ The detection efficiency $\langle \varepsilon \rangle_d = \langle f_{76} f_{act} f_{FEP} \rangle_d$ accounted for the enrichment fraction, f_{76} , the active volume fraction, f_{act} , and the efficiency for detecting the full energy peak, f_{FEP} , of data set d . It was needed to convert the expected number of signal events into an estimate of $T_{1/2}^{0\nu}$, see Equations (11.11) and (11.25).

The total detection efficiency for data set d was defined as the exposure-weighted average efficiency over all N_d detectors in the data set,

$$\langle \varepsilon \rangle_d = \frac{\sum_{i=1}^{N_d} \mathcal{E}_{i,d} \cdot f_{76,i} \cdot f_{act,i} \cdot f_{FEP,i}}{\mathcal{E}_d}, \quad (11.32)$$

with $\mathcal{E}_{i,d}$ the exposure of detector i in data set d . Note that in order to increase the statistical significance, the $\mathcal{E}_{i,d}$ for the golden and the silver data set were summed and one common value for $\langle \varepsilon \rangle$ was calculated. This was possible since the detectors contributing to the data sets were identical.

The values of the enrichment fraction and active volume fraction for the single detectors, $f_{76,i}$ and $f_{act,i}$, were those reported in Sec. 6.2.1.

The individual efficiencies for detecting the full energy peak, $f_{FEP,i}$, were determined from MC simulations [196]. For each of the six enriched coaxial detectors (four enriched BEGe detectors), the primary spectrum of 10^6 (10^7) $0\nu\beta\beta$ decays was sampled using DECAY0 [163]. It was then fed into the MAGE [153] framework for the propagation of the decay products. In case of the coaxial detectors, all decays were placed in the active volume of the detector under study, whereas for the BEGe detectors, the decays were located in the total detector volume. For

the latter, the confinement of the decays to the active volume of the detectors was realized during post-processing. No energy smearing was applied. For each detector, the number of events with an energy deposit in a 1 keV-window around $Q_{\beta\beta}$, $N_{FEP,i}$, was counted. The detection efficiency for the full energy peak for detector i , $f_{FEP,i}$ was determined as the ratio of the events contributing to the peak and the number of events simulated in the active volume of the detector, $N_{MC,act,i}$, $\varepsilon_{FEP,i} = N_{FEP,i}/N_{MC,act,i}$. No decays in other detectors or in the dead volume of the detector had to be taken into account as they cannot contribute to the full energy peak. The statistical uncertainty due to the MC simulation was $\approx 0.14\%$. The systematic uncertainty included contributions from uncertainties on the accuracy of the MC tracking and the precision of the geometry model. It amounted to a total of $\approx 2\%$. The total uncertainty on $f_{FEP,i}$ was obtained by summing in quadrature the statistical and systematic uncertainties, resulting in 2% for all detectors.

In order to calculate the uncertainty on $\langle\varepsilon\rangle_d$, the MC approach from [197] was adapted. The value of $\langle\varepsilon\rangle_d$ was calculated 10^8 times. Each time, the values for $f_{76,i}$, $f_{act,i}$, and $f_{FEP,i}$ were sampled from Gaussian probability distribution functions with mean and standard deviation according to Table 11.1. The uncertainty on $f_{FEP,i}$ was considered completely correlated among the detectors, since it was dominated by the uncertainties from the MC simulation. Also a part of the uncertainty on $f_{act,i}$ was correlated among the detectors. This was taken into account when sampling the respective values¹. For each step of the sampling, the value for $\langle\varepsilon\rangle_d$ was filled into a histogram. A Gaussian function was fitted to the distribution. The mean value and uncertainty for $\langle\varepsilon\rangle_d$ were determined as the mean and standard deviation of the Gaussian function. The distributions for the coaxial enriched detectors and the BEGe detectors with the fit function are shown in Figs. D.1 and D.2 in Appendix D. For the coaxial enriched detectors, $\langle\varepsilon\rangle_d$ resulted to be 0.688 ± 0.031 , whereas for the BEGe sum data set a value of 0.720 ± 0.019 was calculated.

Signal acceptance after PSA, $\varepsilon_{PSA,d}$ The signal acceptance after the application of PSA methods was defined by the results presented in Sec. 11.2. For the golden and the silver data set, it resulted to be $\varepsilon_{PSA,golden} = \varepsilon_{PSA,silver} = 0.90^{+0.05}_{-0.09}$, whereas for the BEGe sum data set the acceptance efficiency was $\varepsilon_{PSA,BEGe} = 0.92 \pm 0.02$.

Width of the counting window, ROI_d For the counting method, the width of the window in which the events around $Q_{\beta\beta}$ were counted had to be defined. The efficiency for a signal event to fall within ROI_d , $\varepsilon_{ROI,d}$, is defined in Equation (11.12). It depends on ROI_d and the energy resolution of the data set, $FWHM_d$. The efficiency rises with increasing ROI_d , since more and more of the

¹In practice, the correlation between two parameters p_1 and p_2 , described by Gaussian functions with means μ_1 and μ_2 and standard deviations σ_1 and σ_2 , respectively, was taken into account by sampling a random number r from a Gaussian distribution centered at zero and with standard deviation $\sigma = 1$. The random values for p_1 and p_2 were then defined as $p_1 = \mu_1 + r \cdot \sigma_1$ and $p_2 = \mu_2 + r \cdot \sigma_2$.

signal falls inside the window, until $\varepsilon_{ROI,d} = 1$ is reached, when all signal events are comprised inside ROI_d . On the other hand, also the number of expected background events, given by Equation (11.9), depends on the width of ROI_d . The wider the window, the more background events are expected inside ROI_d , so that the sensitivity to the signal might be reduced. Therefore, the optimal ROI_d has to be a trade-off between the largest possible efficiency and the smallest possible number of expected background events.

The ROI_d was optimized for the best expected average limit on $T_{1/2}^{0\nu}$ following the procedure described in [194]. The average of the expected limit for a data set d with a given exposure, \mathcal{E}_d , background index, BI_d^{PSA} , detection efficiency, $\langle\varepsilon\rangle_d$, signal acceptance after PSA, $\varepsilon_{PSA,d}$, and energy resolution, $FWHM_d$, can then be expressed as

$$\langle T_{1/2}^{0\nu} \rangle = \sum_{x_d=1}^{\infty} P(x_d | \xi_d, \omega_d = 0, \bar{H}) \cdot \langle\varepsilon\rangle_d \cdot \varepsilon_{PSA,d} \cdot \varepsilon_{ROI,d} \cdot \kappa_0 \cdot \mathcal{E}_d \frac{1}{\omega_d(90\%)}, \quad (11.33)$$

with $P(x_d | \xi_d, \omega_d = 0, \bar{H})$, ξ_d , ω_d , and κ_0 defined via Equations (11.2), (11.9), and (11.11). The expression $\omega_d(90\%)$ indicates the number of expected signal counts corresponding to the 90% quantile of the marginalized posterior probability. In Fig. 11.2, $\langle T_{1/2}^{0\nu} \rangle$ is shown as a function of ROI_d for the three data sets. The optimal width for ROI_d can be identified in all three cases as the one that maximizes $\langle T_{1/2}^{0\nu} \rangle$. They resulted in $ROI_{\text{golden}} = 8.0 \text{ keV}$, $ROI_{\text{silver}} = 9.5 \text{ keV}$, and $ROI_{\text{BEGe}} = 8.0 \text{ keV}$. The optimal window for the silver data set was larger than those of the other two data sets, since the smaller exposure lead to a small number of expected background events, allowing to maximize the efficiency without loss of sensitivity. The efficiency resulted in $\varepsilon_{ROI} = 98.4\%$ for the silver data set. For the BEGe sum data set, the small BI after application of PSA and the smaller exposure compared to the golden data set allowed a window of the same size as that of the golden data set. Since the energy resolution was better than in the case of the coaxial detectors, ε_{ROI} was very high, 99.6%, compared to 94.9% for the golden data set.

The uncertainty on ROI_d was dominated by the uncertainty on $FWHM_d$. In order to estimate its size, the optimal window size was determined assuming an energy resolution of $FWHM_d + \sigma_{FWHM_d}$ and $FWHM_d - \sigma_{FWHM_d}$, respectively, with σ_{FWHM_d} the uncertainty on $FWHM_d$, as given in Table 11.2. This gave the final results for the optimal window size, $ROI_{\text{golden}} = (8.0 \pm 0.3) \text{ keV}$, $ROI_{\text{silver}} = (9.5 \pm 0.4) \text{ keV}$, and $ROI_{\text{BEGe}} = (8.0 \pm 0.4) \text{ keV}$.

Background index after application of PSA, BI_d^{PSA} The background index after the application of PSA methods was used as input to the prior probabilities for the counting method. It was determined in the window between 1930 keV and 2190 keV excluding the $\pm 5 \text{ keV}$ -windows around the background peaks at 2104 keV and 2119 keV and the $\pm 5 \text{ keV}$ -window ($\pm 4 \text{ keV}$ -window for the BEGe sum data set) around $Q_{\beta\beta}$. The results were $BI_{\text{golden}}^{PSA} = 10.9_{-1.6}^{+1.9} \cdot 10^{-3} \text{ cts}/(\text{keV} \cdot \text{kg} \cdot$

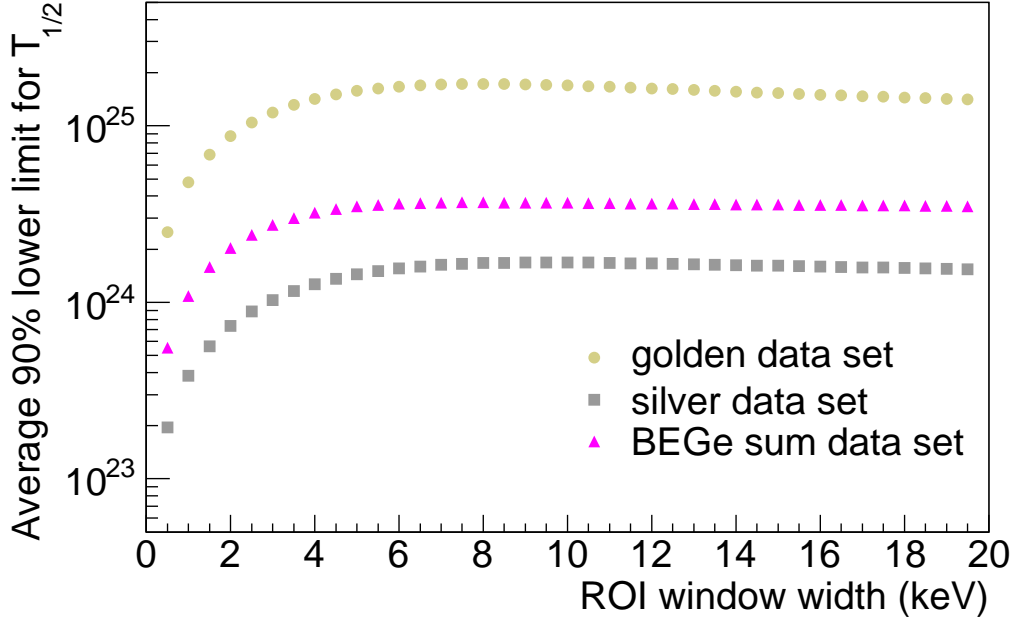


Figure 11.2: Average limit $\langle T_{1/2}^{0\nu} \rangle$ as a function of the width of ROI_d for the golden, silver, and BEGe sum data sets.

$$\text{yr}), BI_{\text{silver}}^{PSA} = 30.1_{-9.8}^{+13.7} \cdot 10^{-3} \text{ cts}/(\text{keV} \cdot \text{kg} \cdot \text{yr}), \text{ and } BI_{\text{BEGe}}^{PSA} = 5.4_{-2.9}^{+5.2} \cdot 10^{-3} \text{ cts}/(\text{keV} \cdot \text{kg} \cdot \text{yr}).$$

11.4 Sensitivity

The sensitivity of GERDA Phase I to $0\nu\beta\beta$ was estimated following the approach in [166]. Possible outcomes of the experiment were sampled using MC methods. To this scope, the number of background events between 1930 keV and 2190 keV for each data set d was sampled from a Poisson distribution with mean according to BI_d^{PSA} . Since the background was assumed to be constant in this region, the event energies were distributed between 1930 keV and 2190 keV according to a flat random distribution. The number of signal events was sampled from a Poisson distribution with mean according to the expectation for a certain $T_{1/2}^{0\nu}$. The energies for the signal events were drawn from a Gaussian random distribution with width defined by FWHM_d and mean value $\mu = Q_{\beta\beta}$. The combined signal and background spectra for the three data sets were then used as input for the two statistical approaches described above.

In order to study the sensitivity in the absence of $0\nu\beta\beta$, 1000 energy spectra were sampled without signal contributions. The hypothesis including a signal contribution, \bar{H} , was rejected by $BF < 1$ in 99.8% of all cases for the counting method and in 100% of all cases for the spectral fit. In none of the experiments, $BF > 100$, so that \bar{H} was never assumed true. The distributions of BF are shown in Fig. 11.3(a) and 11.3(b).

Table 11.1: Main characteristics of the detectors used in this analysis: total exposure, \mathcal{E} , isotopic abundance of ^{76}Ge , f_{76} , fraction of active mass, f_{act} , and the efficiency for detecting the full energy peak, f_{FEP} . For the coaxial detectors, the first uncertainty on f_{act} is the uncorrelated part, the second one the correlated contribution.

Detector	\mathcal{E} (kg·yr)	f_{76} (%)	f_{act} (%)	f_{FEP} (%)
Enriched Coaxial Detectors				
ANG2	3.81	86.6 ± 2.5	$87.1 \pm 4.3 \pm 2.8$	92 ± 2
ANG3	3.21	88.3 ± 2.6	$86.6 \pm 4.9 \pm 2.8$	92 ± 2
ANG4	3.19	86.3 ± 1.3	$90.1 \pm 4.9 \pm 2.9$	92 ± 2
ANG5	3.69	85.6 ± 1.3	$83.1 \pm 4.0 \pm 2.7$	92 ± 2
RG1	2.84	85.5 ± 1.5	$90.4 \pm 5.2 \pm 2.9$	92 ± 2
RG2	2.47	85.5 ± 1.5	$83.1 \pm 4.6 \pm 2.7$	91 ± 2
Enriched BEGe Detectors				
GD32B	0.55	87.7 ± 1.3	89.0 ± 2.7	90 ± 2
GD32C	0.62	87.7 ± 1.3	91.1 ± 3.0	90 ± 2
GD32D	0.56	87.7 ± 1.3	92.3 ± 2.6	90 ± 2
GD35B	0.67	87.7 ± 1.3	91.4 ± 2.9	90 ± 2

Table 11.2: Main characteristics of the data sets used in this analysis: total exposure, \mathcal{E} , FWHM at $Q_{\beta\beta}$, average efficiency, $\langle \varepsilon \rangle = \langle f_{76} f_{act} f_{FEP} \rangle$, the signal acceptance after application of PSA, ε_{PSA} , the optimized window for the counting method, ROI , and the background index after PSA, BI^{PSA} .

Data set	\mathcal{E} (kg·yr)	FWHM (keV)	$\langle \varepsilon \rangle$ (%)	ε_{PSA} (%)	ROI (keV)	BI^{PSA} (10^{-3} cts/(keV · kg · yr))
golden	17.9	4.83 ± 0.19	68.8 ± 3.1	90_{-9}^{+5}	8.0 ± 0.3	$10.9_{-1.6}^{+1.9}$
silver	1.3	4.63 ± 0.24	68.8 ± 3.1	90_{-9}^{+5}	9.5 ± 0.4	$30.1_{-9.8}^{+13.7}$
BEGe sum	2.4	3.24 ± 0.17	72.0 ± 1.9	92 ± 2	8.0 ± 0.4	$5.4_{-2.9}^{+5.2}$

For the counting method (spectral fit), in 86.0% (86.6%) of all experiments, the smallest 68% probability interval of the marginalized distribution for $\text{inv}_-t_{1/2}^{0\nu}$ extended down to $\text{inv}_-t_{1/2}^{0\nu} = 0$, corresponding to infinite $T_{1/2}^{0\nu}$. For each experiment, the upper limit on $\text{inv}_-t_{1/2}^{0\nu}$ was defined as the 90% quantile of the marginalized distribution. The median sensitivity was then obtained as the median of the frequency distribution of these limits. In case of the counting method, it resulted in $\text{inv}_-t_{1/2}^{0\nu} < 0.534$, corresponding to $T_{1/2}^{0\nu} > 1.87 \cdot 10^{25}$ yr. For the spectral fit, the sensitivity was slightly higher with $\text{inv}_-t_{1/2}^{0\nu} < 0.489$, corresponding to $T_{1/2}^{0\nu} > 2.04 \cdot 10^{25}$ yr. Figures 11.3(c) and 11.3(d) depict the frequency distributions of the 90% quantiles of all samples.

The sensitivity study was also performed assuming a signal with $T_{1/2}^{0\nu} = 1.19 \cdot 10^{25}$ yr, as claimed by [9]². Again, 1000 possible outcomes of the experiment were simulated.

When analyzing all samples with the counting method, for 11.1% the hypothesis \bar{H} of the presence of a signal was accepted due to $BF > 100$. In 63.3% of all cases $BF < 1$, so that \bar{H} would have been rejected and only a limit would have been calculated. Figure 11.3(a) shows the distribution of BF . When looking at the marginalized distribution for $\text{inv}_-t_{1/2}^{0\nu}$, in only 5.7% of all cases the mode was consistent with zero within the interval of 68% probability. The median of the frequency distribution of the marginalized modes was $\text{inv}_-t_{1/2}^{0\nu} = 0.811$, corresponding to $T_{1/2}^{0\nu} = 1.23 \cdot 10^{25}$ yr and thus in agreement with the assumptions for the generation of the energy spectra. The median limit on $T_{1/2}^{0\nu}$, derived as described above, was $T_{1/2}^{0\nu} > 0.71 \cdot 10^{25}$ yr. The distributions of the marginalized modes and the 90% quantiles are depicted in Figs. 11.3(e) and 11.3(c), respectively.

When the spectral fit method was applied, $BF > 100$ in 16.5% of all cases. The signal hypothesis was rejected in 60.6% of all cases due to $BF < 1$. The corresponding distribution of BF is shown in Fig. 11.3(b). The 68% probability interval of the marginalized $\text{inv}_-t_{1/2}^{0\nu}$ distribution extended down to zero only for 4.7% of the samples. The median mode was $\text{inv}_-t_{1/2}^{0\nu} = 0.811$, corresponding to $T_{1/2}^{0\nu} = 1.23 \cdot 10^{25}$ yr, as expected from the assumption used for the sample generation. Also in this case, only a very weak median limit on $T_{1/2}^{0\nu}$ of $T_{1/2}^{0\nu} > 0.66 \cdot 10^{25}$ yr could be given. Figures 11.3(f) and 11.3(d) depict the respective frequency distributions of the marginalized modes and 90% quantiles of $\text{inv}_-t_{1/2}^{0\nu}$.

Summarizing, in absence of a contribution from $0\nu\beta\beta$ to the energy spectra, the signal hypothesis is expected to be clearly refuted by the GERDA experiment. The median sensitivity of the counting method was determined to be $T_{1/2}^{0\nu} > 1.87 \cdot 10^{25}$ yr, whereas that of the spectral fit was calculated to be $T_{1/2}^{0\nu} > 2.04 \cdot 10^{25}$ yr. Note that no systematic uncertainties were considered for the sensitivity calculations.

In the presence of the signal process with a half-life corresponding to [9], the signal hypothesis was accepted in 11.1% (16.5%) of all cases when analyzing the data with the counting method (spectral fit). The background-only hypothesis was not refuted in 63.3% (60.6%) of all cases. However, for almost all samples the mode of $\text{inv}_-t_{1/2}^{0\nu}$ was

²An update of the analysis from [9] was reported in [106]. However, inconsistencies were found for this second analysis [107]. Therefore, all comparisons of this work refer to the result presented in [9].

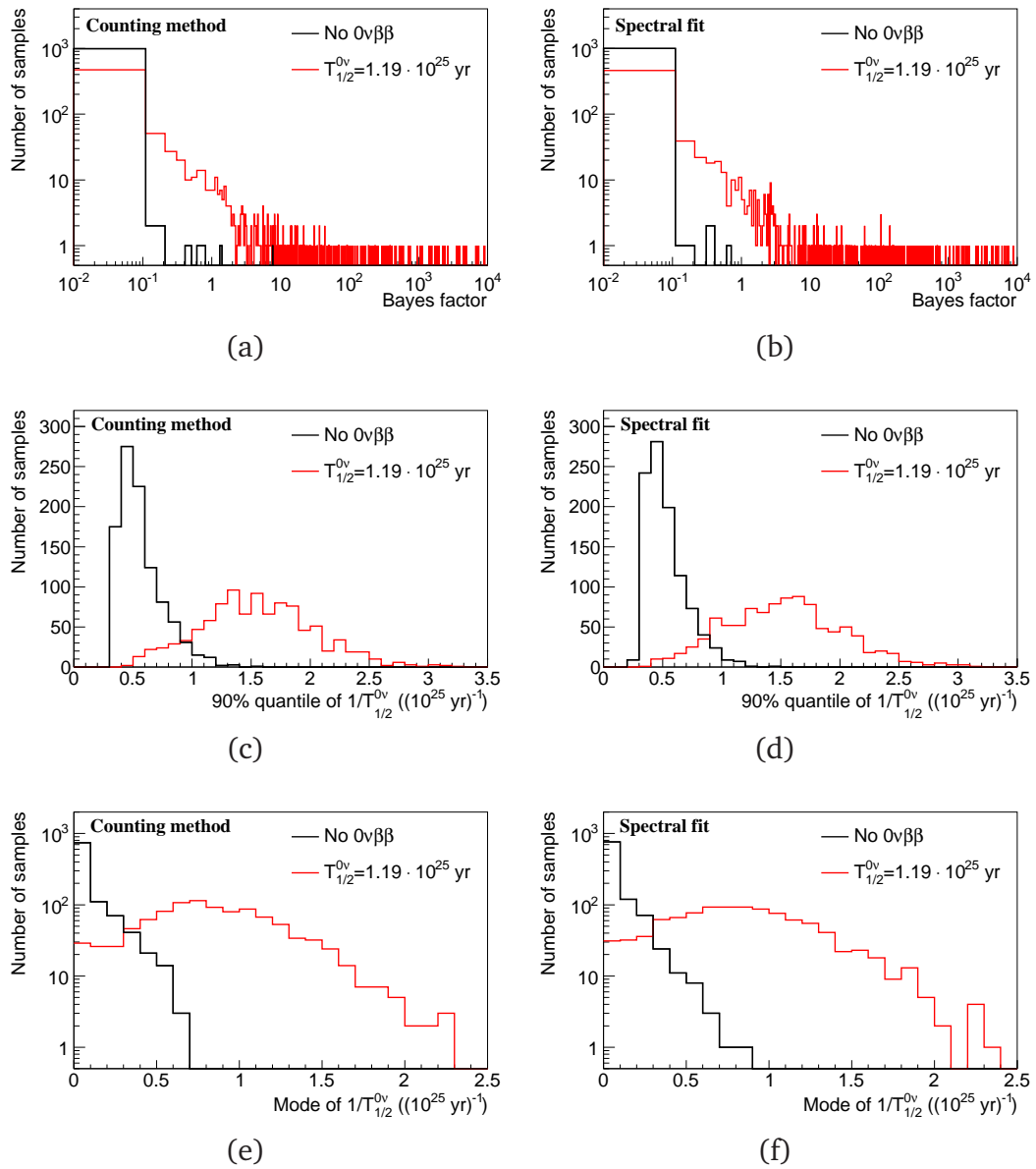


Figure 11.3: Distributions of the Bayes' factor, BF , for the analysis with (a) the counting method and (b) the spectral fit, the 90% quantile of $\text{inv-}t_{1/2}^{0\nu}$ for the analysis with (c) the counting method and (d) the spectral fit, and the marginalized mode of $\text{inv-}t_{1/2}^{0\nu}$ for the analysis with (e) the counting method and (f) the spectral fit.

not consistent with zero, indicating tension with the no-signal hypothesis. In addition, the lower limit on $T_{1/2}^{0\nu}$ was much weaker than in the absence of the signal process. Therefore, the analysis of the GERDA Phase I data clearly provides the possibility to test the claim of observation of $0\nu\beta\beta$.

Table 11.3: Information about all events contained in $Q_{\beta\beta} \pm 5$ keV. Given is the data set they are contained in, the detector which detected them, the event energy, E , and the date and time of detection. The last column indicates if the event passed the PSA cut.

Data set	Detector	E (keV)	Date	Passed PSA
golden	ANG5	2041.8	Nov 18, 2011 22:52	–
silver	ANG5	2036.9	Jun 23, 2012 23:02	✓
golden	RG2	2041.3	Dec 16, 2012 00:09	✓
BEGe	GD32B	2036.6	Dec 28, 2012 09:50	–
golden	RG1	2035.5	Jan 29, 2013 03:35	✓
golden	ANG3	2037.4	Mar 2, 2013 08:08	–
golden	RG1	2041.7	Apr 27, 2013 22:21	–

11.5 Data Analysis

The data analysis was performed after unblinding also the energy region around $Q_{\beta\beta}$. From the BI before PSA, derived in Chapter 9, the number of expected background events in the 10 keV-wide (8 keV for the BEGe sum data set) window could be calculated. The expectations were 3.3 ± 0.4 events for the golden data set and 0.8 ± 0.2 for the silver and for the BEGe sum data set, respectively.

When the blinded windows were opened, they contained five events in the golden data set, one event in the silver data set and one event in the BEGe sum data set. The probability to observe five or more events, when 3.3 were expected, is 24%, whereas the probability to observe at least one event when 0.8 were anticipated is 55%. Table 11.3 lists the details of all seven events contained in the previously blinded window. After the use of PSA methods, in the golden data set, two events remained and in the silver data set, one event remained³. The event in the BEGe sum data set was rejected by the A/E cut. From BI_d^{PSA} , a total of $2.5^{+0.4}_{-0.3}$ events had been expected in the previously blinded windows (2.0 ± 0.3 for the golden data set, $0.4^{+0.2}_{-0.1}$ for the silver data set, and 0.1 ± 0.1 for the BEGe sum data set). The probability to observe three or more events, when 2.5 were expected, is 46%.

This allows to deduce that the observations did not hint at any excess beyond the background expectation.

None of the remaining events was contained in $Q_{\beta\beta} \pm \sigma_d$, with $\sigma_d = 1/(2\sqrt{2\ln(2)}) \cdot FWHM_d$. All three remaining events were contained in the respective ROI_d . The sum data spectrum for all three data sets between 1930 keV and 2190 keV before and after PSA is shown in Fig. 11.4. Also, a zoom to the ± 20 keV-window around $Q_{\beta\beta}$ is depicted.

The analysis was performed running 10^7 iterations of the MCMC for both the

³For five of the six events in the coaxial detectors, the classification was in agreement with at least one of the alternative PSA methods.

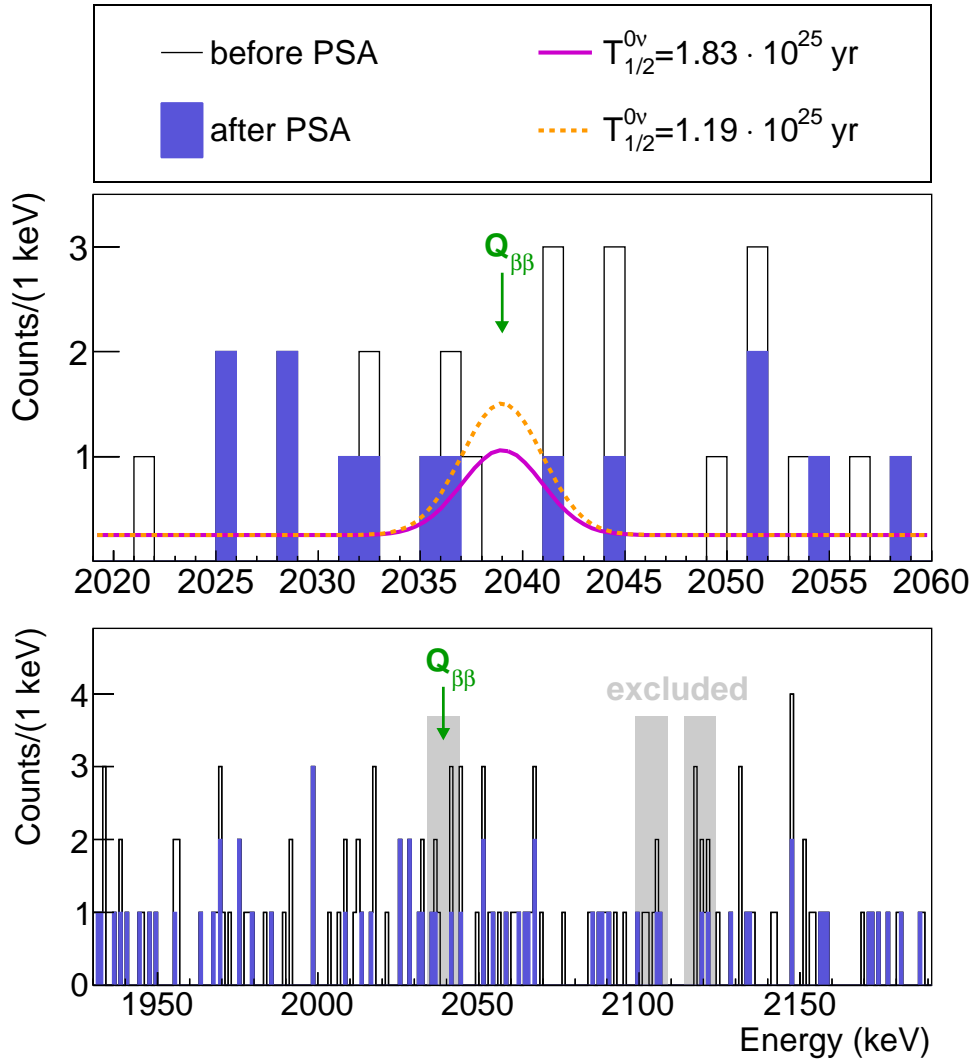


Figure 11.4: Sum spectrum from the data of the golden, silver, and BEGe sum data sets before and after the application of PSA. The upper panel shows the ± 20 keV region around $Q_{\beta\beta}$. In the lower panel, the region between 1930 keV and 2190 keV used for the determination of the BI is depicted. The regions that are excluded for the BI calculation are indicated. In the upper panel, also the expectation assuming $T_{1/2}^{0\nu} = 1.83 \cdot 10^{25}$ yr, corresponding to the 90% quantile derived in this work, is shown. In addition, the expectation for $T_{1/2}^{0\nu} = 1.19 \cdot 10^{25}$ yr, corresponding to the claim in [9], is indicated.

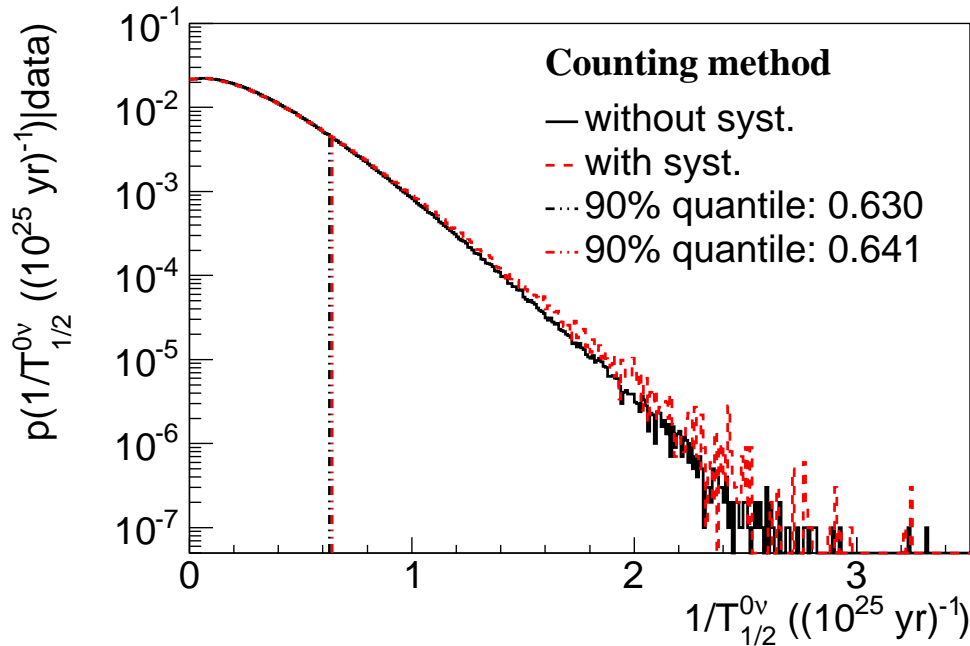


Figure 11.5: Marginalized posterior probability distribution $P(\text{inv}_t_{1/2}^{0v} | \mathbf{x})$ for the parameter $\text{inv}_t_{1/2}^{0v}$, which represents $1/T_{1/2}^{0v}$ in units of $(10^{25} \text{ yr})^{-1}$ for the analysis performed with the counting method. The 90% quantile is marked. Also drawn is the posterior probability distribution with folded in systematic uncertainties and the resulting 90% quantile.

counting method and the spectral fit.

The analysis of the data with the counting method clearly indicated a preference for the background-only model, as $BF = 1.7 \cdot 10^{-5}$. Figure 11.5 depicts the marginalized posterior distribution of $\text{inv}_t_{1/2}^{0v}$ for the fit assuming a signal contribution. The smallest interval of 68% probability extends down to zero, implying an infinite half-life. The quantile of 90% probability is at 0.630, corresponding to a limit on the half-life of $T_{1/2}^{0v} > 1.59 \cdot 10^{25} \text{ yr}$ or an expectation of < 3.6 signal events for the golden data set, < 0.3 signal events for the silver data set, and < 0.5 signal events for the BEGe sum data set in the respective ROI_d .

Also when performing the analysis with the spectral fit method, the hypothesis of a signal contribution was clearly rejected, as $BF = 2.7 \cdot 10^{-6}$. Again, the mode of the marginalized posterior distribution of $\text{inv}_t_{1/2}^{0v}$, shown in Fig. 11.6, is consistent with zero. The 90% quantile was determined to be 0.535, so that a lower limit of $T_{1/2}^{0v} > 1.87 \cdot 10^{25} \text{ yr}$ could be given, corresponding to an expectation of < 3.3 signal events for the golden data set, < 0.2 signal events for the silver data set, and < 0.5 signal events for the BEGe sum data set.

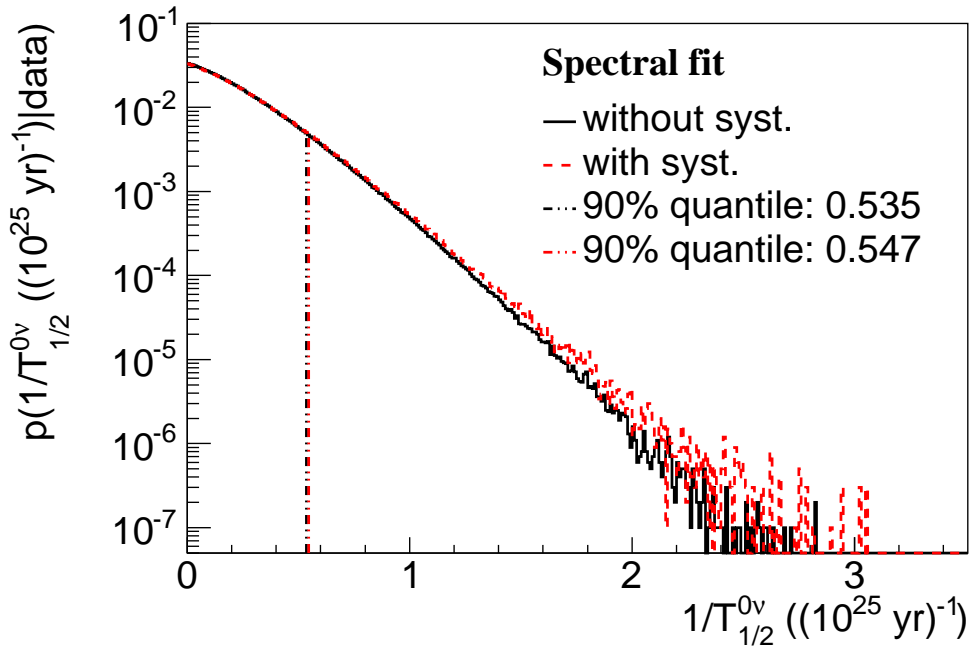


Figure 11.6: Marginalized posterior probability distribution $P(\text{inv}_t_{1/2}^{0v} | \mathbf{N})$ for the parameter $\text{inv}_t_{1/2}^{0v}$, which represents $1/T_{1/2}^{0v}$ in units of $(10^{25} \text{ yr})^{-1}$ for the analysis performed with the spectral fit. The 90% quantile is marked. Also drawn is the posterior probability distribution with folded in systematic uncertainties and the resulting 90% quantile.

11.6 Systematic Uncertainties

The analysis described above does not yet account for the uncertainties on the input parameters used in the analysis. In order to take these uncertainties into account when determining $T_{1/2}^{0v}$, a Monte Carlo approach was followed. For each source of uncertainty, a probability distribution was provided, so that each parameter used as input to the analysis could be drawn as a random number from these probability distributions. Possible correlations between parameters could be considered by the definition of the distributions.

For both the counting method as well as the spectral fit, the analysis was repeated 1000 times, each time sampling a new set of input parameters. Each repetition provided a marginalized posterior distribution of $\text{inv}_t_{1/2}^{0v}$. All 1000 posterior distributions were added up to the final posterior distribution for the respective analysis method. The final posterior distributions incorporated all statistical as well as systematic uncertainties. For each individual repetition of the analysis, 10^4 steps of the MCMC were performed, so that the final posterior distributions for both methods contained the same number of entries as in the case of the fits without consideration of systematic uncertainties. In a last step, the final posterior distributions were normalized to the number of entries. The final value for the limit on $\text{inv}_t_{1/2}^{0v}$ for each analysis method was determined as the quantile of 90% probability of the respective final distribution.

The uncertainties of the following parameters had to be accounted for in the analysis:

Detection efficiency, $\langle \varepsilon \rangle_d$ The detection efficiencies for all three data sets can be described by Gaussian distributions with mean and standard deviation according to Table 11.2. Since one common value had been determined for the golden and the silver data set, the uncertainty was completely correlated for these two data sets. No correlation was taken into account for the uncertainty on $\langle \varepsilon \rangle_{\text{BEGe}}$.

Energy resolution, FWHM_d The energy resolutions were given by Gaussian distributions defined by the values listed in Table 11.2. No correlations were taken into account between FWHM_d of different data sets.

Width of the counting window, ROI_d The optimal width for the counting window of a data set, ROI_d , was directly dependent on its energy resolution, FWHM_d . This correlation was taken into account when sampling ROI_d from its Gaussian distribution, defined by the mean and standard deviation given in Table 11.2. Note that a change of the window width could lead to a change in the number of observed events attributed to the ROI_d and to the background region, respectively. The uncertainty on ROI_d entered only the analysis based on the counting method.

Signal acceptance after PSA, $\varepsilon_{\text{PSA},d}$ For the BEGe sum data set, $\varepsilon_{\text{PSA},d}$ was sampled from a Gaussian distribution, described by the values in Table 11.2. For the golden and the silver data sets, the probability distribution was defined by an asymmetric Gaussian function, with the standard deviations of the left and right half according to the lower and upper uncertainties given in the table. The uncertainty was completely correlated for the golden and the silver data set, whereas no correlation was considered for the BEGe sum data set.

Position of the signal peak, $\mu_{0\nu}$ For the spectral fit, the possibility of a shift in the signal peak position $\mu_{0\nu}$ due to systematic shifts in the energy calibration was taken into account. It was described by a Gaussian function centered at $Q_{\beta\beta}$. The standard deviation was 0.2 keV. The shift was correlated for all data sets.

For both analysis methods, the lower limit on the half-life of $0\nu\beta\beta$ was weakened by $\approx 2\%$. The analysis with the counting method gave $\text{inv}_-t_{1/2}^{0\nu} < 0.641$, corresponding to a limit on the half-life of $T_{1/2}^{0\nu} > 1.56 \cdot 10^{25}$ yr, or < 3.7 , < 0.3 , and < 0.6 events in the ROI_d for the golden, silver, and BEGe sum data set, respectively. When the spectral fit method was applied, the result was $\text{inv}_-t_{1/2}^{0\nu} < 0.547$, that is $T_{1/2}^{0\nu} > 1.83 \cdot 10^{25}$ yr, corresponding to < 3.3 signal events for the golden data set, < 0.2 signal events for the silver data set, and < 0.5 signal events for the BEGe sum data set. The corresponding marginalized posterior probability distributions of $\text{inv}_-t_{1/2}^{0\nu}$ are shown in Figs. 11.5 and 11.6, respectively.

11.7 Final Results and Discussion

The analysis of the GERDA Phase I data did not indicate the presence of a peak at $Q_{\beta\beta}$. A model accounting for contributions from $0\nu\beta\beta$ as well as from a flat background was rejected by two different statistical approaches, one based on a counting method, the other one based on a spectral fit. Instead, the background-only model was favored by both methods. The lower limits on the half-life of $0\nu\beta\beta$ of ^{76}Ge resulted in

$$T_{1/2}^{0\nu} > 1.56 \cdot 10^{25} \text{ yr} \quad (11.34)$$

in case the counting method was used for the analysis and

$$T_{1/2}^{0\nu} > 1.83 \cdot 10^{25} \text{ yr} \quad (11.35)$$

in case a spectral fit was used for the analysis. Both results account for statistical as well as systematic uncertainties. The latter limit on the half-life corresponds to an expectation of < 4.0 signal events in the combined energy spectrum from the golden, silver, and BEGe sum data set. This expectation is drawn together with the sum data spectrum in Fig. 11.4.

The result is one of the most stringent lower limits on $0\nu\beta\beta$ of ^{76}Ge obtained to date. The low background in the GERDA experiment allowed to extract it from data with a total exposure of only $21.6 \text{ kg} \cdot \text{yr}$, collected in less than 19 months of data taking.

Assuming the half-life of $0\nu\beta\beta$ claimed in [9], $T_{1/2}^{0\nu} = 1.19_{-0.23}^{+0.37} \cdot 10^{25} \text{ yr}$, and summing the expected signal events in the respective ROI_d for all data sets, gives a total expectation of 5.9 ± 1.4 signal events. The corresponding total expectation from background, when considering the respective ROI_d for each data set, was 2.0 ± 0.3 events. Figure 11.4 shows the superposition of the expectation with the GERDA data, where a total of three events was observed inside the ROI_d . The hypothesis accounting for contributions from $0\nu\beta\beta$ was rejected by both analysis methods due to $BF < 1^4$. In both cases, the mode of the marginalized posterior distribution for $\text{inv}_{-}t_{1/2}^{0\nu}$ was consistent with zero, corresponding to infinite $T_{1/2}^{0\nu}$, and strong limits on $T_{1/2}^{0\nu}$ were found. Following the observations in Sec. 11.4, it was concluded that the claim of observation of $0\nu\beta\beta$ was not supported by the GERDA Phase I data.

The lower limits on $T_{1/2}^{0\nu}$ were in agreement with those derived by HdM [105] and IGEX [104].

From the lower limit on $T_{1/2}^{0\nu}$, an upper limit on the effective Majorana neutrino mass $\langle m_{\beta\beta} \rangle$ can be derived using Equation (3.5), if the exchange of light Majorana neutrinos is assumed as the dominating mechanism leading to $0\nu\beta\beta$. The phase space factor, $G^{0\nu}$, was taken from [184] and the nuclear matrix elements, $|M^{0\nu}|$, were those of [187–193]. The matrix elements were scaled as discussed in [198] to account for differences in their calculation. Using the more stringent limit on $T_{1/2}^{0\nu}$ derived with

⁴For the counting method, a Bayes' factor of $BF = 1.7 \cdot 10^{-5}$, and for the spectral fit, a Bayes' factor of $BF = 2.7 \cdot 10^{-6}$ was determined (see Sec. 11.5).

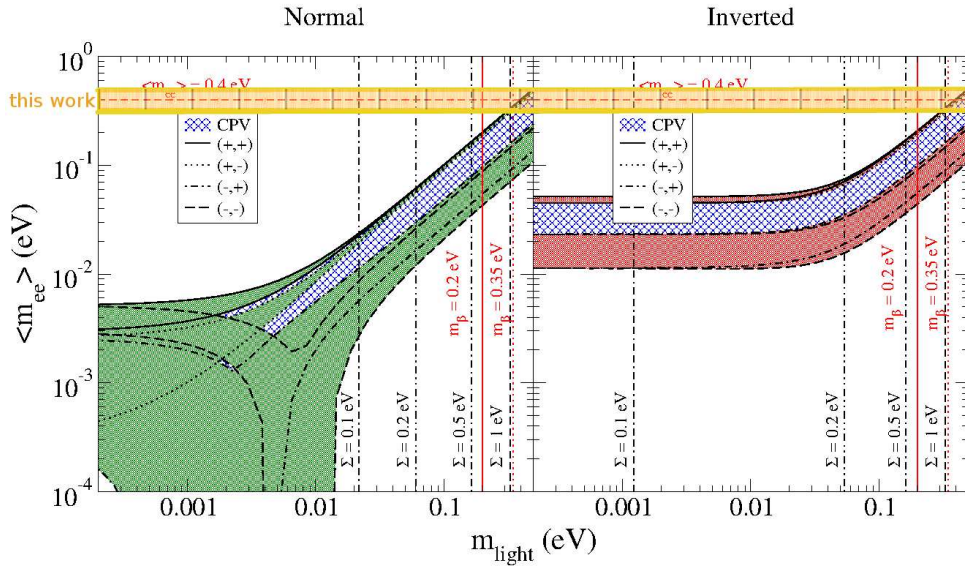


Figure 11.7: Effective Majorana neutrino mass as a function of the lightest neutrino mass [65]. The result from this work is indicated.

the spectral fit method gave

$$\langle m_{\beta\beta} \rangle < (0.3 - 0.5) \text{ eV}. \quad (11.36)$$

Figure 11.7 shows $\langle m_{\beta\beta} \rangle$ as a function of the lightest neutrino mass, see Chapter 3, superposed with the result from this work. It explores the region of degenerate hierarchy.

An alternative analysis of the GERDA Phase I data based on a profile likelihood approach is described in [6]. Its final result gave $T_{1/2}^{0\nu} > 2.1 \cdot 10^{25} \text{ yr}$ (90% C.L.). The reference also presents an extended analysis accounting for two additional data sets, one containing the HdM data and one containing the IGEX data. The combined analysis again strongly disfavored the claim and allowed to extract a lower limit of $T_{1/2}^{0\nu} > 3.0 \cdot 10^{25} \text{ yr}$. The exclusion of the claim was confirmed, when the results for ^{76}Ge were combined with those derived from ^{136}Xe [7, 8]. Note that in this case the strength of the exclusion depends on the choice of the matrix elements.

Chapter 12

Conclusions and Outlook

The GERDA experiment, located at the INFN Laboratori Nazionali del Gran Sasso (LNGS) in Italy, was designed for the search of neutrinoless double beta decay ($0\nu\beta\beta$) of ^{76}Ge . The background due to environmental radiation was much reduced compared to previous experiments, thanks to the graded shielding design and the novel technique of submerging the germanium detectors directly into liquid argon (LAr). The first phase of the experiment was conducted between November 2011 and May 2013. A total of ten enriched germanium detectors, six coaxial and four BEGe detectors, accumulated a total exposure of $21.6\text{ kg}\cdot\text{yr}$. The data was divided into three subsets according to their background level around the Q-value of $0\nu\beta\beta$, $Q_{\beta\beta} = 2039\text{ keV}$. The golden data set contained data recorded with the coaxial detectors. It made up 83% of all data. The BEGe sum data set contained all data accumulated with the BEGe detectors. It accounted for 11% of the exposure. The remaining 6% of the total exposure, the silver data set, was collected with the coaxial detectors during a period affected by higher background contamination following the immersion of the BEGe detectors. The data energy spectra were blinded in the 40 keV-window around $Q_{\beta\beta}$ in order to allow for an unbiased analysis.

In a first step, the most prominent background contaminations above 570 keV were identified by their characteristic photon lines in the energy spectra. They comprised isotopes from the natural decay chains of ^{238}U and ^{232}Th , ^{40}K , ^{60}Co , as well as ^{42}K , the daughter-isotope of ^{42}Ar . The analysis of the high-energy part of the spectra also suggested the presence of alpha contaminations from the ^{238}U decay chain on and in the vicinity of the p^+ -surface of the detectors. Screening measurements of a variety of components used in the setup of the experiment confirmed these observations.

A Monte Carlo campaign was launched in order to obtain a complete set of simulations describing all possible contributions in the data energy spectra. The simulations were carried out within the GEANT4 based MAGE framework, which incorporates a detailed description of the experimental setup of the GERDA experiment, including the individual characterization of all detectors. All contributions that had been identified in the energy spectra or by screening measurements were simulated, taking into account a variety of different positions of each source. The simulation comprised alpha and beta decays of the ^{238}U chain, beta decays of the ^{232}Th chain, as well as the decays

of ^{60}Co , ^{40}K , and ^{42}K . In addition, the contributions from neutrino accompanied double beta decay ($2\nu\beta\beta$), as well as the intrinsic contaminations from ^{68}Ga , the successor of ^{68}Ge , and ^{60}Co , which are produced by cosmic activation, were simulated.

The simulated energy spectra were used to decompose the energy spectra of the golden and the BEGe sum data set above 570 keV into their single contributions. With the help of a maximum likelihood fit, the individual contributions from each background contamination were identified and complete background models were developed.

The background composition around $Q_{\beta\beta}$ was examined in great detail. For both data sets, the dominating contributions to the energy spectrum in this region were alpha and beta decays of the ^{238}U chain, beta decays of the ^{232}Th chain, as well as decays of ^{42}K . For the BEGe sum data set, the contributions from ^{42}K decays on the detector surfaces were enhanced compared to the golden data set. The stability of the background model was verified by several cross-checks of the analysis. In a first step of unblinding, a part of the data in the 40 keV-window around $Q_{\beta\beta}$ was made available for analysis. Only the innermost ± 5 keV (± 4 keV) remained blinded, whereas the rest of the window was opened for the golden and silver (BEGe sum) data sets. The predictions of the background models for the opened window were in good agreement with the data.

The window between 1930 keV and 2190 keV was used to determine the background index (BI). The ± 5 keV windows around the single-escape peak of ^{208}Tl at 2104 keV and the ^{212}Bi photon line at 2119 keV, as well as the ± 5 keV (± 4 keV) blinded window for the golden data set (BEGe sum data set) around $Q_{\beta\beta}$ were excluded. It was shown that the spectral shape of the background model in this window could be approximated by a flat distribution. Hence, the BI could be determined by counting all events in the window and dividing by its width and the exposure of the data set. For the golden data set, $BI = 18.5^{+2.3}_{-2.2} \cdot 10^{-3}$ cts/(keV · kg · yr), whereas for the BEGe sum data set $BI = 41.3^{+10.4}_{-8.4} \cdot 10^{-3}$ cts/(keV · kg · yr). Due to the limited exposure of the silver data set, no individual background model could be developed. However, its background composition was assumed to be similar to that of the golden data set, with additional contributions from the natural decay chains of ^{232}Th and ^{238}U . Therefore, also in this case a constant background around $Q_{\beta\beta}$ could be assumed. It was determined to be $BI = 63.4^{+18.0}_{-14.3} \cdot 10^{-3}$ cts/(keV · kg · yr).

A combined analysis of the energy spectra of the golden and the BEGe sum data sets with an analogous approach as the one used to define the background model composition allowed to measure the half-life of $2\nu\beta\beta$, $T_{1/2}^{2\nu}$. This lepton number conserving Standard-Model permitted process has been observed for several isotopes. Thanks to the extremely low background level in the GERDA experiment, a signal-to-background ratio of 3 : 1 could be reached. This allowed for a precision of the measurement of $T_{1/2}^{2\nu}$ of ^{76}Ge unprecedented by previous experiments. The half-life was determined to be

$$T_{1/2}^{2\nu} = (1.96 \pm 0.13) \cdot 10^{21} \text{ yr.}$$

The result was in good agreement with a previous analysis of a subset of the golden

data set.

Several theories exist that predict neutrinoless double beta decay with emission of an additional particle, the majoron ($0\nu\beta\beta\chi$), or even two majorons ($0\nu\beta\beta\chi\chi$). According to the theory, these beyond-Standard Model processes can be lepton number conserving or lepton number violating. The various models predicting $0\nu\beta\beta\chi$ or $0\nu\beta\beta\chi\chi$ can be grouped into categories defined by the energy spectrum of the electrons released in the decay. They are classified by their spectral index, n , with $n = 1, 2, 3$, and 7.

In order to search for $0\nu\beta\beta\chi(\chi)$ in the GERDA data, the analysis framework developed to measure the half-life of $2\nu\beta\beta$ was expanded to allow also for the contributions of the decay mode corresponding to a certain spectral index. The analysis was performed for all four possibilities of n . No indication for a contribution of $0\nu\beta\beta\chi$ or $0\nu\beta\beta\chi\chi$ was found in any of the cases. Lower limits on the half-lives, $T_{1/2}^{0\nu\chi(\chi)}$, were determined from the quantiles of 90% probability of the posterior probability distributions. The results constitute the most stringent limits on $0\nu\beta\beta\chi(\chi)$ of ^{76}Ge obtained to date. For the standard mode ($n = 1$), the lower limit was determined to be

$$T_{1/2}^{0\nu\chi} > 4.15 \cdot 10^{23} \text{ yr.}$$

From the lower limit on $T_{1/2}^{0\nu\chi}$, an upper limit on the effective neutrino-majoron coupling constant, $\langle g \rangle$, can be inferred,

$$\langle g \rangle < (3.5 - 8.8) \cdot 10^{-5}.$$

Finally, a search for $0\nu\beta\beta$ of ^{76}Ge was conducted using the GERDA Phase I data. This process violates lepton number by two and is therefore not allowed by the Standard Model. The existence of $0\nu\beta\beta$ would establish the Majorana nature of at least a part of the neutrino mass. If the exchange of a light Majorana neutrino is assumed as the dominating mechanism leading to the decay, its half-life, $T_{1/2}^{0\nu}$, would allow direct conclusions on the mass and the Majorana nature of the neutrino. The experimental signature of $0\nu\beta\beta$ is a peak at $Q_{\beta\beta}$.

A combined analysis of the golden, silver, and BEGe sum data sets was performed. The previously blinded $\pm 5 \text{ keV}$ windows ($\pm 4 \text{ keV}$ for the BEGe sum data set) around $Q_{\beta\beta}$ contained a total of seven events, whereas 4.9 ± 0.5 events were expected from background. After the application of pulse shape analysis (PSA) methods, three events remained, none of them within one standard deviation of the energy resolution of $Q_{\beta\beta}$. The expected number of background events after the application of PSA was $2.5^{+0.4}_{-0.3}$.

Two statistical approaches were adapted to analyze the energy spectra around $Q_{\beta\beta}$, one based on a counting method, the other one based on a spectral fit. In both cases, a model envisaging not only the contributions from a flat background, but also from $0\nu\beta\beta$ was clearly rejected, whereas the background-only model was favored. Thus, there was no indication for a contribution from $0\nu\beta\beta$ of ^{76}Ge in the GERDA Phase I data. Lower limits on $T_{1/2}^{0\nu}$ were extracted as the quantiles of 90% probability of the posterior probability distributions. The most stringent limit was obtained with the

spectral fit method, which gave

$$T_{1/2}^{0\nu} > 1.83 \cdot 10^{25} \text{ yr.}$$

The result was in agreement with limits from previous experiments and an alternative analysis of the GERDA Phase I data. When the exchange of a light Majorana neutrino is assumed as the dominating mechanism of the process, the lower limit on $T_{1/2}^{0\nu}$ allows to calculate an upper limit on the effective Majorana neutrino mass,

$$\langle m_{\beta\beta} \rangle < (0.3 - 0.5) \text{ eV.}$$

The excellent performance of the GERDA experiment in its first phase allowed the most precise measurement of $T_{1/2}^{2\nu}$ of ^{76}Ge to date, improved lower limits on $T_{1/2}^{0\nu\chi(\chi)}$ of ^{76}Ge for all modes of $0\nu\beta\beta\chi(\chi)$ with $n = 1, 2, 3,$ and $7,$ as well as a very stringent lower limit on $T_{1/2}^{0\nu}$.

The second phase of the experiment envisages 30 BEGe detectors with a total of 20 kg in addition to the coaxial detectors. The good performance of the PSA for the BEGe detectors, as well as the read-out of scintillation light in the LAr will reduce the background by one order of magnitude compared to Phase I. With an exposure of 100 kg, a sensitivity corresponding to $T_{1/2}^{0\nu} > 2.0 \cdot 10^{26}$ yr could be reached. Also, important improvements on the precision of $T_{1/2}^{2\nu}$ and the lower limits of $T_{1/2}^{0\nu\chi(\chi)}$ are expected.

Appendix A

List of Monte Carlo Simulations

This appendix gives a summary of all MC simulations used for data analysis. For details about the simulation procedure refer to Chapter 8. The number of decays simulated for each source was chosen such that the statistical uncertainty due to the MC spectra would be negligible in the fitting procedures.

A.1 Alpha Model

Table A.1: Summary of all MC simulations needed for the alpha model. The simulations were used for the analysis of the golden as well as for the BEGe sum data set. Given are the simulated sources, the location of the decays, the simulation mode, the configuration, and the number of simulated decays, N_{sim} . For the simulation modes, the abbreviations **FA** for **Full array**, **SD in FA** for **Single detectors in full array**, and **SD** for **Single detector** are used. For all isotopes, the simulations were performed for p^+ -layer thicknesses of 100 nm, 200 nm, ..., 1000 nm.

Isotope	Location	Mode	Configuration	N_{sim}
^{210}Po	p^+ -surface	SD	<i>configANG3</i>	10^8
^{226}Ra	p^+ -surface	SD	<i>configANG3</i>	10^7
^{222}Rn	p^+ -surface	SD	<i>configANG3</i>	10^7
^{218}Po	p^+ -surface	SD	<i>configANG3</i>	10^7
^{214}Po	p^+ -surface	SD	<i>configANG3</i>	10^7
^{226}Ra	LAr at p^+ -surface	SD	<i>configANG3</i>	10^7
^{222}Rn	LAr at p^+ -surface	SD	<i>configANG3</i>	10^7
^{218}Po	LAr at p^+ -surface	SD	<i>configANG3</i>	10^7
^{214}Po	LAr at p^+ -surface	SD	<i>configANG3</i>	10^7

A.2 Golden Data Set

Table A.2: Part I: Summary of all MC simulations for the golden data set, excluding those for the alpha model. Given are the simulated sources, the location of the decays, the simulation mode, the configuration, and the number of simulated decays, N_{sim} . For the simulation modes, the abbreviations **FA** for **Full array**, **SD in FA** for **Single detectors in full array**, and **SD** for **Single detector** are used.

Isotope	Location	Mode	Configuration	N_{sim}
^{214}Pb	p^+ -surface	SD	<i>configANG3</i>	10^7
^{214}Pb	n^+ -surface	SD	<i>configANG3</i>	10^7
^{214}Pb	LAr at p^+ -surface	SD	<i>configANG3</i>	10^7
^{214}Pb	holders	FA	<i>configNAT</i>	10^8
^{214}Pb	mini-shrouds	FA	<i>configNAT</i>	10^8
^{214}Pb	shroud	FA	<i>configNAT</i>	10^9
^{214}Bi	p^+ -surface	SD	<i>configANG3</i>	10^7
^{214}Bi	n^+ -surface	SD	<i>configANG3</i>	10^7
^{214}Bi	LAr at p^+ -surface	SD	<i>configANG3</i>	10^7
^{214}Bi	holders	FA	<i>configNAT</i>	10^8
^{214}Bi	mini-shrouds	FA	<i>configNAT</i>	10^8
^{214}Bi	shroud	FA	<i>configNAT</i>	10^9
^{228}Ac	holders	FA	<i>configNAT</i>	10^8
^{228}Ac	shroud	FA	<i>configNAT</i>	10^9
^{212}Bi	holders	FA	<i>configNAT</i>	10^8
^{212}Bi	shroud	FA	<i>configNAT</i>	10^9
^{208}Tl	holders	FA	<i>configNAT</i>	10^8
^{208}Tl	shroud	FA	<i>configNAT</i>	10^9
^{208}Tl	heatexchanger	FA	<i>configNAT</i>	10^{10}

Table A.3: Part II: Summary of all MC simulations for the golden data set, excluding those for the alpha model. Given are the simulated sources, the location of the decays, the simulation mode, the configuration, and the number of simulated decays, N_{sim} . For the simulation modes, the abbreviations **FA** for **Full array**, **SD in FA** for **Single detectors in full array**, and **SD** for **Single detector** are used. For the isotopes marked with “*”, the simulations were used for the determination of systematic uncertainties.

Isotope	Location	Mode	Configuration	N_{sim}
^{42}K	in LAr	FA	<i>configNAT</i>	10^9
^{42}K	p^+ -surface	SD	<i>configANG3</i>	10^6
^{42}K	n^+ -surface	SD	<i>configANG3</i>	10^8
$^{42}\text{K}^*$	n^+ -surface	SD	<i>configANG3</i> ^a	10^8
$^{42}\text{K}^*$	n^+ -surface	SD	<i>configANG3</i> ^b	10^8
^{60}Co	holders	FA	<i>configNAT</i>	10^7
^{60}Co	in active volume	SD in FA	<i>configNAT</i>	9×10^6 ^c
^{60}Co	in dead volume	SD in FA	<i>configNAT</i>	9×10^6 ^c
^{40}K	holders	FA	<i>configNAT</i>	10^8
$2\nu\beta\beta$	in active volume	SD in FA	<i>configNAT</i>	9×10^6 ^c
$2\nu\beta\beta$	in dead volume	SD in FA	<i>configNAT</i>	9×10^6 ^c
$0\nu\beta\beta\chi$ (n=1)	in active volume	SD in FA	<i>configNAT</i>	9×10^6 ^c
$0\nu\beta\beta\chi$ (n=1)	in dead volume	SD in FA	<i>configNAT</i>	9×10^6 ^c
$0\nu\beta\beta\chi$ (n=2)	in active volume	SD in FA	<i>configNAT</i>	9×10^6 ^c
$0\nu\beta\beta\chi$ (n=2)	in dead volume	SD in FA	<i>configNAT</i>	9×10^6 ^c
$0\nu\beta\beta\chi(\chi)$ (n=3)	in active volume	SD in FA	<i>configNAT</i>	9×10^6 ^c
$0\nu\beta\beta\chi(\chi)$ (n=3)	in dead volume	SD in FA	<i>configNAT</i>	9×10^6 ^c
$0\nu\beta\beta\chi\chi$ (n=7)	in active volume	SD in FA	<i>configNAT</i>	9×10^6 ^c
$0\nu\beta\beta\chi\chi$ (n=7)	in dead volume	SD in FA	<i>configNAT</i>	9×10^6 ^c

^a $d_{n^+} = \mu(d_{n^+}) - \sigma(d_{n^+}) = 1.2$ mm

^b $d_{n^+} = \mu(d_{n^+}) + \sigma(d_{n^+}) = 2.6$ mm

^c 10^6 decays for each of the nine coaxial detectors in the array, excluding the two natural detectors in the 1-string arm.

A.3 BEGe Sum Data Set

Table A.4: Part I: Summary of all MC simulations for the BEGe sum data set, excluding those for the alpha model. Given are the simulated sources, the location of the decays, the simulation mode, the configuration, and the number of simulated decays, N_{sim} . For the simulation modes the abbreviations **FA** for **Full array**, **SD in FA** for **Single detectors in full array**, and **SD** for **Single detector** are used.

Isotope	Location	Mode	Configuration	N_{sim}
^{214}Pb	p^+ -surface	SD	<i>configGD32B</i>	10^6
^{214}Pb	n^+ -surface	SD	<i>configGD32B</i>	10^7
^{214}Pb	LAr at p^+ -surface	SD	<i>configGD32B</i>	10^8
^{214}Pb	holders	FA	<i>configBEGE</i>	10^8
^{214}Pb	mini-shrouds	FA	<i>configBEGE</i>	10^8
^{214}Pb	shroud	FA	<i>configBEGE</i>	10^9
^{214}Bi	p^+ -surface	SD	<i>configGD32B</i>	10^6
^{214}Bi	n^+ -surface	SD	<i>configGD32B</i>	10^7
^{214}Bi	LAr at p^+ -surface	SD	<i>configGD32B</i>	10^8
^{214}Bi	holders	FA	<i>configBEGE</i>	10^8
^{214}Bi	mini-shrouds	FA	<i>configBEGE</i>	10^8
^{214}Bi	shroud	FA	<i>configBEGE</i>	10^9
^{228}Ac	holders	FA	<i>configBEGE</i>	10^8
^{228}Ac	shroud	FA	<i>configBEGE</i>	10^9
^{212}Bi	holders	FA	<i>configBEGE</i>	10^8
^{212}Bi	shroud	FA	<i>configBEGE</i>	10^9
^{208}Tl	holders	FA	<i>configBEGE</i>	10^8
^{208}Tl	shroud	FA	<i>configBEGE</i>	10^9

Table A.5: Part II: Summary of all MC simulations for the BEGe sum data set, excluding those for the alpha model. Given are the simulated sources, the location of the decays, the simulation mode, the configuration, and the number of simulated decays, N_{sim} . For the simulation modes the abbreviations **FA** for **Full array**, **SD in FA** for **Single detectors in full array**, and **SD** for **Single detector** are used.

Isotope	Location	Mode	Configuration	N_{sim}
^{42}K	in LAr	FA	<i>configBEGE</i>	10^9
^{42}K	p^+ -surface	SD	<i>configGD32B</i>	10^6
^{42}K	n^+ -surface	SD	^a	4×10^8
^{60}Co	holders	FA	<i>configBEGE</i>	10^8
^{60}Co	in active volume	SD in FA	<i>configBEGE</i>	5×10^6 ^b
^{60}Co	in dead volume	SD in FA	<i>configBEGE</i>	5×10^6 ^b
^{68}Ga	in active volume	SD in FA	<i>configBEGE</i>	5×10^6 ^b
^{68}Ga	in dead volume	SD in FA	<i>configBEGE</i>	5×10^6 ^b
^{40}K	holders	FA	<i>configBEGE</i>	10^8
$2\nu\beta\beta$	in active volume	SD in FA	<i>configBEGE</i>	5×10^6 ^b
$2\nu\beta\beta$	in dead volume	SD in FA	<i>configBEGE</i>	5×10^6 ^b
$0\nu\beta\beta\chi$ (n=1)	in active volume	SD in FA	<i>configBEGE</i>	5×10^6 ^b
$0\nu\beta\beta\chi$ (n=1)	in dead volume	SD in FA	<i>configBEGE</i>	5×10^6 ^b
$0\nu\beta\beta\chi$ (n=2)	in active volume	SD in FA	<i>configBEGE</i>	5×10^6 ^b
$0\nu\beta\beta\chi$ (n=2)	in dead volume	SD in FA	<i>configBEGE</i>	5×10^6 ^b
$0\nu\beta\beta\chi(\chi)$ (n=3)	in active volume	SD in FA	<i>configBEGE</i>	5×10^6 ^b
$0\nu\beta\beta\chi(\chi)$ (n=3)	in dead volume	SD in FA	<i>configBEGE</i>	5×10^6 ^b
$0\nu\beta\beta\chi\chi$ (n=7)	in active volume	SD in FA	<i>configBEGE</i>	5×10^6 ^b
$0\nu\beta\beta\chi\chi$ (n=7)	in dead volume	SD in FA	<i>configBEGE</i>	5×10^6 ^b

^a Separate MC simulation for each of the four active BEGe detectors, taking into account a transition layer.

^b 10^6 decays for each of the five BEGe detectors in the array.

Appendix B

First Measurement of the Half-life of Neutrino Accompanied Double Beta Decay with GERDA Phase I

An analysis to determine the half-life of $2\nu\beta\beta$ in ${}^{76}\text{Ge}$, $T_{1/2}^{2\nu}$, was performed on a subset of the golden data set [86, 199, 200].

B.1 The Data Set

The data with a total exposure of $5.04\text{ kg}\cdot\text{yr}$ was recorded with detectors ANG2-ANG5, RG1 and RG2 between November 2011 and March 2012. The live time was 125.9 d for all six detectors. The data was processed analogously to the procedure described in Chapter 7. Since during this time period the detectors ANG1 and RG3 had not yet been completely turned off, their energy information could be used for the detector anti-coincidence cut. The energy range between 600 keV and 1800 keV was analyzed. This range lies well above the endpoint of the ${}^{39}\text{Ar}$ spectrum and is dominated by $2\nu\beta\beta$. From MC it was determined, that a $2\nu\beta\beta$ decay taking place in the active volume of an enriched coaxial detector has a probability of 63.5% to leave an energy deposit inside the analyzed energy range. The probability to contribute to the spectrum above 1800 keV is $< 0.02\%$. The energy spectra of all six active enriched coaxial detectors contained a total of 8796 events in the analyzed energy region. The single detector spectra were not summed up, but considered separately for the analysis.

B.2 The Monte Carlo Simulation

The Monte Carlo (MC) simulation described in Chapter 8 for the golden data set was used. While the simulation procedure was identical, the post-processing differed in some points. The energy smearing of the spectra was based on the average FWHM curves derived from the calibration runs during the data taking period of the analyzed

data set, that is between November 2011 and March 2012. For the detector anti-coincidence cut, also ANG1 and RG3 were considered in analogy to the data. After the smearing procedure and the anti-coincidence cut, the single detector spectra of each simulation of a background contamination were normalized in the range between 600 keV and 1800 keV. The normalized distribution describing the energy spectrum of contamination c in detector j is referred to as $\varphi_j^{c,\text{norm}}(E)$.

The spectra resulting from the simulations of $2\nu\beta\beta$ in the active and dead volumes of the six detectors considered for the analysis were normalized according to the number of simulated events to represent the detection efficiencies of the corresponding detector for the active and dead volume, $\varepsilon_{act,j} \cdot \varphi_{act,j}^{2\nu,\text{norm}}(E)$ and $\varepsilon_{dead,j} \cdot \varphi_{dead,j}^{2\nu,\text{norm}}(E)$.

B.3 Statistical Analysis Method and Fit Model

The analysis adapted the binned maximum likelihood approach described in [166]. The energy region between 600 keV and 1800 keV was divided into 40 bins of 30 keV width each. The model fitted to the data spectra contained the contributions from $2\nu\beta\beta$, ^{42}K in LAr, ^{214}Bi in the holders, and ^{40}K in the holders. Due to the small statistical significance of the contributions from ^{228}Th , ^{228}Ac , and ^{60}Co and the resulting lack in discriminating power, these contributions were not included in the fit. Also, no contributions for different source positions were considered in the model, since the small exposure of the data set would not have allowed a distinction. An estimate of the impact of additional model components and varying source positions was determined for the systematic uncertainty.

In contrast to the analysis described in Chapter 9, the energy spectra of the six detectors were kept separate for the analysis. An individual background model was developed for each of them, with the only common parameter being $T_{1/2}^{2\nu}$. Equation (9.2) then becomes

$$P(\mathbf{n}|\boldsymbol{\lambda}) = \prod_i \prod_j P(n_{ij}|\lambda_{ij}) = \prod_i \prod_j \frac{e^{-\lambda_{ij}} \lambda_{ij}^{n_{ij}}}{n_{ij}!}, \quad (\text{B.1})$$

with n_{ij} describing the number of events in the i -th bin of the measured data spectrum of the j -th detector. For the background contaminations, c , the expectation for the i -th bin of detector j is

$$\lambda_{ij}^c = \mathcal{N}_j^c \int_{\Delta E_i} \varphi_j^{c,\text{norm}}(E) dE. \quad (\text{B.2})$$

For the contributions due to $2\nu\beta\beta$, the expected number of events in the i -th bin of detector j is

$$\lambda_{i,j}^{2\nu} = \frac{k_0}{t_{1/2}} M_j f_{76,j} T_j \cdot [f_{act,j} \varepsilon_{act,j} \mathcal{F}_{act,i,j}^{2\nu} + (1 - f_{act,j}) \varepsilon_{dead,j} \mathcal{F}_{dead,i,j}^{2\nu}], \quad (\text{B.3})$$

with

$$\mathcal{F}_{act,i,j}^{2\nu} = \int_{\Delta E_i} \varphi_{act,j}^{2\nu,\text{norm}}(E) dE \quad (\text{B.4})$$

Table B.1: Main characteristics of the detectors used in this analysis: isotopic abundance of ^{76}Ge , f_{76} , total mass, M , fraction of active mass, f_{act} , with the uncorrelated and correlated uncertainty. The last column gives the results for $T_{1/2}^{2\nu}$ from an individual analysis of each detector.

Detector	f_{76} (%)	M (kg)	f_{act} (%)	$T_{1/2}^{2\nu}$ (10^{21} yr)
ANG2	86.6 ± 2.5	2.833	$87 \pm 4 \pm 3$	$1.99^{+0.14}_{-0.15}$
ANG3	88.3 ± 2.6	2.391	$87 \pm 5 \pm 3$	$1.69^{+0.15}_{-0.14}$
ANG4	86.3 ± 1.3	2.372	$90 \pm 5 \pm 3$	$1.94^{+0.14}_{-0.15}$
ANG5	85.6 ± 1.3	2.746	$83 \pm 4 \pm 3$	$1.79^{+0.12}_{-0.14}$
RG1	85.5 ± 1.5	2.110	$90 \pm 5 \pm 3$	$1.94^{+0.18}_{-0.14}$
RG2	85.5 ± 1.5	2.166	$83 \pm 5 \pm 3$	$1.93^{+0.16}_{-0.16}$

and

$$\mathcal{F}_{dead,i,j}^{2\nu} = \int_{\Delta E_i} \varphi_{dead,j}^{2\nu, \text{norm}}(E) dE, \quad (\text{B.5})$$

as already described in Equation (9.7). The factor $k_0 = (\ln(2) \cdot N_A) / (m_{76} \cdot 10^{21} \cdot 365 \text{ d}) = 15.06 (\text{kg} \cdot \text{d})^{-1}$, with N_A Avogadro's number and $m_{76} = 75.95 \text{ g/mol}$ the molar mass of ^{76}Ge , gives the decay rate of 1 kg of germanium enriched to 100% of ^{76}Ge for $T_{1/2}^{2\nu} = 10^{21} \text{ yr}$. The parameter determined in the fit was $t_{1/2}$, which represents $T_{1/2}^{2\nu}$ in units of 10^{21} yr . The contributions in detector j from decays in other detectors are below 0.1% and not taken into account in this analysis.

In addition to the model contributions, also the active volume fraction, $f_{act,j}$, and the enrichment fraction, $f_{76,j}$, of the single detectors were considered parameters in the fit.

The fit was performed using the Bayesian Analysis Toolkit BAT [150]. The prior probabilities were chosen flat and non-negative for ^{42}K , ^{40}K , and ^{214}Bi for all six detectors. Also the prior distribution for $t_{1/2}$ was uninformative: flat between 0 and 10, with $t_{1/2} = 10$ corresponding to $T_{1/2}^{2\nu} = 10^{22} \text{ yr}$, which is much larger than previous results, as given in Table 4.1. For $f_{act,j}$ and $f_{76,j}$, priors based on the knowledge about these parameters from measurements, see Table 6.1, were given as input to the fit. The uncertainty on $f_{act,j}$ is divided into an uncorrelated contribution, individual for each detector, and a correlated contribution, in common to all six detectors. The first had a Gaussian prior with the mean according to the measured value and σ according to the uncorrelated uncertainty. The latter had a Gaussian prior centered on zero and with a width corresponding to the correlated uncertainty. The priors on $f_{76,j}$ were Gaussian with mean value and standard deviation according to the measurements. Both $f_{76,j}$ and $f_{act,j}$ were required to be between 0% and 100%. All values used for the prior probabilities are summarized in Table B.1.

The total number of parameters was $1 + 5 \cdot N_{det} + 1 = 32$ ($t_{1/2}$, $\mathcal{N}_j^{214\text{Bi}}$, $\mathcal{N}_j^{42\text{K}}$, $\mathcal{N}_j^{40\text{K}}$,

$f_{act,j}, f_{76,j}$ for $j = 1, \dots, N_{det}$ with $N_{det} = 6$ the number of detectors, and one parameter for the correlated uncertainty on the active volume fraction).

Figure B.1 shows the sum of the best-fit model energy spectra of all six detectors together with the data energy spectrum. The global modes of the posterior probability distributions are used to scale the background contributions and the $2\nu\beta\beta$ energy spectrum of the single detectors before adding them up to the total model. The single background components are also shown. The 8796 events in the measured spectrum are matched with 8797.0 events in the model. The model is composed to 79.9% of the $2\nu\beta\beta$ spectrum, 14.1% of the ^{42}K spectrum, 3.8% of the ^{214}Bi spectrum, and 2.1% of the ^{40}K spectrum. The signal-to-background ratio is 4:1, and thus much improved compared to the previous measurement by the HdM experiment, which reached a ratio of 1:1 [4]. The p -value, calculated according to [169], is 0.77, indicating a very good agreement between model and data. The good agreement is confirmed by the ratio between data and model, shown in the lower panel of Fig. B.1. Also shown are the smallest intervals of 68%, 95%, and 99.9% probability of the ratio assuming the best-fit expectations. The intervals contain 30, 39, and 40 of the 40 ratio points, respectively. This matches very well the theoretical expectations for the fluctuations of 27.2, 38.0, and 40.0.

The half-life of $2\nu\beta\beta$ is determined from the marginalized posterior probability distribution, which is shown in Fig. B.2. The mode and smallest 68% probability interval result in

$$T_{1/2}^{2\nu} = 1.84 [1.76, 1.93] \cdot 10^{21} \text{ yr.} \quad (\text{B.6})$$

The uncertainty interval already incorporates the uncertainties from the nuisance parameters, that is the uncertainty on the active volume fraction and the enrichment fraction. In fact, the uncertainties on these values drive the uncertainty on $T_{1/2}^{2\nu}$. If they were known with infinite precision, the smallest probability interval would shrink to $[1.81, 1.87] \cdot 10^{21} \text{ yr.}$

Fits with individual $t_{1/2,j}$ for each detector were also performed. The results for these individual half-lives are listed in Table B.1. The results are mutually consistent, with $\chi^2/\nu = 3.02/5 = 0.60$.

B.4 Crosschecks and Systematic Uncertainties

Whereas the effects of the uncertainty on f_{76} and f_{act} were already included in the fitting procedure, several other components had to be taken into account when estimating the systematic uncertainty. They can be grouped into three categories:

Fit model As mentioned above, the possible contributions from ^{60}Co , ^{228}Ac , ^{228}Th or even other contaminations were not included in the fit model due to the small exposure of the data set and the thus reduced discrimination power. In order to estimate the related systematic uncertainty, a fit was performed with a model including also the spectra from ^{60}Co in the holders, ^{228}Ac in the holders, and a constant contribution. The latter was added to describe the contributions from

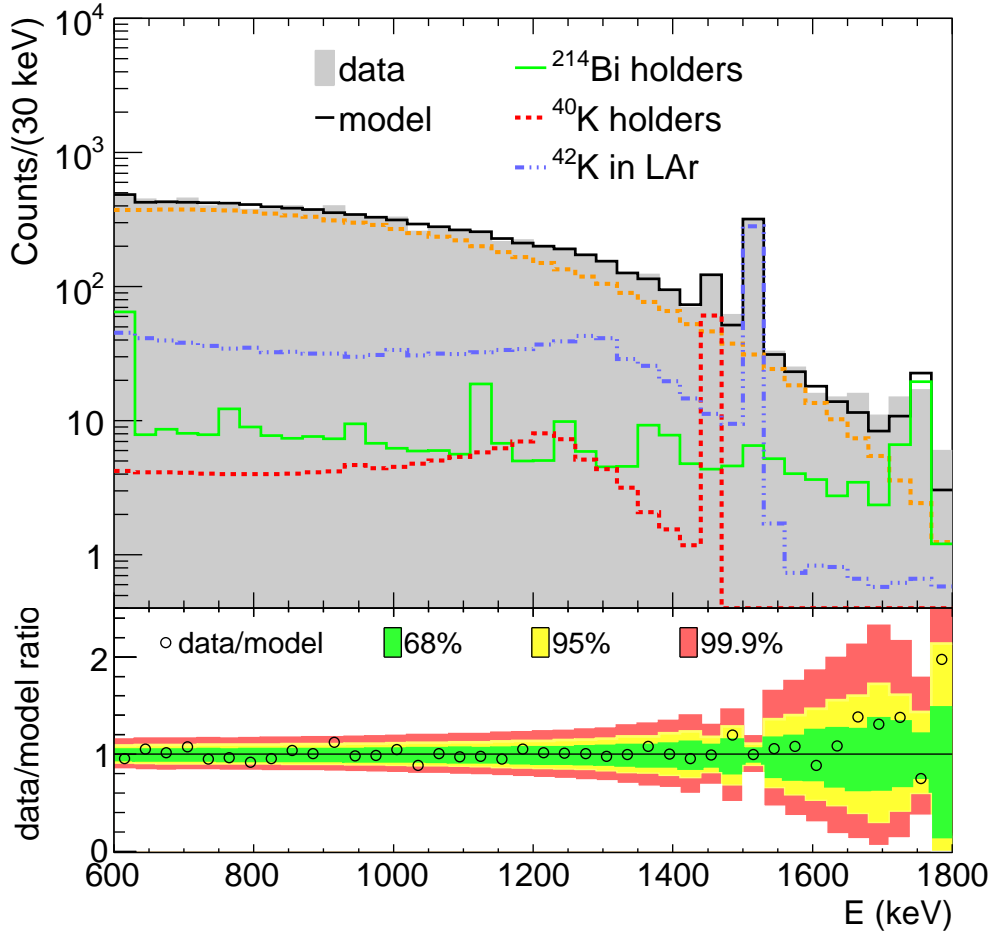


Figure B.1: Best-fit model and data energy spectrum for the sum of the six detectors. The sum of the individual model components scaled according to the global modes are also drawn. The lower panel shows the ratio of data and model and the smallest intervals of 68 % (green), 95 % (yellow), and 99.9 % (red) probability for the ratio assuming the best-fit parameters.

^{228}Th , whose distribution can be approximated as flat due to the small number of counts expected in the fit window, and to account for possible unidentified sources. This added additional 18 parameters to the fit ($\mathcal{N}_j^{60\text{Co}}$, $\mathcal{N}_j^{228\text{Ac}}$, constant \mathcal{K}_j , for $j = 1, \dots, N_{det}$, with $N_{det} = 6$). The uncertainty is asymmetric, since any further background component can only reduce the number of events attributed to $2\nu\beta\beta$ and thus lead to a longer $T_{1/2}^{2\nu}$. It is estimated to be +5.3%.

Another uncertainty arises from the shape of the energy spectra of the background contributions used in the model, that is of ^{214}Bi , ^{42}K , and ^{40}K . Their decays were simulated in the holders and no other source positions were taken into account. Different source positions would lead to different peak-to-continuum ratios in the energy spectra. Several fits were performed for different source positions for all three contributions. Also, artificial variations of the peak-to-continuum ratios were applied. For ^{42}K , these were as large as 5%, while for

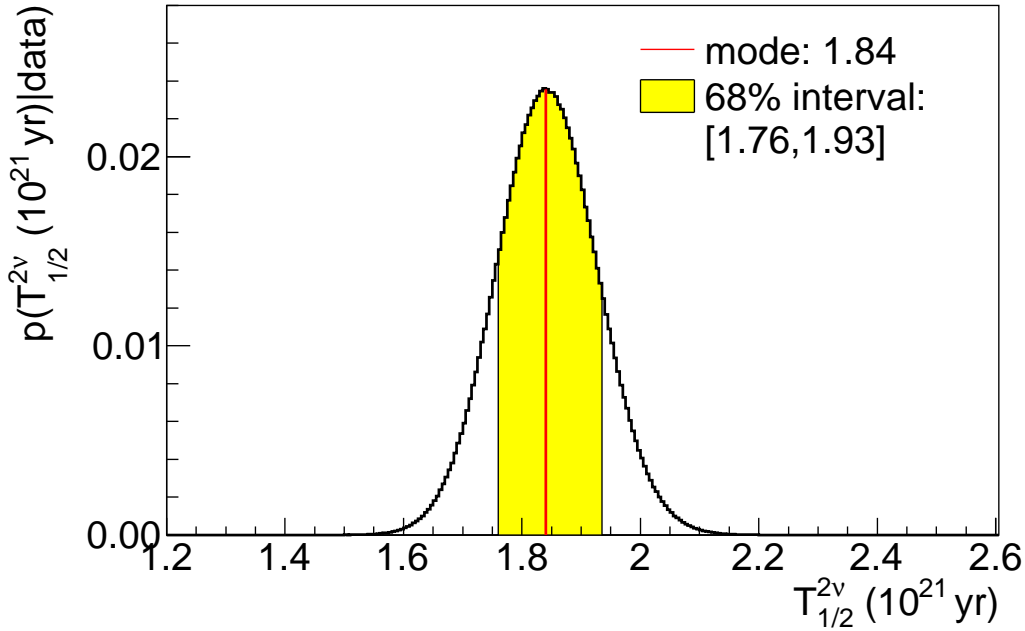


Figure B.2: Marginalized posterior probability distribution $P(t_{1/2}|\mathbf{n})$ for the parameter $t_{1/2}$, which represents $T_{1/2}^{2\nu}$ in units of 10^{21} yr. The mode and smallest 68% interval are marked.

^{40}K , the continuum was completely removed in one case and doubled in another case. The total uncertainty derived from these variations was estimated to be $\pm 2.1\%$.

For the primary spectrum of $2\nu\beta\beta$, the code DECAY0 was used. Its description has been cross-checked for several isotopes, such as ^{82}Se , ^{96}Zn , and ^{150}Nd with high-statistics data of the NEMO experiment [83,93,96,201,202]. An alternative description for the decay spectrum is the Primakoff-Rosen approximation [57], used for earlier measurements of $T_{1/2}^{2\nu}$ of ^{76}Ge [180]. Rerunning the analysis with the energy spectrum deriving from the parametrization of [180] leads to a difference of the order of 1%.

MC simulation A different source of uncertainty derives from the MC simulations. There will always be small differences between the implementation of the experimental geometry into the simulation framework and the real experimental setup. These can be variations in dimensions, placements, or small details that are not simulated. One example is the total detector mass, which differs by 0.6% from the real total detector mass for the *configNAT* setup, as small details like rounded detector corners are not accounted for by the MC. The contribution to the systematic uncertainty from this item was evaluated by redoing the analysis using simulations with displaced, removed, or resized volumes, for example holders made out of vacuum or lead instead of copper, and changed distances between the detector strings to take into account possible shielding effects. The

Table B.2: Systematic uncertainties on $T_{1/2}^{2\nu}$, which are not included in the fitting procedure.

Item	Uncertainty on $T_{1/2}^{2\nu}$ (%)
Additional background components	+5.3
Shape of ^{42}K , ^{40}K , ^{214}Bi energy spectra	± 2.1
Shape of $2\nu\beta\beta$ energy spectrum	± 1
Total fit model	+5.8 -2.3
Precision of the MC geometry	± 1
Accuracy of the MC tracking	± 2
Total MC	± 2.2
Data acquisition and selection	± 0.5
Total systematic uncertainty	+6.2 -3.3

total uncertainty due to the geometry model in the MC amounts to 1 %.

In addition, the uncertainties on the simulated particle interactions with matter deriving from uncertainties on cross-sections and final states have to be taken into account. From validations of the `GEANT4` particle tracking for electromagnetic processes in the energy range relevant for γ -ray spectroscopy [171–173], this uncertainty can be deduced to be 2 %. It is mainly due to the propagation of the photons from the background contributions. The electrons emitted in $2\nu\beta\beta$ have a small range of the order of 1 mm in germanium and thus deposit their energy very locally, apart from small losses due to escaping Bremsstrahlung photons.

Data acquisition and selection Small uncertainties may derive from the calculation of the live time, as well as the reconstruction and trigger efficiencies. Also, unphysical events might be present in the data set. These effects are expected to be very small and their effect on the fit result was estimated to be not larger than 0.5 %.

The single contributions are summarized in Table B.2. They amount to a total of $^{+6.2}_{-3.3}$ % when summed up in quadrature, resulting in $^{+0.11}_{-0.06} \cdot 10^{21}$ yr.

Cross-checks regarding the stability of the fit were performed. These involved variations of the energy range considered for the fit (but always excluding the region below 570 keV) and of the width of the bins, from 10 keV-bins to 50 keV-bins. The result for $T_{1/2}^{2\nu}$ varied only within its statistical limits.

The fit was also repeated using alternative priors for $f_{76,j}$ and $f_{act,j}$. For $f_{76,j}$, flat prior distributions between 0.8 and 0.9 were chosen, whereas for $f_{act,j}$ the prior probabilities were flat between 0.7 and 1.0. The results were compatible with the one from

the standard analysis, but exhibited larger fit uncertainties.

B.5 Results and Conclusion

The half-life of $2\nu\beta\beta$ of ^{76}Ge was derived from a subset of the golden data set with a total exposure of $5.04\text{ kg}\cdot\text{yr}$. An individual background model containing the contributions from decays of ^{42}K in the LAr, ^{214}Bi in the holders, and ^{40}K in the holders, was developed for each of the six detectors considered in the analysis. The half-life was estimated to be

$$T_{1/2}^{2\nu} = (1.84_{-0.08 \text{ fit}}^{+0.09} \quad {}_{-0.06 \text{ syst}}^{+0.11}) \cdot 10^{21} \text{ yr} = (1.84_{-0.10}^{+0.14}) \cdot 10^{21} \text{ yr}, \quad (\text{B.7})$$

with the fit and systematic uncertainties combined in quadrature.

Appendix C

Fit Models and Posterior Probability Distributions for $0 \nu \beta \beta \chi(\chi)$ with $n = 2, 3$ and 7

In this Appendix, the fit models and posterior probability distributions for the cases of $0 \nu \beta \beta \chi(\chi)$ with $n = 2, 3$ and 7 resulting from the analysis described in Chapter 10 are shown.

C.1 $0\nu\beta\beta\chi$ with $n = 2$

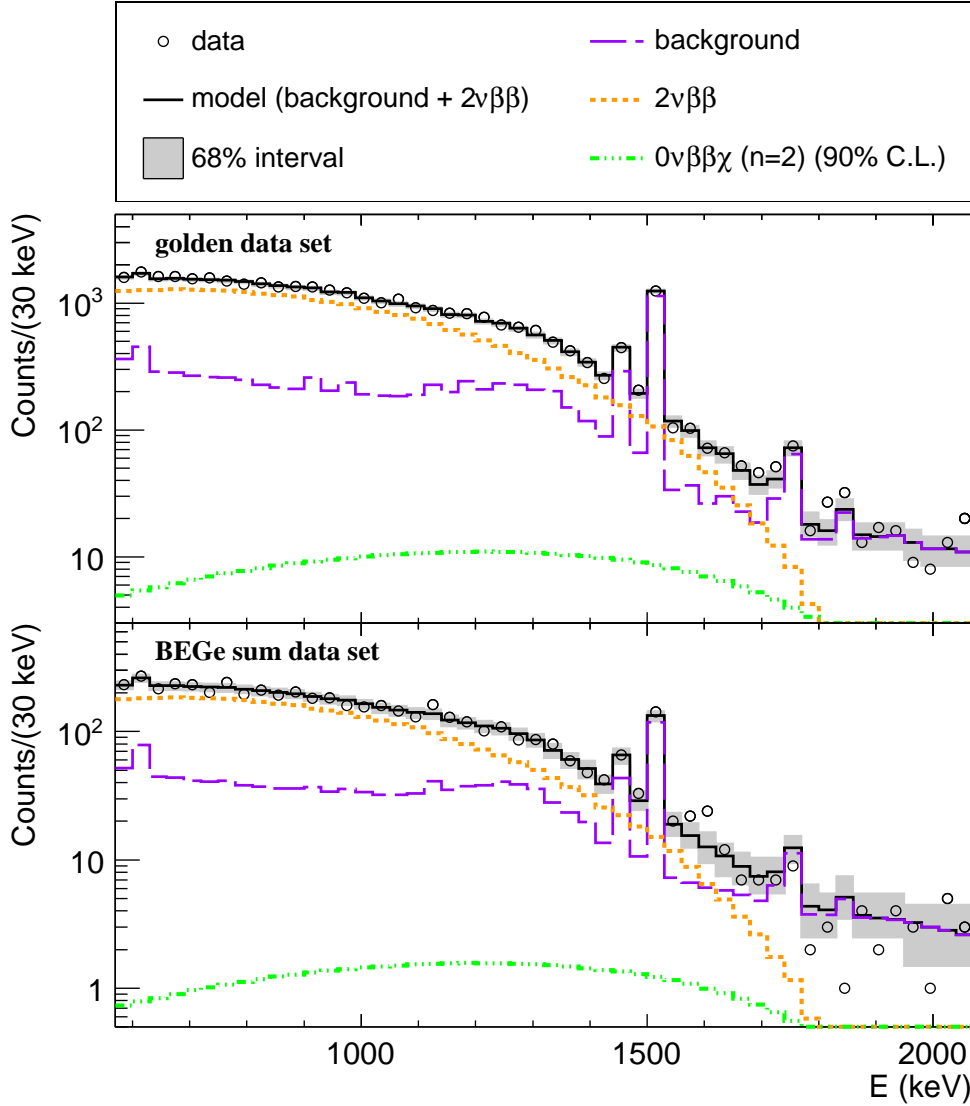


Figure C.1: Best-fit model and data energy spectrum for the golden and the BEGe sum data set for the case of spectral index $n = 2$. The contributions from $2\nu\beta\beta$ and the background contributions are shown separately. The best-fit model does not contain the contributions from $0\nu\beta\beta\chi$. The smallest interval of 68% probability for the model expectation is indicated in grey. Also shown is the upper limit for $0\nu\beta\beta\chi$ with $n = 2$ as determined from the 90% quantile of the marginalized posterior probability for $\text{inv-}t_{1/2}^{0\nu\chi(\chi)}$.

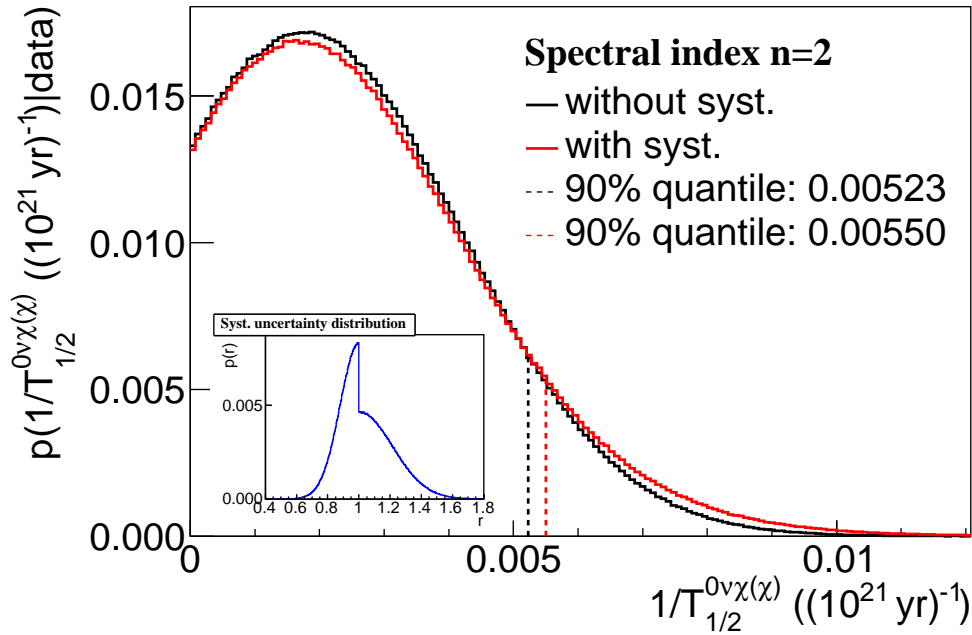


Figure C.2: Marginalized posterior probability distribution $P(\text{inv}_{t_{1/2}}^{0\nu\chi(\chi)}|\mathbf{n})$ for the parameter $\text{inv}_{t_{1/2}}^{0\nu\chi(\chi)}$, which represents $1/T_{1/2}^{0\nu\chi(\chi)}$ in units of $(10^{21} \text{ yr})^{-1}$ for the case of spectral index $n = 2$. The 90% quantile is marked. Also drawn is the posterior probability distribution after folding in the systematic uncertainty distribution, shown in the inset, and the resulting 90% quantile.

C.2 $0\nu\beta\beta\chi(\chi)$ with $n = 3$

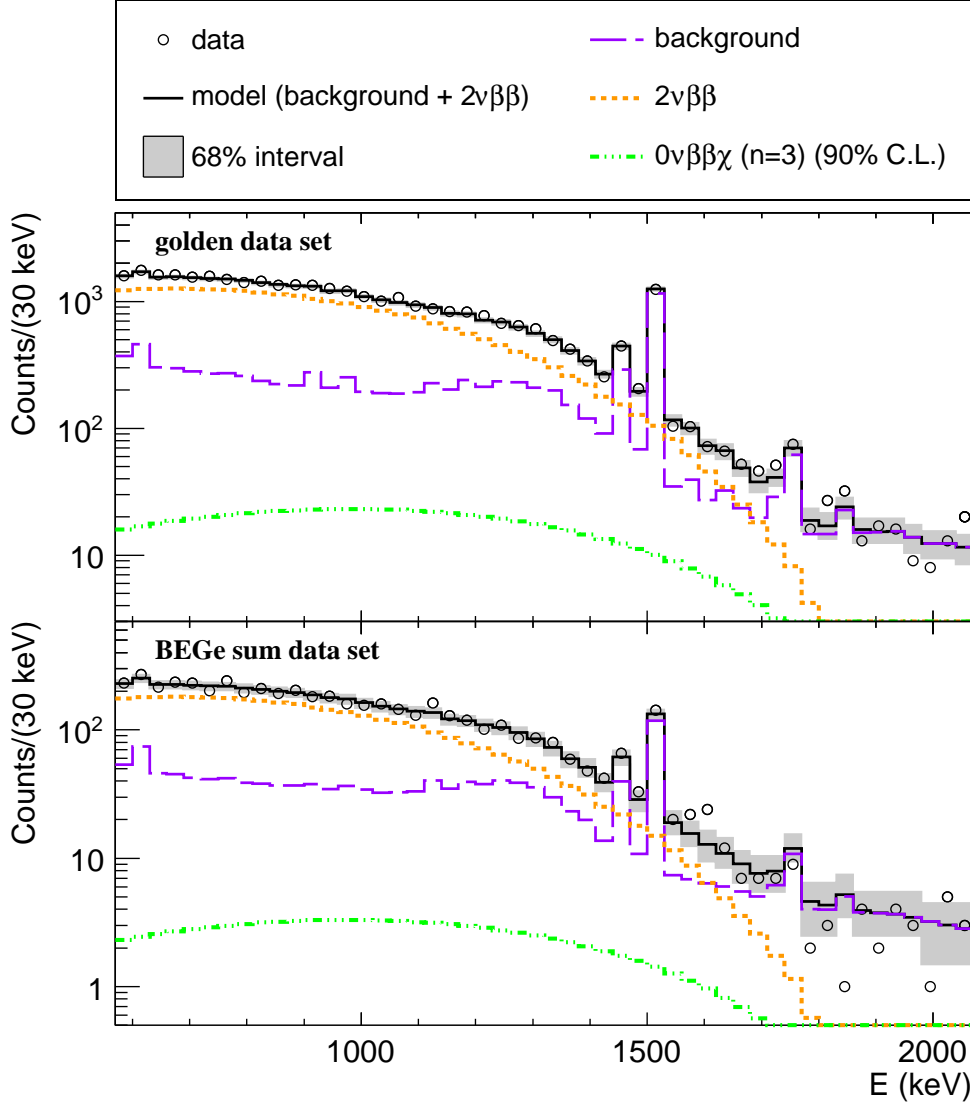


Figure C.3: Best-fit model and data energy spectrum for the golden and the BEGe sum data set for the case of spectral index $n = 3$. The contributions from $2\nu\beta\beta$ and the background contributions are shown separately. The best-fit model does not contain the contributions from $0\nu\beta\beta\chi$. The smallest interval of 68% probability for the model expectation is indicated in grey. Also shown is the upper limit for $0\nu\beta\beta\chi$ with $n = 3$ as determined from the 90% quantile of the marginalized posterior probability for $\text{inv-}t_{1/2}^{0\nu\chi(\chi)}$.

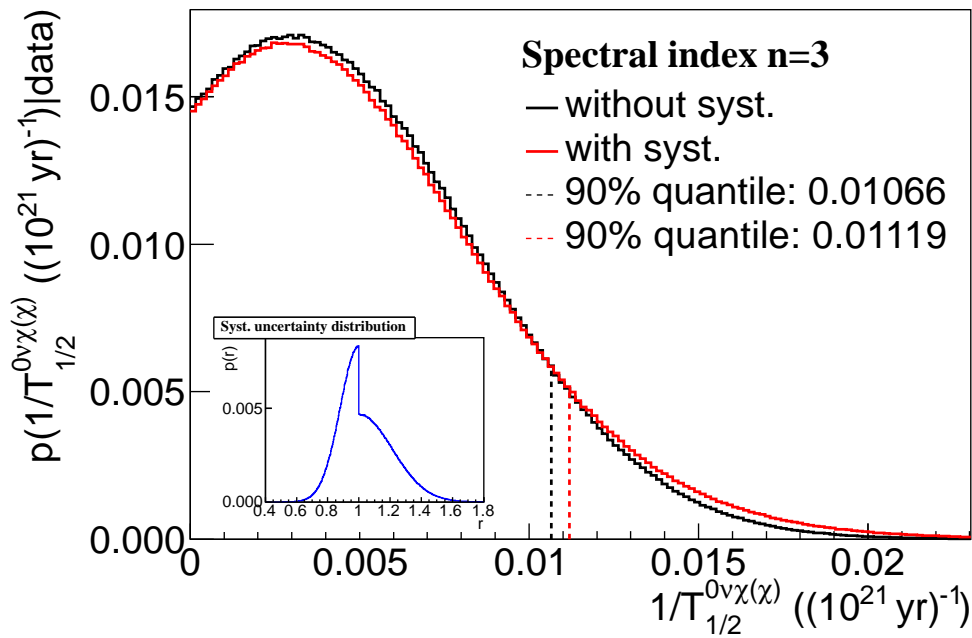


Figure C.4: Marginalized posterior probability distribution $P(\text{inv}_{t_{1/2}}^{0\nu\chi(\chi)}|\mathbf{n})$ for the parameter $\text{inv}_{t_{1/2}}^{0\nu\chi(\chi)}$, which represents $1/T_{1/2}^{0\nu\chi(\chi)}$ in units of $(10^{21} \text{ yr})^{-1}$ for the case of spectral index $n = 3$. The 90% quantile is marked. Also drawn is the posterior probability distribution after folding in the systematic uncertainty distribution, shown in the inset, and the resulting 90% quantile.

C.3 $0\nu\beta\beta\chi\chi$ with $n = 7$

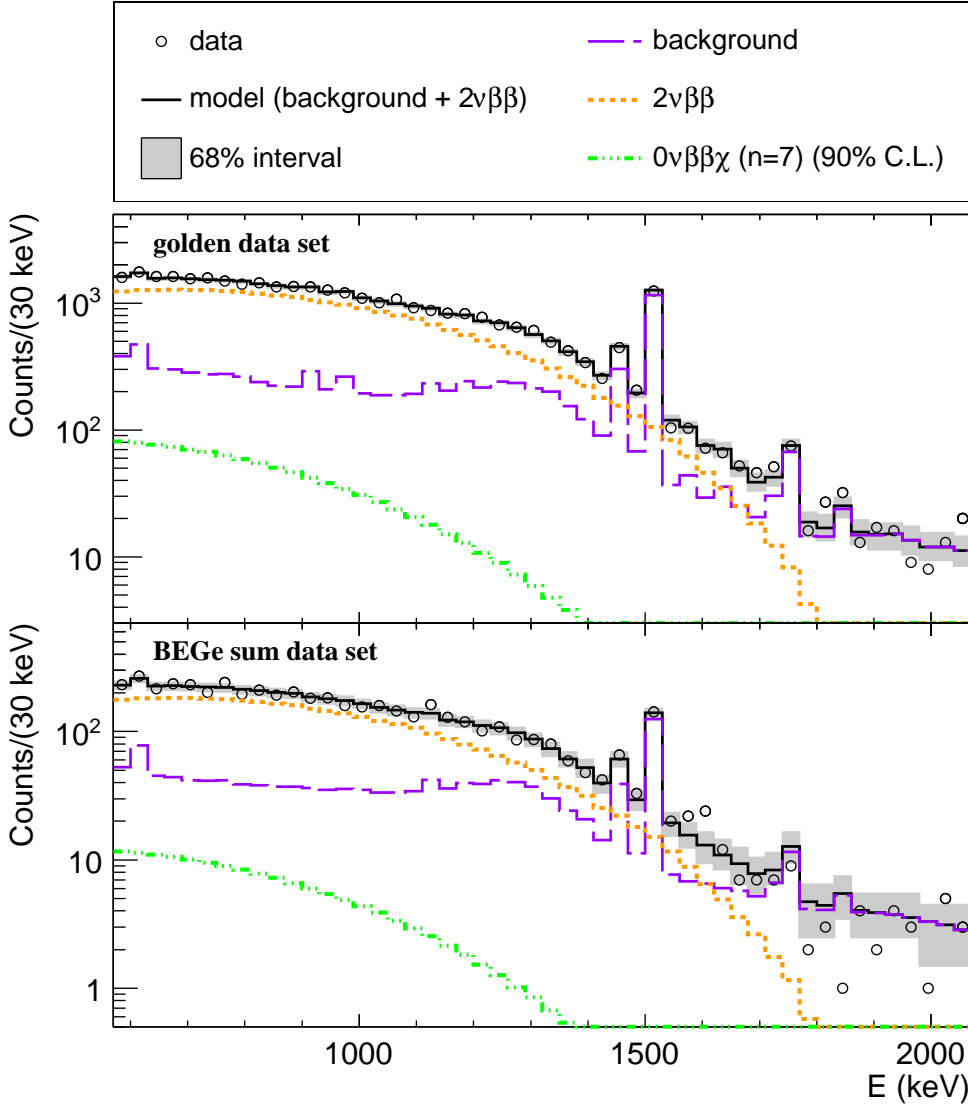


Figure C.5: Best-fit model and data energy spectrum for the golden and the BEGe sum data set for the case of spectral index $n = 7$. The contributions from $2\nu\beta\beta$ and the background contributions are shown separately. The best-fit model does not contain the contributions from $0\nu\beta\beta\chi$. The smallest interval of 68% probability for the model expectation is indicated in grey. Also shown is the upper limit for $0\nu\beta\beta\chi$ with $n = 7$ as determined from the 90% quantile of the marginalized posterior probability for $\text{inv-}t_{1/2}^{0\nu\chi(\chi)}$.

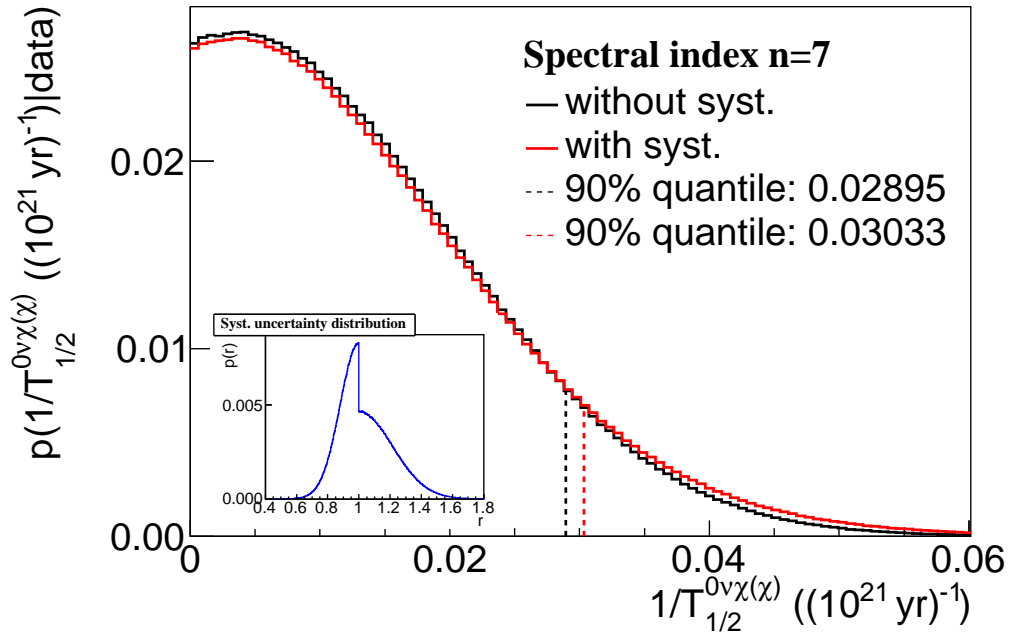


Figure C.6: Marginalized posterior probability distribution $P(\text{inv}_t_{1/2}^{0\nu\chi(\chi)}|\mathbf{n})$ for the parameter $\text{inv}_t_{1/2}^{0\nu\chi(\chi)}$, which represents $1/T_{1/2}^{0\nu\chi(\chi)}$ in units of $(10^{21} \text{ yr})^{-1}$ for the case of spectral index $n = 7$. The 90% quantile is marked. Also drawn is the posterior probability distribution after folding in the systematic uncertainty distribution, shown in the inset, and the resulting 90% quantile.

Appendix D

Average Detection Efficiency $\langle \varepsilon \rangle$ of $0\nu\beta\beta$

Distributions resulting from the sampling method used to determine the average detection efficiency $\langle \varepsilon \rangle$ of $0\nu\beta\beta$ for the golden and silver, as well as for the BEGe sum data sets. For details of the analysis refer to Sec. 11.3.

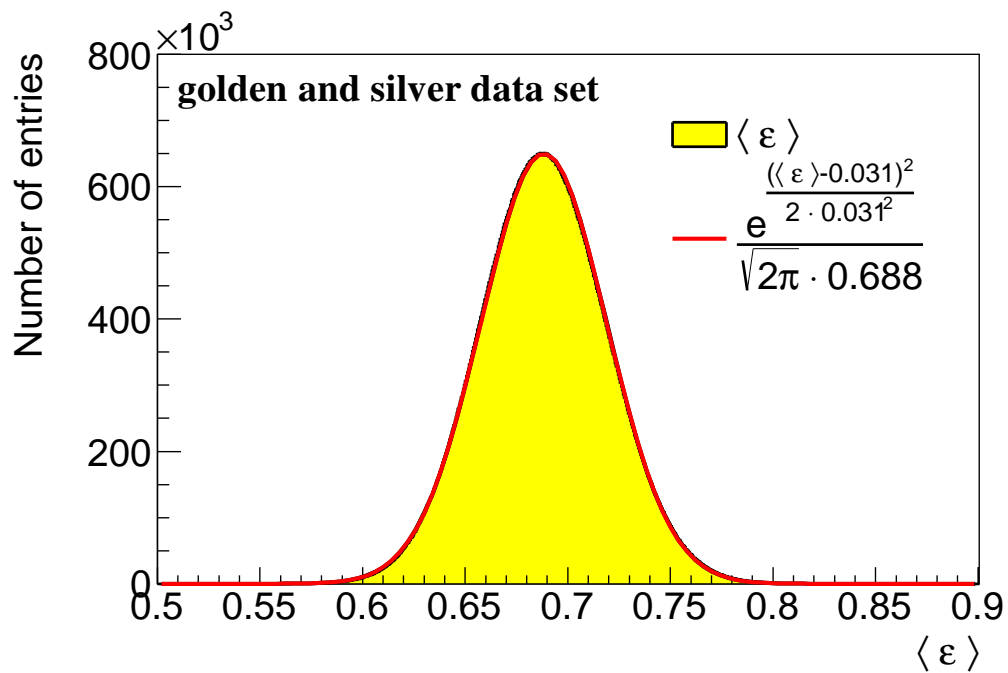


Figure D.1: Distribution resulting from the sampling method used to determine $\langle \varepsilon \rangle$ for the golden and the silver data set.

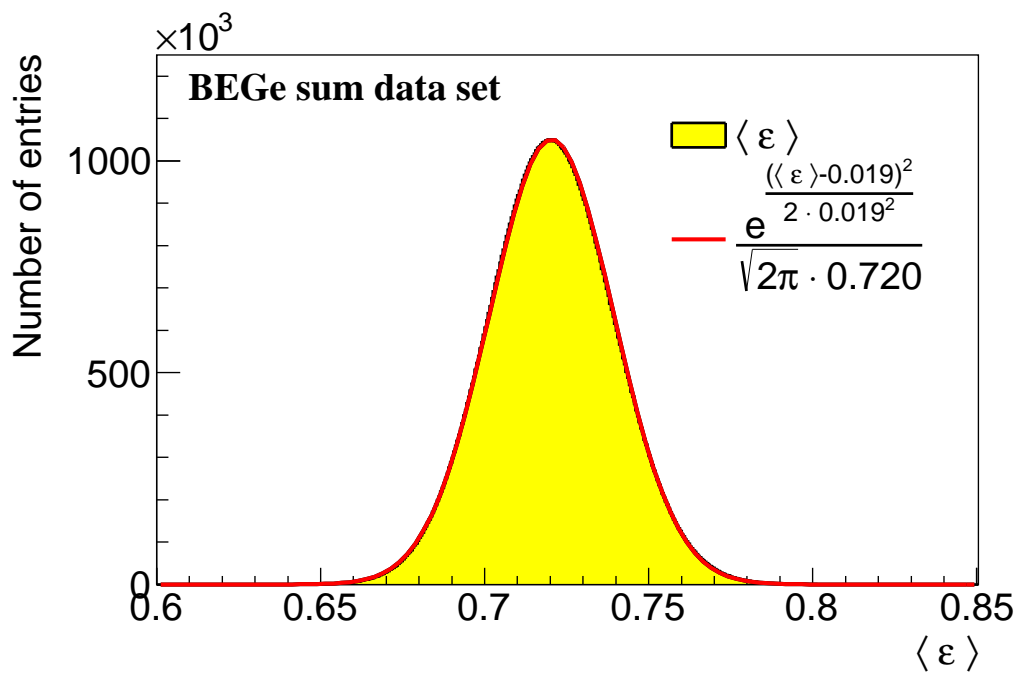


Figure D.2: Distribution resulting from the sampling method used to determine $\langle \varepsilon \rangle$ for the BEGe sum data set.

Bibliography

- [1] J. Schechter and J. Valle, *Neutrinoless double- β decay in $SU(2)\times U(1)$ theories*, Phys. Rev. D **25** (1982), 2951–2954.
- [2] A. S. Barabash, *Double beta decay: Historical review of 75 years of research*, Phys. Atom. Nucl. **74** (2011), 603–613.
- [3] E. Fireman, *Double Beta Decay*, Phys. Rev. **74** (1948), 1238.
- [4] H. V. Klapdor-Kleingrothaus, et al., *Latest results from the HEIDELBERG-MOSCOW double beta decay experiment*, Eur. Phys. J. A **12** (2001), 147–154.
- [5] C. E. Aalseth, et al., *IGEX ^{76}Ge neutrinoless double-beta decay experiment: Prospects for next generation experiments*, Phys. Rev. D **65** (2002), 092007.
- [6] M. Agostini, et al., *Results on neutrinoless double beta decay of ^{76}Ge from Gerda Phase I*, Phys. Rev. Lett. **111** (2013), 122503.
- [7] M. Auger, et al., *Search for Neutrinoless Double-Beta Decay in ^{136}Xe with EXO-200*, Phys. Rev. Lett. **109** (2012), 032505.
- [8] A. Gando, et al., *Limit on Neutrinoless $\beta\beta$ Decay of ^{136}Xe from the First Phase of KamLAND-Zen and Comparison with the Positive Claim in ^{76}Ge* , Phys. Rev. Lett. **110** (2013), 062502.
- [9] H. V. Klapdor-Kleingrothaus, I. V. Krivosheina, A. Dietz, and O. Chkvorets, *Search for neutrinoless double beta decay with enriched ^{76}Ge in Gran Sasso 1990-2003*, Phys. Lett. B **586** (2004), 198–212.
- [10] I. Abt et al., *A New ^{76}Ge Double Beta Decay Experiment at LNGS*, arXiv:hep-ex/0404039 (2004).
- [11] K.-H. Ackermann, et al., *The Gerda experiment for the search of $0\nu\beta\beta$ decay in ^{76}Ge* , Eur. Phys. J. C **73** (2013), 1–29.
- [12] K. Winter (ed.), *Neutrino Physics*, 1 ed., Cambridge University Press, 1991.
- [13] E. Fermi, *Tentativo di una teoria dell' emissione dei raggi β* , Ricerca Scient. **4** (1933), 491–495.

- [14] ———, *Versuch einer Theorie der β -Strahlen*, Z. Physik **88** (1934), 161–171.
- [15] E. Majorana, *Teoria simmetrica dell' elettrone e del positrone*, Nuovo Cimento **14** (1937), 171–184.
- [16] F. Reines and C. L. Cowan, *The Neutrino*, Nature **178** (1956), 446–449.
- [17] C. L. Cowan, et al., *Detection of the Free Neutrino: A Confirmation*, Science **124** (1956), 103–104.
- [18] R. Davis, *Attempt to Detect the Antineutrinos from a Nuclear Reactor by the $\text{Cl}^{37}(\bar{\nu}, e^-)\text{A}^{37}$ Reaction*, Phys. Rev. **97** (1955), 766–769.
- [19] T. D. Lee and C. N. Yang, *Question of parity conservation in weak interactions*, Phys. Rev. **104** (1956), 254–258.
- [20] C. S. Wu, et al., *Experimental Test of Parity Conservation in Beta Decay*, Phys. Rev. **105** (1957), 1413–1415.
- [21] R. L. Garwin, L. M. Lederman, and M. Weinrich, *Observations of the Failure of Conservation of Parity and Charge Conjugation in Meson Decays: the Magnetic Moment of the Free Muon*, Phys. Rev. **105** (1957), 1415–1417.
- [22] T. D. Lee and C. N. Yang, *Parity Nonconservation and a Two-Component Theory of the Neutrino*, Phys. Rev. **105** (1957), 1671–1675.
- [23] L. Landau, *On the conservation laws for weak interactions*, Nuclear Physics **3** (1957), 127–131.
- [24] A. Salam, *On parity conservation and neutrino mass*, Nuovo Cimento **5** (1957), 299–301.
- [25] M. Goldhaber, L. Grodzins, and A. W. Sunyar, *Helicity of Neutrinos*, Phys. Rev. **109** (1958), 1015–1017.
- [26] ALEPH, DELPHI, L3, OPAL, SLD Collaborations, LEP Electroweak Working Group, SLD Electroweak Group and SLD Heavy Flavour Group, *Precision Electroweak Measurements on the Z Resonance*, Phys. Rept. **427** (2006), 257–454.
- [27] R. Davis, D. S. Harmer, and K. C. Hoffman, *Search for Neutrinos from the Sun*, Phys. Rev. Lett. **20** (1968), 1205–1209.
- [28] J. N. Bahcall, N. A. Bahcall, and G. Shaviv, *Present Status of the Theoretical Predictions for the ^{37}Cl Solar-Neutrino Experiment*, Phys. Rev. Lett. **20** (1968), 1209–1212.
- [29] B. Pontecorvo, *Mesonium and Anti Mesonium*, Zh. Eksp. Teor. Fiz **33** (1957), 549–551.
- , *Mesonium and Anti-Mesonium*, Sov. Phys. JETP **6** (1957), 429.

- [30] B. Pontecorvo, *Inverse Beta Processes and Nonconservation of Lepton Charge*, Zh. Eksp. Teor. Fiz **34** (1957), 247.
———, *Inverse Beta Processes and Nonconservation of Lepton Charge*, Sov. Phys. JETP **7** (1958), 172–173.
- [31] Z. Maki, M. Nakagawa, and S. Sakata, *Remarks on the Unified Model of Elementary Particles*, Prog. Theor. Phys. **28** (1962), 870–880.
- [32] K. S. Hirata, et al., *Observation of ^8B solar neutrinos in the Kamiokande-II detector*, Phys. Rev. Lett. **63** (1989), 16–19.
- [33] A. I. Abazov, et al., *Search for neutrinos from the Sun using the reaction $^{71}\text{Ga}(\nu_e, e^-)^{71}\text{Ge}$* , Phys. Rev. Lett. **67** (1991), 3332–3335.
- [34] P. Anselmann, et al., *Solar neutrinos observed by GALLEX at Gran Sasso*, Phys. Lett. B **285** (1992), 376 – 389.
- [35] T. J. Haines, et al., *Calculation of Atmospheric Neutrino-Induced Backgrounds in a Nucleon-Decay Search*, Phys. Rev. Lett. **57** (1986), 1986–1989.
- [36] K. Hirata, et al., *Experimental study of the atmospheric neutrino flux*, Phys. Lett. B **205** (1988), 416–420.
- [37] Y. Fukuda, et al., *Evidence for Oscillation of Atmospheric Neutrinos*, Phys. Rev. Lett. **81** (1998), 1562–1567.
- [38] Q. R. Ahmad, et al., *Measurement of the Rate of $\nu_e + d \rightarrow p + p + e^-$ Interactions Produced by ^8B Solar Neutrinos at the Sudbury Neutrino Observatory*, Phys. Rev. Lett. **87** (2001), 071301.
- [39] L. Wolfenstein, *Neutrino oscillations in matter*, Phys. Rev. D **17** (1978), 2369–2374.
- [40] S. Mikheyev and A. Smirnov, *Resonance enhancement of oscillations in matter and solar neutrino spectroscopy*, Sov. J. Nucl. Phys. **42** (1985), 913–917.
———, *Resonant amplification of ν oscillations in matter and solar-neutrino spectroscopy*, Nuovo Cimento C **9** (1986), 17–26.
- [41] A. Strumia and F. Vissani, *Neutrino masses and mixings and...*, arXiv:hep-ph/0606054v3 (2010).
- [42] D. V. Forero, M. Tórtola, and J. W. F. Valle, *Global status of neutrino oscillation parameters after Neutrino-2012*, Phys. Rev. D **86** (2012), 073012–073020.
- [43] G. L. Fogli, et al., *Global analysis of neutrino masses, mixings, and phases: Entering the era of leptonic CP violation searches*, Phys. Rev. D **86** (2012), 013012.

- [44] C. Giunti and C. W. Kim, *Fundamentals of Neutrino Physics and Astrophysics*, Oxford University Press, 2007.
- [45] P. Minkowski, $\mu \rightarrow e\gamma$ at a rate of one out of 109 muon decays?, *Phys. Lett. B* **67** (1977), 421 – 428.
- [46] M. Gell-Mann, P. Ramond, and R. Slansky, *Supergravity*, North Holland, 1979.
- [47] R. N. Mohapatra and G. Senjanović, *Neutrino Mass and Spontaneous Parity Non-conservation*, *Phys. Rev. Lett.* **44** (1980), 912–915.
- [48] T. Yanagida, *Horizontal Symmetry and Masses of Neutrinos*, *Prog. Theor. Phys.* **64** (1980), 1103–1105.
- [49] K. Abazajian, et al., *Cosmological and astrophysical neutrino mass measurements*, *Astropart. Phys.* **35** (2011), 177 – 184.
- [50] <<http://www.rssd.esa.int/index.php?project=Planck>>.
- [51] P. A. R. Ade, et al., *Planck 2013 results: Cosmological parameters*, arXiv:astro-ph/1303.5076 (submitted to A&A) (2013).
- [52] C. Kraus, et al., *Final results from phase II of the Mainz neutrino mass search in tritium β decay*, *Eur. Phys. J. C* **40** (2005), 447–468.
- [53] V. N. Aseev, et al., *Upper limit on the electron antineutrino mass from the Troitsk experiment*, *Phys. Rev. D* **84** (2011), 112003.
- [54] C. Weinheimer, *KATRIN, a next generation tritium β decay experiment in search for the absolute neutrino mass scale*, *Prog. Part. Nucl. Phys.* **48** (2002), 141 – 150.
- [55] L. Ekström and R. Firestone, *WWW Table of Radioactive Isotopes*, database version 2/28/99 from URL <http://ie.lbl.gov/toi/index.htm>.
- [56] J. Suhonen and O. Civitarese, *Weak-interaction and nuclear-structure aspects of nuclear double beta decay*, *Phys. Rep.* **300** (1998), 123 – 214.
- [57] H. Primakoff and S. P. Rosen, *Double beta decay*, *Rep. Prog. Phys.* **22** (1959), 121.
- [58] F. T. Avignone, S. R. Elliott, and J. Engel, *Double beta decay, Majorana neutrinos, and neutrino mass*, *Rev. Mod. Phys.* **80** (2008), 481–516.
- [59] W. H. Furry, *On Transition Probabilities in Double Beta-Disintegration*, *Phys. Rev* **56** (1939), 1184–1193.
- [60] M. Duerr, M. Lindner, and A. Merle, *On the quantitative impact of the Schechter-Valle theorem*, *JHEP* **2011** (2011), 1–19.

- [61] W. Rodejohann, *Neutrino-less double beta decay and particle physics*, J. Mod. Phys. E **20** (2011), 1833–1930.
- [62] M. Doi, T. Kotani, and E. Takasugi, *Double Beta Decay and Majorana Neutrino*, Prog. Theor. Phys. Suppl. **83** (1985), 1–175.
- [63] J. J. Gómez-Cadenas, et al., *The search for neutrinoless double beta decay*, Riv. Nuovo Cimento **35** (2012), 29–98.
- [64] H. Primakoff and S. P. Rosen, *Nuclear Double-Beta Decay and a New Limit on Lepton Nonconservation*, Phys. Rev. **184** (1969), 1925–1933.
- [65] W. Rodejohann, *Neutrinoless double-beta decay and neutrino physics*, J. Phys. G **39** (2012), 124008.
- [66] K. N. Abazajian, et al., *Light Sterile Neutrinos: A White Paper*, arXiv:hep-ph/1204.5379 (2012).
- [67] Y. Chikashige, R. N. Mohapatra, and R. D. Peccei, *Spontaneously Broken Lepton Number and Cosmological Constraints on the Neutrino Mass Spectrum*, Phys. Rev. Lett. **45** (1980), 1926–1929.
- [68] Y. Chikashige, R. Mohapatra, and R. Peccei, *Are there real goldstone bosons associated with broken lepton number?*, Phys. Lett. B **98** (1981), 265 – 268.
- [69] C. Aulakh and R. Mohapatra, *The neutrino as the supersymmetric partner of the majoron*, Phys. Lett. B **119** (1982), 136–140.
- [70] G. Gelmini and M. Roncadelli, *Left-handed neutrino mass scale and spontaneously broken lepton number*, Phys. Lett. B **99** (1981), 411–415.
- [71] Z. Berezhiani, A. Smirnov, and J. Valle, *Observable majoron emission in neutrinoless double beta decay*, Phys. Lett. B **291** (1992), 99–105.
- [72] A. Masiero and J. Valle, *A model for spontaneous R parity breaking*, Phys. Lett. B **251** (1990), 273–278.
- [73] R. N. Mohapatra and P. B. Pal, *Massive Neutrinos in Physics and Astrophysics*, World Scientific Publishing Co, 1991.
- [74] R. Mohapatra and E. Takasugi, *Neutrinoless double beta decay with double majoron emission*, Phys. Lett. B **211** (1988), 192–196.
- [75] C. Burgess and J. Cline, *Majorons without majorana masses and neutrinoless double beta decay*, Phys. Lett. B **298** (1993), 141–148.
- C. P. Burgess and J. M. Cline, *New class of Majoron-emitting double- β decays*, Phys. Rev. D **49** (1994), 5925–5944.

- [76] P. Bamert, C. Burgess, and R. Mohapatra, *Multi-majoron modes for neutrinoless double-beta decay*, Nucl. Phys. B **449** (1995), 25–48.
- [77] C. D. Carone, *Double beta decay with vector majorons*, Phys. Lett. B **308** (1993), 85–88.
- [78] J. Montero, C. de S. Pires, and V. Pleitez, *Neutrinoless double beta decay with and without Majoron-like boson emission in a 3-3-1 model*, Phys. Rev. D **64** (2001), 096001.
- [79] R. Mohapatra, A. Pérez-Lorenzana, and C. de S. Pires, *Neutrino mass, bulk majoron and neutrinoless double beta decay*, Phys. Lett. B **491** (2000), 143–147.
- [80] V. I. Tretyak and Y. G. Zdesenko, *Tables of double beta decay data*, At. Data Nucl. Data Tables **61** (1995), 43–90.
- [81] ———, *Tables of double beta decay data - an update*, At. Data Nucl. Data Tables **80** (2002), 83–116.
- [82] M. Hirsch, H. Klapdor-Kleingrothaus, S. Kovalenko, and H. Päs, *On the observability of Majoron emitting double beta decays*, Phys. Lett. B **372** (1996), 8–14.
- [83] R. Arnold, et al., *Limits on different majoron decay modes of ^{100}Mo and ^{82}Se for neutrinoless double beta decays in the NEMO-3 experiment*, Nucl. Phys. A **765** (2006), 483–494.
- [84] F. T. Avignone, G. S. King, and Y. G. Zdesenko, *Next generation double-beta decay experiments: metrics for their evaluation*, New J. Phys. **7** (2005), 6.
- [85] S. Umehara, et al., *Neutrino-less double- β decay of ^{48}Ca studied by $\text{CaF}_2(\text{Eu})$ scintillators*, Phys. Rev. C **78** (2008), 058501.
- [86] M. Agostini, et al., *Measurement of the half-life of the two-neutrino double beta decay of ^{76}Ge with the GERDA experiment*, J. Phys. G: Nucl. Part. Phys. **40** (2013), 035110.
- [87] A. S. Barabash and V. B. Brudanin, *Investigation of double-beta decay with the NEMO-3 detector*, Phys. At. Nucl. **74** (2011), 312–317.
- [88] J. Argyriades, et al., *Measurement of the two neutrino double beta decay half-life of Zr-96 with the NEMO-3 detector*, Nucl. Phys. A **847** (2010), 168 – 179.
- [89] F. A. Danevich, et al., *Search for 2β decay of cadmium and tungsten isotopes: Final results of the Solotvina experiment*, Phys. Rev. C **68** (2003), 035501.
- [90] E. Andreotti, et al., *^{130}Te neutrinoless double-beta decay with CUORICINO*, Astropart. Phys. **34** (2011), 822 – 831.

- [91] J. Albert, et al., *An improved measurement of the $2\nu\beta\beta$ half-life of Xe-136 with EXO-200*, arXiv:nucl-ex/1306.6106 (2013).
- [92] A. Gando, et al., *Limits on Majoron-emitting double- β decays of ^{136}Xe in the KamLAND-Zen experiment*, Phys. Rev. C **86** (2012), 021601.
- [93] J. Argyriades, et al., *Measurement of the double- β decay half-life of ^{150}Nd and search for neutrinoless decay modes with the NEMO-3 detector*, Phys. Rev. C **80** (2009), 032501.
- [94] A. Barabash, *Limit on $2\beta(0\nu\chi^0)$ -decay of ^{48}Ca* , Phys. Lett. B **216** (1989), 257 – 258.
- [95] M. Günther, et al., *Bounds on new Majoron models from the Heidelberg-Moscow experiment*, Phys. Rev. D **54** (1996), 3641–3644.
- [96] R. Arnold, et al., *Limits on different Majoron decay modes of ^{100}Mo , ^{116}Cd , ^{82}Se and ^{96}Zr for neutrinoless double beta decays in the NEMO-2 experiment*, Nucl. Phys. A **678** (2000), 341–352.
- [97] R. Arnold, et al., *Measurement of the $\beta\beta$ Decay Half-Life of ^{130}Te with the NEMO-3 Detector*, Phys. Rev. Lett. **107** (2011), 062504.
- [98] C. Arnaboldi, et al., *A calorimetric search on double beta decay of ^{130}Te* , Phys. Lett. B **557** (2003), 167–175.
- [99] R. Arnold, et al., *Technical design and performance of the NEMO 3 detector*, Nucl. Instr. Meth. A **536** (2005), 79–122.
- [100] L. Simard et al., *The NEMO-3 results after completion of data taking*, J. Phys. **375** (2012), 042011.
- [101] C. Arnaboldi, et al., *Results from a search for the $0\nu\beta\beta$ -decay of ^{130}Te* , Phys. Rev. C **78** (2008), 035502.
- [102] A. Gando, et al., *Measurement of the double- β decay half-life of ^{136}Xe with the KamLAND-Zen experiment*, Phys. Rev. C **85** (2012), 045504.
- [103] M. Auger, et al., *The EXO-200 detector; part I: detector design and construction*, JINST **7** (2012), P05010.
- [104] C. Aalseth, et al., *Recent results from the IGEX double-beta decay experiment*, Nucl. Phys. B **48** (1996), 223 – 225.
- [105] M. Günther, et al., *Heidelberg-Moscow $\beta\beta$ experiment with ^{76}Ge : Full setup with five detectors*, Phys. Rev. D **55** (1997), 54–67.
- [106] H. V. Klapdor-Kleingrothaus and I. V. Krivosheina, *The evidence for the observation of $0\nu\beta\beta$ decay: the identification of $0\nu\beta\beta$ events from the full spectra*, Mod. Phys. Lett. A **21** (2006), 1547–1566.

- [107] B. Schwingenheuer, *Status and prospects of searches for neutrinoless double beta decay*, *Ann. Phys.* **525** (2013), 269–280.
- [108] T. Bernatowicz, et al., *Neutrino mass limits from a precise determination of $\beta\beta$ -decay rates of ^{128}Te and ^{130}Te* , *Phys. Rev. Lett.* **69** (1992), 2341–2344.
- [109] H. V. Thomas, et al., *Geochemical constraints on the half-life of ^{130}Te* , *Phys. Rev. C* **78** (2008), 054606.
- [110] Y. Farzan, *Bounds on the coupling of the Majoron to light neutrinos from supernova cooling*, *Phys. Rev. D* **67** (2003), 073015.
- [111] R. Tomàs, H. Päs, and J. W. F. Valle, *Generalized bounds on Majoron-neutrino couplings*, *Phys. Rev. D* **64** (2001), 095005.
- [112] M. Kachelriess, R. Tomàs, and J. W. F. Valle, *Supernova bounds on Majoron-emitting decays of light neutrinos*, *Phys. Rev. D* **62** (2000), 023004.
- [113] A. Lessa and O. Peres, *Revising limits on neutrino-Majoron couplings*, *Phys. Rev. D* **75** (2007), 094001.
- [114] G. F. Knoll, *Radiation detection and measurement*, 3rd ed., John Wiley & Sons, Inc., 2000.
- [115] M. J. Berger et al., *XCOM: Photon Cross Section Database (version 1.4)*, <http://physics.nist.gov/xcom>, National Institute of Standards and Technology, Gaithersburg, MD (2009).
- [116] C. Grupen, B. Shwartz, and H. Spieler, *Particle Detectors*, 2nd ed., Cambridge University Press, 2008.
- [117] K. Kleinknecht, *Detektoren für Teilchenstrahlung*, 4th ed., Teubner, 2005.
- [118] T. Mukoyama, *Range of electrons and positrons*, *Nucl. Instr. Meth.* **134** (1976), 125–127.
- [119] I. Abt, et al., *Operation of an 18-fold segmented n-type HPGe detector in liquid nitrogen*, *JINST* **4** (2009), P11008.
- [120] H. G. Reik and H. Risken, *Drift Velocity and Anisotropy of Hot Electrons in n Germanium*, *Phys. Rev.* **126** (1962), 1737–1746.
- [121] W. Sasaki et al., *Anisotropy of hot electrons in germanium*, *J. Phys. Chem. Sol.* **8** (1959), 250–256.
- [122] Z. He, *Review of the Shockley-Ramo theorem and its application in semiconductor gamma-ray detectors*, *Nucl. Instr. Meth. A* **463** (2001), 250–267.

- [123] B. Majorovits and H. V. Klapdor-Kleingrothaus, *Digital pulshape analysis by neural networks for the Heidelberg-Moscow-Double-Beta-Decay-Experiment*, Eur. Phys. J. A **6** (1999), 463–469.
- [124] D. González, et al., *Pulse-shape discrimination in the IGEX experiment*, Nucl. Instr. Meth. A **515** (2003), 634–643.
- [125] M. Agostini et al., *Pulse shape discrimination for Gerda Phase I data*, Eur. Phys. J. C **73** (2013), 1–17.
- [126] D. Budjáš, et al., *Pulse shape discrimination studies with a Broad-Energy Germanium detector for signal identification and background suppression in the GERDA double beta decay experiment*, JINST **4** (2009), P10007.
- [127] M. Barnabé-Heider, D. Budjáš, K. Gusev, and S. Schönert, *Operation and performance of a bare broad-energy germanium detector in liquid argon*, JINST **5** (2010), P10007.
- [128] M. Agostini, et al., *Signal modeling of high-purity Ge detectors with a small read-out electrode and application to neutrinoless double beta decay search in ^{76}Ge* , JINST **6** (2011), P03005.
- [129] M. Agostini, et al., *Characterization of a broad energy germanium detector and application to neutrinoless double beta decay search in ^{76}Ge* , JINST **6** (2011), P04005.
- [130] G. Heusser, *Low-Radioactivity Background Techniques*, Annu. Rev. Nuc. Part. Sci. **45** (1995), 543–590.
- [131] H. V. Klapdor-Kleingrothaus, et al., *GENIUS-TF: a test facility for the GENIUS project*, Nucl. Instr. Meth. A **481** (2002), 149–159.
- [132] E. Andreotti, et al., *HEROICA: an underground facility for the fast screening of germanium detectors*, JINST **8** (2013), P06012.
- [133] M. Agostini, L. Pandola, and P. Zavarise, *Off-line data processing and analysis for the GERDA experiment*, J. Phys.: Conf. Ser. **368** (2012), 012047.
- [134] P. Zavarise, et al., *Off-line data quality monitoring for the GERDA experiment*, J. Phys.: Conf. Ser. **375** (2012), 042028.
- [135] M. Agostini, *Signal and background studies for the search of neutrinoless double beta decay in GERDA*, Ph.D. thesis, Technische Universität München, 2013.
- [136] P. Zavarise, *Analysis of the first data of the GERDA experiment at LNGS*, Ph.D. thesis, Università degli Studi dell'Aquila, 2013.

- [137] M. Agostini, D. Budjáš, L. Pandola, and P. Zavarise, *GERDA off-line analysis of HPGe detector signals*, GERDA Scientific Technical Reports (2011), GSTR-11-012.
- [138] M. Agostini, A. Lazzaro, and L. Pandola, *Performance of the quality cuts in GERDA Phase I*, GERDA Scientific Technical Reports (2013), GSTR-13-022.
- [139] G. Benato, *FWHM at $Q_{\beta\beta}$ and Energy Reconstruction Uncertainty for the GERDA Phase I Data*, GERDA Scientific Technical Reports (2013), GSTR-13-015.
- [140] _____, *Calibration of the GERDA Phase I data*, GERDA Scientific Technical Reports (in preparation).
- [141] M. Agostini, L. Pandola, P. Zavarise, and O. Volynets, *GELATIO: a general framework for modular digital analysis of high-purity Ge detector signals*, JINST **6** (2011), P08013.
- [142] R. Brun and F. Rademakers, *ROOT - An object oriented data analysis framework*, Nucl. Instr. Meth. A **389** (1997), 81–86.
- [143] S. W. Smith, *The Scientist and Engineer's Guide to Digital Signal Processing*, California Technical Publishing, 1999.
- [144] M. Tarka, *Studies of neutron flux suppression from a γ -ray source and the GERDA calibration system*, Ph.D. thesis, Universität Zürich, 2012.
- [145] F. Froberg, *Calibration of Phase I of the GERDA double beta decay experiment*, Ph.D. thesis, Universität Zürich, 2012.
- [146] L. Baudis, A. Ferella, F. Froberg, and M. Tarka, *Monte Carlo studies and optimization for the calibration system of the Gerda experiment*, Nucl. Instr. Meth. A **729** (2013), 557 – 564.
- [147] K. Debertin and R. G. Helmer, *Gamma- and x-ray spectrometry with semiconductor detectors*, North Holland, Amsterdam, 1988.
- [148] P. Benetti, et al., *Measurement of the specific activity of ^{39}Ar in natural argon*, Nucl. Instr. Meth. A **574** (2007), 83 – 88.
- [149] M. Agostini, et al., *The background in the $0\nu\beta\beta$ experiment GERDA*, arXiv:insdet/1306.5084 (accepted for publication by Eur. Phys. J. C) (2013).
- [150] A. Caldwell, D. Kollár, and K. Kröninger, *BAT - The Bayesian analysis toolkit*, Comput. Phys. Commun. **180** (2009), 2197 – 2209.
- [151] O. Chkvorets, *Search for double beta decay with HPGe detectors at the Gran Sasso underground laboratory*, Ph.D. thesis, Universität Heidelberg, 2008.

- [152] S. Agostinelli, et al., *Geant4 - a simulation toolkit*, Nucl. Instr. Meth. A **506** (2003), 250–303.
J. Allison, et al., *Geant4 developments and applications*, Nuclear Science, IEEE Trans. Nucl. Sci. **53** (2006), 270–278.
- [153] M. Boswell, et al., *MaGe - a Geant4-Based Monte Carlo Application Framework for Low-Background Germanium Experiments*, IEEE Trans. Nucl. Sci. **58** (2011), 1212–1220.
- [154] L. Pandola, et al., *Monte Carlo evaluation of the muon-induced background in the GERDA double beta decay experiment*, Nucl. Instr. Meth. A **570** (2007), 149–158.
- [155] G. Meierhofer, et al., *Prompt γ rays in ^{77}Ge and ^{75}Ge after thermal neutron capture*, Eur. Phys. J. A **48** (2012), 1–22.
- [156] I. Barabanov, et al., *Shielding of the GERDA experiment against external gamma background*, Nucl. Instr. Meth. A **606** (2009), 790 – 794.
- [157] D. Mei, et al., *Neutron inelastic scattering processes as a background for double- β decay experiments*, Phys. Rev. C **77** (2008), 054614.
- [158] G. Zuzel and H. Simgen, *High sensitivity radon emanation measurements*, Appl. Rad. Isot. **67** (2009), 889 – 893.
- [159] D. Lenz, *Pulse Shapes and Surface Effects in Segmented Germanium Detectors*, Ph.D. thesis, Technische Universität München, 2010.
- [160] N. Becerici-Schmidt, *Background modeling and signal search in the first phase of the neutrinoless double beta decay experiment GERDA*, Ph.D. thesis, in preparation.
- [161] R. Aggarwal and A. Caldwell, *Error bars for distributions of numbers of events*, Eur. Phys. J. Plus **127** (2012), 1–8.
- [162] N. Becerici-Schmidt and B. Majorovits, *Estimation of an upper limit on the Thorium activity in the Heat Exchanger*, GERDA Scientific Technical Reports (2012), GSTR–12–008.
- [163] O. Ponkratenko, V. Tretyak, and Y. Zdesenko, *Event generator DECAY4 for simulating double-beta processes and decays of radioactive nuclei*, Phys. At. Nucl. **63** (2000), 1282–1287.
- [164] E. Aguayo, et al., *Characteristics of signals originating near the lithium-diffused $n+$ contact of high purity germanium p -type point contact detectors*, Nucl. Instr. Meth. A **701** (2013), 176 – 185.
- [165] B. Lehnert, *private communication and contributions at GERDA General Meetings*.

- [166] A. Caldwell and K. Kröniger, *Signal discovery in sparse spectra: A Bayesian analysis*, Phys. Rev. D **74** (2006), 092003.
- [167] M. Barnabé-Heider, *Performance and stability tests of bare high purity germanium detectors in liquid argon for the GERDA experiment*, Ph.D. thesis, Ruperto-Carola Universität Heidelberg, 2009.
- [168] F. Avignone, et al., *Theoretical and experimental investigation of cosmogenic radioisotope production in germanium*, Nucl. Phys. B (Proc. Suppl.) **28** (1992), 280 – 285.
- [169] F. Beaujean, A. Caldwell, D. Kollár, and K. Kröniger, *p-values for model evaluation*, Phys. Rev. D **83** (2011), 012004.
- [170] C. O’Shaughnessy, *contribution at GERDA General Meeting, 5-7 November 2012*.
- [171] K. Amako, et al., *Comparison of Geant4 Electromagnetic Physics Models Against the NIST Reference Data*, IEEE Trans. Nucl. Sci. **52** (2005), 910–918.
- [172] E. Poon and F. Verhaegen, *Accuracy of the photon and electron physics in GEANT4 for radiotherapy applications*, Med. Phys. **32** (2005), 1696–1711.
- [173] G. Cirrone, et al., *Validation of the Geant4 electromagnetic photon cross-sections for elements and compounds*, Nucl. Instr. Meth. A **618** (2010), 315 – 322.
- [174] A. Vasenko et al., *NEW RESULTS IN THE ITEP/YePI DOUBLE BETA-DECAY EXPERIMENT WITH ENRICHED GERMANIUM DETECTORS*, Mod. Phys. Lett. A **05** (1990), 1299–1306.
- [175] H. S. Miley, et al., *Suggestive evidence for the two-neutrino double- β decay of ^{76}Ge* , Phys. Rev. Lett. **65** (1990), 3092–3095.
- [176] F. Avignone, et al., *Confirmation of the observation of $2\nu\beta\beta$ decay of ^{76}Ge* , Phys. Lett. B **256** (1991), 559 – 561.
- [177] F. Avignone, *Double-beta decay: Some recent results and developments*, Prog. Part. Phys. **32** (1994), 223 – 245.
- [178] A. Morales, *Review on double beta decay experiments and comparison with theory*, Nucl. Phys. B (Proc. Suppl.) **77** (1999), 335–345.
- [179] A. Morales and J. Morales, *The neutrinoless double beta decay: The case for germanium detectors*, Nucl. Phys. B (Proc. Suppl.) **114** (2003), 141–157.
- [180] C. Dörr and H. Klapdor-Kleingrothaus, *New Monte-Carlo simulation of the HEIDELBERG-MOSCOW double beta decay experiment*, Nucl. Instr. Meth. A **513** (2003), 596 – 621.

- [181] A. Bakalyarov, et al., *Results of the experiment on investigation of Germanium-76 double beta decay. Experimental data of Heidelberg-Moscow collaboration November 1995 - August 2001*, Phys. Part. Nucl. Lett. **2** (2005), 77–81.
———, *Results of the experiment on investigation of Germanium-76 double beta decay. Experimental data of Heidelberg-Moscow collaboration November 1995 - August 2001*, Pisma Fiz. Elem. Chast. Atom. Yadra **2** (2005), 21–28.
- [182] B. Pritychenko, *B(E2) and double beta decay nuclear data projects*, Proc. Nuclear Structure (East Lansing, MI, 3-6 June) (2008).
- [183] A. S. Barabash, *Precise half-life values for two-neutrino double- β decay*, Phys. Rev. C **81** (2010), 035501.
- [184] J. Kotila and F. Iachello, *Phase space factors for double- β decay*, Phys. Rev. C **85** (2012), 034316.
- [185] E.-W. Grewe, et al., *The ($d^2\text{He}$) reaction on ^{76}Se and the double- β -decay matrix elements for $A = 76$* , Phys. Rev. C **78** (2008), 044301.
- [186] J. H. Thies, et al., *The ($^3\text{He}, t$) reaction on ^{76}Ge and the double- β -decay matrix element*, Phys. Rev. C **86** (2012), 014304.
- [187] F. Šimkovic, V. Rodin, A. Faessler, and P. Vogel, *$0\nu\beta\beta$ and $2\nu\beta\beta$ nuclear matrix elements, quasiparticle random-phase approximation, and isospin symmetry restoration*, Phys. Rev. C **87** (2013), 045501.
- [188] M. T. Mustonen and J. Engel, *Large-scale calculations of the double- β decay of ^{76}Ge , ^{130}Te , ^{136}Xe , and ^{150}Nd in the deformed self-consistent Skyrme quasiparticle random-phase approximation*, Phys. Rev. C **87** (2013), 064302.
- [189] T. R. Rodriguez and G. Martinez-Pinedo, *Energy Density Functional Study of Nuclear Matrix Elements for Neutrinoless $\beta\beta$ Decay*, Phys. Rev. Lett. **105** (2010), 252503.
- [190] J. Menéndez, A. Poves, E. Caurier, and F. Nowacki, *Disassembling the nuclear matrix elements of the neutrinoless $\beta\beta$ decay*, Nucl. Phys. A **818** (2009), 139 – 151.
- [191] J. Barea, J. Kotila, and F. Iachello, *Nuclear matrix elements for double- β decay*, Phys. Rev. C **87** (2013), 014315.
- [192] J. Suhonen and O. Civitarese, *Effects of orbital occupancies and spin-orbit partners on $0\nu\beta\beta$ -decay rates*, Nucl. Phys. A **847** (2010), 207 – 232.
- [193] A. Meroni, S. Petcov, and F. Šimkovic, *Multiple CP non-conserving mechanisms of $(\beta\beta)_{0\nu}$ -decay and nuclei with largely different nuclear matrix elements*, J. High Energy Phys. **2013** (2013), 1–29.

-
- [194] A. Caldwell, *Example Analysis and Opening the blinded window(s)*, GERDA Scientific Technical Reports (2012), GSTR-12-500v1.
- [195] H. Jeffreys, *The Theory of Probability*, OUP Oxford, 1998.
- [196] N. Becerici-Schmidt, S. Hemmer, B. Lehnert, and L. Pandola, *Detection efficiency of $0\nu\beta\beta$ decays of the Phase I detectors*, GERDA Scientific Technical Reports (2013), GSTR-13-010.
- [197] L. Pandola, *Parameters and facts for the analysis dataset of the $0\nu\beta\beta$ decay of GERDA Phase I*, GERDA Scientific Technical Reports (2013), GSTR-13-012.
- [198] A. Smolnikov and P. Grabmayr, *Conversion of experimental half-life to effective electron neutrino mass in $0\nu\beta\beta$ decay*, Phys. Rev. C **81** (2010), 028502.
- [199] N. Becerici-Schmidt, et al., *Measurement of the half-life of the $\beta\beta$ decay with GERDA*, GERDA Scientific Technical Reports (2012), GSTR-12-008.
- [200] ———, *Addendum to GSTR-12-009: Measurement of the half-life of the $2\nu\beta\beta$ decay*, GERDA Scientific Technical Reports (2012), GSTR-12-010.
- [201] R. Arnold, et al., *Double- β decay of ^{82}Se* , Nucl. Phys. A **636** (1998), 209 – 223.
- [202] R. Arnold, et al., *Double beta decay of ^{96}Zr* , Nucl. Phys. A **658** (1999), 299 – 312.

Acknowledgments

An enormous thank-you goes to Riccardo Brugnera for being the best supervisor I could have wished for. His great knowledge, constant support, and endless encouragement guided me through all ups and downs of the past three years. I also would like to thank Alberto Garfagnini, whose never-ending energy and helpfulness were so essential for this work. I am grateful to both of them for making me feel at home in their group from the first moment on.

A big thank-you toast goes to the members of GERDA for the good collaboration (and even better collaboration meetings). I especially want to thank Luciano Pandola for his immense patience and all the help and support he provided, independently of what time and day it was. I would like to thank Giovanni for countless discussions about everything between physics and the sense of life and for doing such a good job as my “second husband”. I thank Katharina for the great smile and good mood she brings by my office every morning and for bringing a little bit of Germany to Padova. I want to thank Neslihan for all the enlightening and encouraging phone calls over the past years.

I would like to thank Antonio, Rosanna, Angela, Daniele, and Angelo for their friendship and all the fun that lightened up the long office days, beginning with five o'clock tea and ending with the great frittella-contest.

Thank you also to the nine-thirty coffee round, who eased the start into the day with humor and some good pieces of advice.

A thank-you also to Alessio, Lucio, Marina, Melissa, and Mario, who reminded me how much fun science is.

Special thanks go to Vroni, who is always there for me.

I am endlessly grateful to my family: Mosè, Lucia, Daniela, Fulvio, Arianna and Laura, who accepted me without hesitation. My parents and my brother, whose support and encouragement carry me through my life. My husband Gianluca, who pushes me, when I need to be pushed, slows me down, when I need to be slowed down, and makes me feel special every single day of my life.

